

AD-A068 190

MASSACHUSETTS INST OF TECH CAMBRIDGE GAS TURBINE AND--ETC F/G 20/5
FUNDAMENTAL MECHANISMS OF NONEQUILIBRIUM MHD LASING PHENOMENA. (U)
DEC 78 J L KERREBROCK

F44620-76-C-0067

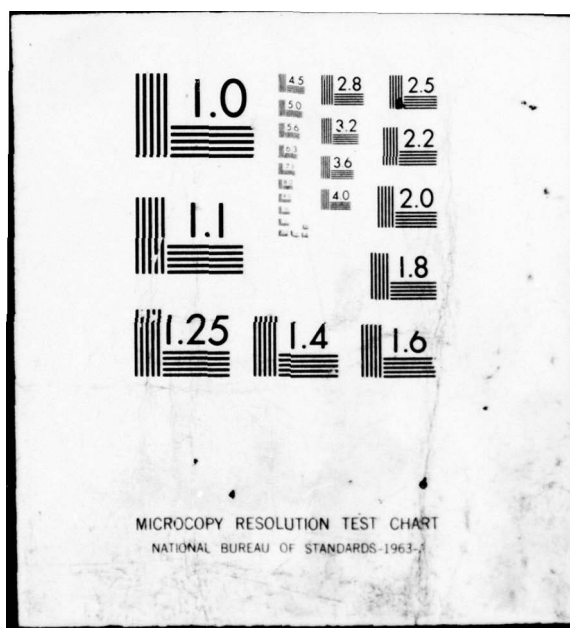
AFOSR-TR-79-0506

NL

UNCLASSIFIED

1 OF 5
AD
A068190





AFOSR-TR- 79-0506

12

LEVEL

11
A068190

ADA068190

FUNDAMENTAL MECHANISMS OF NONEQUILIBRIUM
MHD LASING PHENOMENA

J. L. KERREBROCK

GAS TURBINE AND PLASMA DYNAMICS LABORATORY
MASSACHUSETTS INSTITUTE OF TECHNOLOGY
CAMBRIDGE, MASSACHUSETTS 02139

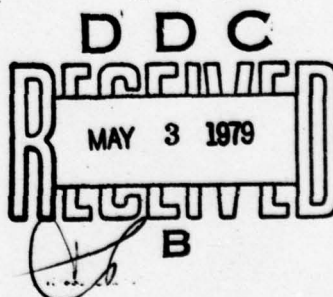
DDC FILE COPY

DECEMBER 1978

FINAL REPORT 01 MARCH 1977 - 28 FEBRUARY 1978

Approved for public release; distribution unlimited

AIR FORCE OFFICE OF SCIENTIFIC RESEARCH
BOLLING AIR FORCE BASE, D C 20332
AIR FORCE SYSTEMS COMMAND
UNITED STATES AIR FORCE



79 04 26 384

AFOR-TR-40-000

INFORMATIONAL MECHANISMS OF NON-OUTER-PLANET
AND LASTING PHENOMENA

U. S. RESEARCH
EDUCATIONAL AND PRACTICAL DYNAMICS LABORATORY
RESEARCHERS INSTITUTE OF TECHNOLOGY
CAMBRIDGE, MASSACHUSETTS, 02139

DECEMBER 10, 19

DDC FILE COPY

ADVOGATO

Approved for public release by the Air Force Research Laboratory
Distribution is unlimited.

AIR FORCE SCIENTIFIC RESEARCH
SUPPORT LABORATORY REPORT NO. 3213
AIR FORCE SCIENTIFIC RESEARCH
UNITED STATES AIR FORCE



AIR FORCE OFFICE OF SCIENTIFIC RESEARCH (AFSC)
NOTICE OF TRANSMITTAL TO DDC
This technical report has been reviewed and is
approved for public release IAW AFM 100-12 (7B)
Distribution is unlimited.

A. D. BLOSE
Technical Information Officer

UNCLASSIFIED

SECURITY CLASSIFICATION OF THIS PAGE (When Data Entered)

19 REPORT DOCUMENTATION PAGE		READ INSTRUCTIONS BEFORE COMPLETING FORM	
18 REPORT NUMBER AFOSR-TR- 79-0506	2. GOVT ACCESSION NO.	3. RECIPIENT'S CATALOG NUMBER	
4. TITLE (and Subtitle) FUNDAMENTAL MECHANISMS OF NONEQUILIBRIUM MHD LASING PHENOMENA	5. TYPE OF REPORT & PERIOD COVERED FINAL REPORT 31 March 1977 - 28 Feb 1978		
7. AUTHOR(s) JACK L. KERREBROCK	8. CONTRACT OR GRANT NUMBER(s) F44620-76-C-0067		
9. PERFORMING ORGANIZATION NAME AND ADDRESS MASSACHUSETTS INSTITUTE OF TECHNOLOGY GAS TURBINE & PLASMA DYNAMICS LABORATORY CAMBRIDGE, MA 02139	10. PROGRAM ELEMENT, PROJECT, TASK AREA & WORK UNIT NUMBERS 2308 C1 61102F		
11. CONTROLLING OFFICE NAME AND ADDRESS AIR FORCE OFFICE OF SCIENTIFIC RESEARCH/NA BLDG 410 BOLLING AIR FORCE BASE, D.C. 20332	12. REPORT DATE 11 December 1978		
14. MONITORING AGENCY NAME & ADDRESS (if different from Controlling Office)	13. NUMBER OF PAGES 393		
	15. SECURITY CLASS. (of this report) UNCLASSIFIED		
	15a. DECLASSIFICATION/DOWNGRADING SCHEDULE		
16. DISTRIBUTION STATEMENT (of this Report) Approved for public release; distribution unlimited.			
17. DISTRIBUTION STATEMENT (of the abstract entered in Block 20, if different from Report)			
18. SUPPLEMENTARY NOTES			
19. KEY WORDS (Continue on reverse side if necessary and identify by block number) LASER MHD (MAGNETOHYDRODYNAMICS) PLASMA DYNAMICS			
20. ABSTRACT (Continue on reverse side if necessary and identify by block number) A feasibility study of MHD lasers has been carried out, consisting of a comprehensive numerical modeling and an experimental study of the gain of MHD laser plasma. The numerical model combines an improved model of MHD generator behavior with a three-level model for the CO ₂ module which recognizes the lower level energy transfer by CO ₂ -CO ₂ collisions as the major limiting process. It predicts specific powers as high as 60 kW/kg at efficiencies near 3%. The experimental study has identified He + 0.014 CO ₂ + 10 ⁻⁵ Cs as the optimum plasma mixture, and verified that 0.3%/cm gain can be attained at a current density			

UNCLASSIFIED

SECURITY CLASSIFICATION OF THIS PAGE(When Data Entered)

20. (cont'd) 58. cm.

of 0.3 amp/cm² and electric field of 20V/cm. It has yielded a rate of
 $(3.3 \pm 0.03) \times 10^7$ atm⁻¹ sec⁻¹ for the lower level deactivation.

+ or -

10 to the 7th power

UNCLASSIFIED

SECURITY CLASSIFICATION OF THIS PAGE(When Data Entered)

FOREWORD

This Final Scientific Report was prepared by the Gas Turbine and Plasma Dynamics Laboratory, Department of Aeronautics and Astronautics of the Massachusetts Institute of Technology, under contract F44620-76-C-0067 to the United States Air Force Office of Scientific Research.

Dr. B. T. Wolfson was the AFOSR Program Manager. Professor J. L. Kerrebrock was the Principal Investigator, directing the experimental and numerical modeling phases of the study, assisted by S. P. Sharma and R. F. Walter. This Final Report presents a detailed description of both phases and reaches conclusions based on the entire study.

ACCESSION for	
NTIS	White Section <input checked="" type="checkbox"/>
DDC	Buff Section <input type="checkbox"/>
UNANNOUNCED <input type="checkbox"/>	
JUSTIFICATION _____	
BY _____	
DISTRIBUTION/AVAILABILITY CODES	
Dist. AVAL. and/or SPECIAL	
A	

TABLE OF CONTENTS

		<u>Page</u>
PART I	<u>EXECUTIVE SUMMARY</u>	1a
	INTRODUCTION	1
	SUMMARY CONCLUSIONS	5
	REFERENCES	7
PART II	<u>NUMERICAL MODEL OF A MAGNETOHYDRODYNAMIC LASER</u>	8a
I	INTRODUCTION	18
	1.1 Overview of the Present Investigation	18
	1.2 Review of Previous Work	20
	1.3 MHD Laser Fundamentals	26
II	PHYSICS OF CO ₂ LASERS	33
	2.1 CO ₂ Molecular Structure	33
	2.2 Small Signal Gain	35
	2.3 Power Extraction	43
III	DESCRIPTION OF PLASMA	51
	3.1 Basic Assumptions	51
	3.2 Gasdynamic Equations	56
	3.3 Plasma Equations	61
IV	EXCITATION AND RELAXATION PROCESSES	81
	4.1 Hierarchy of Reaction Rates	81
	4.2 Electron Excitation of CO ₂	88
	4.3 Collisional Deactivation of the Lower Laser Level	95
V	NUMERICAL CALCULATIONS	112
	5.1 Complete System of Equations	112
	5.2 Results of Parametric Study	121

	<u>Page</u>
VI DISCUSSION AND CONCLUSIONS	130
6.1 Effect of Lower Level Relaxation Rate on Laser Performance	130
6.2 Optimum Operating Conditions	135
6.3 Comparison with Experimental Results	143
6.4 Conclusions	147
6.5 Suggestions for Future Work	150
 APPENDICES:	
A CALCULATION OF THE OPTICAL INTENSITY	153
B EFFECTS OF PLASMA NONUNIFORMITIES ON OPTICAL OUTPUT	159
C COMPUTER PROGRAM LISTING	166
REFERENCE	200
FIGURES	206
 <u>PART III EXPERIMENTAL INVESTIGATION OF THE PHYSICAL PROCESSES</u> 251a	
<u>IN A MAGNETOHYDRODYNAMIC LASER</u>	
I INTRODUCTION	258
1.1 MHD Laser Concept	258
1.2 Review of Previous Work	259
1.3 Summary of Results and Discussion	265
II PHYSICS OF CO ₂ LASERS	268
2.1 CO ₂ Laser Kinetics	268
2.2 Electron Excitation in an MHD Laser	271
2.3 Relaxation Processes	275
III EXPERIMENTAL APPARATUS	280
3.1 The Pulsed Simulation Technique	280
3.2 Pulsed Flow System	280

	<u>Page</u>
3.3 Plasma Diagnostics	283
3.4 CO ₂ Probe Laser	286
IV EXPERIMENTAL RESULTS AND ANALYSIS OF THE DATA	287
4.1 Calibration and Preliminary Tests	288
4.2 Measurements Without Magnetic Field	290
4.3 Measurements With Magnetic Field	301
4.4 Relaxation Rates for the Lower Laser Level	303
4.5 Rate of Cs-CO ₂ Chemical Interaction	307
V DISCUSSION OF RESULTS	309
VI SUMMARY	313
6.1 Power Extraction	320
6.2 Suggestions for Future Work	322
APPENDICES:	
A MEASUREMENT OF Cs BOUND-FREE CONTINUUM	324
B CALIBRATION OF Cs ABSORPTION DIAGNOSTICS	328
C PLASMA EQUATIONS	334
REFERENCES	339
TABLES	345
FIGURES	349

PART I

EXECUTIVE SUMMARY

I. INTRODUCTION*

The MHD laser is a nonequilibrium generator in which the disequilibrium between the electron gas and the translational degrees of freedom of the carrier gas is used to produce a population inversion in a molecular additive, such as CO_2 . As the difference between the electron and gas temperatures can be as large as 3000°K , and the power density, measured by the Joule heating rate, also very large (up to 500 watts/cm³ in generators), there is the possibility of gain and very high lasing power densities.

There are several appealing features of this concept. As the electric power generated by the MHD process is delivered locally to the molecular gas, entirely within the flow, there is no need to take high powers out of the power source, and in turn put it back into a gas discharge. This eliminates many uncertainties stemming from power conditioning and from electrode phenomena. Further, while a high speed gas flow may have to be provided in an electric discharge laser in order to remove the energy rejected to the lower laser level, this flow is intrinsic to the MHD laser. The process for inversion production being essentially local, there is a chance of achieving more uniform gain, hence better beam quality than in externally excited devices. Consideration of the potential efficiencies of MHD lasers must recognize that it converts thermal energy into optical energy. Various estimates have placed the efficiency of such conversion between 3 and 5 percent. This is much higher than is achieved by gas dynamic lasers. Although gas discharge lasers may approach 20 percent efficiency of conversion from

* The serious reader will note that the initial paragraphs of this introduction are identical to those of Ref. 1. It is felt they are needed because of the arcane nature of the subject. New aspects of the work are discussed on pp. 3-5.

electric power to optical power, this efficiency must be multiplied by that of the electric power system (and power conditioning) for which 25 percent seems optimistic. Thus, the overall efficiencies of MHD and gas discharge lasers may be comparable.

The research reported here is an outgrowth of research on high power density nonequilibrium MHD generators at MIT. This research has led to the demonstration that very high levels of dissipation can be achieved in supersonic nonequilibrium generators, up to 500 watts cm^{-3} , with differences between electron temperature and gas temperature approaching 3000°K .² In a parallel program, it was also demonstrated that high levels of vibrational excitation, near equilibrium with the electron gas, can be achieved in such generators. Excitation of carbon monoxide was demonstrated in the MIT generator in 1969.³

The possibility of direct excitation of molecular gases to produce a, single-cavity high power density laser immediately suggested itself. Such a concept, using carbon dioxide in a cesium-helium plasma has been analyzed in Ref. 4.

The analysis and experience with nonequilibrium plasmas suggested that the physical phenomena of such a device might be exceedingly complex, since the kinetic and thermochemical complexity of molecular excitation is added to the already intricate behavior of the electrothermally unstable non-equilibrium plasma. Accordingly, a study was undertaken of the behavior of a nonequilibrium plasma, with molecular addition, in a strong magnetic field, but in a pulsed experiment which stimulates the kinetic situation of an MHD laser without the complexity and expense of a high speed flow system.

The technique of modeling the flow-induced electric field of an MHD laser by an applied electric field has the great advantage that it enables the uncoupling of fluid dynamic and bulk plasma phenomena. This technique was used to obtain the first experimental data on electrothermal (ionization) instabilities in nonequilibrium plasmas,⁵ and this data has since been correlated by theory⁶ and corroborated by measurements in nonequilibrium generators.⁷ A further advantage of the pulsed technique is that the very complex kinetic processes which occur in the plasma as it flows downstream in the actual laser, are displayed as a (temporal) transient in the pulsed experiment, vastly simplifying the diagnostic problem.

Preliminary experiments carried out by this technique were reported in Ref. 8. These experiments demonstrated the usefulness of the pulsed technique, and also demonstrated gain and net power output from a Cs seeded mixture of He, CO₂ and N₂ at electron densities and current densities appropriate to MHD laser operation.

A theoretical treatment⁹ of the physical processes in the MHD laser produced results in qualitative agreement with the experiments, but overestimated the importance of deexcitation of Cs by CO₂, leading to a pessimistic estimate of performance.

The results of a major study of MHD lasers have been reported in Ref. 10. A theoretical evaluation of the MHD laser concept is presented, along with experimental results from flow systems in which U x B induced gain was observed in Cs seeded He-CO₂ plasmas. The results were very erratic, evidently because of chemical reaction between the Cs and the CO₂, and difficulty with the salt windows, which were chemically attacked. This led the investigators to substitute Xe for Cs as a seed; they acquired more consistent data but gain only with applied electric fields, not with U x B excitation.

The purposes of the work described here are: 1) to carry out a systematic experimental study of the gain and optical properties of plasmas suitable for MHD lasers, and 2) to develop a complete numerical model for the MHD laser which can provide a basis for feasibility assessments of the MHD laser concept. These two objectives have been met in two distinct research efforts which are reported in Parts II and III of this report. Part II is the PhD dissertation of Dr. R. F. Walter, Part III is the PhD dissertation of S. P. Shamma.

There is general agreement that the MHD laser requires a plasma composition of about 10^{-2} CO_2 and 10^{-5} Cs in He for successful operation. The CO_2 fraction is limited by the Joule heating available to raise the electron temperature to the levels required to pump the upper laser level (around 2500°K). The Cs is needed to provide the required electron density at these electron temperatures. This gas composition poses two problems which are unique to the MHD laser among CO_2 lasers.

First, the low CO_2 concentration and absence of N_2 alter the pumping and deactivation mechanisms. The upper level pumping is directly by electrons and is well understood.⁴ In most treatments of CO_2 lasers the two lower levels (100 and 010) have generally been assumed to be tightly coupled and deactivated by atomic collisions (by He in the MHD laser). We find this assumption invalid at the low CO_2 concentrations required by the MHD laser because the lower laser level (100) is deactivated by collision with CO_2 , the rate being limiting. Thus a three-level model is required for the CO_2 . Such has been included in the MHD laser model to be discussed in Part II. It is shown there that the $(100 \rightarrow 010)$ transfer rate is critical to MHD laser performance, if lasing at 10.6μ is required. It may be that the MHD laser should operate at 9.6μ , but this question has not been explored in depth as yet.

Secondly, the low Cs fraction and chemical reactivity of Cs and CO_2 raise the question whether these two species can in fact coexist in the plasma. Early estimates of the reaction rate suggested that they could for the flow times required in full scale MHD lasers such as were projected in Ref. 4, but the reaction has led to great uncertainties in the results of all small scale feasibility experiments. Indeed a great deal of the effort of the research described here has gone to developing the gas handling system for the pulsed apparatus so that the chemical reaction between Cs and CO_2 can be controlled, and so that the amount of Cs present during the experiment can be accurately determined. Part III presents the methods evolved, which do work.

The overall results and conclusions of this investigation of the MHD laser are presented in the next section. More complete results will be found in Parts II and III.

SUMMARY CONCLUSIONS

Part II of this report presents a comprehensive numerical model of the MHD laser. This model includes the effects of kinetics of ionization and of electro-thermal instability in a channel flow representation of the flow through an MHD laser channel. It combines the rather full understanding of MHD generator behavior developed at MIT with the molecular kinetics of the CO_2 laser.

A major finding of this work is that the bottlenecking of the lower laser level limits the performance of the MHD laser. Proper representation of this effect requires a three-level model for the CO_2 . Because the lower laser level is deactivated by CO_2 - CO_2 collisions, a minimum CO_2 mole fraction of about 0.01 is required to ensure maintenance of an adequate inversion during power extraction.

From the numerical modeling it is concluded that an MHD laser operating with a mixture of He, 0.03 CO_2 , 10^{-5} Cs with a stagnation temperature of 2000°K ,

stagnation pressure of 20 atm, Mach number of 4 and magnetic field strength of 4 T, should have an efficiency of conversion from thermal energy to 10.6μ radiation in excess of 2%, with specific power of 60 ki/kg. These values make competitive with high-powered laser concepts currently under development.

Part III of the report presents a thorough experimental study of the gain of MHD laser plasmas. This experiment confirms the viability of the plasma conditions judged most suitable from the numerical modeling. From gain measurements carried out over a wide range of plasma conditions, a set of parameters giving maximum small signal gain was found. The optimum gas mixture was found to be He, 0.014 CO_2 , 10^{-5} Cs , which gave a gain of $0.3\%/\text{cm}$. The current density was 0.3 amp/cm^2 , and the electric field 20 v/cm at a pressure of 40 torr. This level of induced field is readily available in an MHD laser, as it implies a magnetic field strength of only 0.67 tesla at a flow velocity of 3000 m/s.

In addition to the gain optimization results, the experiment provided a measurement of the lower level depopulation rate found to be crucial in the numerical modeling. The measured rate of $(3.3 \pm 0.03) \times 10^7 \text{ atm}^{-1} \text{ sec}^{-1}$ agrees with the theoretical result of Seeber.¹¹ The experiment has also provided a measurement of the Cs-CO_2 reaction rate, which is sufficiently low that this reaction should not be a problem in an MHD laser.

From these results, it is concluded that the MHD Laser could be a serious competitor to the gas dynamic, electric discharge and chemical lasers when large powers are desired. A feasibility experiment could be based on the findings of this report.

References

1. Kerrebrock, J.L., "Fundamental Mechanisms of Nonequilibrium MHD Lasing Phenomena," Final Scientific Report AFOSR-74-2680, Oct. 1976 M.I.T. Gas Turbine & Plasma Dynamics Lab.
2. Hsu, M.S.S., "Experimental Investigation of a Nonequilibrium Magneto-hydrodynamic Generator with Slanted Electrode Walls," Ph.D. Thesis, M.I.T., June (1971).
3. Draper, J.S., and Kerrebrock, J.L., "Molecular Behavior in Non-equilibrium MHD Generators," 5th Int. Conf. on MHD Elec. Power Gen., Munich (1971).
4. Brown, R.T., Hall, R.J., and Nighan, W.L., "Laser Excitation Using a Nonequilibrium MHD Generator," United Aircraft Research Lab. Report, East Hartford, CT (1969).
5. Kerrebrock, J.L., and Dethlefsen, R., "Experimental Investigation of Fluctuations in a Nonequilibrium Plasma," J. AIAA, 6, 11, 2115, Nov. (1968).
6. Solbes, A., "Quasi-Linear Plane Wave Study of Electrothermal Instabilities," SM-107/26, 4th Int. Conf. on MHD Elec. Power Gen., Warsaw (1968).
7. Louis, J.F., "Studies of a Disk Hall Generator Driven in a Shock Tunnel," 8th Symp. on Eng. Aspects of MHD, Stanford (1967).
8. Oliver, D. A., Solbes, A., Kerrebrock, J. L., et al., "Ionization Instabilities and Discharge Characteristics of an MHD Laser," 12th Symp. on Eng. Aspects of MHD, Argonne, Illinois, March (1972).
9. Lowenstein, A., "Physical Processes in a Magnetohydrodynamic Laser," Ph.D. Thesis, M.I.T., Feb. (1974).
10. Biberman, L. M., Vorobjev, V. S., Ivanov, R. S., et al., "Some Results of MHD-Laser Investigation," Proc. 16th Symp. on Eng. Aspects of MHD, Pittsburgh, PA (1977).
11. Seeber, K. N., "Radiative and Collisional Transitions between Coupled Vibrational Modes of CO₂," J. Chem. Phys. 55, 10, 5077 (1971).

PART II

NUMERICAL MODEL OF A MAGNETOHYDRODYNAMIC LASER

LIST OF SYMBOLS

a - total absorption coefficient of gas

a_1, a_2 - mirror absorption coefficient

A - geometric area

A_D - geometric area corrected for boundary layer displacement thickness

A_e - nozzle exit area

A^* - nozzle throat area

A_{10} - Einstein coefficient for alkali $6^2 P_{1/2} - 6^2 S_{1/2}$ transition

A_{21} - Einstein coefficient for spontaneous emission

A'_{21} - Einstein coefficient for spontaneous emission (dimensionless)

ASM - asymmetric stretch mode

\bar{B} - magnetic induction

B_{12} - Einstein coefficient for absorption

B_{21} - Einstein coefficient for stimulated emission

BM - bending mode

c - speed of light

C_i - constants used to evaluate collision frequency

\bar{c}_{ij} - relative collision velocity between species i and j

c_p - specific heat at constant pressure

d_o - Landau impact parameter

\bar{E} - electric field in gas frame

E_1, E_2, E_3 - energy density of CO_2 vibrational modes

E_{12} - energy density of combined BM-SSM modes

$F(J)$ - fractional population of J th rotational level

F - generalized force

g - gain

g_{OSC} - saturated gain in laser oscillator

$g(v_0)$ - lineshape function

G_0 - small signal gain

h - Planck's constant

$h(x)$ - channel height

i - interaction parameter

I - total integrated optical intensity

I_v - optical intensity per frequency

I_{SAT} - saturation intensity

J - rotational quantum number

\bar{J} - electric current density

J_x, J_y - x, y components of current density vector

k - Boltzmann's constant

k_{i-j} - kinetic rate constant

K - Gladstone-Dale constant

K - generalized load factor

K_{ie} - rate constant for electron excitation

K_∞ - transverse electric load factor

L - optical cavity width

L_{CAV} - optical cavity length
 L_{CHAN} - channel length
 L_{ENERGY} - length scale for energy-limited ionization growth
 L_{EXT} - length scale for optical power extraction
 L_{NOZ} - nozzle length
 L_{RATE} - length scale for rate-limited ionization growth
 m_e - mass of electron
 m_H - mass of heavy neutral particle
 \dot{m} - mass flow rate
 M - molecular weight
 n - total number density of the gas
 n_{CO_2} - CO_2 number density
 n_e - electron number density
 n_e^* - a measure of the electron temperature expressed as an electron density through the Saha equation
 n_j - number density of the jth neutral particle
 N_1, N_{100} - lower laser level population
 N_2, N_{001} - upper laser level population
 p - pressure
 p_o - stagnation pressure
 P - channel perimeter
 P - generalized power

P_{ABS} - optical power absorbed by mirrors
 P_{OUT} - optical power transmitted by mirrors
 Q - partition function
 Q_i - cross section
 \dot{Q} - volumetric energy addition rate
 \dot{Q}_{VT} - volumetric rate of energy addition from vibrational to translational modes
 v, v^* - derivatives of collision frequency with respect to n_e, n_e^*
 r_1, r_2 - mirror reflectivities
 R - gas constant, kg/m
 R - universal gas constant
 R - Hinov-Hirschberg three-body recombination coefficient
 R_1, R_2 - pumping rates of lower, upper laser levels
 S - ratio of effective to average conductivity
 SSM - symmetric stretch mode
 t - tangent of angle between wave vector of nonuniformities and current
 t_1, t_2 - mirror transmission coefficients
 T - gas static temperature
 T_0 - gas stagnation temperature
 T_e - electron temperature
 T_{e_∞} - asymptotic electron temperature
 T_{vj} - vibrational temperature of j th species

T_1, T_{100} - vibrational temperature of SSM

T_2, T_{010} - vibrational temperature of BM

T_3, T_{001} - vibrational temperature of ASM

U - gas velocity

v - expression for Mach number:

$$\frac{\gamma-1}{2} M^2$$

\bar{v}_e - electron diffusion velocity

w_i - stimulated transition rate per molecule

x - axial coordinate

x_i - parameter describing sum of electron translational and ionizational energy

y - transverse coordinate in electric field and optical axis direction

z - transverse coordinate in magnetic field direction

GREEK SYMBOLS

β - Hall parameter

$\langle\beta\rangle, \beta_{app}, \beta_{crit}, \beta_{eff}$ - average, apparent, critical, and effective Hall parameters

γ - ratio of specific heats

Γ, Γ^* - growth rates of nonuniformities

δ - elastic loss parameter

δ_D - boundary layer displacement thickness

ϵ - correction term for average elastic losses

$\hat{\epsilon}$ - effective radiation escape parameter

ϵ_R - resonance escape parameter

ϵ_a - energy of alkali $6^2P_{1/2} - 6^2S_{1/2}$ transition

n, n^* - fluctuation in n_e, n_e^*

η_L - fractional electrical power transfer to BM

η_{LOC} - local (adiabatic) optical efficiency

η_p - fractional electrical power transfer to ASM

η_p - polytropic efficiency

θ - angle between wave vector and optical axis

θ_{ROT} - rotational temperature

λ - wavelength

λ' - parameter describing growth of nonuniformities

Λ - ratio of Debye length to Landau impact parameter

μ - index of refraction

ν - frequency

ν_0 - laser transition frequency at line center
 ν_1, ν_2, ν_3 - characteristic vibrational frequencies of SSM, BM, ASM
 ν_c - total CO_2 intermolecular collision frequency
 $\Delta\nu$ - pressure broadened linewidth
 ν_e - total electron collision frequency
 $\nu_+, \nu_{\text{Cs}}, \nu_{\text{He}}$ - electron - ion, electron - cesium, electron - helium momentum transfer collision frequency
 ϕ - ratio of η^* to η
 ρ - gas density
 σ - electrical conductivity
 $\langle\sigma\rangle, \sigma_{\text{app}}, \sigma_{\text{eff}}$ - average, apparent, and effective conductivity
 σ_i - collision cross section
 σ_Q - quenching cross section
 $\tau_{1\text{REL}}, \tau_{2\text{REL}}, \tau_{3\text{REL}}$ - relaxation times of SSM, BM, ASM
 τ_{2e}, τ_{3e} - electron excitation times of BM, ASM
 τ_{21} - spontaneous decay time
 τ'_{21} - spontaneous decay time (dimensionless)
 τ_{RES} - residence time of fluid element in channel
 ω - angular frequency
 ω_p - plasma frequency
 ω_{20}, ω_{10} - total decay time of ASM, SSM

LIST OF FIGURES

1. Schematic of MHD Laser Configuration
2. CO₂ Modes of Vibration
3. CO₂ Energy Level Diagram
4. Relationship of Physical Processes in an MHD Laser
5. Inverse of Laser Radiation Decay Time
6. Calculated Small Signal Gain for Two- and Three-Temperature Models
7. Effect of Initial Stagnation Temperature on Calculated Small Signal Gain
8. Effect of Lower Laser Level Relaxation Rate on Specific Power Growth
9. Temperature Response Profile, Three-Temperature Model
10. Temperature Response Profile, Two-Temperature Model
11. Effect of Lower Level Relaxation Rate on Fractional Electrical Power Transfer
12. Effect of Lower Level Relaxation Rate on Upper and Lower Level Populations
13. Effect of Lower Level Relaxation Rate on Local Efficiency
14. Effect of CO₂ Concentration on Optical Output (M = 4)
15. Effect of CO₂ Concentration on Specific Power Growth (M = 4)
16. Effect of CO₂ Concentration on Electron Temperature Profile (M = 4)
17. Effect of CO₂ Concentration on Electron Number Density (M = 4)
18. Effect of CO₂ Concentration on Gas Static Pressure (M = 4)
19. Effect of CO₂ Concentration on Upper Laser Level Population (M = 4)

LIST OF FIGURES (Cont.)

20. Effect of CO_2 Concentration on Lower Laser Level Population ($M = 4$)
21. Effect of CO_2 Concentration on Local Efficiency ($M = 4$)
22. Effect of CO_2 Concentration on Optical Efficiency ($M = 4$)
23. Effect of CO_2 Concentration on Fractional Power Transfer to Upper Laser Level ($M = 4$)
24. Effect of CO_2 Concentration on Intracavity Flux Development ($M = 4$)
25. Effect of CO_2 Concentration on Fluctuation Parameter Growth ($M = 4$)
26. Effect of CO_2 Concentration on Effective Conductivity of Plasma ($M = 4$)
27. Effect of Stagnation Pressure on Intracavity Flux
28. Effect of Initial Stagnation Temperature on Optical Output
29. Effect of Initial Stagnation Temperature on Upper Laser Level Population
30. Effect of Initial Stagnation Temperature on Gas Static Temperature
31. Temperature Response Profile, Three Temperature Model ($x_{\text{Cs}} = 10^{-4}$)
32. Effect of Preionization on Optical Output
33. Effect of Quenching of Electron Number Density with Preionization
34. Effect of Quenching on Small Signal Gain Coefficient with Preionization
35. Effect of Quenching on Electron Temperature Profile with Preionization

LIST OF FIGURES (Cont.)

36. Evolution of Stagnation Pressure and Mach Number
($x_{CO_2} = 0.03$)
37. Evolution of Static Pressure and Temperature
($x_{CO_2} = 0.03$)
38. Temperature Response Profile ($x_{CO_2} = 0.03$)
39. Fractional Electrical Power Transfer to CO_2 Vibrational Excitation ($x_{CO_2} = 0.03$)
40. Development of Critical, Effective, and Apparent Hall Parameters ($x_{CO_2} = 0.03$)
41. Effect of Lasing on Upper and Lower Level Populations
42. Effect of CO_2 Concentration on Small Signal Gain ($M = 2$)
43. Effect of CO_2 Concentration on Electron Temperature
($M = 2$)
44. Effect of CO_2 Concentration on Electron Number Density
($M = 2$)
45. Orientation of Electrothermal Wave Striations

I. INTRODUCTION

1.1 Overview of the Present Investigation

A magnetohydrodynamic laser is a nonequilibrium MHD generator which contains a lasing molecular species in addition to the usual alkali seed and noble buffer gas. Energetic electrons in the MHD plasma selectively excite certain of the vibrational modes of the lasing molecules to produce a population inversion. If mirrors are added to the sides of the channel, laser oscillation can begin. Very high lasing power densities are conceivable in such a device because of the large Joule dissipation, which maintains the electron temperature above that of the gas. Moreover, the high speed flow which appears to be essential for the removal of waste heat in high energy continuous wave lasers is an intrinsic feature of the MHD laser.

Several investigators have presented analytical models of MHD laser performance, but none of these has been entirely satisfactory in explaining the experimental results which have been accumulated thus far. In an attempt to define the physical processes which limit the device performance several of these studies identified quenching collisions between CO_2 and the alkali seed which disturb the equilibrium of the bound electrons. However, as we shall see in the following section,

significant small signal gains have been measured at CO_2 concentrations well beyond the maximum limits established by the quenching theory. In addition to the quenching phenomenon, another physical process may be important in determining the quality of the optical output. This is the ionization instability, which leads to the propagation of electrothermal waves through the plasma whenever the Hall parameter exceeds a critical value. These result in temporal and spatial non-uniformities in the electron temperature and density which reduce the bulk electrical conductivity of the plasma.

In the succeeding pages a new theory of the performance of an MHD laser will be presented. This model differs from the previous MHD laser analyses in that it combines an improved theory of nonequilibrium MHD generator processes with a new view of the kinetic behavior of the CO_2 molecule. Equations are developed to describe the evolution of the gasdynamic and plasma properties as the fluid is expanded through an MHD nozzle-channel combination. The analysis employs the quasi-linear theory of Solbes⁽¹⁵⁾ to describe the average bulk properties of the flowing plasma in the presence of ionization instabilities. This theory is extended to include the effects of molecules on the electron energy balance. The present analysis also includes the effects of CO_2 excitation and relaxation processes with finite rate coefficients.

The result is a self-consistent set of equations coupling the gasdynamics and the electron kinetics with the CO_2 vibrational kinetics. Because of the complicated nature of these equations a computer program was developed to facilitate calculations with the model. This program was used as the basis of a parameter study of the effects of various input conditions on the optical output of the laser. This led to a determination of the processes which limit CO_2 MHD laser performance, as well as a set of near-optimal operating conditions for the laser device.

1.2 Review of Previous Work

The electric field set up inside a nonequilibrium generator accelerates free electrons produced by thermal ionization, giving them a thermal energy (temperature) above that of the heavier particles. This comes about because the electrons cannot efficiently transfer their kinetic energy to the much heavier monatomic gas particles via elastic collisions. However, the electrons can impart a significant fraction of their kinetic energy to the internal storage modes of a polyatomic gas molecule. Thus the addition of a molecular species to a nonequilibrium MHD plasma could sharply reduce the elevation of the electron temperature over the gas temperature. Furthermore, collisions between the molecules and the alkali seed atoms that are usually provided as a source of electrons

could result in quenching of the bound electron states which are in equilibrium with the free electrons. This would upset the detailed balancing processes at work in the nonequilibrium MHD plasma and reduce the electron number density. Initially, then, there is some question about whether a molecular species can be tolerated in a nonequilibrium MHD generator.

The first aspect of this question was investigated by Draper,^(1,2) who studied the effects of adding CO and N₂ to nonequilibrium MHD plasmas. In addition to demonstrating that high levels of vibrational excitation could be achieved, Draper's results indicated that molecular mole fractions on the order of 1% would not seriously reduce the electron temperature. The second aspect was originally studied by Mnatsakanyan⁽³⁾ in connection with the quenching of electronically excited alkali atoms by molecular collisions in a plasma consisting of N₂-Ar-Cs. His results indicated that a molecular mole fraction of less than 1% could cause a considerable depopulation of the excited bound states, with a resulting sharp drop in the free electron number density.

The importance of the quenching process and the uncertainty about its effects led Lowenstein⁽⁴⁾ to undertake a further study of its influence on the performance of an MHD laser. By noting the essential equivalence of collision-induced quenching by molecules to the quenching produced by

radiative decay of excited atomic states, he extended the work of Mnatsakanyan and Shaw⁽⁵⁾ to calculate the effects of collisions with CO₂ on the bound state populations of Cs.

A key parameter for evaluating these effects is the rate at which the first excited state of Cs is depopulated by CO₂ collisions. As the first state is depopulated, the upper states in turn lose member atoms as they reach a new equilibrium with it. This rate is proportional to the cross section for the encounter, a number which has never been reliably measured. In his calculations Lowenstein assumed a large value ($7 \times 10^{-19} \text{ m}^2$) for this cross section. This led to the prediction that a CO₂ mole fraction much in excess of 10^{-3} would lead to a severe decrease in the free electron number density. Lowenstein's analysis indicated that the maximum small signal gain would occur at a CO₂ concentration of 0.22%; the small signal gain at this point is 0.011%/cm for $T_e = 2500^\circ\text{K}$ and $T = 300^\circ\text{K}$.

Lowenstein also studied the influence of CO₂, both with and without an accompanying laser radiation field, on the ionization instability that is known to occur in nonequilibrium MHD plasmas. His results here indicated that the radiation field does not have a significant effect on the instability because its influence is an indirect one through the coupling with the vibrational modes of the molecules. He did show,

however, that the introduction of molecules reduces the critical Hall parameter at which the plasma becomes unstable. A major limitation of Lowenstein's analysis is his assumption of uniform steady flow at a constant velocity and temperature. His solution then corresponds to conditions which might prevail at a single station along an MHD channel. It ignores the effects of kinetic processes with finite rates on the evolution of the flow.

The first laser experiments with a supersonic MHD channel were performed at the United Aircraft Research Laboratories.⁽⁶⁻⁸⁾ Results from these investigations indicated that electron pumping produced an appreciable positive small signal gain in the range 0.05-0.15%/cm, but efforts to extract optical power from an oscillator were inconclusive. Analytical modeling produced a computer simulation of the MHD expansion and CO₂ vibrational kinetics. This model assumed functional forms for several important MHD parameters and utilized CO₂ vibrational relaxation models available in 1970. It predicted that approximately 20% of the Joule dissipation power could be converted to coherent radiation, with an overall efficiency of about 5% if the CO₂ mole fraction could be maintained at 0.0175. Such a large CO₂ fraction cannot be permitted if Lowenstein's quenching theory is valid. Finally, the UARL investigation yielded the significant experimental result that

chemical reactions between CO_2 and Cs are important, depleting the available quantities of both gases and creating uncertainty as to the concentrations that were present during the measurements.

Shock tunnel studies with an MHD laser channel were performed by Zauderer, Tate, and Marston^(9,10) for mixtures of 78% He, 18% Ar, 4% CO_2 with either 1% Xe or 0.1% Cs added for seeding. Despite the fact that Lowenstein's theory forbids any appreciable gain with such a high CO_2 loading, these authors measured small signal gains of 0.2%/cm. In these tests external voltage augmentation was required to maintain electrode conduction, but the authors attributed this to the short axial channel length and the tendency of gas convective effects to extinguish a transverse discharge in the ionization buildup region. The Cs- CO_2 chemical reaction was also observed in these experiments, but it was found that positive gain could be obtained if the CO_2 fraction was kept well above that of Cs.

In 1977 a group at the Institute of High Temperature Physics in the Soviet Union reported the results of a major study of MHD lasers.⁽¹¹⁾ Both small signal gain and power extraction experiments were performed with a complete nozzle-channel combination using a pulsed gas flow. Subsonic tests were run with a mixture of He, Cs, and CO_2 , the CO_2 mole fraction being 1%. A small signal gain of about 0.1%/cm was

estimated, and a specific power of about 10 kw/kg/sec was measured under conditions which produced a self-sustained discharge. It was estimated that approximately 15% of the Joule dissipation was converted to radiation. These results were very erratic, however, apparently because the Cs reacted chemically with both CO_2 and the salt windows. To avoid this problem the investigators substituted Xe as the seed and ran the tests in a supersonic channel. A small signal gain of 0.3%/cm was again reported with specific power falling in the same range as before (10 kw/kg/sec). For this series of tests it was necessary to apply an external voltage to sustain the discharge.

The results of a series of ongoing experiments at MIT are consistent with those of the previously cited investigations. In a static discharge tube employing a pulsed electric field and gas flow system, Sharma has measured small signal gains in the neighborhood of 0.3%/cm with a CO_2 fraction of 0.8%.⁽¹²⁾ The success of this apparatus in producing positive gain indicates that the problem of chemical reaction between Cs and CO_2 can be overcome even in a small scale experiment with slow-moving gases. In addition, it was demonstrated by applying a pulsed magnetic field that the same levels of gain could be attained in an electrothermally unstable plasma.

Thus there is a body of experimental evidence which indicates that a gain of 0.1-0.3%/cm can be achieved with a

CO_2 fraction on the order of 1%, in both pulsed discharge and supersonic flow experiments. This is in direct violation of the Lowenstein quenching theory, so it seems evident that this theory overstated the importance of depopulating collisions between Cs and CO_2 . At the same time the other analyses have been unable to explain the experimental results with any consistency. It would therefore seem desirable to reconstruct the theoretical model in order to obtain a better understanding of the physical processes which govern MHD laser performance. Accordingly, the present investigation was undertaken.

1.3 MHD Laser Fundamentals

The selection of the optically active species for use in an MHD laser depends largely on the nature of nonequilibrium MHD generator plasmas. There are essential differences between these plasmas and those in conventional electric discharge lasers. The former are characterized by relatively high electron number densities (10^{19} - 10^{20} m^{-3}) and low average energies (0.2-0.3 eV). In contrast, the EDL plasma has rather low electron densities (10^{15} - 10^{16} m^{-3}) but high average energies (~ 2 eV). Thus the MHD plasma would not seem to be a good candidate for pumping an electronic transition laser, which has energy level spacings on the order of several electron volts. Considering the average thermal energy of

the electrons, a more appropriate choice would be the vibrational modes of a molecular species. Furthermore, since helium is the predominant species in nonequilibrium MHD plasmas, it would be desirable to employ as the gain medium a gas whose lower laser level is effectively relaxed by collisions with He.

In the present work an analysis of the performance of an MHD laser was conducted for a plasma consisting of helium, cesium, and carbon dioxide. CO_2 was chosen as the laser medium for a variety of reasons:

- (1) It has been successfully employed in other gas laser systems.
- (2) It has a high quantum efficiency (approximately 41%).
- (3) The upper laser level for the most common CO_2 laser transitions, $\text{CO}_2 (00^01)$, is separated from the ground state by 0.29 eV, which is comparable to the average electron energy in an MHD generator.
- (4) Helium, the primary constituent in nonequilibrium MHD plasmas, has been effectively employed as the lower level relaxant in other high energy CO_2 laser systems.
- (5) Most of the work performed to date on MHD lasers has used CO_2 as the active medium.

Conventional CO_2 electric discharge lasers use electron impact excitation for pumping the vibrational levels of N_2 :

this energy is effectively transferred to the $\text{CO}_2(00^1)$ level via resonant collisions. It should be noted that for electron temperatures in the $2000-3000^{\circ}\text{K}$ range, the vibrational excitation rate for the $\text{CO}_2(00^1)$ level is one to two orders of magnitude greater than that for N_2 .⁽⁶⁾ This is in contrast to the situation in conventional EDL's, where the average electron energy is in the neighborhood of 1 eV and electron vibrational excitation of N_2 dominates. Thus it does not appear that N_2 would be particularly useful in maintaining the CO_2 population inversion in the electron temperature range encountered in MHD plasmas.

In a fairly straightforward manner we can determine the best electrical connection for MHD laser operation.⁽⁶⁾ For a uniform fluid the Ohm's Law with Hall effect may be written as:

$$\bar{J} + \bar{J} \times \bar{B} = \sigma \bar{E}' \quad (1-1)$$

where $\bar{E}' = \bar{E} + \bar{u} \times \bar{B}$ is the electric field seen in a frame moving with the gas. By taking the inner product with the current density vector one obtains

$$\bar{u} \cdot \bar{J} \times \bar{B} = \bar{J} \cdot \bar{E} + J^2/\sigma \quad (1-2)$$

This equation states that the total work performed by the fluid ($\bar{u} \cdot \bar{J} \times \bar{B}$) is equal to the electrical power output ($\bar{J} \cdot \bar{E}$) plus the power dissipated in the fluid (the Joule dissipation J^2/σ). The latter term results in electron heating and should be maximized for an MHD laser.

It is clear from Eq. (1-2) that all the electrical power goes into electron heating if $\bar{J} \cdot \bar{E}$ is zero. This implies that the MHD channel should be short-circuited in the direction of current flow for a laser. It also follows that the maximum power dissipation occurs when \bar{u} , \bar{J} , and \bar{B} are mutually orthogonal. These considerations point to the short-circuited Faraday connection as best for MHD laser applications.

(Short circuiting the channel in the axial or Hall direction will not increase the Joule heating because for a given current density, the Hall effect does not increase the Joule dissipation.⁽¹³⁾ Furthermore, the Hall current would produce a transverse pressure gradient in the gas which could lead to unwanted nonuniformities and possibly boundary layer separation.) Figure 1 features a schematic diagram of such a configuration.

Experience with nonequilibrium MHD generators indicates that it may prove desirable to include a preionizer in the nozzle just before the flow encounters the magnetic field. The most successful type employs a DC discharge between offset electrodes which ionizes the seed to provide an appreciable electron number density (and conductivity) in the channel entrance region. Since free electron energy losses will be greater with a molecular additive, and in view of the concern about quenching of the bound electronic states of the seed, a preionizer may prove to be an essential part of an

MHD laser. We will investigate the effects of preionization later in this dissertation.

In the work to be reported in the following chapters, we shall confine our attention to those operating conditions which have been identified as suitable for MHD laser applications by the previously cited analyses and experiments.

It has been shown⁽¹⁴⁾ that optimum pumping efficiency for a CO_2 -He laser mixture occurs when $E/n \approx 10^{-16} \text{ V cm}^2$. Here E is the induced electric field ($E = uB$ in our case) and $n = p/kT$. This establishes a range of values for the Mach number, the magnetic field strength, the stagnation pressure, and the stagnation temperature.

It has also been demonstrated that an upper limit exists for the electron number density n_e . Lowenstein⁽⁴⁾ shows that when n_e/n_{He} exceeds 10^{-5} , electron pumping of the bending mode becomes significant. This reduces the gain and saturation intensity of the laser medium. Because the electron number density has an exponential dependence on the electron temperature, a small change in T_e can produce a large variation in n_e . To keep n_e in the acceptable range in a plasma where T_e varies greatly, it is desirable to use a seed fraction of 10^{-5} . Then even near full ionization the lower laser level will not become excited by electron pumping. (A seed fraction of 10^{-5} also meets the recommendation of Zauderer⁽⁹⁾ that the cesium

concentration be kept well below the CO_2 fraction in order to minimize the effects of the chemical reaction.)

The treatment of the electron kinetics is considerably simplified if the energy distribution of the free electrons can be taken to be Maxwellian. When this is the case the electron energy can be described by an electron temperature T_e . This is a valid assumption if the rate of energy transfer in electron-electron collisions is much greater than the rates of energy loss through the various elastic and inelastic collisional mechanisms. Lowenstein⁽⁴⁾ indicates that in a CO_2 MHD laser plasma this condition is satisfied for

$n_e/n_{\text{CO}_2} > 10^{-3}$. Since we are limiting the seed fraction (hence n_e/n_{He}) to 10^{-5} , the Maxwellian assumption will be valid for CO_2 concentrations of about 1% or less.

It is also assumed that the energy levels within each of the three vibrational modes of the CO_2 molecule are in equilibrium so that the population of each level may be determined by the Boltzmann relation. In this case each mode may be described by a vibrational temperature. This assumption is valid if the intramode energy transfer rate is much greater than the rates for the other collisional (and radiative) processes which populate and depopulate the energy levels of the mode. As will be seen in Chapter 4, these conditions are usually satisfied, but there is some question about applying

the equilibrium assumption to the lower levels of the bending mode.

The major qualitative and quantitative difference between the present work and the earlier studies appears in the equations describing the CO_2 molecular kinetics. The previous analyses assumed that the removal of energy from the lower laser level through interatomic and intermolecular collisions was extremely rapid, implying that the bending and symmetric stretch modes of the CO_2 molecule were in equilibrium at approximately the same vibrational temperature. Since 1969 a good deal of experimental evidence has been accumulated which indicates that this assumption is not correct when the CO_2 mole fraction is much less than ten percent, as is the case in an MHD laser.

If this is true, the bending and symmetric stretch modes cannot be combined in a single vibrational energy equation, as is usually done in analyses of CO_2 lasers. This analysis employs separate energy equations for each of the CO_2 vibrational modes. We will investigate this question in much greater detail in Chapter 4. However, it should be noted that the effect of weak coupling between bending and symmetric stretch modes is most pronounced during peak power extraction. If the collisional deactivation rate of the lower laser level is small, then the rate of energy removal from the upper laser level may be limited by bottlenecking, rather than by the pumping rate.

II. PHYSICS OF CO₂ LASERS

2.1 CO₂ Molecular Structure

It is appropriate to begin our discussion of CO₂ laser behavior with a look at the structure of the molecule and how this affects collisional energy transfer processes. CO₂ is a linear triatomic molecule with three normal modes of vibration⁽¹⁷⁾ (see Figure 2). These are designated ν_1 (symmetric stretch mode, or SSM), ν_2 (doubly degenerate bending mode, or BM), and ν_3 (antisymmetric stretch mode, or ASM). Each mode consists of a series of energy levels which are nearly equally spaced, enabling the modes to be modeled as harmonic oscillators with very little error. In addition, each vibrational level has superimposed upon it a series of rotational energy levels with very close spacing.

Figure 3 shows an energy level diagram of the CO₂ molecule. Two laser transition bands have been observed; both originate on the 00°1 level (the first excited level of the ASM). The 10.6 micron band terminates on the first excited SSM level (10°0), whereas the 9.6 micron band terminates on the second excited level of the bending mode (02°0). In order for a laser to function, the upper level of the transition must be selectively overpopulated by some means (in our case by electron impact excitation). When the upper level population exceeds that of the lower level, a population inversion

is said to exist. The CO_2 is then capable of amplifying a beam of light passing through the gas at the laser transition frequency.

Since the population inversion is the essence of laser action, the key problem in building a laser is the attainment of this condition in the gas. To create a population inversion one must add energy to a large number of ground state CO_2 molecules. The internal degrees of freedom of a molecule can gain energy by absorption of photons or through collisions with other particles (either molecules or electrons). It is difficult to scale up optical pumping techniques for use in large devices. Collisional processes are the important energy transfer mechanisms in an MHD laser.

Vibrational excitation by low energy electrons proceeds by a dipole interaction and has been studied experimentally to a sufficient degree to give accurate cross section data. Since the ASM and BM vibrations produce an internal dipole moment within the CO_2 molecule, electrons have a considerably higher cross section for these modes than for the SSM, which produces no internal dipole moment. (This is true for electrons with energies below 2-3 eV, i.e., most of the electrons in an MHD laser plasma.) Moreover the cross sections for excitation of higher levels (020, 002, etc.) have been estimated to be much smaller than those for the first excited levels of the three modes.⁽²¹⁾

Thus in a CO_2 laser employing direct electron excitation, virtually all the discharge energy goes into the 01'0 and

00°1 levels. Energy input into the bending mode represents a parasitic energy loss; indeed some of this energy may be transferred to the lower laser level via collisions, reducing the population inversion. The amount by which the energy transferred to the 00°1 level exceeds that pumped into the 01°0 level is a measure of the efficiency of the excitation process. This is an important figure of merit in the evaluation of laser system feasibility.

2.2 Small Signal Gain

As an introduction to the laser performance analysis, we review here the basic equations which describe the generation and amplification of coherent radiation in a laser medium. The natural starting point for our discussion is the equation of radiative transfer: (22)

$$\frac{dI_v}{dx} = (A_{21} N_2 + B_{21} I_v N_2 - B_{12} I_v N_1) \hbar v \quad (2-1)$$

Here A_{21} , B_{21} , and B_{12} are the Einstein coefficients for spontaneous emission, stimulated emission, and absorption, respectively. N_2 and N_1 are the populations of the upper and lower laser levels, and I_v is the optical intensity of radiation at frequency v . From elementary statistical arguments it can be shown that

$$B_{12} = B_{21}$$

and

$$A_{21} = (2h\nu^3/c^2) B_{21}.$$

So it is possible to make the following comparisons:

$$\frac{\text{stimulated emission}}{\text{spontaneous emission}} = \frac{c^2}{2h\nu^2} I_\nu$$

$$\frac{\text{absorption}}{\text{spontaneous emission}} = \frac{c^2}{2h\nu^3} I_\nu e^{h\nu/kT}$$

Now even in a small CO_2 laser $I_\nu \approx 5 \times 10^{-6}$ watt/cm²/sec/steradian, so that stimulated emission exceeds spontaneous emission by a factor of 10^8 .

It follows that we can ignore spontaneous emission in the radiative transfer equation which becomes:

$$\frac{dI_\nu}{dx} = (B_{21} I_\nu N_2 - B_{12} I_\nu N_1) h\nu \quad (2-2)$$

Rearrangement of some factors yields:

$$\begin{aligned} \frac{dI_\nu}{I_\nu} &= B_{21} (N_2 - N_1) h\nu dx \\ &= \frac{c^2}{2\nu} A_{21} (N_2 - N_1) dx \end{aligned} \quad (2-3)$$

The relation $c = \lambda\nu$ leads to the result

$$\frac{dI_v}{I_v} = \frac{\lambda^2 A_{21}}{2} (N_2 - N_1) dx \quad (2-4)$$

Now the small signal gain (or absorption) coefficient G_o is defined by

$$\frac{dI_v}{I_v} = G_o dx \quad (2-5)$$

Equating these last two expressions, we find

$$G_o = \frac{\lambda^2 A_{21}}{2} (N_2 - N_1) \quad (2-6)$$

By our convention A_{21} is defined per unit solid angle, so after integration over all angles we have

$$A'_{21} = 4\pi A_{21}$$

= number of spontaneous transitions per molecule per unit frequency in all directions

The radiative lifetime is related to the Einstein spontaneous emission coefficient by

$$\tau'_{21} = \frac{1}{A'_{21}}$$

Then

$$G_o = \frac{\lambda^2}{8\pi \tau'_{21}} (N_2 - N_1) \quad (2-7)$$

Thus far we have assumed that the transition takes place at a distinct frequency. However, the natural radiative transition is smeared over a finite frequency interval. The true lifetime τ'_{21} actually observed would be an integrated value over the whole transition linewidth. To account for this integration we introduce the lineshape function $g(v_o)$ into Eq. (2-7):

$$G_o = \frac{\lambda^2}{8\pi \tau'_{21}} (N_2 - N_1) g(v_o) \quad (2-8)$$

To determine the lineshape factor we must look at the processes which lead to broadening of the spectral line. If the pressure of the gas is below 10 torr, the broadening is primarily due to the Doppler effect. For pressures very much above 10 torr the dominant contribution to the linewidth is from collisional (pressure) broadening. In this case, which corresponds to the pressure regime encountered in MHD laser systems, the lineshape is given by the Lorentzian profile:

$$g(v_o) = \frac{\Delta v}{2\pi [(v_o - v)^2 + (\frac{\Delta v}{2})^2]} \quad (2-9)$$

For collision broadening the linewidth is given by

$$\Delta v = \frac{v_c}{\pi}$$

where v_c is the total collision frequency between CO_2 and all species:

$$v_c = \sum_i N_i \sigma_i \bar{c}_{\text{CO}_2-i}$$

where

$$\bar{c}_{\text{CO}_2-i} = \sqrt{\frac{8RT}{\pi} \frac{\frac{M_{\text{CO}_2}}{M_i} + \frac{M_i}{M_{\text{CO}_2}}}{M_i}}$$

Then for pressures above 10 torr the small signal gain at line center ($v = v_0$) is

$$G_0 = \frac{\lambda^2}{4\pi\tau_{21} v_c^2} (N_2 - N_1) \quad (2-10)$$

where

$$\lambda = 10.6 \times 10^{-6} \text{ m}$$

and

$$\tau_{21} = 5.38 \text{ sec.}$$

The population inversion exists for transitions between two distinct vibration-rotation levels. So N_2 and N_1 are functions not only of the vibrational level, but also of the rotational level:

$$N_2 = N_{001} F(J)$$

$$N_1 = N_{100} F(J \pm 1).$$

Because of the selection rules for dipole transitions the rotational quantum number J must change by ± 1 between the upper and lower laser levels.

Here

$$N_{001} = n_{CO_2} Q^{-1} e^{-hv_3/kT_3}$$

and

$$N_{100} = n_{CO_2} Q^{-1} e^{-hv_1/kT_1}$$

where

$$Q = (1 - e^{-hv_1/kT_1}) (1 - e^{-hv_2/kT_2})^2 \\ \times (1 - e^{-hv_3/kT_3})$$

= vibrational energy partition function.

The fraction of CO_2 molecules in the J th rotational level is given by:

$$F(J) = (2J + 1) \frac{\theta_{ROT}}{T} \exp [-J(J+1) \frac{\theta_{ROT}}{T}].$$

The characteristic rotational temperature θ_{ROT} is about $0.56^{\circ}K$. The rotational relaxation rate is several orders of magnitude faster than the intermode vibrational transfer rate. Furthermore, the electron mole fraction is small enough (10^{-5}) that electron excitation of the rotational levels will not be comparable to heavy particle relaxation.⁽⁸⁾ Thus we may assume here that the rotational levels follow a Boltzmann distribution at the gas translational temperature T .

For values of T between 300 and 400°K the maximum population occurs on the $J = 20$ level. Then the transition with the highest gain will be $P(20)$, for which J jumps from 20 to 21. This will be the first line to lase in an oscillator. If the rotational reequilibration rate is rapid enough, this level will be continually repopulated by collisions. Reference (25) indicates that this will indeed be the case even for the low CO_2 concentration in an MHD laser. We may then use Anderson's approximation to Eq. (2-10) to calculate the small signal gain on the $P(20)$ transition. (22)

$$G_o = \frac{\lambda^2}{4\pi\tau_{21} v_c} (N_{001} - N_{100}) \left(\frac{45.6}{T}\right) e^{-234/T} \quad (2-11)$$

As the fluid moves down the channel, the vibrational level populations and the temperature will change as a result of collisional excitation-relaxation processes and gasdynamic effects. Then the gain itself is a function of x , the axial coordinate. We can determine this axial variation in gain by solving the rate equations for the populations N_{001} and N_{100} .

There are two alternate approaches to writing these equations. The first is to write a separate rate equation for each level which has a significant population. In the case where the degree of vibrational excitation is significant, a large number of levels will be populated. Hence the number of rate equations requiring solution by numerical integration could become rather large.

This situation can be simplified considerably if the energy levels within each mode of vibration are in Boltzmann equilibrium with one another. We noted in Chapter 1 that this was true if the intramode energy transfer rate was rapid enough. Then to calculate the population of any one level we merely evaluate the Boltzmann relation at the correct vibrational temperature. This temperature is determined from a knowledge of the energy in the mode. In the case of CO_2 the rate equations for all the vibrational energy levels reduce to a set of three equations, one for each mode of vibration. Schwartz, Slawsky, and Herzfeld showed that when the energy levels of a mode are in equilibrium, the rate equation for the mode takes the form of the Landau-Teller equation.⁽²⁶⁾ This was derived originally for a system composed of diatomic harmonic oscillators in a bath of vibrationally inactive particles. Then the rate equations for the three modes are:

$$\frac{DE_1}{Dt} = -\frac{E_1(T_1) - E_1(T_2)}{\tau_{1\text{REL}}} \quad (2-12)$$

$$\begin{aligned} \frac{DE_2}{Dt} &= \frac{E_2(T_e) - E_2(T_2)}{\tau_{2e}} + \frac{E_3(T_3) - E_3(T_2)}{\tau_{3\text{REL}}} \\ &+ \frac{E_1(T_1) - E_1(T_2)}{\tau_{1\text{REL}}} - \frac{E_2(T_2) - E_2(T)}{\tau_{2\text{REL}}} \end{aligned} \quad (2-13)$$

$$\frac{DE_3}{Dt} = \frac{E_3(T_e) - E_3(T_3)}{\tau_{3e}} - \frac{E_3(T_3) - E_3(T_2)}{\tau_{3\text{REL}}} \quad (2-14)$$

Here we have neglected certain low-probability collisional processes which we shall describe in Chapter 4.

Also,

$$E_i = \frac{h\nu_i}{e^{\frac{h\nu_i}{kT_i} - 1}} n_{CO_2}$$

is the vibrational energy density of the i th mode, $E_i(T_j)$ is E_i evaluated at temperature T_j , and τ_{ie} and τ_{iREL} are the excitation and relaxation times for mode i . Once the energy densities of the three modes are known, it is a simple matter to calculate the vibrational temperatures via a numerical technique such as the Newton-Raphson method. Then the level populations and the small signal gain can be computed in a straightforward manner.

2.3 Power Extraction

The gain calculation discussed in the previous section implicitly assumed that the optical intensity was small enough that it did not significantly disturb the level populations via induced transitions. In small signal gain experiments where the inverted medium is used as an amplifier for a weak probe laser beam this is a valid assumption. The small signal gain is a frequently quoted figure of merit which can be measured with standard experimental techniques. However, for high energy laser applications the key question centers on how much average power can be extracted from the gas. In order to calculate the performance of devices where the optical intensity is not small, we must include in the rate equations the effects of stimulated emission in depopulating the upper laser

level and filling the lower one.

This involves the addition of one term to each of Eqs. (2-12) and (2-14). The rate of optical energy production per unit volume is given by gI , where g is the local (saturated) gain and I is the optical intensity. The saturated gain is related to the small signal gain via⁽²⁷⁾

$$g = \frac{G_0}{1 + I/I_{SAT}} \quad (2-15)$$

Here I_{SAT} is the saturation intensity, which depends on the relaxation rates of the various energy levels.

In a laser oscillator with planar mirrors of constant reflectivity the gain is clamped at a fixed value by the cavity parameters. Assuming that energy is lost only at the mirrors, a steady state energy balance for the cavity shows that the rate of optical energy production by the molecules must equal the energy flux through the mirrors (transmission plus absorption). This gain-equals-loss condition may be expressed by⁽²⁷⁾

$$g = - \frac{1}{2L} \ln(r_1 r_2) \quad (2-16)$$

where

L = cavity width

and

r_1, r_2 = mirror reflectivities.

For simplicity we shall restrict our analysis to a single pass resonator with planar mirrors of constant spacing and reflectivity. With the gain fixed during lasing we can proceed to calculate the optical intensity I . The technique is the same as that used in References (4), (8), and (28); it is described in detail in Appendix A. To summarize this calculation briefly, we solve the energy transfer equations for the optical intensity in the cavity with g fixed by Eq. (2-16). We do not consider the cavity mode structure or the effects of diffraction.

Whenever an induced transition occurs, the upper laser level loses energy $h\nu_0$ to the radiation field. The lasing molecule initially has the energy of vibration $h\nu_3$. The difference between $h\nu_3$ and $h\nu_0$ goes into Mode 1, and is equal to $h\nu_1$. Then the rate of energy lost per unit volume by Mode 3 may be written in terms of the optical energy production rate as $\frac{v_3}{v_3 - v_1} gI$. We may now write the complete rate equations for the three CO_2 vibrational modes as

$$\frac{DE_1}{Dt} = -\frac{E_1(T_1) - E_1(T_2)}{\tau_{1\text{REL}}} + \frac{v_1}{v_3 - v_1} gI \quad (2-17)$$

$$\begin{aligned} \frac{DE_2}{Dt} = & \frac{E_2(T_e) - E_2(T_2)}{\tau_{2e}} + \frac{E_3(T_3) - E_3(T_2)}{\tau_{3\text{REL}}} \\ & + \frac{E_1(T_1) - E_1(T_2)}{\tau_{1\text{REL}}} - \frac{E_2(T_2) - E_2(T)}{\tau_{2\text{REL}}} \end{aligned} \quad (2-18)$$

$$\frac{DE_3}{Dt} = \frac{E_3(T_e) - E_3(T_3)}{\tau_{3e}} - \frac{E_3(T_3) - E_3(T_2)}{\tau_{3REL}} - \frac{v_3}{v_3 - v_1} gI \quad (2-19)$$

As the fluid moves down the channel, a certain amount of time and distance is required before a population inversion develops which is large enough to permit lasing. Until this occurs Eqs. (2-12) - (2-14) are adequate to describe the state of the vibrational modes. The gain is monitored until the threshold value is reached. Then laser power output is calculated based on the assumption that the laser transitions occur at a rate that just balances the pumping mechanisms in order to maintain the gain at threshold.

Let us imagine that the output coupling is effected entirely through mirror 2, which has absorptivity a_2 and transmissivity t_2 such that $r_2 = 1 - a_2 - t_2$. Then the output power per unit area is given by $t_2 I$. It should be understood that this is a local quantity, since I varies with x in the one-dimensional fluid flow approximation. A quadrature is required to calculate the output power:

$$P_{OUT}(x) = \int_{x_0}^x t_2 I(x) h(x) dx \quad (2-20)$$

where x_0 is the point at which oscillation begins and $h(x)$ is the height of the mirrors.

The total power removed from the plasma is equal to the output power P_{OUT} plus the power absorbed by the mirror P_{ABS} . The latter is also calculated by a quadrature:

$$P_{ABS}(x) = \int_{x_0}^x (a_1 + a_2) I(x)h(x) dx. \quad (2-21)$$

We shall assume throughout the remainder of this analysis that $a_1 = a_2 = 0.02$, a representative value for the type of oscillator cavity we are considering. The transmission coefficient will be treated as a free parameter.

Several efficiency parameters are useful in describing the performance of an MHD laser. Since the process of converting the thermal energy of the gas to coherent optical energy involves several intermediate steps, the overall efficiency can be divided into the product of several step or stage efficiencies. Of prime interest here are quantities which we shall refer to as the pumping, optical, and local efficiencies. We define the pumping efficiency η_p as the fraction of the Joule dissipation power which is transferred to the upper laser level $CO_2(00^01)$. In general, this fraction depends on the state of the plasma and is expressed mathematically as

$$\eta_p = \frac{[E_3(T_e) - E_3(T_3)]/\tau_{3e}}{J^2/\sigma_{eff}} \quad (2-22)$$

Note that the rate of energy transfer to the CO_2 depends not only upon the excitation time τ_{3e} , but also upon the difference between the electron temperature T_e and the upper laser level temperature T_3 . In conjunction with this we can also define η_L as the fraction of the Joule dissipation that is transferred to the bending mode $\text{CO}_2(01'0)$:

$$\eta_L = \frac{[E_2(T_e) - E_2(T_2)]/\tau_{2e}}{J^2/\sigma_{\text{eff}}} \quad (2-23)$$

This is not really an efficiency, but a parasitic loss term, because it is power that is lost to the upper laser level.

Closely related to the pumping efficiency is the optical efficiency η_{OPT} , defined as the fraction of the Joule dissipation which is actually converted to optical power:

$$\eta_{\text{OPT}} = \frac{gI}{J^2/\sigma_{\text{eff}}} \quad (2-24)$$

The numerator gI is not the total optical output, but rather the intracavity flux density. With this dissipation η_{OPT} is a measure of the importance of collisional deactivation of the upper laser level. η_{OPT} approaches η_p when all the molecules in the upper laser level are deactivated by stimulated transitions.

From an overall performance viewpoint, the most important efficiency parameter is the local efficiency η_{LOC} , which we define as the ratio of the energy actually extracted from the

laser cavity to the energy that could be extracted if the process were adiabatic:

$$\eta_{LOC} = \frac{t_2 g I h(x) dx}{\dot{m} c_p T_{01} [1 - (\frac{P_{02}}{P_{01}})^{(\gamma-1)/\gamma}]} \quad (2-25)$$

This is closely related to the concept of turbine efficiency in the turbomachinery literature. For a given pressure drop the denominator represents the maximum amount of work which can be done according to the laws of thermodynamics. Thus η_{LOC} is also a measure of the cavity length required to produce a desired amount of optical power. Excessively long optical cavities are undesirable for a variety of reasons. Among these are the high cost of large mirrors, the increased loss of molecules from the upper laser level due to collisional deactivation, and the increased importance of viscous losses in a longer channel. We can define an extraction length L_{EXT} , which is the distance the fluid must travel in order for a desired optical power P_{TOT} to be removed:

$$L_{EXT} = \frac{P_{TOT}}{\Delta P/\Delta x} \quad (2-26)$$

Here $\frac{\Delta P}{\Delta x}$ is the amount of power extracted per unit length, which is related to the local efficiency:

$$\begin{aligned}\eta_{LOC} &= \frac{\Delta P}{\Delta H_{ad}} \\ &= \frac{\Delta P / \Delta x}{\Delta \dot{H}_{ad} / \Delta x} \quad (2-27)\end{aligned}$$

Then

$$\begin{aligned}\frac{\Delta P}{\Delta x} &= \eta_{LOC} \frac{\Delta \dot{H}_{ad}}{\Delta x} \\ &= \eta_{LOC} \frac{\dot{m} c_p T_{01} [1 - (\frac{P_{02}}{P_{01}})^{(\gamma-1)/\gamma}]}{\Delta x} \quad (2-28)\end{aligned}$$

Thus the extraction length can be reexpressed as

$$L_{EXT} = \frac{P_{TOT} \Delta x}{\eta_{LOC} \dot{m} c_p T_{01} [1 - (\frac{P_{02}}{P_{01}})^{(\gamma-1)/\gamma}]} \quad (2-29)$$

This shows clearly that when the local efficiency is high, the length required to produce a desired power output is relatively short. On the other hand a low value of η_{LOC} means that a longer MHD channel and optical cavity will be required.

III. DESCRIPTION OF PLASMA

3.1 Basic Assumptions

In this chapter we will present a self-consistent analytical formulation describing the behavior of the fluid in a magnetohydrodynamic laser. A model of the flow in an MHD channel must employ a set of coupled equations describing the neutral gas species and the electron gas. The coupling is effected by the retarding Lorentz force which results from the interaction between the electric current and the magnetic field, and by the Joule dissipation. In a nonequilibrium MHD device the electron temperature is elevated above that of the neutral gas, and the description of the fluid is further complicated by the dependence of the electrical conductivity on both the current and the thermodynamic variables. In addition, an accurate model must account for such effects as ionization instabilities (electrothermal waves), finite ionization and recombination kinetics, and Hall currents arising from finite segmentation of electrodes.

A theory of the nonequilibrium MHD generator including all of these phenomena has been developed by Solbes.⁽¹⁵⁾ Parma⁽²⁹⁾ and Cole⁽¹⁶⁾ have used this theory to analyze the results of nonequilibrium MHD experiments conducted at MIT, in particular experiments run at short circuit. (We have already seen that short circuit is the optimum loading condition

for an MHD laser.) Their numerical computations of the fluid properties were found to agree quite well with the experimental measurements. In order to apply this model to the flow in an MHD laser it will be necessary to extend it to include the effects of CO_2 vibrational excitation and relaxation. Since the molecules exchange energy with both the electrons and the other neutral species, these processes introduce a further degree of coupling between the electron kinetics and the fluid mechanics.

As an overview of what follows, Figure 4 illustrates the interrelationship of the various physical properties of the plasma. Besides the already discussed link between the heavy particles and the electrons, we should note the energy transfer channel between the electrons and the CO_2 vibrational levels, the channels between the vibrational levels themselves, and the channel between the vibrational levels and heavy particle translation. Through these transfer mechanisms the electrons lose a large fraction of their energy to the asymmetric stretch and bending modes. Also, after an excited molecule emits a photon it returns to the ground state through collisions with helium atoms. The energy transferred to the translational modes serves to heat the gas.

In addition to these coupling effects a number of other physical phenomena should be considered before the flow model is presented. As described in Section 1.B the chemical reaction between Cs and CO_2 has proved to be an important factor

in several experimental MHD laser feasibility studies performed to date. The analytical studies have ignored this reaction and further narrowed their scope to consideration of inviscid MHD flows. We shall do the same in the present formulation, but let us first attempt to justify why it is appropriate to model the laser flow in this way.

The residence time of an element of fluid in the laser cavity is given by

$$\tau_{\text{RES}} \approx \frac{L_{\text{CAV}}}{U}$$

where L_{CAV} is the length of the cavity in the x direction and U is the flow velocity. For $L_{\text{CAV}} = 1 \text{ m}$ and $U = 4000 \text{ m/sec}$ τ_{RES} is 0.25 milliseconds. In order for the chemical reaction between Cs and CO_2 to be important the characteristic time scale on which it occurs must be considerably less than τ_{RES} . Because the reaction mechanism is unknown, calculation of the characteristic reaction time using known reaction rates is not possible. However, experimental evidence indicates that the phenomenon is more likely to be a problem in small scale feasibility experiments with slow-moving gases than in full scale MHD lasers.

Zauderer, et al.,⁽¹⁰⁾ indicates that positive gain can be produced if the CO_2 mole fraction is kept well above the Cs mole fraction, allowing most of the CO_2 to remain unreacted. The Russian investigation demonstrated power extraction from

a self-sustained discharge with $n_{Cs}/n_{He} \approx 10^{-4} - 10^{-3}$ and $n_{CO_2}/n_{He} \approx 10^{-2}$. However, addition of CO_2 to the He-Cs flow led to a reduction of the free cesium concentration by an order of magnitude, i.e., $n_{Cs}/n_{He} \approx 10^{-5} - 10^{-4}$. Results from Sharma's pulsed gas-handling system, designed to minimize the $Cs-CO_2$ reaction, confirm these findings. (12)

In the present study, attention is directed at a realistic MHD laser configuration consisting of a supersonic nozzle and channel. On the basis of conclusions drawn from the experimental studies we shall assume here that the chemical reaction is confined to the mixing plenum upstream of the nozzle throat and that after the reaction $10^{-6} < x_{Cs} < 10^{-4}$ as in the Russian experiment. Then products of the reaction will be so few as to be of no consequence to the flow processes in the nozzle and channel. We shall not consider the $Cs-CO_2$ reaction any further in this work.

One of the features of a well-designed MHD channel is a Reynolds number large enough that frictional and heat transfer losses associated with the fluid flow are small. The ratio of length to hydraulic diameter for MHD generators is approximately 10, whereas the L/D required for a fully developed boundary layer is in the range 50-100. Under such conditions the momentum and energy losses are confined to a thin area near the wall. The flow in the core of the channel is affected only by the reduction in effective cross-sectional area due to the growth of the boundary layer displacement

thickness. (This feature is shared in common with the flows in high speed gasdynamic lasers. The supersonic nozzle in these devices is usually contoured to offset the boundary layer growth.)

Both the Russian study (Ref. 11) and the UARL investigation (Ref. 6-8) indicate that the major boundary layer effect in the MHD laser is also displacement thickness growth. Since the wall divergence half angle is usually small ($<1^\circ$), the flow can be accurately modeled as a quasi-one dimensional inviscid core flow with a two dimensional displacement boundary layer. This is the approach used by Cole in his numerical treatment of nonequilibrium MHD generator performance.⁽¹⁶⁾ A more accurate analysis would of course entail a complicated boundary layer calculation involving turbulent flow, large heat transfer, compressibility, and MHD effects. However, this goes beyond the purpose of the present work, which is to determine which of several key physical processes set the limits on MHD laser performance and which set of operating conditions leads to optimum output characteristics. The effects of the boundary layer are henceforth assumed to be confined to displacement thickness growth. In accordance with the result obtained by Parma⁽²⁹⁾ we shall assume that the displacement boundary layer grows linearly with x . The core flow is then effectively bounded not by the original inviscid contour, but by the inner surface of an annulus formed by the boundary layer.

We now proceed to develop a set of equations for the core flow assuming:

- (a) the MHD approximations of charge neutrality and negligible induced magnetic field (small magnetic Reynolds number) are valid
- (b) the flow is one-dimensional, steady, inviscid, and non-heat-conducting
- (c) gasdynamic properties are uniform over a channel cross section
- (d) transverse pressure gradients due to axial Hall current flow are insignificant.
- (e) the electron Hall parameter is low enough (less than 10) that ion slip can be ignored.

3.2 Gasdynamic Equations

The evolution of the core flow is described by four fundamental equations: the continuity equation, the axial momentum equation, the energy equation, and the equation of state. These equations are derived in detail in any standard fluid mechanics text such as Reference 30. For the inviscid core flow in an MHD channel they take the following forms:

STATE

$$p = nkT \quad (3-1)$$

CONTINUITY

$$\dot{m} = \rho_{\infty} U_{\infty} A_D \quad (3-2)$$

MOMENTUM

$$\rho_\infty U_\infty \frac{dU_\infty}{dx} + \frac{dp}{dx} = J_y B \quad (3-3)$$

ENERGY

$$\rho_\infty U_\infty C_p \frac{dT_o}{dx} = 0 \quad (3-4)$$

Here ρ_∞ and U_∞ refer to the density and velocity of the core flow while A_D represents the effective cross section of the core region (total area minus area of the annulus formed by the boundary layer). Q is the volumetric energy addition to the gas.

In terms of the Mach number and the stagnation pressure and temperature we can write the continuity equation as

$$\dot{m} = A_D p_0 \frac{2\gamma}{(\gamma-1)RT_0} \frac{v}{(1+v)(\gamma+1)/(\gamma-1)} \quad (3-5)$$

where $v = \frac{\gamma-1}{2} M^2$.

By the definition of the displacement thickness,

$$A_D = A - P\delta_D$$

where

A = actual channel cross section

P = channel perimeter

δ_D = boundary layer displacement thickness

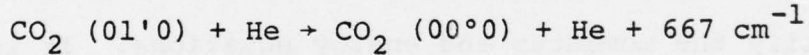
In accord with the results of Refs. 16 and 29, δ_D was taken as $0.003x$ for these calculations.

(From this point on we shall restrict our attention to the core flow, so the subscript ∞ will be dropped from the notation.)

The only difference between the equations for MHD generator flow and Eqs. (3-1) through (3-4) is in the form of the right hand side of the energy equation. In a generator Q is equal to the rate of the elastic energy loss from the electrons to the gas minus the mechanical work done by the gas:

$$\begin{aligned} Q &= \frac{3}{2} \delta \frac{m_e}{m} k (T_e - T) n_e v_e + J_y UB \\ &= \frac{3}{2} \delta \frac{m_e}{m} k (T_e - T) n_e v_e - |J_y| UB \end{aligned} \quad (3-6)$$

When CO_2 is present in the plasma one more energy gain term is added to this equation, corresponding to the vibration-translation (VT) collisional relaxation process



Using the Landau-Teller formulation of Eq. (2-18) we may write this extra term as

$$Q_{\text{VT}} = \frac{E_2(T_2) - E_2(T)}{\tau_{2\text{REL}}} \quad (3-7)$$

Then the complete volumetric energy addition term for the MHD laser becomes

$$Q = \frac{3}{2} \delta \frac{m_e}{m} k (T_e - T) n_e v_e + \frac{E_2(T_2) - E_2(T)}{\tau_{2REL}} - |J_y| UB \quad (3-8)$$

Let us consider for a moment the effect of adding the vibrational relaxation term to the energy equation. The sign of this term is always positive since $T_2 \geq T$. It is well known from one-dimensional gasdynamics that heat addition tends to choke a supersonic flow, driving the Mach number toward 1 and decreasing the stagnation pressure.⁽³¹⁾ For a subsonic flow the Mach number will likewise be driven toward 1, and the stagnation pressure again decreases. Then during intense lasing, if the lower level relaxation rate is rapid enough the flow may come close to choking as it moves downstream.

As they are now written the state and continuity equations are in usable form, but it would be beneficial to simplify the momentum and energy equations. It is convenient to define now the generalized load factor K. The right hand side of the energy equation may be thought of as a general power P; similarly the right hand side of the momentum equation may be written as a generalized force F. Then the generalized load factor is defined as

$$K = \frac{P}{FU}$$

In our case $F = J_y B = -|J_y| B$

and

$$P = \frac{3}{2} \delta \frac{m_e}{m} k (T_e - T) n_e v_e + \frac{E_2(T_2) - E_2(T)}{\tau_{2REL}} - |J_y|_{UB}$$

so the load factor is

$$K = 1 - \frac{1}{|J_y|_{UB}} \left[\frac{3}{2} \delta \frac{m_e}{m} k (T_e - T) n_e v_e + \frac{E_2(T_2) - E_2(T)}{\tau_{2REL}} \right] \quad (3-9)$$

With this definition and some algebraic manipulation it is easy to show that the momentum and energy equations reduce to

$$\frac{d(\ln p_o)}{dx} = -i \quad (3-10)$$

$$\frac{d(\ln T_o)}{dx} = -\frac{\gamma-1}{\gamma} \eta_p i \quad (3-11)$$

where

$$i = \frac{|J_y|_B}{p} \frac{1 + v(1 - K)}{1 + v}$$

= interaction parameter

$$\eta_p = \frac{K}{1 + v(1 - K)}$$

= polytropic efficiency

Eqs. (3-1), (3-5), (3-10), and (3-11) constitute the set required to calculate the gasdynamic variables.

3.3 Plasma Equations

Because of the coupling provided by the MHD interaction the gasdynamic equations cannot be solved without simultaneously determining the electrical properties of the gas. In the regime we are considering ($\beta < 10$) the electrical behavior is governed primarily by the electron kinetics. The three equations describing the electrons in the plasma are the electron continuity (rate) equation, the electron momentum equation (Ohm's Law), and the electron energy equation. It is known that if the Hall parameter exceeds a critical value, the plasma becomes unstable and electro-thermal waves may propagate^(32, 33). These result in spatial and temporal nonuniformities in n_e and T_e which reduce the values of β and the conductivity σ . We shall first present the equations describing the plasma in their local form. Then by a quasilinear averaging technique developed by Solbes we can account for these reductions by calculating effective values β_{eff} and σ_{eff} for the bulk plasma.

The local continuity equation may be written

$$\frac{\partial n_e}{\partial t} + \nabla \cdot (n_e \bar{U}) = R n_e [n_e^{*2} - n_e^2] \quad (3-12)$$

This states that the rate at which the free electron population changes is equal to the difference between the ionization and three-body recombination rates. Here n_e is the

electron number density and R is the Hinnov-Hirschberg three-body recombination coefficient, given by

$$R = 2.29 \times 10^{-34} \left(\frac{1100}{T_e} \right)^{9/2} \quad (3-13)$$

in MKS units. (34) (It is assumed here that only electrons are important as the stabilizing body in the recombination process.) The ionization coefficient is evaluated by the principle of detailed balancing when equilibrium exists between the free and bound electrons. It is given by $R n_e^{*2}$, where

$$n_e^{*2} = n_s (1-\alpha) \left(\frac{2\pi m_e kT_e}{n^2} \right)^{3/2} \exp\left(-\frac{eV_i}{kT_e}\right) \quad (3-14)$$

n_e^* is the electron density that would exist if the electron population were in Saha equilibrium at the electron temperature.

Eq. (3-12) assumes that the only collisional processes of importance are electron impact ionization of cesium and three-body electron recombination. However, we saw in Section 1.A that previous studies of the MHD laser have indicated that quenching collisions between CO_2 and Cs may be a crucial factor. We also saw that the effects of these collisions are essentially equivalent to those resulting from the radiative decay of excited Cs states. McGregor, Mitchner, and Shaw have calculated an effective ionization rate for cesium

when radiation escape is important. ⁽³⁵⁾ Their results were found to be approximated within a factor of two by the following empirical relation: ⁽⁸⁾

$$\frac{\partial n_e}{\partial t} + \nabla \cdot (n_e \bar{U}) = \dot{n}_e = \frac{n_e n_e^*^2 R}{1 + \frac{2 \times 10^{19}}{n_e} + \frac{10^{50} \epsilon_R}{n_e^{5/2}}} - R n_e^3 \quad (3-15)$$

where ϵ_R is the radiation escape parameter, defined such that $0 \leq \epsilon_R \leq 1$.

Mnatsakanyan's results ⁽³⁾ indicated that ϵ_R could be modified to include the effects of molecular quenching collisions. This effective escape parameter is

$$\hat{\epsilon} = \frac{\epsilon_R + \sum_j \frac{n_j k_{j-Cs}}{A_{10}} [1 - \exp[-\frac{\epsilon_{01}}{k} (\frac{1}{T_{vj}} - \frac{1}{T_e})]]}{1 + \sum_j \frac{n_j k_{j-Cs}}{n_e k_{e-Cs}} \exp[-\frac{\epsilon_{01}}{k} (\frac{1}{T_{vj}} - \frac{1}{T_e})]} \quad (3-16)$$

In the electron temperature range encountered in an MHD laser this reduces to

$$\hat{\epsilon} = \epsilon_R + \frac{n_{CO_2} k_{CO_2-Cs}}{A_{10}} \quad (3-17)$$

Here A_{10} = Einstein coefficient for $6^2P_{1/2} \rightarrow 6^2S_{1/2}$ transition of Cs
 $= 2.63 \times 10^7$ sec

$$k_{CO_2-Cs} = \bar{C}_{CO_2-Cs} \sigma_{CO_2-Cs}$$

σ_{CO_2-Cs} = quenching cross section summed over all vibrational levels

ϵ_R will be small in a nonequilibrium MHD plasma (0.01 or less) so that for typical conditions, $\hat{\epsilon} = \frac{n_{CO_2} k_{CO_2-Cs}}{A_{10}}$. This is the quantity that goes into the denominator of Eq. (3-15) in place of ϵ_R . This equation is used in the studies of quenching effects described in Section 6.B. In the remainder of the work, however, the quenching cross section is assumed to be zero so that Eq. (3-12) is the more appropriate version to use.

In writing the Ohm's law we include the Hall effect but neglect ion slip and electron pressure gradients:

$$\bar{J} + \bar{J} \times \bar{\beta} = \sigma (\bar{E} + \bar{U} \times \bar{B}) \quad (3-18)$$

The Hall parameter $\bar{\beta}$ and conductivity σ are given by

$$\bar{\beta} = \frac{e \bar{B}}{m_e v_e} \quad (3-19)$$

$$\sigma = \frac{e^2 n_e}{m_e v_e} \quad (3-20)$$

The Lin-Resler-Kantrowitz mixing rule⁽³⁶⁾ gives an accurate expression for the electron collision frequency v_e :

$$v_e = \sum_i v_i$$

$$v_i = C_i \frac{8k T_e}{\pi m_e} n_i Q_i(T_e) \quad (3-21)$$

The summation is taken over gas atoms, seed atoms, and ions.

In this generalized expression for the collision frequency

Q_i is the Maxwell-averaged momentum transfer cross section while C_i depends on the force law and energy for the encounter.

For Cs mole fractions below 10^{-3} and CO_2 fractions less than 0.1 the electron-helium collisions dominate neutral gas momentum transfer, so electron- CO_2 collisions can be ignored in Ohm's law. At $T_e = 2500^\circ\text{K}$ the appropriate factors in Eq. (3-18) are: $Q_{\text{He}} = 6.25 \times 10^{-20} \text{ m}^2$, $C_{\text{He}} = 3\pi/8$;

$Q_{\text{Cs}} = 2.2 \times 10^{-18} \text{ m}^2$, $C_{\text{Cs}} = 3\pi/8$, $Q_+ = (9\pi^2/16) d_o^2 \ln \Lambda$, $C_+ = 1/0.582$.

Here d_o = Landau impact parameter

$$= e^2 / (12\pi \epsilon_o k T_e)$$

and Λ = ratio of Debye length to d_o

$$= \frac{\epsilon_o k T_e}{e^2 n_e} \frac{1}{d_o}$$

Finally, the energy equation for electrons is:

$$\begin{aligned}
 \frac{\partial}{\partial t} [n_e (eV_i + \frac{3}{2} kT_e)] + \nabla \cdot [n_e (eV_i + \frac{3}{2} kT_e) \bar{V}_e] \\
 + n_e kT_e \nabla \cdot \bar{V}_e = \frac{J^2}{\sigma} - \delta \frac{m_e}{m} \frac{3}{2} k(T_e - T) n_e v_e \\
 - \frac{E_3(T_e) - E_3(T_3)}{\tau_{3e}} - \frac{E_2(T_e) - E_2(T_2)}{\tau_{2e}}
 \end{aligned}
 \tag{3-22}$$

In writing this we have neglected heat conduction and radiation losses (a justifiable assumption when helium is the buffer gas)⁽¹⁵⁾ and the energy stored in the excited electronic states of the seed (justifiable for an alkali metal vapor). This equation differs from the one for an MHD generator plasma in that we have included on the right hand side the loss of energy by electrons to Modes 2 and 3 of the CO₂ molecule. One might argue that these two terms ought to be included in the elastic energy loss rate, using experimentally determined values of δ for CO₂. Craggs and Massey⁽³⁷⁾ have summarized the results of many experimental investigations and give tabulated data for the elastic loss parameters for many gases; for CO₂ in the range of electron temperatures of interest to us δ is approximately 2500.

However, Draper⁽³⁸⁾ has pointed out that most of this data comes from electron swarm experiments in ground state CO₂ and is not representative of a gas which has undergone significant vibrational excitation. That is δ actually depends on the internal state of the CO₂ molecule rather than on the

electron temperature alone. Thus the adoption of this elastic loss parameter formulation could lead to significant errors in the electron energy loss rates if we use the existing data for δ . For this reason we have employed the Landau-Teller formulation, which explicitly states the dependence of the energy transfer rates on the degree of vibrational excitation.

In Eq. (3-19) \bar{V}_e is the electron velocity measured in the laboratory frame. δ is given by

$$\delta = \frac{m}{v_e} \sum_i 2C'_i \frac{v_i}{m_i} \quad (3-23)$$

where again the summation is over helium atoms, cesium atoms, and cesium ions. m is the average atomic mass of the plasma; m_i is the atomic mass of species i ; and C'_i is a constant which depends on the force law for the encounter:

$$\begin{aligned} C'_i &= 1 \text{ for Maxwellian encounter} \\ &= \frac{4}{3} \frac{8}{3\pi} \text{ for hard spheres} \\ &= 1.97 \text{ for Coulomb collisions} \end{aligned}$$

The electron-neutral collisions in an MHD laser plasma are modeled as hard sphere encounters.

By making use of $\nabla \cdot \bar{J} = 0$ and defining

$$x_i = \frac{eV_i}{kT_e} + \frac{3}{2} \quad (3-24)$$

we can simplify the lefthand side of the energy equation:

$$\begin{aligned}
 kT_e x_i \left[\frac{\partial n_e}{\partial t} + \nabla \cdot (n_e \bar{U}) \right] + \frac{3}{2} \frac{n_e}{n_e^*} \frac{2-\alpha}{1-\alpha} \frac{1}{x_i} \left[\frac{\partial n_e^*}{\partial t} + \bar{V}_e \cdot \nabla n_e^* \right] \\
 + n_e \nabla \cdot \bar{V}_e = \frac{J^2}{\sigma} - \delta \frac{m_e}{m} \frac{3}{2} k(T_e - T) n_e v_e \\
 - \frac{E_3(T_e) - E_3(T_3)}{\tau_{3e}} - \frac{E_2(T_e) - E_2(T_2)}{\tau_{2e}} \quad (3-25)
 \end{aligned}$$

For $T_e = 3000^\circ K$ Eq. (3-24) gives $x_i = 16.5$. Then the first term in the brackets is typically $\frac{1}{3} x_i^2$ (~ 100) times larger than the second term (except near full ionization of the seed) and x_i (~ 20) times larger than the third term. This allows us to neglect the second and third terms of Eq. (3-25), giving

$$\begin{aligned}
 kT_e x_i \left[\frac{\partial n_e}{\partial t} + \nabla \cdot (n_e \bar{U}) \right] = \frac{J^2}{\sigma} - \delta \frac{m_e}{m} \frac{3}{2} k(T_e - T) n_e v_e \\
 - \frac{E_3(T_e) - E_3(T)}{\tau_{3e}} - \frac{E_2(T_e) - E_2(T_2)}{\tau_{2e}} \quad (3-26)
 \end{aligned}$$

Eqs. (3-12), (3-18), and (3-26) together describe the local electrical behavior of the MHD laser plasma. In order to apply these equations to the description of the plasma flow through a channel, it is necessary to develop averaged versions to account for the nonuniformities in n_e and T_e that are caused by electrothermal waves. We characterize these spatial and temporal variations in the plasma properties by writing n_e

and n_e^* as the sum of an average term plus a small perturbation:

$$n_e = \langle n_e \rangle (1 + n)$$

$$n_e^* = \langle n_e^* \rangle (1 + n^*) \quad (3-27)$$

The average is performed over the channel cross section and time. To determine these new parameters it is necessary to average the three plasma equations, a procedure which produces equations for $\langle n_e \rangle$ and $\langle n_e^* \rangle$.

CONTINUITY

$$\langle \frac{\partial n_e}{\partial t} \rangle + \langle \nabla \cdot (n_e \bar{U}) \rangle = \langle R n_e (n_e^*{}^2 - n_e^2) \rangle \quad (3-28)$$

OHM'S LAW

$$\langle \bar{J} \rangle + \langle \bar{J} \times \beta \rangle = \langle \sigma (\bar{E} + \bar{U} \times \bar{B}) \rangle \quad (3-29)$$

ENERGY

$$\begin{aligned} \langle kT_e \times_i [\frac{\partial n_e}{\partial t} + \nabla \cdot (n_e \bar{U})] \rangle &= \langle \frac{J^2}{\sigma} \rangle \\ &- \langle \delta \frac{m_e}{m} \frac{3}{2} k (T_e - T) n_e v_e \rangle \\ &- \langle \frac{E_3(T_e) - E_3(T_3)}{\tau_{3e}} \rangle \\ &- \langle \frac{E_3(T_e) - E_2(T_2)}{\tau_{2e}} \rangle \quad (3-30) \end{aligned}$$

Let us first consider the continuity equation in more detail. If the laser operates at steady state conditions, $\frac{\partial n_e}{\partial t} = 0$. Then by applying the divergence theorem, one can show that

$$\langle \nabla \cdot (n_e \bar{U}) \rangle = \frac{1}{A_D} \frac{d}{dx} (\langle n_e \rangle U A_D).$$

Substituting Eq. (3-27) for n_e and n_e^* into the right hand side of the continuity equation, averaging, and ignoring the fluctuations in R relative to fluctuations in $n_e n_e^*$ and n_e^3 gives:

$$\begin{aligned} \frac{1}{A_D} \frac{d}{dx} (\langle n_e \rangle U A_D) &= \langle R \rangle \langle n_e \rangle [\langle n_e^* \rangle^2 (1 + \langle \eta \eta^* \rangle^2 \\ &+ 2 \langle \eta \eta^* \rangle) - \langle n_e \rangle^2 (1 + 3 \langle \eta^2 \rangle)] \end{aligned} \quad (3-31)$$

Solbes showed⁽³⁹⁾ that Ohm's law can be averaged by defining effective values for the conductivity and Hall parameter such that

$$\langle \bar{J} \rangle + \langle \bar{J} \rangle \times \beta_{\text{eff}} = \sigma_{\text{eff}} [\langle \bar{E} \rangle + \bar{U} \times \bar{B}] \quad (3-32)$$

This can be rewritten as

$$\langle J_Y \rangle = -\sigma_{\text{eff}} U B (1 - K_\infty) \frac{1 + \beta_{\text{eff}} \beta_{\text{app}}}{1 + \beta_{\text{eff}}^2} \quad (3-33)$$

where K_∞ is the average load factor for the core flow region (not to be confused with the generalized load factor introduced by Eq. (3-9) into the gasdynamic momentum and energy equations):

$$K_\infty = \frac{\langle E_x \rangle}{UB} \quad (3-34)$$

β_{app} is the apparent Hall parameter which is a measure of the success of the electrode segmentation in preventing inter-electrode current leakage. It is defined by

$$\beta_{app} = \frac{\langle E_x \rangle}{UB (1 - K_\infty)} \quad (3-35)$$

Thus a high value of β_{app} indicates that a large axial Hall field has built up between the electrodes. The evaluation of β_{app} requires a knowledge of the electrode geometry. In this analysis we shall use a modified version of the technique developed by Cole⁽¹⁶⁾ for calculating β_{app} .

The effective values of σ and β depend on the microscopic average conductivity and Hall parameter and on the distribution of the fluctuations in n_e and n_e^* . If we assume the nonuniformities have a plane wave structure (a reasonably good assumption; see Ref. 33) we obtain

$$\frac{\sigma_{eff}}{\langle \sigma \rangle} = S \quad (3-36)$$

$$\beta_{eff} = \langle \beta \rangle S + t(1 - S) \quad (3-37)$$

where t is the tangent of the angle between the average current and the wave propagation vector. The growth rate of the nonuniformities is maximum in the direction corresponding to

$$t = - \frac{1 - r - r^*}{\langle \beta \rangle} - \sqrt{\frac{(1 - r - r^*)^2}{\langle \beta \rangle} + 1} \quad (3-38)$$

Here r and r^* provide a measure of the dependence of the collision frequency on n_e and T_e :

$$r = \frac{\partial \ln v_e}{\partial \ln n_e} = \frac{v_+}{v_e} \left(1 - \frac{1}{2 \ln(\Lambda)}\right) \quad (3-39)$$

$$r^* = \frac{\partial \ln v_e}{\partial \ln n_e^*} = \frac{1}{2} \frac{v_{He} + v_{Cs}}{v_e} \frac{2-\alpha}{(1-\alpha)x_i} - \frac{v_+}{v_e} \frac{3}{2} \frac{2-\alpha}{(1-\alpha)x_i} \quad (3-40)$$

For $\langle \beta \rangle$ greater than β_{crit} , the expression for S is

$$S = \left[\frac{(1 - r - r^*)^2 + \beta_{crit}^2}{(1 - r - r^*)^2 + \langle \beta \rangle^2} \right]^{1/2} \quad (3-41)$$

β_{crit} is the critical Hall parameter for the development of ionization instabilities. In the limit of low CO_2 concentration it will be unaffected by the presence of molecules.

For helium seeded with cesium it can be shown to be

$$\beta_{crit} = \left[1 + \frac{2 - \alpha}{1 - \alpha} \frac{3T_e - T}{2(T_e - T)} \frac{1}{x_i} - (1 - r - r^*)^2 \right]^{1/2} \quad (3-42)$$

The average values of σ and β over the local cross section

are given by

$$\langle \sigma \rangle = \sigma_{\langle \rangle} [1 + \langle (r\eta + r^*n^*) (r\eta + r^*n^* - \eta) \rangle] \quad (3-43)$$

$$\langle \beta \rangle = \beta_{\langle \rangle} [1 + \langle (r\eta + r^*n^*)^2 \rangle] \quad (3-44)$$

where $\sigma_{\langle \rangle}$ and $\beta_{\langle \rangle}$ are σ and β evaluated at the average T_e and n_e .

Let us turn now to the averaged electron energy equation. The left hand side of Eq. (3-26) reduces to $kT_e x_i \frac{1}{A_D} \frac{d}{dx} (\langle n_e \rangle U A_D)$ for steady flow. Combination of Eqs. (3-32) to (3-35) allows us to evaluate the average Joule heating term, which is

$$\langle J^2 / \sigma \rangle = \langle \bar{J} \cdot \bar{E}' \rangle$$

$$= \sigma_{\text{eff}} U^2 B^2 (1 - K_{\infty})^2 \frac{1 + \beta_{\text{app}}^2}{1 + \beta_{\text{eff}}^2} \quad (3-45)$$

Fluctuations in the elastic loss term result from fluctuations in n_e , δ , T_e , and v_e . For a helium-cesium combination the elastic losses to the seed are negligible so that δv_e varies as v_{He} , or as $T_e^{1/2}$. Then

$$\begin{aligned} \langle \delta \frac{m_e}{m} \frac{3}{2} k (T_e - T) n_e v_e \rangle &= \delta_{\langle \rangle} v_{\langle \rangle} \frac{m_e}{m} \frac{3}{2} \frac{k}{\langle T_e \rangle^{1/2}} \\ &\quad \langle T_e^{1/2} (T_e - T) n_e \rangle \end{aligned} \quad (3-46)$$

where $v_{<>}$ is v_e evaluated at the average T_e and $\delta_{<>}$ is δ calculated with $v_{<>i}$. By using the differential form of the Saha equation one can show that

$$\langle T_e^{1/2} (T_e - T) \rangle = \langle T_e \rangle^{1/2} \langle T_e - T \rangle (1 + \frac{3T_e - T}{2T_e - T} \frac{2-\alpha}{(1-\alpha)x_i} \eta^*) \quad (3-47)$$

Then if we retain the largest second order terms, we may write Eq. (3-46) as

$$\begin{aligned} \langle \delta \frac{m_e}{m} \frac{3}{2} k (T_e - T) n_e v_e \rangle &= \delta_{<>} v_{<>} \frac{m_e}{m} \frac{3}{2} k (\langle T_e \rangle - T) \langle n_e \rangle \\ &\quad \cdot (1 + \eta (1 + \frac{3T_e - T}{2(T_e - T)} \frac{2-\alpha}{(1-\alpha)x_i} \eta^*) \rangle \\ &= \delta_{<>} \frac{m_e}{m} \frac{3}{2} k (\langle T_e \rangle - T) \langle n_e \rangle v_{<>} \\ &\quad [1 + \frac{3\langle T_e \rangle - T}{2(\langle T_e \rangle - T)} \frac{2-\alpha}{(1-\alpha)x_i} \langle \eta \eta^* \rangle] \\ &= \delta_{<>} \frac{m_e}{m} \frac{3}{2} k (\langle T_e \rangle - T) \langle n_e \rangle v_{<>} \\ &\quad (1 + \varepsilon \langle \eta \eta^* \rangle) \end{aligned} \quad (3-48)$$

where we have defined the parameter ε as

$$\varepsilon = \frac{3\langle T_e \rangle - T}{2(\langle T_e \rangle - T)} \frac{2-\alpha}{(1-\alpha)x_i} \quad (3-49)$$

For small fluctuations in the vibrational temperature, the function $E_i(T_j)$ is averaged as

$$\begin{aligned}\langle E_i(T_j) \rangle &= \frac{h\nu_i n_{CO_2}}{\exp(h\nu_i/kT_j) - 1} \\ &\approx \frac{h\nu_i n_{CO_2}}{\exp(h\nu_i/k\langle T_j \rangle) - 1}\end{aligned}$$

Similarly the excitation times are averaged by evaluating τ_{2e} and τ_{3e} at the average electron temperature. Finally, the averaged electron energy equation becomes

$$\begin{aligned}k\langle T_e \rangle x_i \frac{1}{A_D} \frac{d}{dx} (\langle n_e \rangle U A_D) &= \sigma_{eff} U^2 B^2 (1-K_\infty)^2 \frac{1 + \beta_{app}^2}{1 + \beta_{eff}^2} \\ &\quad - \delta_{\langle \rangle} \frac{m_e}{m} \frac{3}{2} k (\langle T_e \rangle - T) \langle n_e \rangle v_{\langle \rangle} \\ &\quad (1 + \epsilon \langle \eta \eta^* \rangle) \\ &\quad - \frac{E_3(\langle T_e \rangle) - E_3(T_3)}{\tau_{3e\langle \rangle}} \\ &\quad - \frac{E_2(\langle T_e \rangle) - E_2(T_2)}{\tau_{2e\langle \rangle}} \quad (3-50)\end{aligned}$$

Hereafter the average symbols on n_e and T_e will be omitted. n_e and T_e should be taken to mean the average values of the electron density and temperature. Unless stated otherwise, all functions of n_e and T_e will be evaluated at these average values.

The electron energy equation may be rewritten in the form

$$\frac{1}{A_D} \frac{d}{dx} (n_e U A_D) = \frac{3}{2} \frac{\delta}{x_i} \frac{m_e}{m} n_e v_e (1 + \epsilon \eta \eta^*) \left(\frac{T_{e_\infty}}{T_e} - 1 \right) \quad (3-51)$$

where T_{e_∞} is the average electron temperature that would be experienced if the average Joule heating were balanced by the elastic and inelastic losses. It is defined by

$$T_{e_\infty} = T \left[1 + \frac{2\gamma}{3\delta} M^2 \beta^2 \frac{\sigma_{eff}}{\sigma} \frac{1 + \beta_{app}^2}{1 + \beta_{eff}^2} \frac{(1 - K_\infty)^2}{1 + \epsilon \eta \eta^*} \right. \\ \left. - \frac{2\gamma}{3\delta} \frac{M^2}{U^2} \frac{1}{m_e n_e v_e (1 + \epsilon \eta \eta^*)} \left(\frac{E_3(T_e) - E_3(T_3)}{\tau_{3e}} \right. \right. \\ \left. \left. + \frac{E_2(T_e) - E_2(T_2)}{\tau_{2e}} \right) \right] \quad (3-52)$$

The difference between T_{e_∞} and T_e is due to the finite rate of ionization growth.

In a flowing plasma this growth rate may be characterized by the length scale over which it occurs. Ionization by electron impact requires both electrons and energy. When electrons are relatively scarce (at low electron temperatures), the rate at which n_e grows is limited by rate kinetics. At higher temperatures electrons are more plentiful and the growth rate is energy limited. Thus there are two length scales which determine the growth of the ionization. These are obtained by writing the continuity and energy equations as follows:

CONTINUITY

$$\frac{d}{dx} (n_e U A_D) = \frac{n_e U A_D}{L_{RATE}} \left[1 - \frac{n_e^2}{n_e^{*2}} \frac{1 + 3\langle \eta^2 \rangle}{1 + 2\langle \eta \eta^* \rangle + \langle \eta^* \rangle^2} \right] \quad (3-53)$$

ENERGY

$$\frac{d}{dx} (n_e U A_D) = \frac{n_e U A_D}{L_{ENERGY}} \frac{x_i}{2} \left(\frac{T_{e_\infty}}{T_e} - 1 \right) \quad (3-54)$$

Then L_{RATE} and L_{ENERGY} are defined by

$$L_{RATE} = \frac{1}{R n_e^{*2} [1 + 2\langle \eta \eta^* \rangle + \langle \eta^* \rangle^2]} \quad (3-55)$$

$$L_{ENERGY} = \frac{U x_i^2}{3 \frac{m}{m_e} \delta v_e [1 + \epsilon \langle \eta \eta^* \rangle]} \quad (3-56)$$

To completely specify the problem it is necessary to determine the fluctuation parameters η and η^* . Relations for these quantities can be obtained by subtracting the averaged electron continuity and energy equations from the local versions. The continuity equations give

$$\frac{\partial \eta}{\partial t} + U \frac{\partial \eta}{\partial x} = 2 \frac{U}{L_{RATE}} \frac{1}{\lambda^2} [(\Gamma + \Gamma^*) \eta - \Gamma^* \eta^*] \quad (3-57)$$

From the energy equations we have

$$\frac{\partial \eta}{\partial t} + U \frac{\partial \eta}{\partial x} = 2 \frac{U}{L_{RATE}} \frac{1}{\lambda} [(\Gamma + \Gamma^*) \eta - \Gamma^* \eta^*]$$

$$\frac{1 - \langle \eta^2 \rangle}{1 + \langle \eta^*^2 \rangle + 2 \langle \eta \eta^* \rangle} \quad (3-58)$$

where

$$\lambda' = 4 \frac{L_{ENERGY}}{L_{RATE}} \frac{1}{x_i} \frac{1 - \langle \eta^2 \rangle}{1 + \langle \eta^*^2 \rangle + 2 \langle \eta \eta^* \rangle} \quad (3-59)$$

$$\Gamma = \frac{T_{e_\infty} - T}{T_e - T} S \sqrt{(1 - r - r^*)^2 + \langle \beta \rangle^2}$$

$$- \sqrt{(1 - r - r^*)^2 + \beta_{crit}^2} \quad (3-60)$$

$$\Gamma^* = \frac{T_{e_\infty} - T}{T_e - T} S \sqrt{(1 - r^*)^2 + \langle \beta \rangle^2} - 1 - \Gamma \quad (3-61)$$

By equating the right hand sides of Eqs. (3-57) and (3-58) we obtain a relation between η and η^* :

$$\eta^* = \frac{\Gamma + \Gamma^* + \lambda' \frac{n_e^2}{n_e^*^2}}{\Gamma^* + \lambda'} \eta \quad (3-62)$$

This direct relationship indicates that the fluctuations in n_e and n_e^* are in phase. Then we may write the averages of the products $\eta \eta^*$ and η^*^2 as

$$\langle \eta \eta^* \rangle = \phi \langle \eta^2 \rangle$$

and

$$\langle \eta^* \rangle^2 = \phi^2 \langle \eta^2 \rangle$$

The only variable still undefined is $\langle \eta^2 \rangle$. We can derive an expression for it by first multiplying the continuity equation by η , then averaging:

$$\begin{aligned} \frac{d}{dx} \langle \eta^2 \rangle &= \frac{4}{L_{\text{RATE}}} \frac{1 - \langle \eta^2 \rangle}{1 + \phi(\phi+2) \langle \eta^2 \rangle} \left(\phi - \frac{n_e^2}{n_e^{*2}} \right) \langle \eta^2 \rangle \\ &= \langle \eta^2 \rangle \frac{4}{L_{\text{RATE}}} \frac{1 - \langle \eta^2 \rangle}{1 + \phi(\phi+2) \langle \eta^2 \rangle} \frac{1}{\lambda'} \frac{\Gamma + \Gamma^* (1 - \frac{n_e^2}{n_e^{*2}})}{1 + \Gamma^*/\lambda'} \end{aligned} \quad (3-63)$$

The parameter λ' introduced by Eq. (3-59) involves the ratio $L_{\text{ENERGY}}/L_{\text{RATE}}$; it thus serves as a measure of the speed of the kinetics. When λ' is small the electron number density is low and the rate at which ionization instabilities develop is limited by the ionization kinetics. For large λ' , the growth rate is energy limited and the nonuniformities rapidly reach a fully developed asymptotic state such that $\frac{d}{dx} \langle \eta^2 \rangle$ is approximately 0. The conductivity and effective Hall parameter also approach asymptotic values.

Eqs. (2-17), (2-18), (2-19), (3-10), (3-53), and (3-63) constitute a self-consistent set of seven coupled first order linear differential equations which determine the problem completely. In the present analysis they are integrated numerically by a fourth-order Runge-Kutta method with step

size control to assure stability. The length of each integration step is restricted so that the function with the largest derivative changes by no more than 1% across the interval. An iterative search method is used to calculate β_{app} , T_e , and ϕ from Eqs. (3-35), (3-54), and (3-62). (See Ref. 16 for details.) When the gasdynamic and plasma variables are known at a given value of x , they are used to compute the optical intensity I . This is then used along with the other variables to calculate the derivatives for the next integration step.

During the initial set of computations it was noted that the set of equations exhibited "stiffness" if the magnetic induction and electron excitation were "turned on" after the vibrational temperatures had equilibrated with the static temperature in the cavity. In this case the large difference between T_e and the vibrational temperatures produces large derivatives in Eqs. (2-13), (2-14), (2-18), and (2-19). A simple solution is to initiate the channel and magnetic field closer to the nozzle throat, where these temperature differences are considerably smaller. This represents a wiser design choice from a thermodynamic standpoint, because the entropy produced by the relaxation of the vibrational energy modes is less than in the former case.

IV. EXCITATION AND RELAXATION PROCESSES

4.1 Hierarchy of Reaction Rates

In principle a large number of energy transfer processes are possible in an electrically excited CO_2 laser. The optically active species gains energy as a result of electron-neutral interactions and loses energy through the stimulated emission process. In addition the molecules in the laser cavity can gain or lose energy through three other mechanisms:

(1) spontaneous emission, (2) diffusion of species members out of the region of optical interaction, and (3) collisional transfer. Fortunately many of these processes have a very low or a very high probability of occurrence, allowing us to set their rates either to zero or infinity (depending upon whether the process in question is orders of magnitude slower or faster than the rate of flow through the laser cavity). An infinite rate corresponds to a very fast reaction which produces equilibrium between the reacting components.

It has been demonstrated experimentally and theoretically that the spontaneous emission rates for CO_2 vibrational-rotational transitions are slow in comparison with typical collisional relaxation rates. (24, 40, 41) Representative times for collisional deactivation are on the order of microseconds. In contrast, the fastest measured spontaneous emission time for an isolated CO_2 molecule is about 5 milliseconds. If resonant radiation trapping is important, this time can increase

by orders of magnitude. So spontaneous emission is negligible compared to collisional energy transfer. It is also small in comparison with electron excitation, which occurs on a time scale between 1 and 10 microseconds.

The diffusion of excited molecules from the active region before they can lase has similarly been shown to be unimportant in CO₂ lasers. In a typical gas mixture at 1 atmosphere, a CO₂ molecule diffusing by a random walk process will travel less than 10 microns in 1 microsecond.⁽⁴²⁾ This is much smaller than the size of the active region, which is on the order of 0.1-1 meter.

Thus the only mechanisms we need examine in detail are electron excitation and collisional relaxation. We saw in Section 2A that in the electron temperature range 3000-5000°K two excitation processes are important. Excitation of the upper laser level, CO₂ (00°1), is favored and occurs on a time scale of 1 microsecond. Excitation of the lower level can be important if electron number densities are very high; for $n_e/n_{He} < 10^{-5}$, however, this process has a characteristic time of about 10 microseconds.

A number of energy transfer processes are effected through intermolecular collisions; their rates vary over several orders of magnitude. The fastest rate is the kinetic collision frequency, which is the average number of times a CO₂ molecule encounters another particle per second. This rate is proportional to the number density of particles in the gas, to the col-

lision cross section for the encounter, and to the relative velocity of the collision partners.

$$k_{TOT} = \sum_j (n_j \sigma_{CO_2-j} \bar{c}_{CO_2-j}) \quad (4-1)$$

where the summation is over all neutral species. We can also define k_{TOT} as the kinetic collision rate per torr pressure. For the 99% He - 1% CO_2 mixture typical of an MHD laser, this has the value 1.5×10^7 torr $^{-1}$ sec $^{-1}$; in Table I it is compared with other rates of interest. (43)

Since all energy transfer processes under consideration at this point depend on collisions, they must occur at rates less than the kinetic collision rate. Rotational relaxation by rotation-rotation (RR) or translation-rotation (TR) exchange has been found to occur very rapidly in CO_2 . In a pure CO_2 gas a Boltzmann equilibrium in the rotational degrees of freedom is established with the rate (44, 45).

$$k_{ROT} \approx 0.5 - 1.0 \times 10^7 \text{ torr}^{-1} \text{ sec}^{-1} \quad (4-2)$$

This is about one quarter to one half the kinetic collision rate, which means that from two to four collisions are required (on the average) to bring about equilibration of the rotational modes with the translational modes.

Intramode vibration-vibration (INTRA VV) is generally assumed to be very rapid, leading to a Boltzmann distribution of energy level populations within each vibrational mode of the

CO_2 molecule. We shall see that in the case of the bending mode (BM) this assumption is open to serious question for the low CO_2 concentration characteristic of an MHD laser. For VV transfer within the asymmetric stretch mode (ASM) Stark has reported the rate⁽⁴⁶⁾

$$k_{\text{INTRA VV}}^{\text{ASM}} \geq 4 \times 10^6 \text{ torr}^{-1} \text{ sec}^{-1} \quad (4-3)$$

which is about one-fourth the kinetic collision rate.

Intermode vibration-vibration (INTER VV) involves the transfer of vibrational energy quanta from one mode to another. Processes of this type are of the utmost importance in determining the workability of the CO_2 molecular gas laser, and for reliable calculations it is essential to have accurate values of the rates involved. To this end these processes have undergone intensive investigation with varying degrees of success.

In order for a CO_2 laser to operate, the collisional relaxation rate of the upper laser level (the 00^11 level of the ASM) must be considerably slower than that of the lower laser level (either the 10^00 level of the SSM or the 02^00 level of the BM). Otherwise during continuous lasing the lower laser level population will grow until the population inversion disappears. The 00^11 rates have been found to be extremely slow. (References 47, 48) At a temperature of 350°K they are:

$$k_{\text{AB}}^{\text{CO}_2} \approx 360 \text{ torr}^{-1} \text{ sec}^{-1} \quad (4-4)$$

for the VV process

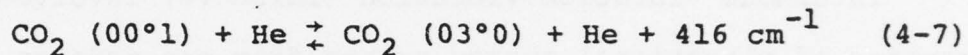


(4-5)

and

$$k_{AB}^{\text{He}} \approx 90 \text{ torr}^{-1} \text{ sec}^{-1} \quad (4-6)$$

for the process



This last reaction mechanism is an example of the final type of transfer process that we need to consider, namely the vibration-translation (VT) process. Encounters of this type result in the transfer of energy between the quantized levels of the CO_2 vibrational modes and the translational-rotational modes of the neutral gas particles (mainly helium).

Because of confusion over the basic mechanism of lower laser level relaxation the rate for this process is far from certain. Since 1966 at least ten experiments have been performed to investigate this mechanism, but there is not yet available a universally accepted result. Much of the difficulty arises from the fact that the second quantum level of the BM is doubly degenerate and coupled to the $10^{\circ}0$ level of the SSM by Fermi resonance. Experiments to determine the deactivation rate

of the lower laser level have confused the $10^{\circ}0 - 02^{\circ}0$ transfer rate with the overall rate of relaxation of $10^{\circ}0$ vibrational energy to the translational modes. As will be shown in Section 4.C, it now seems clear that the deactivation of the $10^{\circ}0$ state is a multistep process with several sequential rates involved. Apparently because of the lack of an internal dipole moment in the SSM vibration, the rate of direct VT relaxation of the $10^{\circ}0$ level is negligible. Instead of returning to the ground state in this manner, the CO_2 ($10^{\circ}0$) molecule must first reach the $01'0$ state. Estimates of the magnitude of the rate at which this occurs vary over several orders of magnitude. They range from a low value of ⁽⁴⁹⁾

$$k_{\text{SB}}^{\text{CO}_2} \approx 1 \times 10^3 \text{ torr}^{-1} \text{ sec}^{-1} \quad (4-6a)$$

to a high of ⁽⁵⁰⁾

$$k_{\text{SB}}^{\text{CO}_2} \approx 4.5 \times 10^5 \text{ torr}^{-1} \text{ sec}^{-1} \quad (4-6b)$$

Collisions between CO_2 ($10^{\circ}0$) and He are believed to play almost no role in this process. ⁽⁴⁹⁾ Thus the rate constants have been written with the superscript CO_2 .

Nevertheless, a VT process involving He is most important in the final step of the deactivation of the lower laser

AD-A068 190

MASSACHUSETTS INST OF TECH CAMBRIDGE GAS TURBINE AND--ETC F/G 20/5
FUNDAMENTAL MECHANISMS OF NONEQUILIBRIUM MHD LASING PHENOMENA. (U)
DEC 78 J L KERREBROCK

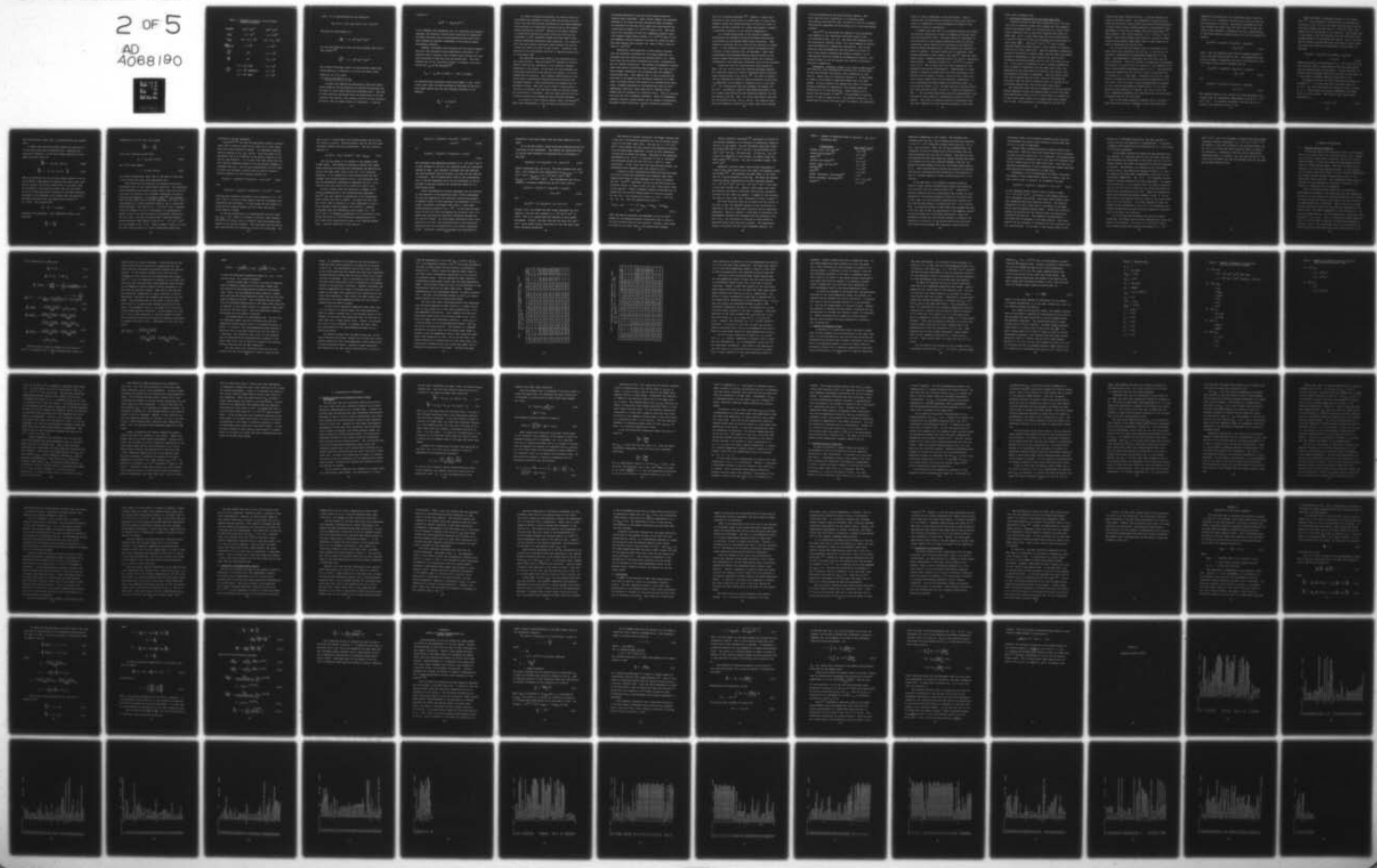
F44620-76-C-0067

UNCLASSIFIED

2 OF 5
AD
4068190

AFOSR-TR-79-0506

NL



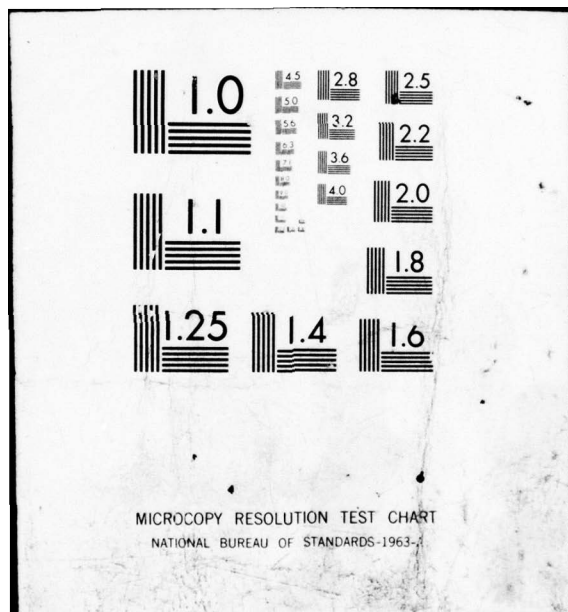
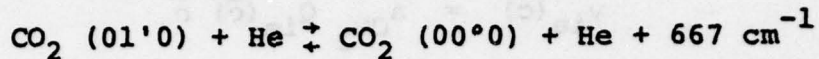


Table 1. Relaxation rates for various energy transfer processes.

PROCESS	$\text{torr}^{-1} \text{ sec}^{-1}$	$\text{atm}^{-1} \text{ sec}^{-1}$
k_{TOT}	1.5×10^7	1.1×10^{10}
k_{ROT}	$0.5 - 1.0 \times 10^7$	$3.8 - 7.6 \times 10^9$
$k_{\text{INTRA VV}}^{\text{ASM}}$	4×10^6	3×10^9
$k_{\text{AB}}^{\text{CO}_2}$	360	2.7×10^5
$k_{\text{AB}}^{\text{He}}$	90	6.8×10^4
$k_{\text{VT}}^{\text{CO}_2}$	4.5×10^5 (RKJ)	3.4×10^8
	1.5×10^4 (BULTHUIS)	1.1×10^7
	2.2×10^3 (MMK)	1.7×10^6

level. It is characterized by the mechanism:



The rate for this process is

$$k_{VT}^{\text{He}} \approx 6 \times 10^3 \text{ torr}^{-1} \text{ sec}^{-1}$$

For the case where CO_2 is the collision partner this rate is much slower: (51)

$$k_{VT}^{\text{CO}_2} \approx 6 \times 10^2 \text{ torr}^{-1} \text{ sec}^{-1}$$

This tenfold difference factor is the principal reason why helium addition is effective in raising the power output capability of a CO_2 laser.

4.2 Electron Excitation of CO_2

We shall now examine the mechanism by which the vibrational modes of the CO_2 molecule are excited by electrons and the rates at which these excitation processes occur. The rate at which exciting collisions occur is proportional to the excitation cross section, the relative velocity of the colliding particles, and the number density of molecules. It may be

written as

$$v_{ie}(\bar{c}) = n_{CO_2} Q_{ie}(\bar{c}) \bar{c}$$

If we integrate this expression over all velocities (or electron energies, the molecule's motion being negligible by comparison) we obtain the total rate at which excitation collisions occur. This integration requires a knowledge of the electron energy distribution function.

However, collisions with electrons can also lead to deexcitation of the molecules through superelastic collisions. We therefore need to define a rate constant which accounts for electron collisions of both the first and second kind. This rate constant for the VT_e excitation process is related to the excitation rate v_{ie} by the expression⁽⁸⁾

$$K_{ie} = v_{ie} \exp(nv_i/kT_e) (1 - \exp(-hv_i/kT_e))$$

The characteristic excitation times which appear in Eqs. (2-18), (2-19), and (3-22) are then evaluated as functions of the electron number density and the rate constant according to the relation

$$\frac{1}{\tau_{ie}} = n_e K_{ie}(T_e)$$

In order to calculate accurately the rates at which the CO_2 bending and asymmetric stretch modes are excited by electrons, one must have precise information on the energy-dependent cross sections for vibrational excitation and on the electron energy distribution function. Because of the great interest in electrically excited CO_2 lasers since the first one was introduced in 1964, extensive studies have been made of the physical mechanisms underlying their operation. As a result of this work the electron excitation cross sections for the CO_2 vibrational modes are known in great detail. Similarly, the behavior of the distribution function is understood quite well at the present time.

Two approaches have been taken in the determination of the cross sections. Hake and Phelps⁽¹⁸⁾ employed an indirect method involving the calculation of the electron transport properties in the plasma. At the start of this procedure the vibrational excitation cross sections are unknown, so initial guesses must be provided. The transport coefficients are computed using a distribution function obtained by solving the Boltzmann equation. These coefficients are compared with experimental values. When the two are found to agree within a fraction of a percent over the entire range of electron energy the calculation is concluded. Both the cross sections and distribution function are provided by this bootstrap procedure.

In contrast to this indirect method, Schulz and Boness⁽¹⁹⁾ made direct measurements of the scattering cross-sections of

low energy electrons in CO_2 using high energy-resolution electron beam techniques. Their results support the essential features of the cross sections reported by Hake and Phelps. For excitation of the CO_2 (01'0) level the cross section has a peak value of about $2.7 \times 10^{-20} \text{ m}^2$ near 0.1 eV. The cross section for excitation of the 00°1 asymmetric stretch vibration reaches a peak value of about $1.5 \times 10^{-20} \text{ m}^2$ near 0.5 eV. The symmetric stretch vibration 10°0 does not reach its maximum cross section until around 4 eV, where it has a value of about $2 \times 10^{-20} \text{ m}^2$.

Theoretical investigations of these results indicate that the excitation processes for low energy electrons are different than for electrons with energies above 3 eV. Below this limit the excitation processes are direct, proceeding by way of a dipole interaction. The bending and asymmetric stretch modes have optical transition dipole moments; thus they have a much stronger interaction with electrons than the symmetric stretch mode does. This implies that if one is searching for molecules to be pumped by the low-energy electrons in an MHD laser, he should confine his attention to infrared-active molecules. Diatomic molecules of the homonuclear type are thus immediately ruled out, since they have no internal dipole moments and are therefore not infrared active. (This is strictly true only for low to moderate pressures. Above 10 atmospheres pressure, electric dipole moments can be induced in homonuclear molecules during collisions, allowing radiative transitions

which are otherwise forbidden.⁽⁵²⁾ However, to apply this principal to the construction of an MHD laser, we would need magnetic fields well beyond the state of the art in order to maintain the Hall parameter at a value high enough to produce a significant elevation of the electron temperature.)

In a dynamic description of the electron ensemble, superelastic and inelastic collisions between electrons and CO₂ molecules do not balance under lasing conditions. Then inelastic collisions act as a sink for the electrons in energy space. If the imbalance is great enough the Maxwellian distribution of free electrons will be disturbed. Under these circumstances the Boltzmann equation must be solved for the electron energy distribution function before the ionization, recombination, and vibrational excitation rates can be evaluated.

Nighan has used the cross-sectional data reported by Refs. (18) and (19) to solve the electron Boltzmann equation for conditions typical of electric discharge lasers containing large concentrations of CO₂ and N₂.⁽²⁰⁾ We noted in Chapter 1 that the thermalizing effect of electron-electron interactions is unimportant if the degree of ionization n_e/n is less than 10^{-5} . In a conventional EDL this parameter is between 10^{-8} and 10^{-6} . Accordingly, Nighan's calculated distribution function showed large deviations from Maxwellian behavior for the pure gases N₂ and CO₂. Ref. (33) gives distribution functions for the mixture 10% CO₂, 10% N₂, 80% He. The computed departures from Maxwellian behavior are rather small when compared

to the calculations for the pure molecular species. However, they are still significant in an absolute sense. The large N_2 cross section near 2 eV acts as a sink for energetic electrons and suppresses the high energy tail of the distribution function.

Murray⁽⁵⁴⁾ has calculated the effects of this non-Maxwellian behavior on the vibrational excitation rates in the 1-1-8 mixture of CO_2 - N_2 - He. The rates were computed using the distribution function of Ref. (54), then compared to similar rates calculated for a Maxwellian distribution. The largest deviation from the Maxwellian rate was found to be about 9%. Since cross section uncertainties produce an effect 3 to 10 times greater than that caused by non-Maxwellian behavior, very little accuracy is lost by assuming the electron distribution function is Maxwellian.

Furthermore, Lowenstein showed in his study of MHD lasers⁽⁴⁾ that even for a CO_2 concentration as high as 5%, the deviation of the free electron distribution from a Maxwellian is less than 3%. Recall that the ionization fraction in an MHD plasma is three to five orders of magnitude higher than in an EDL plasma. In this situation the thermalizing effect of electron-electron collisions is substantial; this process keeps the distribution at or near Maxwellian. These findings are in accord with the results of Judd⁽⁵⁵⁾, who performed an analysis similar to that of Nighan for He - CO_2 mixtures without N_2 . He showed that for helium fractions above 50 percent, the excitation

rates are nearly independent of the gas mixture. This indicates that the distribution function in such a gas lies very close to a Maxwellian or that non-Maxwellian effects on the excitation rates are unimportant.

It seems clear then that in the present study we can assume the electron distribution function is Maxwellian without incurring any significant error. The major source of inaccuracy in the calculation of the electron excitation rates for the CO_2 vibrational levels comes from the excitation cross sections. Hake and Phelps estimates their cross sections are accurate to within 10 percent. The more recent set of vibrational cross sections derived by Lowke, Phelps, and Irwin⁽¹⁴⁾ using the same method gives a somewhat different profile for the 00^11 excitation cross section. A maximum of about $0.8 \times 10^{-20} \text{ m}^2$ is reached near 0.8 eV. This is about half the value reported for the maximum by the earlier investigation. Nevertheless, it lends support to Nighan's estimate that the rates calculated in his analysis were accurate to within a factor of two, futher precision being limited only by cross sectional uncertainty. In this investigation we shall employ the excitation rates v_{ie} calculated by Nighan, et al. for MHD laser gas conditions using the cross sections of Refs. 18 and 19. These are presented in Ref. 7. The calculated excitation rates are approximated in our analysis by cubic spline fit polynomials accurate to within 5 percent. This level of precision should be considered quite good when compared with the available knowledge of the lower

laser level relaxation rate.

4.3 Collisional Deactivation of the Lower Laser Level

Previous analyses of MHD lasers employing CO_2 as the optically active molecular species have assumed that the symmetric stretch and bending modes are in equilibrium at a single vibrational temperature due to the Fermi resonance that exists between them. As it is well known that the rate of deactivation of the $01'0$ level of the BM via collisions with helium atoms is quite rapid ($k_{\text{VT}}^{\text{He}} \approx 6000 \text{ torr}^{-1} \text{ sec}^{-1}$),⁽⁵¹⁾ such a strong coupling between the modes implies a rapid removal of molecules from the 10^00 lower laser level. This has important consequences during the extraction of optical power from the laser gain medium, because it establishes an upper limit on the rate at which stimulated transitions between the 00^01 and 10^00 levels can occur. If this rate of production of 10.6μ photons exceeds the rate of removal of molecules from the lower laser level, the population of the lower level will build up very rapidly until the population inversion is destroyed. Thus the optical power that can be removed from the laser, given by the energy per transition times the photon production rate, is limited by the collisional deactivation rate of the lower laser level.

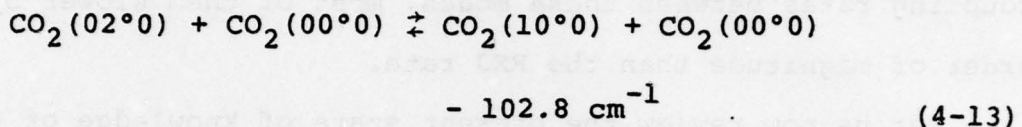
For conditions under which the assumption of strong coupling between symmetric stretch and bending modes is valid, the known rapid deactivation rate of the $01'0$ level leads to a prediction of high optical power output if the upper laser level pumping rate is high. This prediction is confirmed by the high con-

tinuous wave power obtained from $\text{CO}_2 - \text{N}_2 - \text{He}$ gas dynamic and electric discharge lasers. The assumption of equilibrium between SSM and BM has always seemed valid because the performance of these lasers closely matched prediction, and because of the measurement of this rate by Rhodes, Kelly and Javan (RKJ),⁽⁵⁰⁾ which implied a very strong coupling ($\approx 4.5 \times 10^5 \text{ torr}^{-1} \text{ sec}^{-1}$). However, more recent studies have reported a variety of slower coupling rates between these modes, most of them slower by an order of magnitude than the RKJ rate.

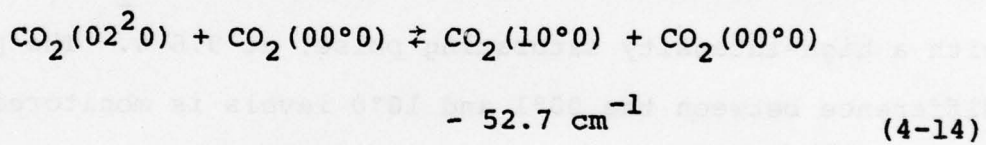
Let us now review the present state of knowledge of the lower laser level relaxation rate for CO_2 , in view of its importance in determining the performance capability of a CO_2 laser. The experiments to determine this rate fall into two basic categories. The first consists of perturbing the Boltzmann distribution of the 00^11 and 02^00 levels in a CO_2 absorption cell with a high-intensity saturating pulse, at 9.6μ . The population difference between the 00^11 and 10^00 levels is monitored with a low-power 10.6μ probe laser. Presumably half the 02^00 population is removed by the saturating pulse and deposited in the 00^11 level. The 10^00 level is then overpopulated with respect to 02^00 , and the SSM population decays until it is in equilibrium with the population of the BM. The rate at which the 10.6μ absorption decreases with time then gives the collisional relaxation rate for the 10^00 level.

This is the method employed by Rhodes, Kelly, and Javan. Three rates were actually observed in their 1968 experiment.

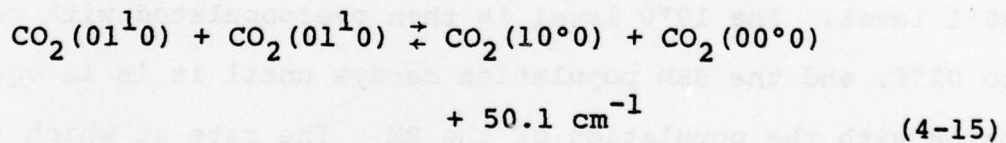
Immediately following the 9.6μ saturating pulse a rapid decrease in 10.6μ absorption occurred with a rate too fast for the electronics to resolve. The authors concluded that this rate constant was faster than $10^6 \text{ torr}^{-1} \text{ sec}^{-1}$ and that the initial rapid decrease in absorption was due to equilibration of the Fermi resonance-coupled levels 10^00 and 02^00 through the process



After $1 \mu\text{sec}$ the absorption was found to increase rapidly at first, then more slowly after $25 \mu\text{sec}$. RKJ proposed that the initial increase in absorption was due to the refilling of the 10^00 level through several processes such as

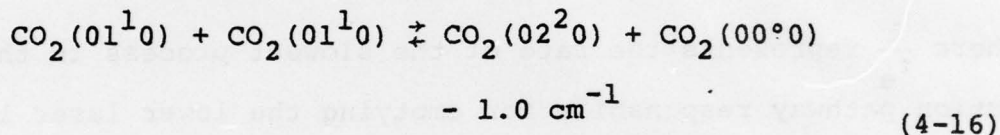


and



The combined effective rate constant for these processes as determined from the experimental measurements is about $4.5 \times 10^5 \text{ torr}^{-1} \text{ sec}^{-1}$. No attention was paid to the slow rate of increase in the absorption after $25 \mu\text{sec}$.

Sharma performed a subsequent analysis of this experiment.⁽⁵⁶⁾ From theoretical considerations he concluded that the process in Eq. (4-14) is the rate limiting step in the deactivation pathway and that the $4.5 \times 10^5 \text{ torr}^{-1} \text{ sec}^{-1}$ rate measured by RKJ corresponds to this reaction. One further step is then needed to get the molecules into the 01^10 state which is depopulated by VT collisions with helium. This is an intra-mode VV process involving BM levels with finite rotation about the figure axis (meaning the superscript quantum number is non-zero):



Sharma calculates a rate constant of $1.8 \times 10^6 \text{ torr}^{-1} \text{ sec}^{-1}$ for this reaction, using a theory based on the long range forces from the Lennard-Jones 6-12 potential. In this the Fermi resonance coupling between levels 10^00 and 02^00 is very rapid, as is the overall intermode relaxation from 10^00 to 01^10 .

The second technique was first introduced by Carbone and Witteman.⁽⁵⁷⁾ It involves monitoring the power decay of a cw $10.6 \mu \text{ CO}_2$ laser whose exciting voltage is short circuited at $t = 0$. This causes the electron temperature and number density to drop rapidly. The radiated laser power decays exponentially:

$$I = I_0 \exp(-t/\tau) \quad (4-17)$$

The characteristic decay time τ is obtained from the recorded data.

A simple rate equation analysis yields the relation of τ to the lower laser level relaxation rate. Modifying the notation of Chapter 2, we may write these equations for the upper and lower levels as

$$\frac{dN_2}{dt} = - R_1 (N_2 - N_1) gI \quad (4-18)$$

$$\frac{dN_1}{dt} = + R_1 (N_2 - N_1) gI - \frac{N_1}{\tau_e} \quad (4-19)$$

where $\frac{1}{\tau_e}$ represents the rate of the slowest process in the reaction pathway responsible for emptying the lower laser level. Here we neglect collisional deactivation of the upper laser level because of the relatively small rate for this level. As long as laser oscillation continues in the short-circuited afterglow of the discharge we can assume that the population difference satisfies the gain-equals-loss criterion of Eq. (2-16). This implies that

$$(N_2 - N_1) = \text{constant} \quad (4-20)$$

throughout the experiment. This immediately leads to the condition

$$\frac{dN_2}{dt} = \frac{dN_1}{dt} \quad (4-21)$$

Combination of (4-18) and (4-21) gives

$$\frac{dN_1}{dt} = -\frac{N_1}{2\tau_e} \quad (4-22)$$

which has a solution of the form

$$N_1 = N_{10} \exp(-t/2\tau_e) \quad (4-23)$$

Eq. (4-18) then leads to

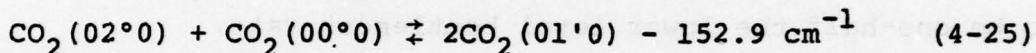
$$I = I_0 \exp(-t/2\tau_e) \quad (4-24)$$

The observed exponential decay rate of the power is then seen to be one-half the lower level bottleneck rate.

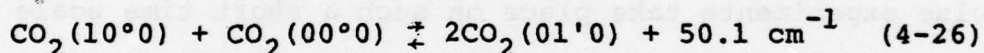
This method has the advantage of directly providing the bottleneck rate for near steady-state conditions. The saturating-pulse experiments take place on such a short time scale that effects due to rotational and intramodal vibrational non-equilibrium may be important. For example, Seeber⁽⁵⁸⁾ has proposed that the very rapid rate in the RKJ experiment ($10^6 \text{ torr}^{-1} \text{ sec}^{-1}$) corresponds not to Fermi-resonance coupling, but to stimulated Raman processes. The rate of $4.5. \times 10^5 \text{ torr}^{-1} \text{ sec}^{-1}$, believed by RKJ and Sharma to be the VV bottleneck, is interpreted by Seeber as due to the redistribution of rotational sublevels of the $00^{\circ}1$ level. He then calculates from a modified Schwartz-Slawsky-Herzfeld (SSH) theory a rate of $4.5. \times 10^4 \text{ torr}^{-1} \text{ sec}^{-1}$ for the process of Eq. (4-15). Thus if Seeber's theory is valid, the rate limiting step is an order of magnitude slower than

indicated by the RKJ experiment.

Bulthuis^(59,60) has used the power-decay method to measure lower level relaxation rates for CO₂ that are in close agreement with those predicted by Seeber. His experiment employed various mixtures of CO₂, H₂O, and He. Plots are given of the bottleneck rate $\frac{2}{\tau}$ as a function of the partial pressure of H₂O and CO₂ (see Figure 5). It is clear from these plots that the rate limiting mechanism changes as the CO₂ partial pressure is increased from zero. For low CO₂ concentrations the 10°0 deactivation rate increases linearly with CO₂ partial pressure. Possible pathways for this limiting reaction are



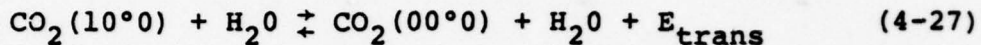
and



From the plots Bulthuis calculates a rate constant of 1.5×10^4 torr⁻¹ sec⁻¹, a value 30 times smaller than the bottleneck rate proposed by RKJ and Sharma. In this regime the H₂O fraction is large and the coupling between the 01°0 level and the CO₂ ground state is strong.

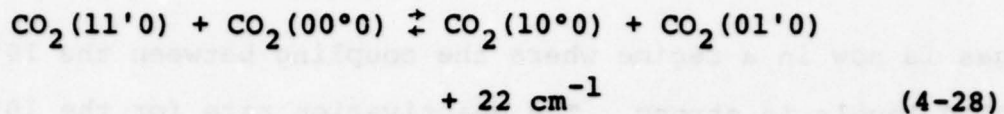
As the CO₂ concentration is raised beyond the point where $n_{\text{CO}_2}/n_{\text{H}_2\text{O}} > 0.12$, there is a change in the bottleneck reaction. The curve of $\frac{2}{\tau}$ levels off at a constant value and becomes independent of CO₂ partial pressure. This indicates that the bottleneck reaction does not include CO₂ as one of its reactants. The

gas is now in a regime where the coupling between the $10^{\circ}0$ and $01'0$ levels is strong. The deactivation rate for the $10^{\circ}0$ level increases linearly with H_2O concentration. The rate limiting reaction is

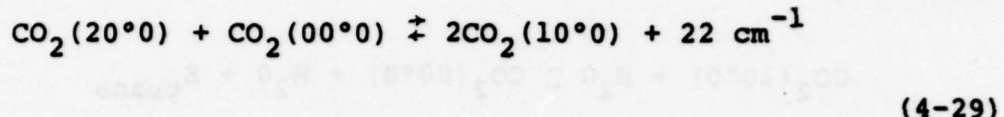


The low CO_2 regime is of interest in the present study of MHD lasers. The findings of Bulthuis indicate that under these conditions the process which determines the deactivation rate of the lower laser level is the $10^{\circ}0 - 01'0$ coupling mechanism. It is imperative to have accurate data for this process, which occurs primarily by $CO_2 - CO_2$ collisions, yet the two experimental techniques to determine the $10^{\circ}0 - 01'0$ coupling rate give results which differ by a factor of 30.

We have already noted the objections of Seeber to the stated interpretations of the saturated pulse experiment. Lyon⁽⁴³⁾ has also offered an explanation of the discrepancy which differs from that of Seeber. He agrees with RKJ that the initial drop in absorption in their experiment is due to Fermi resonance coupling between $10^{\circ}0$ and $02^{\circ}0$. However, he proposes that the intermediate rate process (4.5×10^6 torr⁻¹ sec⁻¹) is actually a combination of VV reactions in the BM and SSM which fill the transiently underpopulated $10^{\circ}0 - 02^{\circ}0$ levels from higher-energy states in the combined BM-SSM modes. Possible reactions of this type are



or

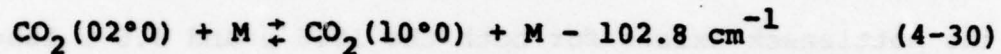


The bottleneck rate measured by Buthuis ($1.5 \times 10^4 \text{ torr}^{-1} \text{ sec}^{-1}$) is then assigned to the slow rate reported by RKJ but thereafter ignored by them. Lyon therefore concludes that RKJ measured the same bottleneck rate as Bulthuis, but they did not identify it correctly. The VV process which leads to the intermediate rate in the RKJ experiment would not be significant in the experiment of Bulthuis because the vibrational modes are in a quasi-steady state.

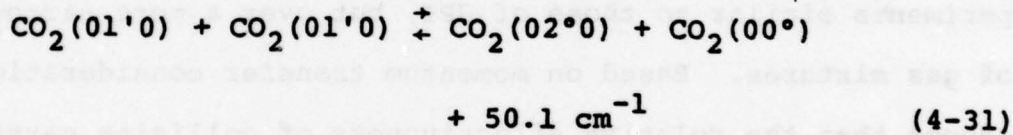
A major shortcoming of the RKJ experiment was the relatively long duration of the saturating pulse (50-100 nanoseconds) and the slow response of the electronic monitoring equipment. An updated version of this experiment was performed in 1974 by Jacobs, Pettipiece, and Thomas (JPT) using a 2 msec mode-locked saturating pulse at 10.6μ .⁽⁶¹⁾ In this case the population of the $10^{\circ}0$ level was depleted by the pulse, and a 9.6μ probe laser monitored the population difference between the $02^{\circ}0$ and $00^{\circ}1$ states. By using faster electronics with a time resolution of 3 nsec, JPT eliminated much of the uncertainty associated with the interpretation of the earlier experiment by RKJ. Rotational relaxation phenomena were determined to

proceed at a rate much faster than the rates observed in the data.

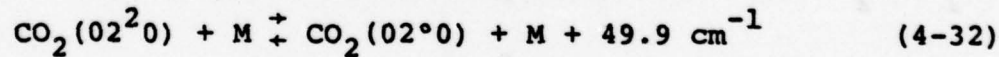
As in the RKJ results, three rates were observed during the time scale of the experiment. The fastest was identified with an initial rapid decrease in absorption due to processes of the type



where M represents CO_2 , He or N_2 . The rate constants for this $02^{\circ}0 - 10^{\circ}0$ relaxation were determined to be $k_{\text{CO}_2-\text{CO}_2} = 3 \times 10^5$ torr $^{-1}$ sec $^{-1}$, $k_{\text{CO}_2-\text{He}} = 0.8 \times 10^5$ torr $^{-1}$ sec $^{-1}$, and $k_{\text{CO}_2-\text{N}_2} = 3 \times 10^5$ torr $^{-1}$ sec $^{-1}$. The intermediate rate corresponded to processes repopulating the $02^{\circ}0$ level such as



and



Process (4-31) was deemed the most likely candidate for this reaction, with the rate constant 3.3×10^4 torr $^{-1}$ sec $^{-1}$ at 300°K. This is in accord with the theories of both Seeber and Sharma. Finally, the slow rate had the value 400 torr $^{-1}$ sec $^{-1}$, which almost surely identifies it with the upper laser level relaxation mechanism.

The results of Jacobs, Pettipiece, and Thomas indicate both a rate and a bottlenecking mechanism for the collisional deactivation of the lower laser level. The rate is $3.3 \times 10^4 \text{ torr}^{-1} \text{ sec}^{-1}$, which agrees with the limiting rate measured by Bulthuis with his power-decay experiment, as well as with theoretical calculations by Seeber and Sharma. Knowledge of the mechanism, represented by Eq. (4-31), is important in that it indicates the bottleneck exists for both the 10.6μ and 9.6μ laser transitions. If Eq. (4-30) were the rate-limiting process, the bottleneck would interfere only with lasing at 10.6μ .

A number of other investigations which have been performed since the original RJK experiment have reported lower level deactivation rates in rough agreement with those of Bulthuis and JPT. Stark⁽⁶²⁾ performed a series of saturating pulse experiments similar to those of JPT, but over a more narrow range of gas mixtures. Based on momentum transfer considerations, he argues that the relative effectiveness of collision partners for the $10^{\circ}0 - 02^{\circ}0$ relaxation process is $1:0.46 : 0.054$ for $\text{CO}_2 : \text{N}_2 : \text{He}$. Then the reported rate value is

$$k_{10^{\circ}0 - 02^{\circ}0} = 1.4 \times 10^5 [p_{\text{CO}_2} + 0.46p_{\text{N}_2} + 0.054p_{\text{He}}] \text{ torr}^{-1} \text{ sec}^{-1} \quad (4-33)$$

where the partial pressures are expressed in torr at 400°K . Except for the momentum-transfer corrections this is close to the value found by JPT for this reaction. However, Stark gives no rates for the other steps in the deactivation pathway.

Murray, Mitchner, and Kruger⁽⁶³⁾ use Stark's collision effectiveness parameters in an analysis of vibrational nonequilibrium in cw CO₂ lasers. For the bottleneck rates they report the values 1200 torr⁻¹ sec⁻¹ for CO₂ - CO₂ collisions and 60 torr⁻¹ sec⁻¹ for CO₂ - He encounters. If only CO₂ - CO₂ collisions are effective in this process, as Rosser, Hoag, and Gerry report,⁽⁴⁹⁾ the CO₂ - CO₂ rate is slightly higher, 2000 torr⁻¹ sec⁻¹.

Apparently the only report since the RKJ experiment of a rapid lower level deactivation rate comes from DeTemple, Suhre, and Coleman.⁽⁶⁴⁾ They measured the power decay in the after-glow of a pulsed discharge in pure CO₂. The decay was characterized by several exponentials with rate constants between 0.8×10^6 torr⁻¹ sec⁻¹ and 1.05×10^6 torr⁻¹ sec⁻¹, more rapid in fact than the RKJ rate. However, Stark argues that these are actually the rates of rotational and velocity relaxation, and that the true rates are masked. A summary of the available rate data on lower laser level relaxation is given in Table II.

The first conclusion that may be drawn from the scatter in the data is that the detailed kinetics of the collisional relaxation of the lower laser level CO₂(10°0) are not completely understood. There is, however, a wide body of theoretical and experimental evidence which suggests that the relaxation rate due to CO₂ - CO₂ collisions is from one to three orders of magnitude slower than previously believed. The experimental results of Bulthuis and JPT, when considered together, are

Table 2. Summary of Reported Values of $\text{CO}_2(10^{\circ}\text{O}) - \text{CO}_2(01^{\circ}\text{O})$
Relaxation Rate.

<u>Investigators</u>	<u>Rate (atm⁻¹ sec⁻¹)</u>
Rhodes, Kelly, and Javan (50)	3.0×10^8
Carbone and Witteman (57)	6.8×10^6
Seeber (58)	3.4×10^7
Bulthuis and Ponsen (59)	9.9×10^6
Rosser, Hoag, and Gerry (49)	7.6×10^5
Bulthuis (60)	7.7×10^6
Stark (62)	1.1×10^8
Jacobs, Pettipiece, and Thomas (61)	$\approx 10^7$
Murray, Mitchner, and Kruger (63)	$0.9 - 1.5 \times 10^6$
Sharma (11)	4.0×10^7

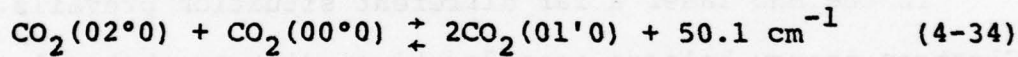
especially compelling in this regard. The evidence also indicates that the $\text{CO}_2 - \text{CO}_2$ collisions are much more effective in the $10^{\circ}0 - 01'0$ relaxation process than either $\text{CO}_2 - \text{He}$ or $\text{CO}_2 - \text{H}_2\text{O}$ collisions. Then, for low CO_2 concentrations, the relaxation of the $01'0$ level by H_2O or He is faster than the coupling between the $10^{\circ}0$ and $01'0$ states. This does not pose any problems for most high power CO_2 lasers, because they generally operate with CO_2 mole fractions between 5 and 15%, and $\text{H}_2\text{O}/\text{He}$ fractions between 10 and 15%, the balance being made up of N_2 . These mixtures easily satisfy the criterion of Bulthuis that the CO_2 concentration must exceed 12% of the fraction of the $01'0$ relaxant species in order to have strong $10^{\circ}0 - 01'0$ coupling.

In the MHD laser a far different situation prevails. Electron energy balance considerations dictate that molecular mole fractions must not greatly exceed 10^{-2} . Lowenstein's analysis restricts the CO_2 concentration even further to avoid quenching of the excited electronic states of the alkali seed. In this case, the rate constants presented here indicate that the rate-limiting process is actually the $10^{\circ}0 - 01'0$ coupling rate. All previous studies of MHD lasers have assumed this rate to be very fast so that the populations of the symmetric stretch and bending modes are in Boltzmann equilibrium. When this assumption is made the rate-limiting process is naturally the relaxation of $\text{CO}_2(01'0)$ to the ground state by He collisions. Since these other analyses have apparently ignored the real

bottleneck, there is the distinct possibility that they have overestimated the optical power extraction from an MHD laser by up to an order of magnitude.

Several other interesting physical aspects present themselves here. When the lower level deactivation rate is extremely rapid (as with strong $10^{\circ}0 - 01'0$ coupling), the process which limits the photon production rate is not the $10^{\circ}0$ relaxation time but the pumping rate of the upper laser level. This must be an important consideration if one is searching for plasma conditions which maximize the performance of an MHD laser.

Furthermore, if the interpretation by Jacobs, Pettipiece, and Thomas of their experimental results is correct, then the rate limiting step is actually the intramode VV process



If the intramode energy transfer rate is really so small ($3.3 \times 10^4 \text{ torr}^{-1} \text{ sec}^{-1}$), the levels of the bending mode are not in Boltzmann equilibrium. This would upset another long-held assumption about CO_2 molecular kinetics. One possible explanation for such a slow rate is the change in the superscript angular momentum quantum number. Before the encounters, neither CO_2 molecule has any rotation about the figure axis; afterwards they both do. From geometric considerations, a third body may be necessary to get them spinning. This would explain the low frequency of occurrence for this process at low CO_2 concentrations. At any rate, if the energy levels of the

BM are not in Boltzmann equilibrium, the mode approach to writing the CO_2 rate equations is inappropriate. An accurate treatment would require the rate equations for all of the levels to be written separately.

In the present analysis we employ the mode equations for two reasons: (1) detailed rates for all the inter- and intra-mode processes are unavailable at this time; and (2) it is uncertain whether the stated interpretation of the JPT experiment is correct. Nevertheless, our modeling of the vibrational kinetics goes a step beyond the analyses of Refs. 4, 8, and 11 by treating the three modes independently, each with its own vibrational temperature. Eqs. (2-17 - 2-19) describe the processes of energy transfer to and from these modes. In comparison with the $10^00 - 01^10$ coupling rate, the rates of deactivation of the 00^11 and 01^10 levels by CO_2 and He collisions are known fairly accurately (within 10%). These are presented by Taylor and Bitterman and updated somewhat in Ref. 8. We use cubic spline fits obtained from the curves in the latter reference in our calculations. It is then possible to study the effects of the uncertainty in the $10^00 - 01^10$ relaxation rate without accumulating too much inaccuracy because of uncertainties in the other rate constants.

It is felt that the bottleneck rate given by Jacobs, Pettipiece, and Thomas gives the best approximation to the time scale of this process. This rate ($3.3 \times 10^4 \text{ torr}^{-1} \text{ sec}^{-1}$) falls midway between that measured by Bulthuis (1.5×10^5

torr⁻¹ sec⁻¹) and a rate measured in Sharma's MHD laser pulsed-discharge simulation experiment (5.2×10^4 torr⁻¹ sec⁻¹).⁽¹²⁾ The effects of this rate constant on the calculated small signal gain in a flowing MHD laser plasma are shown in Figure 6. For comparison, a calculation from the old two-vibrational-temperature model is included. Note the near equality of the curve from this model with the one obtained using the new model and the RKJ relaxation rate.

V. NUMERICAL CALCULATIONS

5.1 Complete System of Equations

We have seen that a wide variation exists in the accepted value of the lower laser level relaxation rate in CO_2 . Depending on which of these rates is accurate, one has two distinct kinetics models to choose from when doing performance calculations for carbon dioxide lasers. The first of these will be referred to as the three-temperature model. In this formulation the three vibrational modes of CO_2 are treated independently. Each energy transfer process is explicitly written in the vibrational energy equations. The vibrational energy stored in each mode is then computed as a function of position in the channel by integrating the rate equations.

Thus, the characteristic temperature of each mode is determined by a balance of the energy gain and loss mechanisms. Unless one of the kinetic rate constants describing the transfer of energy between two modes is very large, the three vibrational temperatures will be different. Then a total of five temperatures describe the state of the different components of the laser plasma: the static temperature of the neutral gas T , the electron temperature T_e , and the characteristic vibrational temperatures T_1 , T_2 , and T_3 . This is a relatively general approach, and it is the one used in deriving the equations presented in Chapters 2 and 3. For convenience, let us now write again the seven differential equations which govern the evolution of the

fluid properties in an MHD laser.

$$\frac{d}{dx} (\ln p_o) = -i \quad (5-1)$$

$$\frac{d}{dx} (\ln T_o) = \frac{\gamma-1}{\gamma} n_p i \quad (5-2)$$

$$\frac{d}{dx} (n_e U A_D) = \frac{n_e U A_D}{L_{RATE}} [1 - \frac{n_e^2}{n_e^*} \frac{1 + 3<\eta^2>}{1 + \phi(\phi+2)<\eta^2>}] \quad (5-3)$$

$$\frac{d}{dx} <\eta^2> = <\eta^2> \frac{4}{L_{RATE}} \frac{1 - <\eta^2>}{1 + \phi(\phi+2)<\eta^2>} \frac{1}{\lambda^2} \frac{\Gamma + \Gamma^*(1 - \frac{n_e^2}{n_e^*})}{1 + \Gamma^*/\lambda^2} \quad (5-4)$$

$$\frac{d}{dx} (E_1 U A_D) = [- \frac{E_1(T_1) - E_1(T_2)}{\tau_{1REL}} + \frac{v_1}{v_3 - v_1} gI] A_D \quad (5-5)$$

$$\begin{aligned} \frac{d}{dx} (E_2 U A_D) = & \frac{E_2(T_e) - E_2(T_2)}{\tau_{2e}} + \frac{E_3(T_3) - E_3(T_2)}{\tau_{3REL}} \\ & + \frac{E_1(T_1) - E_1(T_2)}{\tau_{1REL}} - \frac{E_2(T_2) - E_2(T)}{\tau_{2REL}}] A_D \end{aligned} \quad (5-6)$$

$$\begin{aligned} \frac{d}{dx} (E_3 U A_D) = & \frac{E_3(T_e) - E_3(T_3)}{\tau_{3e}} - \frac{E_3(T_3) - E_3(T_2)}{\tau_{3REL}} \\ & - \frac{v_3}{v_3 - v_1} gI] A_D \end{aligned} \quad (5-7)$$

When the rate of coupling between the 10°0 and 01°0 levels is extremely fast, a second approach may be taken to

modeling the CO_2 kinetic processes. Simplification of the above equations may be obtained by recognizing that very rapid reactions can produce equilibrium between the reacting species. In the previous chapter we saw that the early acceptance of the results of the Rhodes-Kelly-Javan experiment⁽⁵⁰⁾ as well as experience in analysis of CO_2 lasers with large CO_2 mole fractions led to the assumption that the bending and symmetric stretch modes of the CO_2 molecules in an MHD laser are strongly coupled. When this is the case the SSM vibrational temperature is nearly identical to the BM temperature, reflecting the complete equilibrium of the two modes. The bottleneck rate in this case is the one with which $\text{CO}_2(01'0)$ is deactivated through collisions with He atoms. The assumption that $T_1 = T_2$ makes one of the vibrational energy equations redundant. We can combine (5-5) and (5-6) into a single equation, so that the number of differential equations which must be solved by numerical integration is reduced from seven to six. Combination of (5-5) and (5-6) yields

$$\begin{aligned} \frac{d}{dx} (E_{12}^{UA_D}) &= \left[\frac{E_{12}(T_e) - E_{12}(T_2)}{\tau_{2e}} \right. \\ &\quad \left. + \frac{E_3(T_3) - E_3(T_2)}{\tau_{3REL}} - \frac{E_{12}(T_2) - E_{12}(T)}{\tau_{2REL}} \right] A_D \end{aligned} \quad (5-8)$$

where

$$E_{12}(T_i) = \frac{h\nu_1}{e^{h\nu_1/kT_i} - 1} n_{CO_2} + \frac{2h\nu_2}{e^{h\nu_2/kT_i} - 1} n_{CO_2} \quad (5-9)$$

In this two-vibrational-temperature model Eq. (5-1) - (5-4) as well as Eq. (5-7) remain unchanged.

We have already seen in Figure 6 how the two theories lead to different predictions for the small signal gain. Two features of this graph should be noted at the present time. First, the two-temperature model predicts a higher gain than does the three-temperature model with the rate measured by Bulthuis and JPT. This is because the more rapid rate of collisional deactivation of the lower laser level that is inherent in this theory results in a generally lower population for the lower level. Thus the population inversion calculated with this theory is greater.

The second detail is a qualitative one. For the initial conditions shown, the gain calculated with the two-temperature theory quickly rises to a maximum and begins to decay. In contrast, the three-temperature model predicts a monotonic rise in the small signal gain over the range of x indicated. The dropoff in gain is due to the increased rate of deactivation and decreased rate of pumping of the upper laser level, both of which are caused by the pressure buildup resulting from the MHD interaction.

The same effect will eventually cause the gain calculated from the three-temperature theory to peak and then

decay. It increases in the region of our calculations because the lower level population is large due to the high value of T_o . The deactivation rate of this level is slow. As the fluid moves down the channel the lower level population remains partially frozen near the initial value, but it does continue to decrease. This is indicated by the rising gain. The lower level deactivation rate is enhanced by the pressure buildup in the positive x direction. However, eventually the electron temperature will begin to drop and the rate of decrease of the upper level population will exceed that of the lower level population. Then finally the small signal gain predicted by the three-temperature model will also reach a maximum value and start to decay.

If the initial stagnation temperature were lower than it is in Figure 6, we should expect the three-temperature model to predict a higher gain in the entrance region of the channel, as the lower level population does not then have to decay from such a large initial value. Figure 7 illustrates the truth of this statement; it compares the small signal gain calculated with the three-temperature model for $T_o = 1800^{\circ}\text{K}$ and 2090°K .

Of greater interest than the small signal gain is the calculated power extraction, because this is where the bottlenecking predicted by the three-temperature theory should have its most pronounced effects. Results of power extraction calculations for the same initial conditions as in Figure 6,

with the exceptions $p_0 = 20.0$ atm, $x_{CO_2} = 0.0125$, and $x_{Cs} = 10^{-5}$, are presented in Tables 3 and 4. The trends followed by the data in these tables are more clearly illustrated by Figures 8-13. Figure 8 shows the specific power output of the laser with a transmission coefficient of 3% at the output coupling mirror. The two-temperature model predicts a significantly higher power output than the three-temperature model. The principal reason for this is the difference in the deactivation rates for the lower laser level. However, understanding of the intermediate details is aided by Figures 9-11. Note that the difference between T_e and T_3 is considerably greater with the two-temperature model.

The slow lower laser level deactivation rate associated with the three-temperature model results in a higher initial value of n_{100} (hence T_1) at the cavity entrance than in the two-temperature calculation. This, together with the gain-equals-loss restriction on cavity gain given by Eq. (2-16), fixes the upper level population (hence T_3). Since n_{100} is initially higher in the three-temperature theory, then n_{001} and T_3 will be higher as well. This results in a somewhat paradoxical situation where the calculated power output is greater in the two-temperature theory, even though the upper laser level population is less. But as we have seen, the latter condition is a direct result of the rapid lower level deactivation frequency which also allows the higher rate of stimulated transitions in this model. Although the upper

Table 3. Computational Results from Three-Temperature Model ($x_{CO_2} = 0.0125$,
 $x_{Cs} = 10^{-5}$, $P_{O_2} = 20.0$ atm, $T_0 = 2090^{\circ}\text{K}$, $M = 4.0$, $B = 4.0T$,
 $n_{e_O} = 8.5 \times 10^{18} \text{ m}^{-3}$)

x (m)	n_{e_O} (m^{-3})	T_e	T_{100}	T_{10}	T_{001}	T	U (m/sec)	P (atm)	I^2 (w/cm^2)	gI^3 (w/m^3)
0.000	---	---	1567.5	1567.5	1567.5	2329.9	9.762	---	---	---
0.025	---	---	544.0	1041.5	477.3	4232.7	0.437	---	---	---
0.050	---	---	429.0	429.0	998.1	360.2	4376.7	0.215	---	---
0.075	2.27×10^{19}	4154.9	596.9	596.9	1349.5	363.5	4369.5	0.216	97200	6.41×10^7
0.100	3.84×10^{19}	3411.0	838.9	838.9	1905.1	378.0	4347.7	0.225	107000	7.04×10^7
0.150	3.94×10^{19}	3218.5	872.9	872.9	2184.1	428.9	4286.9	0.256	87100	5.75×10^7
0.200	3.95×10^{19}	3203.2	862.2	862.2	2166.5	479.4	4227.6	0.288	83800	5.53×10^7
0.250	3.95×10^{19}	3196.4	847.8	847.8	2169.8	521.5	4177.6	0.319	75700	4.99×10^7
0.300	3.97×10^{19}	3201.3	842.2	842.2	2290.9	584.3	4102.6	0.347	43700	2.88×10^7
0.350	4.00×10^{19}	3203.6	863.2	863.2	2401.3	635.2	4041.9	0.389	3230	2.13×10^6
0.400	4.01×10^{19}	3176.0	912.7	912.7	2269.2	694.1	3973.0	0.429	---	---
0.450	4.01×10^{19}	3154.9	957.0	957.0	2050.0	757.0	3900.0	0.472	---	---
0.500	4.01×10^{19}	3132.8	1006.3	1006.3	1829.3	824.1	3822.0	0.521	---	---

Table 4, Computational Results from Three-Temperature Model ($x_{CO_2} = 0.0125$,
 $x_{Cs} = 10^{-5}$, $P_0 = 20.0$ atm, $T_0 = 2090^{\circ}\text{K}$, $M = 4.0$, $B = 4.0\text{T}$,
 $n_{e_0} = 8.5 \times 10^{18} \text{ m}^{-3}$).

x (m)	n_e (m^{-3})	T_e	T_{100}	T_{001}	T	u (m/sec)	P (atm)	$\frac{q^2}{w/cm^2}$ (W/m^2)	$\frac{q^2}{w/m^3}$ (W/m^3)
0.000	---	---	1567.5	1567.5	1567.5	2329.9	9.762	---	---
0.025	---	---	1221.2	546.7	1020.9	476.2	4231.0	0.436	---
0.050	---	---	1106.0	437.0	979.3	359.6	4374.5	0.214	---
0.075	2.92×10^{19}	4244.5	1005.4	556.8	2031.0	363.5	4367.5	0.216	---
0.100	3.92×10^{19}	3378.5	1219.9	741.6	2680.8	378.1	4349.4	0.225	2.68×10^4
0.150	3.98×10^{19}	3257.6	1268.1	785.8	2955.2	424.0	4310.1	0.252	1.09×10^4
0.200	3.98×10^{19}	3247.6	1207.9	797.3	2915.9	474.4	4269.6	0.282	8368
0.250	3.97×10^{19}	3237.4	1132.2	808.3	2828.5	524.2	4230.5	0.312	6353
0.300	3.96×10^{19}	3224.4	1022.4	836.3	2680.8	581.3	4186.6	0.347	2660
0.350	3.95×10^{19}	3210.2	942.7	877.3	2489.0	641.2	4141.6	0.383	1938
0.400	3.93×10^{19}	3193.9	922.7	925.6	2248.3	706.4	4093.8	0.423	---
0.450	3.92×10^{19}	3179.0	940.3	975.0	2012.7	775.7	4043.9	0.467	---
0.500	3.91×10^{19}	3164.7	983.7	1033.6	1766.7	854.3	3987.9	0.517	---

level population is smaller in the two-temperature calculation, so too is the lower level population. The lower level population in the three-temperature theory is held at a high value by the slow deactivation rate measured by Bulthuis and JPT.

Not only is the calculated power output greater when the two-temperature theory is used, but the laser efficiency is considerably higher as well for a given set of initial conditions. Figure 12 shows the fraction of the Joule dissipation power which goes into the upper and lower laser levels. These fractions are given by η_p and η_L , respectively. The amount of energy transferred to each mode is proportional in the Landau-Teller formulation to the difference $E_i(T_e) - E_i(T_i)$. Then the greater the difference between T_e and T_i (the vibrational temperature of mode i), the greater will be the fractional power transfer to the mode in question. Efficient operation of the laser dictates that η_p be high and η_L low. This occurs when $T_e - T_3$ is large and $T_e - T_2$ is not too great. However, the constraint $T_e > T_3 > T_2$ must always be satisfied. In practice it may turn out that the efficient pumping associated with a low T_e is incompatible with the demands in a high power device for rapid pumping and a high T_e .

For the initial conditions of Figure 8-13 T_e is such that $\eta_p < \eta_L$. However, comparison of Figures 9 and 10 shows that the difference $T_e - T_3$ is considerably greater for the two-temperature calculation. This leads to the expectation that the value of η_p calculated from this theory is higher than it really should be if the three-temperature model is

accurate. Figure 12 shows that this is indeed the case. So the three-temperature model predicts not only less power, but a lower efficiency for the conversion of electrical to optical energy. In addition, we saw in Chapter 2 that the key efficiency parameter is the local or adiabatic efficiency, which is the ratio of the energy actually extracted to the energy that would be removed in an adiabatic process. Figure 13 shows that the calculated local efficiency is also considerably less for the three-temperature model.

It should be stressed at this point that the performance predicted by the three-temperature theory can generally be improved upon by changing the initial conditions. In the present case n_p can be increased relative to n_L by decreasing T_e . This can be accomplished in a variety of ways: changing the geometry to decrease the Mach number, increasing the CO_2 concentration to increase the inelastic losses, or decreasing T_o . These considerations are taken up in the following section, which presents the major quantitative findings of this investigation.

5.2 Results of Parametric Study

In Section 4.C an exhaustive effort was made to determine the most probable rate of deactivation of the lower laser level; it was concluded that this was the rate determined experimentally by Bulthuis and by Jacobs, Pettipiece, and Thomas. Then in the preceding section, we saw how these recent experimental findings led to important quantitative and qualitative differences in the formulation of equations describing

MHD laser performance. On the basis of the discussion in Section 4.C it is felt that the three-temperature model with the Bulthuis - JPT value $k_{SB} \approx 3.3 \times 10^4 \text{ torr}^{-1} \text{ sec}^{-1}$ provides the most accurate description of the CO_2 molecular kinetics. For the parametric study of the effects of various properties on laser performance this is the model that was employed.

We shall now describe the set of initial conditions about which the independent quantities were varied. Table 5 summarizes the values used for this baseline case. This set of conditions was chosen primarily on the basis of results from previous MHD laser studies. Lowenstein's calculations⁽⁴⁾ showed that optimum performance is achieved when $x_{\text{Cs}} = 10^{-5}$ and T_e lies in the range 2500-3000°K. The calculations of Refs. 6-8 indicated that such electron temperatures could be attained with a typical state-of-the-art magnetic induction of 2-4 tesla and a CO_2 fraction of 1% if the nozzle area ratio is designed to provide a Mach number of 4 at the channel entrance. Other cavity properties necessary to maintain the desired plasma conditions are static temperatures in the neighborhood of 300°K and pressures of 0.1-0.2 atm. When combined with the Mach number requirement, these numbers imply initial stagnation conditions $T_0 = 2090^\circ\text{K}$ and $p_0 = 20.0 \text{ atm}$. These values result in a mass flow rate of 1.56 kg/sec.

For the baseline calculations we shall assume the CO_2 - Cs quenching cross section $\sigma_Q = 0$. An initial electron number

density $n_{e_0} = 8.5 \times 10^{18} \text{ m}^{-3}$ due to preionization is specified for the baseline case. Finally, absorption coefficients of 0.02 are assumed for each mirror, with transmission coefficients of 0.03 for the output coupling mirror and 0.00 for the mirror at the other end of the cavity. The output coupling coefficient was chosen on the basis of the small signal gain calculations shown in Fig. 6 and the relation for optimum output coupling given by Ref. 27:

$$t_{\text{OPT}} = -a + \sqrt{G_0 L a} \quad (5-10)$$

where a is the total absorption coefficient (in the absence of internal scattering), G_0 is the small signal gain, and L is the distance between the mirrors.

As a check on the numerical model, the computer program that was developed to perform the calculations was run with no CO_2 and under the same conditions as the MIT nonequilibrium MHD generator experiment. The results were found to match closely those of Cole's analysis. The Mach number considerations result in an area ratio at the nozzle exit $\frac{A_e}{A^*} = 5.6$. With a throat area A^* of 0.0022 m^2 (equal to that in the MIT experimental generator) this condition and the others stated previously lead to a channel section with a width between mirrors (1) of 0.54 m (54 cm) and a height of 0.023 m (2.3 cm). So initially the flow is expanded through a wedge nozzle 0.05 m in length with a divergence half angle of 10.7° and an area

Table 5. Baseline Case.

M = 4
B = 4.0 tesla
 $x_{CO_2} = 0.01$
 $x_{Cs} = 10^{-5}$
 $p_o = 20.0 \text{ atm}$
 $T_o = 2090^\circ K$
 $n_{e_o} = 8.5 \times 10^{18} \text{ m}^{-3}$
 $\sigma_Q = 0.0$
 $\langle \eta^2 \rangle = 0.05$
 $L_{NOZ} = 0.05 \text{ m}$
 $L = 0.54 \text{ m}$
 $r_1 = 0.98$
 $r_2 = 0.95$
 $a_1 = 0.02$
 $a_2 = 0.02$
 $t_1 = 0.00$
 $t_2 = 0.03$

Table 6. Summary of Parameter Variation Runs
with Power Extraction Program.

(1) Vary k_{SB}

- 4.5×10^5 torr $^{-1}$ sec $^{-1}$ (RKJ rate)

- 3.3×10^4 torr $^{-1}$ sec $^{-1}$ (Bulthuis - JPT rate)

(2) Vary x_{CO_2}

- 0.01

- 0.0125

- 0.0165

- 0.02

- 0.03

- 0.04

(3) Vary p_o

- 20.0 atm

- 10.0 atm

(4) Vary T_o

- 2090°K

- 1800°K

(5) Vary x_{Cs}

- 6×10^{-6}

- 10^{-5}

- 10^{-4}

Table 6. Summary of Parameter Variation Runs with Power Extraction Program. (Cont.)

(6) Vary n_{e_0}

$$- 8.5 \times 10^{18} \text{ m}^{-3}$$

$$- 3.0 \times 10^{19} \text{ m}^{-3}$$

(7) Vary σ_Q

$$- 0.0$$

$$- 7.0 \times 10^{-19} \text{ m}^2$$

ratio at the exit of 5.6, yielding an isentropic Mach number of 4. In this region the fluid is preionized so that $n_e = 8.5 \times 10^{18} \text{ m}^{-3}$ at the nozzle exit. The gas next enters the wedge-shaped channel section with a width of 0.54 m and a divergence half angle of 0.3°. A magnetic field of 4.0 tesla is initiated 0.01 m into the channel. The electrode and insulator thicknesses are the same as those used in the MIT generator. Several runs of the program with different ratios of electrode-to-insulator width indicated that this parameter had little effect on performance. Similarly, the transverse voltage distribution was taken to be the same as in Ref. 15, the MIT experiment, but runs with significantly different values indicated that this too had little effect on performance. The initial value of the fluctuation parameter was taken to be $\langle \eta^2 \rangle = 0.05$, as in Ref. 16.

Table 6 summarizes the successful runs of this power extraction program that were performed as part of the parametric analysis of the MHD laser. Each of the following quantities was varied while the other baseline conditions were held constant: lower laser level deactivation rate k_{SB} , CO_2 mole fraction x_{CO_2} , initial stagnation pressure p_o , initial stagnation temperature T_o , seed fraction x_{Cs} , preionized electron number density n_{e_o} , and quenching cross section σ_Q . In addition, several runs were made at a different Mach number ($M = 2$) with p_o and T_o reduced to 1.66 atm and 816°K, respectively, in order to keep p and T in the optical cavity at 0.2 atm and 350°K.

The results of these calculations are presented in Fig. 8-26. Fig. 8-13 show the effects of the lower laser level relaxation rate on laser performance. We have already discussed the ramifications of adopting the three-temperature model. The following thirteen plots, Figures 14-26, then illustrate the effects of varying the CO_2 concentration on the laser output and fluid properties. It can be seen that the mole fraction $x_{\text{CO}_2} = 0.03$ represents an apparent optimum. As discussed in Section 6.B, this optimum shifts to the right on Figure 14 as M is increased. However, in this study we confine our attention primarily to the set $M = 4$, $p_o = 20.0 \text{ atm.}$, and $T_o = 2090^\circ\text{K}$ because these conditions were identified by Refs. 4 and 7 as the most likely operating regime for an MHD laser.

Figure 27 shows how the initial stagnation pressure affects the radiation intensity in the cavity. Clearly the higher value of p_o offers better performance. Figures 28-30 reveal the influence of initial stagnation temperature on the laser output power and the fluid properties in the cavity. These figures indicate the desirability of operating with a lower stagnation temperature than in the baseline case. Figure 10 and Table 4 presented the results of the three-temperature calculation for a seed fraction $x_{\text{Cs}} = 10^{-5}$. The effects of increasing x_{Cs} to 10^{-4} are shown in Figure 31 and Table 7. With such a large seed fraction n_e is high enough under these conditions to significantly excite the bending mode and subsequently the lower laser level, with the result

that no lasing ever occurs. Thus we see some confirmation of Lowenstein's prediction that a seed fraction of 10^{-5} yields the maximum performance. Figure 32 illustrates the effect of the initial electron number density on the laser output of zero quenching. While the higher value of n_{e_0} provides a higher power output, the effect is not significant. Finally, Figures 33-35 demonstrate what happens when the quenching cross section is not equal to zero. We assume here that σ_Q has the rather large value of $7.0 \times 10^{-19} \text{ \AA}^2$ used by Lowenstein. It can be seen that while quenching does have an adverse effect on the small signal gain, as long as the fluid is preionized in the nozzle it should be possible to obtain an appreciable small signal gain (and power output). In the following chapter we shall analyze these results in greater detail in an effort to clarify the basic mechanisms and properties of the MHD laser plasma.

VI. DISCUSSION AND CONCLUSIONS

6.1 Effect of Lower Level Relaxation Rate on Laser Performance

We have seen that the collisional deactivation rate of the lower laser level has a profound influence on the power extraction characteristics of a CO_2 MHD laser. Figures 8-10 indicate that the previous MHD laser performance calculations described in Refs. 4 and 6-8 differ significantly from those which employ the revised molecular kinetics model presented earlier in this work. Because the most recent experimental measurements of the lower level relaxation rate by Bulthuis and by Jacobs, Pettipiece, and Thomas strongly suggest the need to adopt the revised kinetics model, the calculations performed according to this theory should be considerably more accurate than the earlier results. The calculations with the old two-vibrational-temperature theory yield over-optimistic results due to the significantly different set of plasma conditions resulting from the rapid lower level relaxation rate. We shall now analyze the two cases in a general way with the goal of obtaining a set of dimensionless numbers which provide a guideline for judging when plasma conditions are optimum for lasing.

Let us begin by idealizing the relevant CO_2 energy levels as a three-level laser system. The subscripts 2, 1, and 0

will be used to designate the upper, lower, and ground states, respectively. Then the rate equations describing the populations of the upper and lower laser levels are

$$\frac{dN_2}{dt} = -N_2 \omega_{20} - w_i (N_2 - N_1) + R_2 \quad (6-1)$$

$$\frac{dN_1}{dt} = -N_1 \omega_{10} + N_2 \omega_{20} + w_i (N_2 - N_1) + R_1 \quad (6-2)$$

Here ω_{ij} is the decay rate per atom from level i to level j. This includes transitions due to both spontaneous emission and collisional processes. In the high pressure regime of interest in an MHD laser, the latter are completely dominant. w_i is the probability per unit time that a molecule in the upper laser level will undergo a stimulated transition to level 1 (or vice versa). Of course w_i is proportional to the intensity of the radiation field inside the optical cavity. R_2 and R_1 are the pumping rates of the upper and lower laser levels.

Consider now a steady-state situation such that $\dot{N}_1 = \dot{N}_2 = 0$. Then Eqs. (6-1) and (6-2) can be combined to yield an expression for the population inversion:

$$N_2 - N_1 = \frac{R_2 \left\{ 1 - \frac{\omega_{20}}{\omega_{10}} \left[1 + \frac{R_1}{R_2} \right] \right\}}{w_i + \omega_{20}} \quad (6-3)$$

As long as this inversion density remains below the oscillation threshold, the induced transition rate w_i will be essentially zero. $N_2 - N_1$ will be proportional to the

pumping rate under these conditions.

When the pumping rate is increased to the point where it equals the decay rate, the threshold for laser oscillation is attained, at which point the small signal gain reaches the value:

$$G_0 = (N_2 - N_1)_t \frac{c^2}{8\pi v^2 \tau'_{21}} g(v) \quad (6-4)$$

$$= \frac{1}{2L} \ln (r_1 r_2)$$

The threshold inversion density is equal to

$$(N_2 - N_1)_t = \frac{8\pi v^2 \tau'_{21}}{c^2 g(v)} \left[- \frac{1}{2L} \ln (r_1 r_2) \right] \quad (6-5)$$

Under steady-state conditions $N_2 - N_1$ must remain equal to the threshold value regardless of the amount by which the threshold pumping rate is exceeded. Eq. (6-3) indicates that this is possible provided that w_i is allowed to increase once the pumping rate exceeds its threshold value $\omega_{20} (N_2 - N_1)_t$. Eq. (6-3) then relates the electromagnetic energy stored in the resonator cavity to the pumping and relaxation rates. We may solve this equation to obtain an expression for the stimulated transition rate per molecule:

$$w_i = \frac{R_2}{\frac{8\pi v^2 \tau'_{21}}{c^2 g(v)} - \frac{1}{2L} \ln (r_1 r_2)} \left[1 - \frac{\omega_{20}}{\omega_{10}} \left(1 + \frac{R_1}{R_2} \right) \right] - \omega_{20} \quad (6-6)$$

Examination of Eq. (6-6) shows that the optical intensity (which is proportional to W_i) may be large if ω_{20}/ω_{10} is small, if R_1/R_2 is small, and of course if the upper level pumping rate R_2 is itself large. Furthermore the intensity is reduced if the parasitic decay rate of the upper level ω_{20} is large. The dimensionless ratios ω_{20}/ω_{10} and R_1/R_2 are useful in determining which plasma conditions lead to a high power output from the laser. For the electron temperatures encountered in an MHD laser plasma we have seen that direct excitation of the symmetric stretch mode is very slow; hence R_1 is essentially zero in this analysis. The most important parameter in determining power output is then ω_{20}/ω_{10} , the ratio of collisional deactivation rates.

In the two-vibrational-temperature model this ratio is given by

$$\frac{\omega_{20}}{\omega_{10}} = \frac{\tau_2^2}{\tau_3^2}$$

For $x_{CO_2} = 0.0165$ this has the value 0.04. With the three-vibrational-temperature theory the ratio has a different definition:

$$\frac{\omega_{20}}{\omega_{10}} = \frac{\tau_1^2}{\tau_3^2}$$

This is approximately equal to 0.76 for $x_{CO_2} = 0.0165$. Then the first (and dominant) term in Eq. (6-6) comes out higher by the factor $\frac{1-0.04}{1-0.76} = 4.1$ in the two-temperature calculation. If the CO_2 mole fraction is roughly doubled to 0.03, this

factor is reduced to 1.6. This shows how important even a small increase in the CO_2 concentration will be in increasing the lower level relaxation rate under the low CO_2 conditions which are mandatory in an MHD laser. Furthermore, if x_{CO_2} is increased beyond 0.06 the factor ω_{20}/ω_{10} is reduced to unity, indicating identical results from the two kinetics models.

In Section 5.A it was shown that when ω_{20}/ω_{10} is large (corresponding to a slow lower laser level deactivation rate) the lower level population, if large initially, gets frozen at a high value. This and the gain-equals-loss condition imposed during laser oscillation result in a high upper level population in the cavity. It was also indicated that from the standpoint of efficiency, the electron temperature must not be too high. The reason for this lies in the fact that the energy transfer rate from the electrons to the various neutral species in the plasma is roughly proportional to $T_e - T_j$, T_j being the neutral species temperature. A glance at a typical temperature response profile, Figures 9-10 for example, shows that the temperatures follow the hierarchy

$$T_e > T_3 > T_1 > T_2 > T.$$

At very high electron temperatures the elastic loss rate, proportional to $T_e - T$, is significant. However, it decreases in importance relative to the two inelastic loss rates as T_e is lowered. First the bending mode pumping becomes the dominant electron energy loss mechanism; then pumping of the asymmetric stretch mode takes over as T_e is reduced still

further. That these crossover points vary with CO_2 concentration and relaxation rate is an important point to remember when comparing performance calculations for the two kinetics models. The pumping efficiency and local efficiency, which are also dimensionless numbers important in characterizing laser performance, are plotted in Figures 12 and 13 and should be interpreted with this in mind. Although the three-temperature model predicts considerably lower efficiencies than the two-temperature theory for the CO_2 concentration indicated (1.25%), the situation can be altered by decreasing the electron temperature in the former calculation. This can be achieved by increasing the CO_2 concentration. Figures 16, 21, 22 and 23 show that raising x_{CO_2} to 0.03 results in efficiencies which are almost as high as in the two-temperature calculations of Figures 12-13. The same is true of the specific power predictions (compare Figures 8 and 15).

6.2 Optimum Operating Conditions

We shall now discuss in greater depth the results of the parametric study of the effects of various operating conditions on laser performance. In Section 5.B it was shown that better performance occurs at high values of the stagnation pressure and relatively low stagnation temperatures. In order to obtain efficient transfer of the electron energy to the CO_2 upper laser level, it is necessary that the difference $T_e - T_3$ be on the order of 1000°K . At a Mach number of 4 this condition occurs when the CO_2 mole fraction

is about 3 percent. (In the two-temperature theory a CO_2 concentration of 1 percent produces the desired results. We have seen that the similarity factor ω_{20}/ω_{10} is roughly the same in the two cases; hence the equivalent performance calculations). As x_{CO_2} is increased further the electron temperature is severely depressed, and the performance limiting mechanism switches from bottlenecking of the lower laser level to pumping of the upper level.

Let us examine the physical characteristics of the plasma expansion with $x_{\text{CO}_2} = 0.03$. Figures 36-41 present the variations of the important properties with x and aid in interpreting the performance results. In addition we shall refer back to Figures 14-26. As the fluid moves down the channel and interacts with the magnetic field, the Mach number and stagnation pressure fall while the static pressure and temperature both increase (Figures 36-37). This is a direct result of the action of the Lorentz body force over the flow volume. These are general characteristics of all the runs made with the simulation program. Important differences exist between the results for high and low CO_2 concentrations. Reference to Figure 10 indicates that for $x_{\text{CO}_2} = 0.0125$, laser oscillation ceases near $x = 0.30$. In contrast, for $x_{\text{CO}_2} = 0.03$ lasing occurs over the entire channel length with a fairly uniform power output distribution.

This behavior can be understood by referring to the sequence of plots beginning with Figure 16. The higher CO_2

concentrations $x_{CO_2} = 0.03$ and 0.04 are accompanied by increased inelastic losses which depress the electron temperature. This in turn results in a much slower rate of growth of the electron number density. Since the ionization mechanism consists of electron impact with excited cesium atoms the rate of ionization is lower in this case because the free electrons are less energetic and there are fewer cesium atoms in excited electronic states. With fewer charge carrying particles available in these runs with higher CO_2 concentration, the Lorentz force interaction is less. Then the buildup of the static pressure as the flow moves in the downstream direction is not so great in these cases (Figure 18).

The collisional deactivation rates in the CO_2 molecules scale linearly with pressure because of the binary nature of the collisions. This means that the collisional relaxation of the upper laser level far down the channel is considerably greater for the low CO_2 concentrations. This deactivation process is so significant that eventually it reduces the population inversion density below the oscillation threshold; hence in these cases laser action terminates before the end of the channel is reached. For the higher CO_2 concentrations the pressure buildup is much slower and lasing never stops.

Figure 15 shows that the specific power growth rate is very nearly linear in x for a CO_2 concentration of 3 percent. When x_{CO_2} is increased to 4 percent the power production rate begins to drop off because T_e and n_e are too low, and the

upper level pumping rate does not increase as rapidly as the deactivation rate. For a mole fraction of 0.03 these two competing rates are very nearly balanced.

Connected with this is the behavior of the curves for the upper and lower level populations plotted in Figures 19-20. The first of these shows that downstream of $x = 0.35$ the upper level population is greater for the higher CO_2 concentrations. This is due to the fact that in these runs the pressure is lower and collisional relaxation is not as important as for the low- CO_2 -fraction runs.

The lower level population with $x_{\text{CO}_2} = 0.03$ starts out lower because of the faster deactivation kinetics associated with a high CO_2 concentration (Figure 20). As the pressure builds up downstream, lasing stops for the lower CO_2 concentrations and the lower level populations drop below the curve for $x_{\text{CO}_2} = 0.03$ because of the fast kinetics at the higher pressures. With $x_{\text{CO}_2} = 0.03$ lasing never stops and the lower level population is fed by stimulated transitions from the upper level which offset the increased deactivation rate. Thus the lower level population downstream in this case is greater even though the relaxation rate is also greater. However, for $x_{\text{CO}_2} = 0.04$ the lower level relaxation rate is great enough so that the population of the lower level during lasing is below the final asymptotic value calculated for the lower CO_2 concentrations. But as we have seen, the electron temperature is so severely depressed for a CO_2 concentration

this high that the upper level pumping rate is reduced even more than the lower level relaxation time.

For $x_{CO_2} = 0.03$ the electron temperature has dropped below 2500°K, so that the relative elastic loss decreases and the fraction of electron energy transferred to the upper laser level increases. This results in a higher optical efficiency for $x_{CO_2} = 0.03$, and a higher local efficiency. The local efficiency measures the fraction of the flow enthalpy converted to coherent optical radiation output. As indicated by Figure 21, n_{LOC} lies between 2.0 and 2.5 percent for the mole fraction $x_{CO_2} = 0.03$. This is considerably higher than the comparable figure for gasdynamic lasers and comparable to the performance attainable with CO_2 electric discharge lasers.

Especially interesting is the behavior of the electro-thermal instabilities when the CO_2 concentration is high. The evolution of the electron density fluctuation parameter $\langle n^2 \rangle$ is shown in Figure 25 for various CO_2 concentrations. There is a very dramatic difference between the magnitudes of the nonuniformities caused by the instability. For low CO_2 concentrations (high n_e) the ionization instability is fully developed. For the higher concentrations, n_e is considerably lower as the seed is not near the fully ionized condition. The characteristic length for the development of the electro-thermal waves is much greater than the channel length in this case.

Thus we see that $\langle \eta^2 \rangle$ hardly changes from its initially assumed value of 0.05. In the case of $x_{CO_2} = 0.04$, $\langle \eta^2 \rangle$ actually decreases, indicating that the instability is damped for the plasma conditions in this run. For $x_{CO_2} = 0.03$, $\langle \eta^2 \rangle$ is beginning to rise at the end of the channel, coinciding with a rise in electron number density (Figure 17) and effective conductivity (Figure 26). While it may seem somewhat surprising that σ_{eff} should go up as the plasma instabilities develop, it should be noted that the most important factor in determining electrical conductivity is the average electron number density. For low CO_2 concentrations the ionization mechanism is energy-limited, whereas for high CO_2 fractions (low T_e) it is rate-limited. In the case of $x_{CO_2} = 0.03$ the transition from rate-limited to energy-limited ionization growth begins to occur toward the end of the channel. The rise in n_e produces an increase in σ_{eff} which more than offsets the effects of the instabilities.

The fact that the plasma is nearly free of spatial and temporal fluctuations in electron number density for the higher CO_2 concentrations is important from the standpoint of gain medium homogeneity. The far-field beam pattern and intensity are exceedingly sensitive to nonuniformities in the gain medium of a laser. The fact that nonequilibrium MHD generator plasmas display considerable deviations from uniformity was of some concern when the MHD laser concept was initially addressed. However the present analysis shows that for the optimum lasing plasma conditions which occur for

relatively high CO_2 concentrations, the MHD laser gain medium is virtually uniform. Appendix B discusses several other aspects of the medium homogeneity question.

We have indicated in this section that in terms of specific power output, efficiency, and gain medium uniformity the CO_2 mole fraction $x_{\text{CO}_2} = 0.03$ is very nearly optimal. However, the previous study by Lowenstein predicted that such a high concentration of CO_2 was not practical because of the effects of the quenching process. The discrepancy between these two calculations stems from the fact that we are considering in the present study relaxation processes in a flowing plasma to which preionization may be applied (we assume this to be initially uniform).

Figure 34 indicates that as long as the fluid is adequately preionized, an appreciable small signal gain can be obtained from the plasma even if the $\text{CO}_2 - \text{Cs}$ quenching cross section is as high as the $7.0 \times 10^{-19} \text{ m}^2$ assumed by Lowenstein. If the preionization is removed, however, the electron number density gets frozen at a very low value as ionization buildup never occurs. Since the pumping rate of the upper laser level is controlled by the free electron number density, the small signal gain is very small or even negative under these conditions. This is in accord with Lowenstein's prediction, which may be viewed as the limiting result of a more general problem in which preionization of arbitrary degree is permitted.

Once the preionization has reached a sufficiently high

level there is little benefit in raising it further. Figure 32 shows almost no change in the specific power output when the initial specified electron density is increased from $8.5 \times 10^{18} \text{ m}^{-3}$ to $3.0 \times 10^{19} \text{ m}^{-3}$. The former is the value that was employed in the MIT nonequilibrium MHD generator experiments. Thus the present calculations indicate that with existing preionization techniques, a fairly high small signal gain can be produced even if Lowenstein's estimate of quenching cross section is correct.

Several computer runs were made with a modified nozzle geometry such that the Mach number was 2 at the channel entrance. The stagnation temperature and pressure were reduced to 816°K and 1.66 atm, respectively, in order to keep the cavity temperature and pressure at 350°K and 0.2 atm as in the other calculations. The CO_2 mole fraction was varied in the computer runs; successful results were obtained for $x_{\text{CO}_2} = 0.0025, 0.0075$, and 0.010.

With the output coupling coefficient of the baseline case laser oscillation was attained only in the case of $x_{\text{CO}_2} = 0.01$. As a result of the low electron temperature on this run (less than 1500°K) n_e and the excitation rate are very small; hence the output flux is very low in this case. While lasing did occur, the conversion efficiency was very low for this reason. Figures 42-44 illustrate the variation of G_0 , T_e , and n_e on these runs. They show clearly that the concentrations $x_{\text{CO}_2} = 0.01$ and 0.0075 are too large for this Mach number ($M=2$).

We have already seen that for CO_2 mole fractions less than 0.03 the stimulated transition rate is limited by lower level bottlenecking. However, at this low Mach number an even tighter restriction is placed on the output flux by the pumping rate per molecule. This could be increased considerably by lowering the pressure, but this would not remove the limitation set by bottlenecking. The simple fact is that the CO_2 MHD laser works best with $x_{\text{CO}_2} \approx 0.03$, and to operate with a CO_2 fraction this high and still maintain a high electron temperature requires either a high Mach number ($M=4$) or a very low cavity pressure. Since the gain and power output both scale with the CO_2 number density, the latter alternative is not the way to go in constructing a high power device. Only by running with a high Mach number and keeping a fairly high cavity pressure can the twin objectives of high power and high efficiency be met.

6.3 Comparison with Experimental Results

The test of a theoretical model of any physical process is comparison of its predictions with experimental results. Two recent sets of experiments are felt to give fairly reliable data on the gain and power extraction characteristics of CO_2 MHD lasers. The first of these is the pulsed gas flow, pulsed discharge experiment conducted by Sharma at M.I.T. ⁽¹²⁾ In this apparatus an electric current was passed down the discharge tube through a 1% CO_2 -99% He gas mixture

seeded with Cs at an initial temperature of about 400°K.

A small signal gain of 0.3%/cm was measured under these conditions. No attempts at power extraction were made.

Now the effects of the slow lower laser level relaxation rate measured by Bulthuis and by Jacobs, Pettipiece, and Thomas are most pronounced during power extraction. If the initial temperature is high and the gas is expanded rapidly this slow deactivation will also have some adverse effect on the small signal gain, as indicated by Figure 7. In the experiment of Sharma the fluid starts at room temperature, and it is not expanded significantly, thus there is no vibrational freezing of the lower laser level, the effect which produces the results shown in Figure 7. This and the fact that no power was extracted mean that the full ramifications of the slow deactivation rate never present themselves in these test runs.

However, note that the gain predicted by the numerical model rises from 0.10-0.15%/cm for $T_0 = 2090^\circ\text{K}$ to 0.20%/cm for $T_0 = 1800^\circ\text{K}$. These values are of the same order of magnitude as the gain measured by Sharma, and it seems perfectly plausible that if T_0 is reduced further the calculated small signal gain will rise to the measured value of 0.30%/cm.

The fact that a small signal gain of this magnitude was measured in the light of Lowenstein's prediction casts considerable doubt on the validity of his large assumed quenching

cross section. Then in turn, his finding that the quenching process is the performance-limiting mechanism in an MHD laser is called into question. This further supports the findings of the present study that quenching does not really present any serious limitation to MHD laser feasibility. Furthermore, measurements of the gain decay rate in the after-glow of Sharma's discharge yield values of k_{SB} which match closely the rates measured by Bulthuis and by Jacobs et al. Thus the present result that the lower level relaxation rate provides the most important performance limitation is indirectly confirmed by this experiment.

The other important laboratory data come from the Russian experiment described in Ref. 11. The apparatus used in this series of tests was fundamentally different from the M.I.T. device in that it was designed for power extraction. Furthermore, the configuration used with cesium seeding featured a high-subsonic-Mach number flow through a 4-tesla magnetic field. Because the power extraction calculation in the present study is valid only for an optical cavity whose axis is transverse to the flow direction, and the Russian experiment employed a longitudinal cavity, no direct comparison can be made of power extraction. Instead, the small signal gain was calculated and compared to estimates of this quantity made in Ref. 11.

The flow conditions in the Russian experiment are very different from those of the baseline case in this study. The initial values of the stagnation pressure and temperature are 0.03 atm and 473°K, respectively. These lead to a Mach number of about 0.6 and an average Hall parameter in the range 60-70. The effective and apparent Hall parameters are much less than this, being in the neighborhood of 1. At the channel entrance the electron density is $2 \times 10^{18} \text{ m}^{-3}$, also considerably less than in the baseline case. However, the CO_2 fraction in the Russian experiment was estimated to be the same as in the present study, $x_{\text{CO}_2} = 0.01$.

Since precise determination of the CO_2 concentration has proved to be a problem in MHD laser experiments, the computer program simulating the flow in the Russian device was run for both $x_{\text{CO}_2} = 0.01$ and $x_{\text{CO}_2} = 0.001$. In the latter case a maximum small signal gain of 0.02%/cm was calculated. Electron temperatures in this case were on the order of 3500°K. This gain is a factor of five less than the estimate given in Ref. 11, so it does appear that this CO_2 fraction (0.001) is far too low.

In the other run with $x_{\text{CO}_2} = 0.01$ the maximum calculated gain was 0.05%/cm. The electron temperature was severely depressed at this mole fraction, ranging between 1400-1500°K. While the gain is within a factor of two of the experimental estimate, it appears that an even higher value would occur for a CO_2 concentration somewhere between these two extremes.

At this intermediate point the CO_2 number density would still be appreciably higher than for $x_{\text{CO}_2} = 0.001$, but the electron number density would not be so severely depressed as it is for $x_{\text{CO}_2} = 0.01$. The implication of this is that the CO_2 concentration in the Russian experiment may have been less than was reported.

Although it has been stressed that the power extraction calculation of the present analysis is not valid for the Russian optical cavity, it is nevertheless tempting to compare the calculated with the measured specific power output.

The measured value of P_{SP} was about 10 kJ/kg. With $x_{\text{CO}_2} = 0.01$ the three-temperature power extraction model yielded 11.7 kJ/kg for the baseline case conditions, while the two-temperature theory predicted 97.5. This dramatic discrepancy in the calculation of the basic power available from the plasma, and the proximity of the three-temperature result to the measured value, further reinforce our adoption of the new kinetic model.

6.4 Conclusions

A number of new features of MHD laser plasma behavior have come to light as a result of the present research program. The most important finding is that lower level bottlenecking is the mechanism which limits laser performance. This statement is subject to the qualification that the fluid must be adequately preionized. This means that a sufficient

number of electrons must be provided and that they must be distributed uniformly throughout the flow volume by proper spreading of the discharge.

Most of the experimental data which led to the adoption in the present study of the three-vibrational temperature model was unavailable when the previous analytical MHD laser studies were performed. The use of a two-temperature model led to much higher photon emission rates in these older calculations, as well as higher efficiencies. However, it has been shown in the present work that if the CO_2 concentration is increased to the 3% range, practically interesting output fluxes and efficiencies should be attainable.

Since the effects of the lower level bottlenecking become most apparent during power extraction, small signal gain experiments at low gas temperatures cannot convincingly demonstrate whether this mechanism really controls laser behavior. However, comparison of specific power calculated from the two competing kinetic models with that measured in the Russian experiment strongly supports the three-temperature theory. In addition, gain decay rates measured in Sharma's MHD laser plasma are very close to the ones reported by Bulthuis and others which serve as the basis for the present model.

The exact nature of the bottlenecking step remains unclear. If it is the $02^{\circ}0-01^{\circ}0$ transition as we have

postulated, then a curious phenomenon is implied. This is disequilibrium between the energy levels of the bending vibrational mode. It is generally assumed that intramode energy transfer rates are extremely rapid, producing Boltzmann population distributions for the energy levels. However, the experimental measurements of Jacobs, Pettipiece, and Thomas reveal that the 02°0-01'0 transition is indeed the bottleneck. This in turn implies intramode nonequilibrium.

It is interesting to compare the performance of the CO_2 MHD laser with that of other high energy CO_2 lasers. The most highly developed of these is the gasdynamic laser (GDL). Specific powers from these devices range from 1 kJ/kg for a first-generation machine to 5 kJ/kg for a laser of the second generation.⁽²³⁾ Neither of these compares favorably with the 12 kJ/kg calculated here for the baseline case (and measured by Biberman, et al.⁽¹¹⁾), not to mention the 60 kJ/kg predicted for $x_{\text{CO}_2} = 0.03$. The best GDL efficiencies lie between 0.5 and 1.0 percent, which is comparable to the local MHD laser efficiency calculated for $x_{\text{CO}_2} = 0.01$. When the CO_2 mole fraction is increased to 0.03 the local efficiency rises to about 2.0%, which exceeds the best GDL performance.

The CO_2 electric discharge laser offers higher efficiency and higher specific power than the gasdynamic laser. About 10 kJ/kg can be obtained from one of these devices, with a conversion efficiency of 20% of the electrical energy to laser

radiation.⁽⁶⁵⁾ However, to get the total efficiency one must multiply this by factors accounting for losses arising during power generation and power conditioning. An overall efficiency of 5-7% results. Comparing these figures with those for an MHD laser, we may conclude that the latter is best suited for applications which require more power than an EDL can deliver. The conversion efficiency of 2-3% of the thermal energy to laser radiation is fairly high. However, for lower power applications within range of the EDL capability the MHD laser cannot compete with the higher efficiency of its competitor.

6.5 Suggestions for Future Work

The major finding of this investigation that the power extraction from low-CO₂-concentration lasers is limited by bottlenecking was made possible by a number of recent experimental measurements of the lower level relaxation rate. However, there is still considerable ambiguity as to the exact details of the collisional deactivation mechanism. Further basic research in this area is warranted, especially since the question of whether a 9.6 micron laser is subject to the same bottlenecking mechanism is still largely unanswered. Only the JPT experiment offers any evidence. If the JPT result is confirmed, a more complete explanation than that offered here for the intramode nonequilibrium should be forwarded.

The implications of this slow lower laser level relaxation rate are important not only for magnetohydrodynamic lasers, but also for high-pressure CO_2 gasdynamic lasers which must operate in a so-called " CO_2 -starved" mode to avoid deactivation of N_2 .⁽⁶⁶⁾ Indeed, the measurement of the small-signal gain in a gasdynamic laser with 99% He-1% CO_2 composition represents a direct method of checking the slow lower level deactivation rate. If the gas starts out hot the lower level population should become frozen along with that of the upper laser level. Then no gain (and no laser oscillation) is possible.

To improve on the power extraction capability of the MHD laser it is desirable to find ways to increase the lower level relaxation rate. In conventional CO_2 lasers either He, H_2O , or H_2 is added to hasten this process through collisions. However, these gases interact strongly with only the $01'0$ level of the bending mode. In the MHD laser a gas is required which returns molecules in the $10^{\circ}0$ level directly to the ground state. It has been reported that Xe is just as effective as CO_2 in deactivating the $10^{\circ}0$ level.⁽⁴⁹⁾ If this is true, significant quantities of Xe could be added without upsetting the energy balance in the plasma. Further experimental studies are required to determine precisely the effects of Xe (and other gases) on the deactivation rate of $\text{CO}_2(10^{\circ}0)$. Once these new rates are determined they can be incorporated into the present numerical model.

Finally, the MHD laser concept should not be restricted to using CO₂ as the lasing gas. The limitations that have been discovered in CO₂ MHD laser performance do not apply to other gases. However, the CO₂ molecular gas laser is a proven performer for high-energy, high-efficiency applications. The versatility of the concept is demonstrated by the variety of excitation mechanisms which have so far proven successful. The present study indicates that the MHD pumping concept may be added to this list.

APPENDIX A
CALCULATION OF THE OPTICAL INTENSITY

The technique used to determine the radiation intensity I is valid for an oscillator cavity with planar mirrors aligned transverse to the flow direction. For such a situation the number of photons gained by a wavefront moving across the cavity must equal the number of photons leaving the cavity through the output coupling mirror. This is expressed mathematically by the gain restriction equation for an oscillator, the derivation of which may be found in most quantum electronics texts (for example reference 27):

$$g_{OSC} = - \frac{1}{2L} \ln (r_1 r_2) \quad (A-1)$$

where

g_{OSC} = saturated gain in the oscillator cavity

L = cavity width (distance between mirrors)

r_1, r_2 = mirror reflectivities

This expression is homogeneous in the radiation intensity. However, it is not independent of the intensity, as the intensity alters the gain by its presence in the CO_2 vibrational energy equations such that (A-1) is satisfied. Because the radiation field adjusts to changes in the pumping and deactivation rates on a very rapid time scale (equal to the cavity width divided by the speed of light) the gain restriction equation is valid even for an MHD plasma subjected

to electrothermal waves. This is because the time scale for the growth of these instabilities is much longer than that for radiation field adjustments.

The saturated gain in the oscillator cavity is seen to depend only on the optical properties of the mirrors and their geometric spacing, not on the properties of the plasma. As the fluid moves down the channel, laser oscillation cannot begin until the local value of the small signal gain g_0 has built up to the value g_{OSC} given by Equation (A-1). From this point on the saturated gain g will remain constant, if the cavity properties do not change. We then have the condition

$$\frac{dg}{dx} = 0 \quad (A-2)$$

in the optical cavity.

Now g is in fact a function of the thermodynamic properties of the gas, which vary with x (as does the intensity I). We can rewrite this equation as

$$\frac{\partial g}{\partial E_1} \frac{dE_1}{dx} + \frac{\partial g}{\partial E_3} \frac{dE_3}{dx} = 0 \quad (A-3)$$

where

$$\frac{dE_1}{dx} = \frac{1}{UA_D} \left[\frac{d}{dx} (UA_D E_1) - A_D E_1 \frac{dU}{dx} - UE_1 \frac{dA_D}{dx} \right] \quad (A-4)$$

$$\frac{dE_3}{dx} = \frac{1}{UA_D} \left[\frac{d}{dx} (UA_D E_3) - A_D E_3 \frac{dU}{dx} - UE_3 \frac{dA_D}{dx} \right] \quad (A-5)$$

In these last two equations, the first term on the right hand side is just the RHS of the vibrational energy equation for Mode 1 or Mode 3 of the CO_2 molecule. We may write these in symbolic form as

$$\frac{d}{dx} (UA_D E_1) = \alpha_1 + \alpha_2 I \quad (A-6)$$

$$\frac{d}{dx} (UA_D E_3) = \beta_1 + \beta_2 I \quad (A-7)$$

where

$$\alpha_1 = \frac{E_1(T_1) - E_1(T_2)}{\tau_{1\text{REL}}} A_D$$

$$\alpha_2 = -\left(\frac{v_1}{v_3 - v_1}\right) \frac{A_D}{2L} \ln(r_1 r_2)$$

$$\beta_1 = \frac{E_3(T_e) - E_3(T_3)}{\tau_{3e}} A_D - \frac{E_3(T_3) - E_3(T_2)}{\tau_{3\text{REL}}} A_D$$

$$\beta_2 = \left(\frac{v_3}{v_3 - v_1}\right) \frac{A_D}{2L} \ln(r_1 r_2)$$

Then we may rewrite equations (A-4) and (A-5) in symbolic form:

$$\frac{dE_1}{dx} = \alpha'_1 + \alpha'_2 I \quad (A-8)$$

$$\frac{dE_3}{dx} = \beta'_1 + \beta'_2 I \quad (A-9)$$

where

$$\alpha'_1 = \frac{1}{UA_D} (\alpha_1 - A_D E_1 \frac{dU}{dx} - U E_1 \frac{dA_D}{dx})$$

$$\alpha'_2 = \frac{\alpha_2}{UA_D}$$

$$\beta'_1 = \frac{1}{UA_D} (\beta_1 - A_D E_3 \frac{dU}{dx} - U E_3 \frac{dA_D}{dx}),$$

$$\beta'_2 = \frac{\beta_2}{UA_D}$$

At this point we can substitute (A-8) and (A-9) into (A-3) to obtain

$$\frac{\partial g}{\partial E_1} (\alpha'_1 + \alpha'_2 I) + \frac{\partial g}{\partial E_3} (\beta'_1 + \beta'_2 I) = 0 \quad (A-10)$$

Solving for I:

$$I = - \frac{\beta'_1 \frac{\partial g}{\partial E_3} + \alpha'_1 \frac{\partial g}{\partial E_1}}{\alpha'_2 \frac{\partial g}{\partial E_3} + \alpha'_2 \frac{\partial g}{\partial E_1}} \quad (A-11)$$

This is the desired expression for the optical intensity. It is calculated at each value of x in the numerical integration once the flow properties have been determined. I is then used in the evaluation of derivatives for the next integration step.

The two derivatives $\frac{\partial g}{\partial E_1}$ and $\frac{\partial g}{\partial E_3}$ are given by application of the chain rule for partial derivatives:

$$\frac{\partial g}{E_1} = \frac{\partial g}{\partial T_1} \frac{\partial T_1}{\partial E_1}$$

$$= \frac{\partial g}{\partial N_{100}} \frac{\partial N_{100}}{\partial T_1} \left(\frac{\partial E_1}{\partial T_1} \right)^{-1} \quad (A-12)$$

$$\frac{\partial g}{\partial E_3} = \frac{\partial g}{\partial N_{001}} \frac{\partial N_{001}}{\partial T_3} \left(\frac{\partial E_3}{\partial T_3} \right)^{-1} \quad (A-13)$$

Here we have the following relations:

$$\frac{\partial g}{\partial N_{100}} = - \frac{\lambda^2}{4\pi\tau_{21}v_C} \left(\frac{45.6}{T} \right) e^{-234/T} \quad (A-14)$$

$$\frac{\partial g}{\partial N_{100}} = + \frac{\lambda^2}{4\pi\tau_{21}v_C} \left(\frac{45.6}{T} \right) e^{-234/T} \quad (A-15)$$

$$\frac{\partial N_{100}}{\partial T_1} = \frac{N_{CO_2}}{Q_1(T_1)Q_2(T_2)Q_3(T_3)} \frac{h\nu_1}{kT_1^2} e^{-h\nu_1/kT_1}$$

$$[1 - Q_1(T_1) e^{-h\nu_1/kT_1}] \quad (A-16)$$

$$\frac{\partial N_{001}}{\partial T_3} = \frac{N_{CO_2}}{Q_1(T_1)Q_2(T_2)Q_3(T_3)} \frac{h\nu_3}{kT_3^2} e^{-h\nu_3/kT_3}$$

$$[1 - Q_3(T_3) e^{-h\nu_3/kT_3}] \quad (A-17)$$

$$\frac{\partial E_1}{\partial T_1} = E_1 \left[\frac{h\nu_3}{kT_1^2} \frac{e^{-h\nu_3/kT_3}}{e^{-h\nu_3/kT_3} - 1} \right] \quad (A-18)$$

$$\frac{\partial E_3}{\partial T_3} = E_3 \left[\frac{h\nu_3}{kT_3^2} \frac{e^{h\nu_3/kT_3}}{e^{h\nu_3/kT_3} - 1} \right] \quad (A-19)$$

This completes the set of expressions which we need to calculate the optical intensity I . It should be noted that in Equations (A-14) and (A-15) the assumption has been made that the rotational energy transfer rate is rapid enough to maintain a Maxwellian distribution of rotational energy levels during lasing. This means that all the energy in the CO_2 (00°1) vibrational level may be converted to optical radiation.

APPENDIX B

EFFECTS OF PLASMA NONUNIFORMITIES ON OPTICAL OUTPUT

The performance of any high energy gas laser depends critically on the homogeneity of the gain medium. Density nonuniformities in the fluid can lead to local variations in the index of refraction. These in turn produce relative phase shifts in the laser beam as it traverses the medium which could have deleterious effects on the far field mode pattern. Nonuniformities in a supersonic flow laser arise from shock waves, boundary layer effects, heat release accompanying lasing, and turbulent fluctuations. Previous analyses have treated the effects of density inhomogeneities due to these mechanisms on the far field intensity of the laser. (67-69)

Most of these fluid dynamics-related dephasing phenomena are also present in the MHD laser flow. In addition, some new effects arising from the ionization instability can be of importance in this device. The ionization instability produces alternating zones of high and low electron number density. These spatial nonuniformities in the population of charged particles can affect the optical output in several ways. First, the index of refraction can vary locally because of fluctuations in the polarization caused by the nonuniformities in n_e . Also, since the electron pumping rates depend on both T_e and n_e , local variations in the latter two quantities can

lead to spatial nonuniformities in the small signal gain and the saturation intensity.

The index of refraction in an ionized gas is given by

$$\mu \approx 1 - \frac{\omega_p^2}{\omega^2} \quad (B-1)$$

where

$$\omega = \frac{v}{2\pi}$$

$$= 4.63 \times 10^{12} \text{ for 10.6 micron radiation}$$

and

$$\omega_p = \frac{4\pi n_e e^2}{m_e}$$

= plasma frequency

The plasma frequency has its maximum value in areas where n_e is high; its minimum value occurs in regions of low n_e . Then the maximum variation of the refractive index over the distance of one-half wavelength of the instability is given by

$$\frac{\Delta\mu}{\mu_0} = \frac{\mu_{MAX} - \mu_0}{\mu_0} \quad (B-2)$$

where μ_{MAX} is evaluated at $(n_e)_{MAX}$ and μ_0 is calculated at $(n_e)_{MIN}$. Variations in n_e across the instability wavefront in a nonequilibrium MHD device are on the order of 100%. For $(n_e)_{MIN} = 10^{19} \text{ m}^{-3}$ and $(n_e)_{MAX} = 2(n_e)_{MIN}$ we have

$$\frac{\Delta\mu}{\mu_0} \approx 10^{13} \quad (B-3)$$

Let us compare this with the variation in the index of refraction due to density inhomogeneities. The refractive index in a neutral gas is given by

$$\mu = 1 + K\rho \quad (B-4)$$

where ρ = gas density

and K = Gladstone-Dale constant

$$= 2.02 \times 10^{-4} \text{ m}^3/\text{kg} \text{ for He}$$

The relative variation in μ across the boundary of an inhomogeneity is then

$$\frac{\Delta\mu}{\mu_0} = \frac{K\Delta\rho}{1 + K\rho_0} \quad (B-5)$$

For a density perturbation of 1% which is rather typical of conventional cavities, $\frac{\Delta\mu}{\mu}$ is approximately 10^{-8} . This is five orders of magnitude greater than the typical variation due to ionization instabilities. Since the above expression is linear in the gas density, one can easily show that the variation $\Delta\rho$ would have to be reduced to 10^{-8} before refractive index fluctuations due to electrothermal waves become comparable in importance.

The ionization instability has a plane wave structure. It has been shown to propagate along a wave vector perpendicular to the wave fronts with a direction relative to the mean current vector given by Eq. (3-38):

$$t = \frac{1 - r - r^*}{\langle \beta \rangle} - \sqrt{\left(\frac{1 - r - r^*}{\langle \beta \rangle}\right)^2 + 1} \quad (B-6)$$

Here t is the tangent of the angle between the current and wave propagation vectors. This is the direction along which the growth rate of the instabilities is maximum. It represents a preferred direction for the propagation of these electrothermal waves. The result is a striated plasma as shown in Figure 45. Regions of high electron density appear as sheets perpendicular to the direction of motion, and similarly for regions of low n_e .

The equation of radiative transfer is still valid in the nonuniform plasma, but we must be careful in interpreting the terms:

$$\frac{dI}{dy} = (N_2 - N_1) \frac{c^2 g(v)}{8\pi v^2 \tau_{SP}} I \quad (B-7)$$

Rearranging and integrating, we get:

$$I(y) = I(0) e^{\int_0^y (N_2 - N_1) \frac{c^2 g(v)}{8\pi v^2 \tau_{SP}} dy} \quad (B-8)$$

If N_2 and N_1 were constant we could write

$$I(y) = I(0) e^{Gy} \quad (B-9)$$

In the MHD laser $(N_2 - N_1)$ is not constant as we cross the channel, and we have to perform the integration (actually a summation for our purposes) as we move in the transverse direction across the channel. So

$$\begin{aligned}
 G &= \int_0^y (N_2 - N_1) \frac{c^2 g(v)}{8\pi v^2 \tau_{SP}} dy \\
 &= \frac{L}{N} \sum_{n=1}^N (N_2 - N_1)^n \frac{c^2 g(v)}{8\pi v^2 \tau_{SP}}
 \end{aligned} \tag{B-10}$$

$(N_2 - N_1)$ varies with y because of the effects electrothermal waves have on the pumping rate.

These waves affect the pumping times in two ways. Recall that the Landau-Teller expression for excitation by electron bombardment is of the form $\frac{E_j(T_e) - E_j(T_j)}{\tau_{ej}}$. From the form of this expression, we can see that electrothermal waves producing variations in T_e and n_e will affect the energy transfer rate by perturbing $E_j(T_e)$ and τ_{ej} . Note that $E_j(T_e)$ is affected only by variations in T_e while τ_{ej} is affected by variations in both n_e and T_e .

Milora⁽⁷⁰⁾ performed a nonlinear study of the planar electrothermal waves and showed that their structure was closely approximated by a square wave whose peak was 0.4 wavelengths long and whose valley was 0.6λ in length. This considerably simplifies the present problem. Since the electron number density has essentially only two values (a high

and a low one), so does the quantity $(N_2 - N_1)$. If $(N_2 - N_1)_H$ represents the value of the population inversion evaluated at the peak value of n_e and $(N_2 - N_1)_L$ is the inversion density calculated with the minimum value of n_e , we may then write the small signal gain as

$$\begin{aligned}
 G &= \frac{L}{N} \sum_{n=1}^N (N_2 - N_1)^n \frac{c^2 g(v)}{8\pi v^2 \tau_{SP}} \\
 &\approx (N_2 - N_1)_H \frac{c^2 g(v)}{8\pi v^2 \tau_{SP}} (0.4L) \\
 &\quad + (N_2 - N_1)_L \frac{c^2 g(v)}{8\pi v^2 \tau_{SP}} (0.6L) \tag{B-11}
 \end{aligned}$$

Under conditions where the electrothermal waves are not square and steep-edged, but closer to sinusoidal, the above assumption breaks down. We then have to evaluate $(N_2 - N_1)$ at more than just two values of n_e .

This analysis and Eq. (B-11) in particular are valid for arbitrary orientations of the optical axis as long as the disturbance wavelength is much less than the mirror separation (except for the situation where the wave vector is perpendicular to the optical axis and there is no obliquity of the rays with respect to the striation layers). We can see that this is true by noting that the number of peaks a light ray passes through is $\frac{L}{(\lambda/\cos \theta)}$ where θ is the angle between optical axis and wave vector. Then a light ray passes through $\frac{L}{(\lambda/\cos \theta)}$

troughs. The total distance traveled through regions of high electron number density is thus given by

$$\frac{L}{(\lambda/\cos \theta)} (0.4 \lambda/\cos \theta) \approx 0.4L$$

Similarly the distance traveled by a ray through regions of low electron density is $\frac{L}{(\lambda/\cos \theta)} (0.6 \lambda/\cos \theta) = 0.6L$.

In a nonequilibrium MHD plasma similar to that in an MHD laser Grove⁽⁷¹⁾ measured a wavelength of 0.014 m for the electro-thermal waves. This is about forty times smaller than the width of the cavity, so indeed Eq. (B-11) is usually valid.

APPENDIX C

COMPUTER PROGRAM LISTING


```

PROGRAM IV.31 RPLPAS2.0          MAIN          DATE = 78053      20/41/49
0037      RPLPAS2.0 = 8.854190-12
0038      SACNST = (2.*PI*NE*K/H1**2)**1.5
0039      HPL = 6.63 F-34
0040      NU1 = 4, 126E13
0041      NU2 = 2, 187E13
0042      NU3 = 1, 038E13
0043      TAIC02=0,0025
0044      XCAY=.10
0045      ICAY=0
0046      THFTA=H1*NU1/K
0047      THFT2=H1*NU2/K
0048      THFT3=H1*NU3/K
C READ IN CARD DATA
0049      CALL INPUT(MG,MS,YI,THI,THE,LMNOZ,LCCHAN,TS,TOO,POO,NEO,ETASO,DMAX)
0050      MG = MG*1.66044D-27
0051      MS = MS*1.66044D-27
0052      WS = (1.-TS)*WG+TS*WS
0053      R = K/N
C MASS PLUX DEPENDS ON THROAT AREA. AND UPSTREAM STAGNATION PRESSURE
C AND TEMPERATURE
0054      MASS = P00*A(0,DO)*DSORT(GAM/(R*T0)*( (GAM+1.)/2. )**((GAM-1.)/2.))
0055      WRITING(200) HG, MS, R, MASS
0056      200 FORMAT(1X,'UGAS =',1PD2.5,' KG',/1X,'VSPD =',D12.5,' KG',/1X,'GAS CONST R =',D12.5,' J/KG K',/1X,'MASS PLOW =',P8.6,' KG/SEC',/1H)
C INITIALIZE VARIABLES
0057      X = C.
0058      Y = 1.
0059      T0 = T0
0060      T=V0/(1.+V)
0061      P0 = P00
0062      P = P0/(1.+V)**(GAM/(GAM-1.))
0063      U = DSORT(GAM*R*T)
0064      T1=T
0065      T2=T
0066      23=T
0067      NC02=F1*UC02*P/K/T
0068      YAC=THFTA1/T1
0069      YBC=DXP(YAC)
0070      YCC=THFTA2/T2
0071      YAC=THFTA3/T3
0072      YBC=DXP(YAC)
0073      YCC=DXP(YAC)
0074      YAC=THFTA4/T4
0075      YBC=DXP(YAC)
0076      YCC=DXP(YAC)
0077      YCC=DXP(YAC)
0078      E1=4.18611/1000*NC02
0079      E2=2.7*H18*NU2/YCCC*NC02
0080      F2=H18*NU3/YCCC*NC02
0081      YPTE=(Y0,215), P1,E22,E3
0082      215 FORMAT(//,,1X,D16.6,5X,D16.6,5X,D16.6)

```

POSTPONED TV 1 RELEASE 2.0
DATE = 78053
20/4/69

DATE # 78053

20/41/49

```

PORTAN IV G1  RPLRASP 2.0          MAIN          DATE = 78053
0134        204 PCFNT //,1X, "ERROR IN SUBROUTINE DIPEQ, CALLED FROM MAIN.",  

$ 3Y, YER //,1X, "41/49
0135          STOP
0136          4 IF (IPRNT, P0=1) CALL OUTPUT (X)
0137          IF (IPFLAG, P0=1) GC TO 6
0138          XOLD = X
0139          HOLD = 0
0140          C179
0141          1 CCNTINUE
0142          IX = IX-1
0143          WRITE (NO,205) IX
0144          205 FORMAT (//,1X, "PROGRAM TERMINATES AFTER", I5, " STEPS.")
0145          STOP
0146          6 CALL RPLAYR (X, DAREA)
0147          Q = DSQRT (2.*V/GAM-1.)
0148          P=P0*(1.+V)**(GAM/(GAM-1.))
0149          T = T0/(1.+V)
0150          I = M*DSQRT (GAM*P*T)
0151          P0 = P0
0152          T00 = Y(2)
0153          NF = MEL*W*DAREA
0154          V0 = V
0155          EPSI(1) = 5000.
0156          EPSI(2) = 20.
0157          EPSI(3) = 3.D18
0158          EPSI(4) = 5.D-04
0159          EPSI(5) = 0.2
0160          EPSI(6) = 0.05
0161          EPSI(7) = C2
0162          206 FORMAT (//,1X, "THE CHANNEL", //)
0163          ITYPE = 0
0164          X = IN02
0165          Y(1) = P00
0166          Y(2) = T00
0167          Y(3) = WFO
0168          Y(4) = ETIAS20
0169          A1F1 = DAQF11*E1
0170          A1F2 = DAQF12*E1
0171          A1E3 = DAREA*U*E2
0172          Y(5) = WFE1
0173          Y(6) = WFE2
0174          Y(7) = UFE3
0175          V = V0
0176          CALL LOAD (XOLD, UOLD, KOLD)
0177          J1 = .25
0178          J2 = -.05
0179          TFE = TCO
0180          PHJ = 5.
0181          JL = 1.
0182          IPRNT = C
0183          ICHAN = 3
0184          BPCONC = ((GAM-1.)/GAM)
0185

```

PORTMAN IV G1 RELEASE 2.0
 DATE = 78053
 20/41/49

```

      ICH=0
      REP1=0.98
      REP2=0.95
      TRANS=0.98-REP2
      CAVL=(X)/H(X)
      CAVG=(REP1+REP2)/(2.0*CAVL)
      POSPP=PO
      TOSPP=PO
      TOSPP=PO
      CALL DPRINT(X,Y,DX)
      CALL OUTPUT(X)
      ICHAN = 2
      LOUW = 1
      DYOUT=0.01
      XOUT = LN02+DX*OUT
      T2=T
      T3=T
      TCTDIS=0.0
      DISJUL=0.0
      CAVPCU=0.0
      CAV7AD=0.0
      TORPCG=0.0
      CPHP=290.0
      ISTEP=0
      C BPGIN INTEGRATION IN CHANNEL
      Do 7 IX = 1,IMAX
      IPRINT = 0
      P01D=DX
      T01L=0
      X01D = X
      X01D = KINP
      UCID = H
      A01D=DARFA
      J10L = J1
      XCUPD = XCUR
      YC01D = YCUR1
      C SELECTION OF STEP SIZE
      A DMAX = 0.
      DO 2 IT = 1,7
      IP (DABS(DV(II))/Y(II)).GT.DMAX) DMAX = DABS(DV(II))/Y(II)
      2 CONTINUE
      DX=.01/DMAX
      783 FOR * Y(1)/DX,1P8E15.5
      IP (DX.GT.DMAX) DX = DMAX
      IP (X+DX+1,D-06,LT,XOUT) GO TO 17
      IPRINT = 1
      IOUT = IOUT+1
      XOUT = LN02+IOUT*DX*OUT
      TOTDIS=TCTDIS+DISJUL+DX*DARE
      EP=HID=TOTALS/(PASS*CPHE*TOPP)
      IP (GAVN,LT,CAVGN) GO TO 291
      PPRS=(PO/PORP)**RPCONS
      POWOUT=TRANS2*CAVRAD*H(X)*DX
  
```

FORTRAN IV G1 RELEASE 2.0 MAIN DATE = 78053 20/41/49
 0237 TOTCH = TOTPOW+PO*OUT
 0238 PRCFC = (PO/PO*LD)**R*PCONS
 0239 EFF1,IC = POUT/((MASS*CPHE**TQOLD*(1.-PREDPC))
 0240 EFF2 = (C,02+TRANS2)/TRANS2*EFFLOC
 0241 EFFPTUR = TOTPOW/((MASS*CPHE*TOEP*(1.-PRERIS))
 0242 EFFPR = (C,02+TRANS2)/TRANS2*EFFPR
 0243 PWDFT=TCPOW/MASS
 291 CONTINUE
 0244 IF (IIP .LE. 0) GC TC 11
 0245 WRITE (NO,204) IER
 0246 STOP
 0247 C248 11 IF (IPNT .NE. 1) CALL OUTPUT(X)
 0249 IP (IPNT,NE,1) GO TO 790
 0250 IIPW=IIPW+1
 0251 12 IP (IRPW,LT,5) GO TO 790
 0252 ICH=ICH+1
 0253 OUTARI(ICW,1)=X
 0254 OUTARI(ICW,2)=NP
 0255 OUTARI(ICW,3)=TE
 0256 OUTARI(ICW,4)=T1
 0257 OUTARI(ICW,5)=T2
 0258 OUTARI(ICW,6)=T3
 0259 OUTARI(ICW,7)=T
 0260 OUTARI(ICW,8)=U
 0261 OUTARI(ICW,9)=P/101133.
 0262 OUTARI(ICW,10)=M
 C263 OUTARI(ICW,11)=BRTA
 0264 OUTARI2(ICW,1)=X
 0265 OUTARI2(ICW,2)=SPP
 0266 OUTARI2(ICW,3)=EPPL
 0267 OUTARI2(ICW,4)=PPOPT
 0268 OUTARI2(ICW,5)=EFFACC
 0269 OUTARI2(ICW,6)=EFFPUR
 0270 OUTARI2(ICW,7)=EFFMHD
 0271 OUTARI2(ICW,8)=EFFIOI
 0272 OUTARI2(ICW,9)=CARAD
 0273 OUTARI2(ICW,10)=TRANS2*CAVRAD
 0274 OUTARI2(ICW,11)=TOTPOW
 0275 IIPZ=0
 0276 13 IF (IPN=0)
 0277 WRITE (6,781) X, Y(1), DY(2), DY(3), DY(4), DY(5), DY(6), DY(7)
 0278 WRITE (6,793) DYNX, Y(1), Y(2), Y(3), Y(4), Y(5), Y(6), Y(7)
 0279 IF (A,GE,ICAV) ICAV=1
 0280 792 ISTEP=ISTEP+1
 0281 IF (A,GE,LNOZ+LCHAN) GO TO 3
 0282 7 CONTINUE
 0283 IX = IX-1
 0284 WRITE (NO,205) IX
 0285 STOP
 0286 3 WRITE (NO,202)
 0287 FORMAT ('//',1X,'END OF CHANNEL REACHED. NORMAL TERMINATION.')
 0288 WRITE (6,557)
 0289 DO 551 IAR1=1,10

```

PCNTN IV J1  PGLYNSP 2.0          FAINT          DATE = 78053      20/41/49
0291          551 WRITME (6,550) (CUTAR1(IAR1,IAR2),IAR2=1,11)
0291          WRITF (6,553)
0292          DN 552 IAR1=1,10
0292          552 WRITR (6,553) (OUTAR2(IAR1,IAR2),IAR2=1,11)
0293          550 FORMAT (//,1X,P6,2,1PD12.2,4X,0PF6.1,4X,P6,1,4X,
0294          $ P6,1,4X,P6,1,4X,P6,1,4X,P5,3,3X,P6,2,3X,P6,2)
0295          551 FORMAT (//,1X,P6,2,3X,P7,4,3X,P7,4,3X,P7,4,3X,P7,4,
0295          $ 3X,P7,4,3X,P7,4,3X,P7,4,1P3E12.2)
0296          557 FORMAT (1H,4X,X,8X,HE,9I,1T2,8X,T1,8X,T3),
0296          $ 9X,T,BX,9X,P,BX,1H,7X,BET1)
0297          558 FORMAT (1H,4X,X,6X,EPFP,6X,EPFL,5X,EPPT,4X,EPFLC,
0297          $ 4X,EPFTUR,4X,EPFHHD,4X,EPFTOT,5X,CAVRA1D,6X,
0297          $ 'ONTRAD',6X,'TOTPON')
0298          STOP
0299          END

```

PORTS4N IV G1 P5LFA5* 2.1 DEPIV DATE = 78053 20/41/49
 0001 SUBROUTINE DERIV(X,Y,DY)
 0002 IMPLICIT REAL*8 (A-H,O-Z)
 0003 EXTERNAL PCNS
 0004 REAL*8 K,M,IN07,LCHAN,MASS,M,KINP,KCONST,ME,NESTAR,
 \$ NEUA,NEUA1,LAMBDA,MUG,NUS,MU1,MU,LNRG,LRATE,LA8D1,J1,J2,J1,J1,
 \$ J101D,KOLD
 \$ REAL*4 MU1,MU2,MU3,MU2,NEUA2
 REAL*8 JMN,JMAX
 DIVISION YY(3),YY(3),ACC(3),GRAD(3,3),EE(3,3),AUX(3,4)
 DIMENSION Y(7),DY(7)
 0005 COMMON/COMSTS/ K,H1,P,M,P1,SACNST,EPSS0
 COMMON/GAS/ GAM,R1,WGNS,W,V1,PRTS
 COMMON/CHAN/ TH1,THE,LN02,LCHAN,MASS
 COMMON/DERIVS/ D1,C2,D3,D4
 COMMON/OLD/ KOLD,KOLD,JOOLD,XCUR1LD,AOLD
 COMMON/ALFLS/ X1,PO,P,T,V,M,DARE,NEUA,ME,NESTAR,
 \$ TE,TE1P,EPSS,PHI,ETASQ,ALPHA,1,DO,LAMBDA,CE,MUG,MUS,MU1,MU
 \$ DILTA,P,R5,BETA,REFAA,REFAA,REFAA,DCNST1,RCNST2,BETA1,
 \$ B7TA2,J1,J2,CONST,KINP,EL,Z0,ENGT,S,SIGA,SIGAV,SIGPP,
 \$ LKG,LRATE,G,STAR,LAMMEL,I,EL0SS,ECORR,ETAP,LOAD,
 \$ XCUR,CUP,YCUR1,DIPP
 COMMON/FLAGS/ TCHAN,IPRINT
 COMMON/DEVICE/ K1,NO
 COMMON/TFMS/T2,T3,THETA1,THETA2,THETA3,HP1,MPA2,MC02,NU2,NU3
 COMMON/LASER/TANCO2,NU01,M100,E12,E3,V12,E3,V12,TAU2ME,AUE12
 COMMON/WINFS/WHT22,WHT22,WHT32,WHT33,V12E3,V12E3,TAU2P,TAU1P
 COMMON/SIGNAL/CCURAT,WJ,WC,ZIN,ZUL,ZLL,GAIN
 COMMON/DIGS/DHDX,CHDX,CMX,DMX,DMX,JMAK,C2,PITCH,DV1,DV2
 COMMON/KNOB/TE1,TE2,TE3,TANK31,TAUR3C,RERRAT,TAU3RL,
 \$ DV3FEL,D5,D6,C1,DY50,DY60,DYMAX,CB21,CB22,CB23,
 \$ A1R,A2R,A3R,A4R,A5R,AGR,A7R,AGR,PRR,B2R,B3R,BUR,B5R,B6R,
 \$ P7R,P8R,P9R
 COMMON/JA3A/VTBT22,RTTEST
 COMMON/APRIL/IX
 COMMON/RELAY/T1,P1,E2,AUR1,AUR2,D7,VIBT11,VIBT12,VIBT2T,
 \$ DV2T,DV1T,DV12,TAUHE,TAUIC,D12F
 COMMON/JULY/CAVAD,CAV1,DG31,DG32,DG33,DG111,DG112,DG12,DG13,
 \$ DG3TOT,DG1TOT,ALPH1,ALPH2,BLPH1,BLPH2,AR12DU,AR12DU,NE12DA,
 \$ NE1DA,AR3DU,RE3DA,ALPH1P,ALPH2P,BLPH1P,BLPH2P
 COMMON/CNVTY/ICW
 COMMON/OSCILL/CAVAN,CAVPOH,DISJUL,CAVEPP,PODEN,TOTPON,
 \$ DV3E,PPFP,EPFP,EPFOPT,EPFMHD,EFPTOT,TOEFF,POEFF,
 \$ EPPTOT,EPPTER,TOTDIS,REP1,REP2,EPFLC,EPFL
 X1 = X
 P0 = Y(1)
 T0 = Y(2)
 NEUA = Y(3)
 ETASO = Y(4)
 AUR1Y(5)
 AUR2Y(6)
 AUR3Y(7)
 V1 = V
 C FIND V

```

PORTMAN IV G1  REFLPASE 2.0          DERIV          DATE = 78053   20/41/49
          CALBLAYER(X,DAREA)
          VCONST = (2.*GAM/((GAM-1.)*R1*T0)*(PG*DAREA/MASS)**2)**((GAM-1.)/
          $ (GAM+1.))
          DO 1 ICOUNT = 1,100
          V = VCONST*V1*((GAM+1.)/(GAM-1.))-1.
          IP (DARS(V-V1).LT.-0.002) GO TO 2
          1 V1 = V
          WRITE(NU,200)
200  FORMAT(//,1Y,*V PAIRS TO CONVERGE IN SUBROUTINE DPAIV.*,
          $ , PROGRAM TERMINATES.*)
          STOP
2  V = ESORT(2.*V/(GAM-1.))
          T = T0/(1.+V)
          P = P0/(1.+V)**(GAM/(GAM-1.))
          U = *DSQRT(GAM*R*T)
          TINV = (1./T)**(1./-3.)
          PATM = P/0.1133.

          C CHAIC SPLINE FIT FOR DEACTIVATION OF LOWER LASER
          LINV21, BY HF, SOURCE - NACRL
          TAU21H=.37D-07
          TAU21(.37D-07
          IP (TINV.GT.0.09), TAU21=1.37D-07*2.947D-06*(TINV-0.09)
          $ +2.105D-03*(TINV-0.09)**3
          IP (TINV.GT.0.095), TAU21=1.52D-07*3.105D-06*(TINV-0.095)
          $ +1.157D-05*(TINV-0.095)**2+5.477D-03*(TINV-0.095)**3
          IP (TINV.GT.0.1), TAU21H=1.69D-07*3.832D-06*(TINV-0.1)
          $ +1.137D-04*(TINV-0.1)**2-1.601D-02*(TINV-0.1)**3
          IP (TINV.GT.0.105), TAU21=1.99D-07*3.768D-06*(TINV-0.105)
          $ +1.265D-04*(TINV-0.105)**2+1.758D-02*(TINV-0.105)**3
          IP (TINV.GT.0.125), TAU21H=2.07D-07*3.896D-06*(TINV-0.11)
          $ +1.522D-04*(TINV-0.11)**2-3.4D-02*(TINV-0.11)**3
          IP (TINV.GT.0.115), TAU21H=2.26D-07*2.846D-06*(TINV-0.115)
          $ +3.623D-04*(TINV-0.115)**2+6.261D-02*(TINV-0.115)**3
          IP (TINV.GT.0.12), TAU21H=2.39D-07*3.919D-06*(TINV-0.12)
          $ +5.769D-04*(TINV-0.12)**2+5.615D-02*(TINV-0.12)**3
          IP (TINV.GT.0.125), TAU21H=2.66D-07*5.477D-06*(TINV-0.125)
          $ +2.654D-04*(TINV-0.125)**2-6.01D-03*(TINV-0.125)**3
          IP (TINV.GT.0.13), TAU21H=2.86D-07*2.373D-06*(TINV-0.13)
          $ +5.555D-04*(TINV-0.13)**2+6.419D-02*(TINV-0.13)**3
          IP (TINV.GT.0.135), TAU21H=2.97D-07*3.632D-06*(TINV-0.135)
          $ +6.074D-04*(TINV-0.135)**2-1.388D-01*(TINV-0.135)**3
          IP (TINV.GT.0.14), TAU21H=3.13D-07*7.009D-07*(TINV-0.14)
          $ +1.474D-03*(TINV-0.14)**2+0.168*(TINV-0.14)**3
          IP (TINV.GT.0.145), TAU21H=2.91D-07*4.28D-06*(TINV-0.145)
          $ +7.285D-04*(TINV-0.145)**2-4.857D-02*(TINV-0.145)**3
          C CHAIC SPLINE FIT FOR DPAIVATION RATE OF LOWER LASER
          LEVEL BY CO2; SOURCE - NACRL
          TAU2C=.13D-07
          IP (TINV.GT.0.09), TAU2C=6.13D-07*3.334D-05*(TINV-0.09)
          $ +8.227D-02*(TINV-0.09)**3
          IP (TINV.GT.0.095), TAU2C=7.90D-07*3.951D-05*(TINV-0.095)
          $ +1.234D-03*(TINV-0.095)**2+1.267D-02*(TINV-0.095)**3
          IP (TINV.GT.0.1), TAU2C=0.02D-06*5.28D-05*(TINV-0.1)
          $ +1.424D-03*(TINV-0.1)**2-2.37D-01*(TINV-0.1)**3

```

PORTMAN IV G1 RELEASE 2.0 DATE = 78053 20/41/49
 DERIV
 0070 IP (TINV.GT.0.105) TAU2C=1.29D-06*4.927D-05* (TINV-0.105)
 \$ 5 (TINV-0.105)*2.5.605D-01*(TINV-0.105)*3
 0071 IP (TINV.GT.0.11) TAU2C=1.63D-06*9.424D-05* (TINV-0.11)
 \$ +7.95D-03*(TINV-0.11)*2-1.004*(TINV-0.11)*3
 0072 IP (TINV.GT.0.115) TAU2C=2.03D-06*9.969D-05* (TINV-0.115)
 \$ -4.094D-03*(TINV-0.115)*2+5.91D-01*(TINV-0.115)*3
 0073 IP (TINV.GT.0.12) TAU2C=2.5D-06*1.031D-04* (TINV-0.12)
 \$ +4.772D-03*(TINV-0.12)*2+4.376D-01*(TINV-0.12)*3
 0074 IP (TINV.GT.0.125) TAU2C=3.08D-06*1.18D-04*(TINV-0.125)
 \$ -1.792D-03*(TINV-0.125)*2+5.194D-01*(TINV-0.125)*3
 0075 IP (TINV.GT.0.13) TAU2C=3.69D-06*1.39D-04*(TINV-0.13)
 \$ +4.998D-03*(TINV-0.13)*2+2.798D-01*(TINV-0.13)*3
 0076 IP (TINV.GT.0.135) TAU2C=4.5D-06*1.78D-04*(TINV-0.135)
 \$ +1.801D-03*(TINV-0.135)*2+2.8D-01*(TINV-0.135)*3
 0077 IP (TINV.GT.0.14) TAU2C=5.4D-06*1.75D-04*(TINV-0.14)
 \$ -2.4D-03*(TINV-0.14)*2+0.2*(TINV-0.14)*3
 0078 IP (TINV.GT.0.145) TAU2C=6.24D-06*1.66D-04*(TINV-0.145)
 \$ +6.0D-04*(TINV-0.145)*2-4.0D-02*(TINV-0.145)*3
 TAUH=TAU2H
 DEACPT=DATM*(TAU2C/TAU2C+ (1.-TAU2C-TS)/TAU2H)
 TAU2HE=1./DEACRT
 NC02=TAU2C**2/K/T
 C CALCULATE VIBRATIONAL TEMPERATURES
 F1=A1UP/(U*DAREA)
 F2=A1UE/(U*DAREA)
 E3=A1UP3/(U*DAREA)
 C NEWTON-RAPHSON ITERATION FOR T1
 INDEX=0
 350 INDEX= INDEX+1
 YAC=THETA1/T1
 YRC=DRP(YAC)
 YCC=YRC-1.0
 DELT1=-(H1*NU1/YCC*NC02
 DELT2=NC02/K*(H1*NU1/T1)**2*YBC/YCC**2
 ZTEST=DELT1/DELT2
 T1=T1+ZTEST
 AZTEST=ABS(ZTEST)
 IP (INDEX,GT.200) GO TO 351
 IP (AZTEST,GT. 1.0E-08) GO TO 350
 351 CONTINUE
 ENDPX=0
 300 INDEX=INDEX+1
 01C1 YAC=THETA2/T2
 YRC=DRP(YAC)
 YCC=YBC-1.0
 DELT1=-(H1*NU2/YCC*NC02
 DELT2=C*NC02/K*(H1*NU2/T2)**2*YBC/YCC**2
 T2=T2+ZTEST
 AZTEST=ABS(ZTEST)
 IP (INDEX,GT.200) GO TO 301
 IP (AZTEST,GT.1.0E-08) GO TO 300
 301 CONTINUE

FORTRAN IV G1 RELEASE 2.0 DERIV DATE = 78053 20/41/99

```

0112      INDEX=0
0113      400 INDEX=INDEX+1
0114      YACCC=THETAJJ/T)
0115      YACCC=DEXP(YACCC)
0116      YCCCC=YBCCCC-1.0
0117      DFLN1=F3-H1*NU3*YCCCC*NC02
0118      DFLN2=NC02/K*(H1*NU3/T3)**2*YBCCCC/YCCCC**2
0119      XTEST=CRIT/CELT2
0120      T3=F3*2*TRST
0121      ATST=DADS(2*TRST)
0122      IP (LINDFK,GT,200) GO TO 401
0123      IP (LATFST,GT,1.08-8) GO TO 400
0124      401 CONTINUEP
0125      SIGH=.1.7D-19
0126      SIGC(.2=1.3D-18
0127      GCONST=8.370.0
0128      COL=P/K*DSQRT(A.0*GCONST/(PI*T))
0129      CCL2=0.52*SIGH+.213*SIGCO2*TAUCO2
0130      COLRAT=CCL1*COL2
0131      ZA=DEXP(-YAC)
0132      ZAA=1.0-2A
0133      ZB=DEXP(-YACC)
0134      ZB1=-1.0-7B
0135      ZC=DIXN(-YACCC)
0136      ZC1=-1.-2C
0137      ZIL=NC02*AA*2AA*2RB**2*ZCC
0138      ZIL=NC02*ZC*ZAA*ZFB**2*ZCC
0139      WL=1.06D-05
0140      QT=.5,.38
0141      ZINZUL=ZUL
0142      QJ=5.6/TDEXP(-234.0/T)
0143      QC=YU**2/4.0*PI*YU*COLRAT)
0144      GATN=BC*ZLN*UJ
0145      V1R22=H1*W1/2*NC02/(DEXP(THTA2/T2)-1.0)
0146      V1R23=H1*W1/2*NC02/(DEXP(THTA2/T)-1.0)
0147      V1R24=H1*W1/2*NC02/(DEXP(THTA3/T)-1.0)
0148      C CUBIC SPLINE PT FCR DEACTIVATION RATE OF UPPER LASER
0149      C LEVPL BY CO2; SOURCE - UACRL
0150      TAU3C=6.13D-08
0151      IP (TINV,GT,0.09) TAU3C=6.13D-08*9.679D-06*(TINV-0.09)
0152      $ +8.243D-02*(TINV-0.09)**3
0153      IP (TINV,GT,0.095) TAU3C=1.2D-07*1.586D-05*(TINV-0.095)
0154      $ +1.23D-0.3*(TINV-0.095)**2*377D-02*(TINV-0.095)**3
0155      IP (TINV,GT,0.1) TAU3C=2.26D-07*2.569D-05*(TINV-0.1)
0156      IP (TINV,GT,0.11) TAU3C=2.26D-07*2.569D-05*(TINV-0.1)
0157      $ +7.3D-04*(TINV-0.1)**2*2.623D-02*(TINV-0.1)**3
0158      IP (TINV,GT,0.105) TAU3C=3.76D-07*3.49D-05*(TINV-0.105)
0159      $ +1.123D-0.3*(TINV-0.105)**2*6.686D-05*(TINV-0.105)**3
0160      S +1.28D-03*(TINV-0.11) TAU3C=5.8D-07*4.544D-01*(TINV-0.11)
0161      IP (TINV,GT,0.115) TAU3C=8.65D-07*7.1D-05*(TINV-0.115)
0162      $ +1.572D-0.3*(TINV-0.115)**2*2.343D-01*(TINV-0.115)**3
0163      IP (TINV,GT,0.12) TAU3C=1.28D-06*8.91D-05*(TINV-0.12)
0164      $ +5.661D-05*(TINV-0.12)**2*1.83D-01*(TINV-0.12)**3
  
```

PORTMAN IV G1 RELEASE 2.0 DERIV DATE = 78053 20/41/49

0156 IP (TINV.GT.0.125) TAU3C=1.75D-06+1.034D-01* (TINV-0.125)
\$ +2.802D-01* (TINV-0.125)**2-6.177D-01* (TINV-0.125)**3

0157 IP (TINV.GT.0.13) TAU3C=2.26D-06+8.512D-05* (TINV-0.13)
\$ -6.464D-01* (TINV-0.13)**2+8.088* (TINV-0.13)**3

0159 IP (TINV.GT.C=1.35) TAU3C=2.66D-06+1.021D-04* (TINV-0.135)
\$ +0.853D-01* (TINV-0.135)**2-1.333* (TINV-0.135)**3

0159 IP (TINV.GT.0.14) TAU3C=3.25D-06+1.066D-04* (TINV-0.14)
\$ -1.015D-02* (TINV-0.14)**2+4.856D-01* (TINV-0.14)**3

0160 IP (TINV.GT.0.145) TAU3C=3.56D-06+3.554D-05* (TINV-0.145)
\$ -2.863D-03* (TINV-0.145)**2+1.909D-01* (TINV-0.145)**3

C CUBRIC SPLINE FIT FOR DEACTIVATION RATE OF UPPER LASER
LFBEL BY HE; SOURCE = HACR

0161 TAU3H=1.04D-07
0162 IP (TINV.GT.-0.09) TAU3H=1.04D-07+1.769D-05* (TINV-0.09)
\$ +1.403D-01* (TINV-0.09)**3

0163 IP (TINV.GT.-0.095) TAU3H=2.1D-07+2.822D-05* (TINV-0.095)
\$ +2.105D-03* (TINV-0.095)**2+5.832D-02* (TINV-0.095)**3

0164 IP (TINV.GT.0.1) TAU3H=4.11D-07+4.11D-07+2.822D-05* (TINV-0.1)
\$ +2.98D-03* (TINV-0.1)**2+2.904D-01* (TINV-0.1)**3

0165 IP (TINV.GT.0.105) TAU3H=7.9D-07+1.052D-04* (TINV-0.105)
\$ +7.336D-03* (TINV-0.105)**2-3.15D-01* (TINV-0.105)**3

0166 IP (TINV.GT.0.11) TAU3H=1.46D-06+1.549D-04* (TINV-0.11)
\$ +2.598D-01* (TINV-0.11)**2+7.251D-01* (TINV-0.11)**3

0167 IP (TINV.GT.0.115) TAU3H=2.39D-06+2.352D-04* (TINV-0.115)
\$ +1.347D-02* (TINV-0.115)**2+2.458D-02* (TINV-0.115)**3

0168 IP (TINV.GT.0.12) TAU3H=3.40D-06+3.681D-04* (TINV-0.12)
\$ +1.311D-02* (TINV-0.12)**2-1.267* (TINV-0.12)**3

0169 IP (TINV.GT.0.12) TAU3H=5.91D-06+4.042D-04* (TINV-0.125)
\$ -5.896D-01* (TINV-0.125)**2+2.052* (TINV-0.125)**3

0170 IP (TINV.GT.0.13) TAU3H=8.04D-06+4.991D-04* (TINV-0.13)
\$ +2.488D-02* (TINV-0.13)**2+2.86* (TINV-0.13)**3

0171 IP (TINV.GT.0.135) TAU3H=1.08D-05+5.334D-04* (TINV-0.135)
\$ -1.802D-02* (TINV-0.135)**2+1.466* (TINV-0.135)**3

0172 IP (TINV.GT.0.14) TAU3H=1.32D-04+4.631D-04* (TINV-0.14)
\$ +4.006D-03* (TINV-0.14)**2+9.338D-01* (TINV-0.14)**3

0173 IP (TINV.GT.0.145) TAU3H=1.55D-05+4.333D-04* (TINV-0.145)
\$ -0.01* (TINV-0.145)**2+0.6668* (TINV-0.145)**3

0174 TANK3H=TAU3H

0175 TANK3C=TAU3C

0176 PEPAT=PAUT* (TAUCO2/TANK3C* (1.-TAUCO2-TS)/TAUK3H)

0177 TAU1P=1./PFLAT
PAUT1H=PAUT* (1.-TAUCO2-TS)*TAUK1H

C NOTE 1. RELAXATION RATES; SOURCE-MURRAY, MITCHNER, AND KRUGER
WITH STARK MOMENTUM CORRECTION

0178 TANK1H=4.772D04

0179 TANK1C=8.837D06

0180 PAUT1H=PAUT* (1.-TAUCO2-TS)*TAUK1C

0181 PAUT1C=PAUT*TAUCO2*TAUK1C

0182 PAUT1C=1.0/RATIC

0183 VFLT32=H1*NU3*NC02/(DEXP (THETA3/T2)-1.)

0184 VFLT11=H1*NU1*NC02/(DEXP (THETA1/T1)-1.0)

0185 VFLT12=H1*NU1*NC02/(DEXP (THETA2/T2)-1.0)

0186 VFLT2T=H1*NU2*NC02/(DEXP (THETA2/T)-1.0)

0187

PORTION IV G1 RELFASV 2.0 CERTV DATE = 78053 20/41/49
 0188 DV2T=DAPFA/TAU2HE*(VIBT22-VIBT1)
 0189 DV1T=DAPFA/TAU1HE*(VIBT11-VIBT12)
 0190 DV12=DAPFA/TAU1C*(VIBT11-VIBT12)
 0191 DV139 FL=DAREA/TAU3RL*(VIBT33-VIBT32)
 0192 RHO(GAS)=P/(K*T)
 0193 CPHE=528C.0
 0194 IP (LICHAN.GT.1) GO TO 3
 0195 D1 = -V/(P*U*(1.+V))*POWER(X)*Y(1)
 0196 D2 = (GAH-1.)*POWER(X)/(GAM*P*(1.+V))*Y(2)
 0197 D2=D2+DV2T/(DAREA*PHOGAS*CPHE*U)
 C198 C199
 0200 D4 = 0.
 0201 IP (IX.GT.1) GO TO 500
 DV1T=0.
 DV2T=0.
 DV12=0.
 DV139 FL=0.
 509 D6=-DV3T+DV3REL+DV12
 F7=-DV3RFL
 E5=-DV1T-DV12
 DV(1)=D1
 DV(2)=D2
 DV(3)=D3
 DV(4)=D4
 DV(5)=D5
 DV(6)=D6
 DV(7)=D7
 F5TEN
 3 KF = NPHA/(U*DAREA)
 ALPHA = NE*KT/(TS*P)
 12 N1M=3
 4 Q1M1=4
 C DPC*EASING *SCALE* FOR A VARIABLE CAUSES THAT VARIABLE TO CHANGE:
 C LESS WHEN POLINING A FUNCTION GRADIENT
 SCALF1 = 1.
 SCALF2 = 10.
 SCALE3 = .1
 CALL LOAD(X, KINP)
 PW = KINP*(1.+R(X))
 EVCYC = KOLD*HOLD*(XOLD)
 IP (EVCYC, FO, 0.) GC TO 9
 IP (EYXYOLD, LE, 0.) GO TO 9
 ELYDX = DLOG(EY/EYOLD)/(X-XOLD)
 D1PP = KINP/(1.-KINP)*H(1)/2.*EYDX
 GO TO 11
 a D1PP = 0.
 11 KV(1) = J2/SCALE1
 IP (E1PP, LT, -0.01) XX(1) = J1/SCALE1
 XX(2) = TE/SCALE2
 XX(3) = PHI/SCALE3
 X10 = XX(1)
 X20 = XX(2)
 X30 = XX(3)

PORTION IV G1 REFLPSS 2.^a DERIV DATE = 78053 20/41/79

```

0282 KCORR = -1.0-0.0
0283 GO TO 8
0284 7 KCORP = 1.
0285 GO TO 8
0286 KCORP = 1.+PLOSS/(CUR*U*R(X))
0287 8 I = -CNRB(X)*LCHAN/(1.+*(1.-KCORR))/(1.+V)
0288 *TAP = KCOPR/(1.+V*(1.-KCORR))
0289 IF (GAIN LE. CAVGAN) ICAV=0
0290 IF (GAIN GT. CAVGAN) ICAV=1
0291 DV2=DARE/TAUZ*(VITTE2-VITR22)
0292 DV3=DARE/TAU3*(VITTE3-VITR33)
0293 CISHL=(SCTR*2*YCHR*2)/SIGPPP
0294 PFP=DV3*E/DARE/DISJUL
0295 PFP=R*PFP ((1.-DEXP (-THETA1/T1)) * (1.-DEXP (-THETA2/T2)) * 2)
0296 PFP=DV2*E/DARE/DISJUL
0297 1 P (ICAV,ME,1) GO TO 747
0298 PFP=R*PFP ((1.-DEXP (-THETA3/T3)) * (1.-DEXP (-THETA4/T4)) * (1.-DEXP (YACCC)) / (DEXP (YACCC) - 1.0)
0299 DG3=E3*THPTA3*T3**2*DEXP (YACCC)
0300 DG3=W*YJ
0301 DG3=MC0*2*D3EXP (-YACCC)*ZAA*2*BR**2*THETA3/T3**2
$ (1.-G-2.-0*DEXP (-YACCC))
0302 DG111=R*THTA1/T1**2*DEXP (YAC) / (D2EXP (YAC) - 1.0)
0303 DG12=+DG32
0304 DG13=MC0*2*D3EXP (-YAC)*ZBB**2*ZCC*THETA1/T1**2*
$ (1.-C-2.-0*DEXP (-YAC))
0305 ALPH1=-DV1-T-DV12
0306 ALPH2=-1.0 / (2.0*CAV1)*DLOG (REP1*REP2)*NU1/(NU3-NU1)
0307 ALPH2=ALPH2*DAREA
0308 BLPH1=(VITTE3-VITR33)*DAREA/TAU35-DV3REL
0309 ALPH2=1.0/(2.0*CAV1)*DLOG (REP1*REP2)*NU3/(NU3-NU1)
0310 BLPH2=BLPH2*DAREA
0311 ALPH1P=(ALPH1-A1DU-(E1D4))/(U*DAREA)
0312 ALPH2P=ALPH2/(U*DARE2)
0313 ALPH1P=(ALPH1-A1DU-(E1D4))/(U*DAREA)
0314 ALPH2P=ALPH2/(U*DARE2)
0315 U210=U*E1*(DAREA-AOLD)/(X-XOLD)
0316 U210=U*E1*(DAREA-AOLD)/(X-XOLD)
0317 ALPH1P=(ALPH1-A1DU-(E1D4))/(U*DAREA)
0318 BLPH1P=BLPH1/(U*DAREA)
0319 DG310T=DG32*DG31/DG31
0320 CAVAD=- (BLPH1P*DG31TOT+ALPH1P*DGTOR)
0321 $ / (BLPH2P*DGTOT+ALPH2P*DG110T)
0322 CAVDOW=CARAD-CAVGAN
0323 CAVFEP=CAPOV/DISJUL
0324 EPFOPT=CAFFP
0325 FPPOPT="PPMHDF*EPFOPT
0326 747 CONTINUE
0327 D1 = -1/ICHAN*V(1)
0328 D2 = -(GAM-1.)/(LCHAN*GAM)*ETAP*1*V(2)
0329 D2=D2+DV2T/(DAREA*RHOGS*CPEH*U)
0330 D3=FUA1
0331 D4 = XI/LNRS*(G*GSTAR*(1.-(ME/NESTAR)**2))/(1.+GSTAR/LANBD)) * V(4)
  
```

FORTRAN IV G1 RELEASE 2.0 DERIV DATE = 78053 20/41/49
 0312 D5=D11-D12
 0333 D6=D12-D13+D14REL+D12+DV17
 0334 D7=D12-D13+D14REL+D12+DV17
 0335 IP (1CAV EQ. 1) GO TO 750
 0336 GO TO 748
 0337 750 P5=D5+NU1/(NU3-NU1)*CAVRAD*DAREA*CAVGN
 0338 D7=D7-NU3/(NU3-NU1)*CAVRAD*DAREA*CAVGN
 748 CONTINUE
 0339
 0340
 0341 DY(1)=D1
 0342 DY(2)=D2
 0343 DY(3)=D3
 0344 DY(4)=D4
 0345 DY(5)=D5
 0346 DY(6)=D6
 0347 DY(7)=D7
 RETURN
 END
 0348

AD-A068 190

MASSACHUSETTS INST OF TECH CAMBRIDGE GAS TURBINE AND--ETC F/G 20/5
FUNDAMENTAL MECHANISMS OF NONEQUILIBRIUM MHD LASING PHENOMENA. (U)
DEC 78 J L KERREBROCK

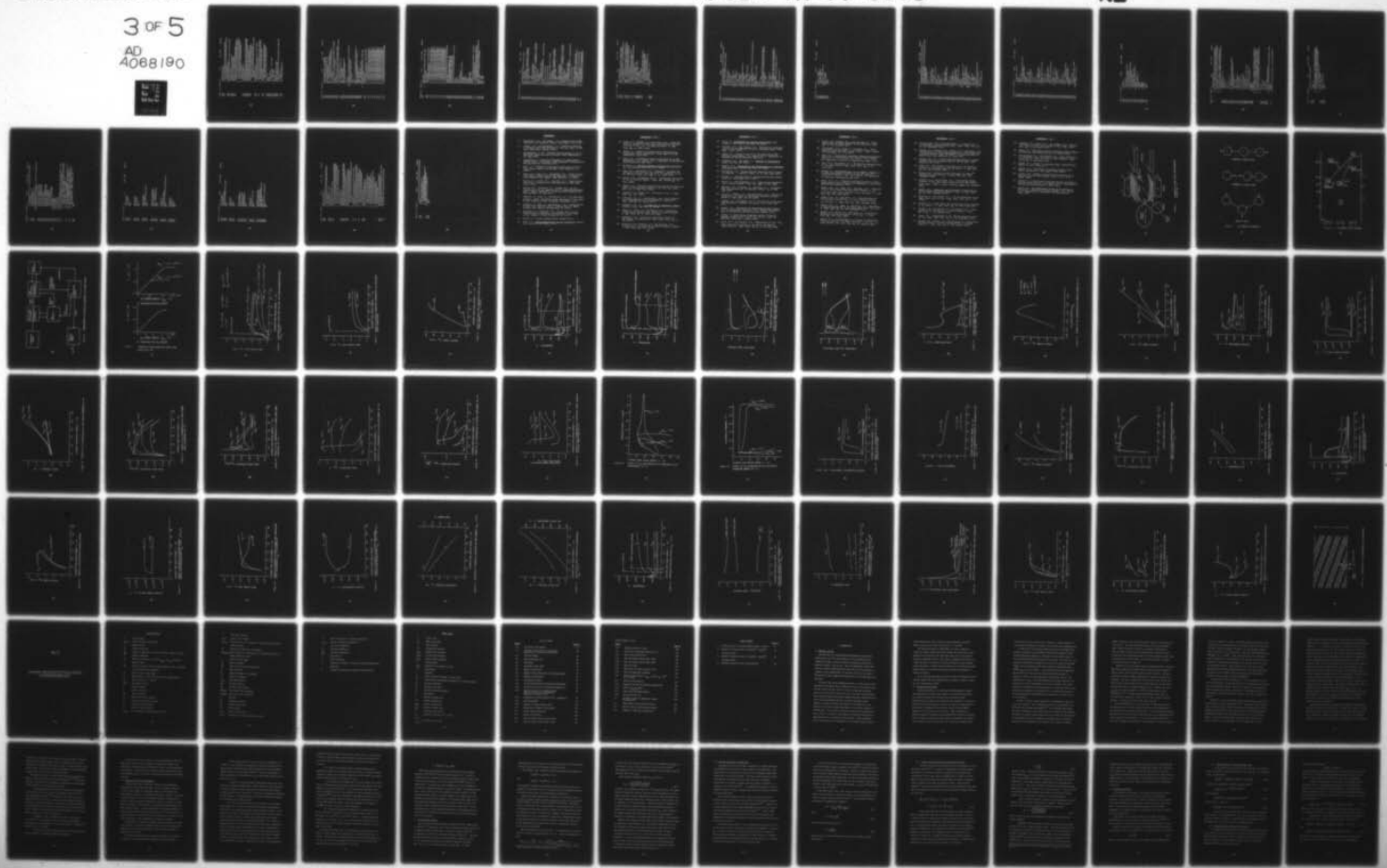
F44620-76-C-0067

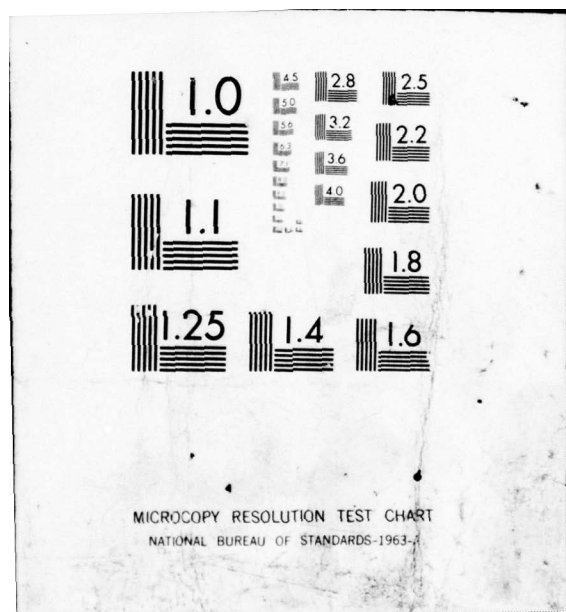
UNCLASSIFIED

3 OF 5
AD
A068190

AFOSR-TR-79-0506

NL





POSTPAN IV G1 RELEASE 2.0 PCNS DATE = 78053 20/41/69

```

0001      SUBROUTINE PCNS(XX,YY)
0002      IMPLICIT REAL*8(A-H,O-Z)
0003      REAL*8 K,MR,LNO,LCHAN,MASS,M,KINP,KCORR,KCONST,ME,NESTAR,
0004      MFLUA,NUFLA,LAMDA,NG,NUS,NUL,NU,LNG,LRATE,LARBD1,J1,J2,J3,J4,
0005      KOLD,JOLD,JFLX,JFLW
0006      REAL*8 NU,NU2,NU3,NUC02,NUH2
0007      DIMENSION XY(3),YY(3),ACC(3),GRAD(3,3),EE(3,3),AUX(3,3)
0008      DIMENSION Y(7),DY(7)
0009      COMMON/CCSTS/K,H1,E,M,E,P,L,S,A,C,H,ST,EP50
0010      COMMON/GRS/GAN,R1,G,WS,W,PR,TS
0011      COMMON/CHAN/TII,THE,AN02,LCIAN,IAS
0012      COMMON/OLD/OLD,OLD,J1OLD,XCURLD,YCR1LD,AOLD
0013      COMMON/ALELS/X,DO,P,T,V,N,DARTA,NUA,NEUA,1,NE,NESTAR,
0014      S,TF,TRIP,EP5,PHI,ETASO,ALPHA,I,DO,LAMBDA,CE,NG,MUS,NU1,NU2,
0015      S,DELTA1,RS,BETA1,BETA,RETA,BETA1,BCHST1,BCHST2,BETA1,
0016      S,BETA2,J1,J2,KCONST,KINP,J1,20,TNGNT,S,SIGA,SIGV,SIGEP,
0017      S,LHGR,1BATE,G,GSAR,LAMBDA,I,BLOSS,KCOPR,ETAP,RELOAD,
0018      S,YCHR,YCHR,YCHR1,DIPP
0019      COMMON/PLGS/ LCHAN,IPRTN
0020      COMMON/DEVIC/MT,NO
0021      COMMON/TPPS/T2,T3,THETA1,THETA2,THETA3,HPL,NEUA2,NUC02,NU2,NU3
0022      COMMON/LASER/TAUCO2,NU01,N00,F12,F3,NU01,AUE3,VIBT,TAU2H,AU812
0023      COMMON/VIBPS/VIBT2,VIBT2,VIBT3,VIBT3,TAU2E,TAU2E
0024      COMMON/SIGNAL/COLRAT,WJ,WC,7IN,2UL,2LL,GAIN
0025      COMMON/DIG/DHDY,CHM,CMIN,CMAX,JMIN,JMAX,C,PITCH,DV1,DV2
0026      COMMON/CLK/RWTR/TEA1,TEA2,TEA3,TANK3H,TANK3L,RELAT,TAU3L,
0027      S,DY3REL,D5,D6,C1,DY50,DY60,DYMAX,CB21,CB22,CB23,
0028      S,AIR,12R,A3R,4R,5R,AGR,A7R,8R,AGR,1R,B2R,B3R,B5R,B6R,
0029      S,B7R,B8R,B9R
0030      COMMON/JAN/VIBT32,VIBTEST
0031      COMMON/RELAX/T,PR,PA,PR1,PR2,D7,VIBT11,VIBT12,VIBT27,
0032      S,DV2T,DV12,TAU1E,TAU1C,DV2E
0033      S,DG3MOT,DG1TOT,ALPH1,ALPH12,BLPH1,BLPH2,ALPH12U,ALPH2U,AE1DU,UE12DA,
0034      S,UE1DA,UE2DU,UE3DU,ALPH1D,ALPH2D,BLPH1P,BLPH2P
0035      COMMON/CAVITY/ICAV
0036      COMMON/OCTILL/CAYGAN,CAYPON,CAYPON,DISJUL,CAYPP,PODEN,TORPON,
0037      S,EPPTBR,EPPTFR,TOTDIS,REP1,REP2,EPPLOC,EPPLAL
0038      SCALE1 = 1.
0039      SCALE2 = 10.
0040      SCALE3 = 1.
0041      IP = (DIFF,LT,--,06) J1 = xx(1)*SCALE1
0042      IP = XY(2)*SCALE2
0043      PHI = XY(3)*SCALE3
0044      TEO = TE
0045      IP = (TE,LT,1,05*7) 1E = 1.05*T
0046      IP = (TE,GT,1,0000,) TE = 10000,
0047      NESTAR = DSORT(P/(K*T)*TS*(1.-ALPHA)*SICNST*TE**1.5*DEXP(-P*TE),
0048      S,(K*TE))
0049      XI = P*V1/(K*T) + 1.5
0050      DN = Ee2/(12.*P*EPS0*K*TE)

```

```

PORTMAN IV G1 RELPASR 2.0          PCNS          DATA = 78053          20/41/49
0038          IP (EPS0*K*TE/ME .LE. 0.)  CALL OUTPUT(M)
0039          IP (K*T/(P1*ME) .LE. 0.)  CALL OUTPUT(R)
0040          LAMMADA = DSORT(EPS0* K*TE/(P1**2*ME))/D0
0041          CR = DSQRT(6.*K*TE/(P1*ME))
0042          NIG = 3.*PI/8.*CEP*(1.-TS)/(K*T)*CG(TE)
0043          NIS = 3.*PI/8.*CEP*TS(1.-ALPHA)/(K*T)*GS(TE)
0044          NUT = 1./.58*CF*ME*9.*PI**2/16.*D0**2*DLOG(LAMBDA)
0045          NI = NIG+NUS*NU
0046          DPLTA = 2.*NU*NU* (4./3.*86./ (3.*PI)*(NIG/ME+NUS/ME)+1.97*NU/ME)
0047          R = NUT/NU* (1.-1./ (2.*DLOG(LAMBDA)))
0048          RTPST=R
0049          RS = (NIG+NUS-3.*NU)*(12.-ALPHA)/ ((1.-ALPHA)* (11.-NU))
0050          BFTAC = DSORT( (1.+(2.-ALPHA)/(1.-ALPHA)*(1.-TE-T)/(TE-T))/ (2.*NU))
*   **2-(1.-RS)* **2)
0051          PNS = DSORT( (1.-RS)* **2* BETAC* **2) - 1.
0052          SIGMA = P**2*ME/ (ME*NU)
0053          BFTAN = P**2*B(1.)/(ME*NU)
0054          BFTAV = BFTAN* (1.-RS*PHI)/(RS*PHI)* **2)
0055          IP (BETAV.GT.BETAC) GO TO 501
0056          S=1.
0057          GO TO 502
0058          S=DSORT( (1.-R-RS)* **2*BFTAC* **2)/ ((1.-R-RS)* **2*BETAV* **2)
0059          S02 = (PFTAV* **2*(1.-RS*PHI)* **2)*ETAS0
0060          IP (DABS(BFTAV) .GT. 1.D-06) GO TO 1
0061          TNGNT = -2.006
0062          S = 1.
0063          GO TO 2
0064          1 TNGT = -(1.-R-RS)/BETAV-DSQRT( (1.-R-RS)/BETAV)* **2+1.)
0065          2 SIGAV = SIGN(1.-P*RS*PHI)*(R+RS*PHI-1.)
0066          BFTAF=BETAV*S*TNGT*(1.-S)
0067          SIGFPP = SIGAV*S
0068          PITCH = (THITHE)/H(X)
0069          DHDX = 100.*H(X+.005)-H(X-.005)
0070          C CUBIC SPLINE PTF FOR EXCITATION RATE OF UPPER LASER
0071          LEVEL, RY, ELECTRONS
          TAUH=2.49D-16*1.136D-18* (TE-1000.)
0072          IP (TE.GT.1000.) TAUH=2.49D-16*1.136D-18* (TE-1000.)
*   +2.346D-25* (TE-1000.) **3
0073          IP (TE.GT.1500.) TAUH=R 59D-16*1.397D-18* (TE-1500.)
*   +5.02D-22* (TE-1500.) **2-3.852D-25* (TE-1500.) **3
0074          IP (TE.GT.2000.) TAUH=1.63D-15*1.6D-18* (TE-2000.)
*   -7.584D-23* (TE-2000.) **2-3.298D-25* (TE-2000.) **3
0075          IP (TE.GT.2500.) TAUH=2.37D-15*1.277D-18* (TE-2500.)
*   -5.706D-22* (TE-2500.) **2+3.526D-25* (TE-2500.) **3
0076          IP (TE.GT.3000.) TAUH=2.91D-15*9.71D-19* (TE-3000.)
*   -4.175D-23* (TE-3000.) **2+4.042D-26* (TE-3000.) **3
0077          IP (TE.GT.3500.) TAUH=3.18D-15*8.98D-19* (TE-3500.)
*   -1.024D-22* (TE-3500.) **2+8.913D-26* (TE-3500.) **3
0078          IP (TE.GT.4000.) TAUH=3.81D-15*8.33D-19* (TE-4000.)
*   -2.87D-21* (TE-4000.) **2-2.361D-25* (TE-4000.) **3
0079          IP (TE.GT.4500.) TAUH=4.19D-15*6.276D-19* (TE-4500.)
*   -1.828D-22* (TE-4500.) **2+2.552D-25* (TE-4500.) **3
          RAY=R2*TAHU+DEXP(H1*NU3)/(K*T2)*(1.-DEXP(-H1*NU3/(K*T2)))

```

PORTMAN IV G1 RPLPASP 2.0 PCNS DATE = 76053 20/41/49
 0086 C CUBRIC SPLINE FIT FOR EXCITATION RATE OF LOWER LASER
 C LEVEL IN ELECTRIC
 TAUL=1, 16D-15
 IP (TE,GT,1000.) TAUL=1, 16D-15+1, 136D-18* (TE-1000.)
 S +3, 346D-25* (TE-1000.) *+3
 IP (TE,GT,1500.) TAUL=0, 08D-15+1, 971D-18* (TE-1500.)
 S +1, 923D-22* (TE-1500.) *+2-1, 388D-24* (TE-1500.) *+3
 IP (TE,GT,2000.) TAUL=0, 99D-15+1, 322D-18* (TE-2000.)
 S -1, 669D-21* (TE-2000.) *+2-8, 891D-25* (TE-2000.) *+3
 IP (TE,GT,2500.) TAUL=5, 34D-15+1, 09-19* (TE-2500.)
 S +1, 555D-22* (TE-2500.) *+2-3, 111D-25* (TE-2500.) *+3
 IP (TE,GT,3000.) TAUL=0, 44D-15+1, 779D-19* (TE-3000.)
 S +1, 113D-22* (TE-3000.) *+2-2, 141D-25* (TE-3000.) *+3
 IP (TE,GT,3500.) TAUL=5, 53D-15+1, 246D-19* (TE-3500.)
 S -2, 096D-22* (TE-3500.) *+2-2, 252D-25* (TE-3500.) *+3
 IP (TE,GT,4000.) TAUL=5, 57D-15+8, 768D-20* (TE-4000.)
 S +1, 280D-22* (TE-4000.) *+2-2, 066D-25* (TE-4000.) *+3
 IP (TE,GT,4500.) TAUL=6, 62D-15+6, 966D-20* (TE-4500.)
 S +1, 82D-22* (TE-4500.) *+2-1, 213D-25* (TE-4500.) *+3
 PA2= W*TAUL*DEXP (H1*NU2/(K*TE)) * (1.-DEXP (H1*NU2/(K*TE)))
 TA12E=1, /RA2
 V1PT2=H1*NU2*NUCO2/(DPP*(THETA2/TE))-1.0
 V1TE3=H1*NU3*NUCO2/(DPP*(THETA3/TE))-1.0
 A21=DEXP (THETA2/TE) * (1.-DEXP (-THETA2/TE))
 A31=DEXP (THETA3/TE) * (1.-DEXP (-THETA3/TE))
 C821=(TP/T-1.)/(2.*GAM/(3.*DETA) * (DETA*H*(1.-KINP)) *+2)
 A58=F
 A67=R(X)
 A73=R(TA)
 A8P=U
 A9P=1.-KINP
 A1P=(U*(1.-KINP)) *+2
 A2P=FB*(1.-DETA)*(H*(1.-KINP)) *+2
 A3P=V1*TP2
 A4P=V1*TP22
 P1P=V1*TP3
 R2R=V1*TP33
 P3P=TP10L
 B4P=TP10H
 R5P=V1*TE2-V1*WT22
 S6P=V1*TE3-V1*BT33
 B7P=RCO?
 CR22=(V1*BT22-V1*TP22)*TAUL/(DETA*(H*(1.-KINP)) *+2)
 S *(1.-DEXP (-THETA3/TE)) *+2
 CR23=(V1*TP23-V1*TP33)*TP20*(H*(1.-DETA)*(H*(1.-KINP)) *+2)
 ACNST1=(1.-DEXP (-THETA3/TE)) *+2-131
 BCNST2=(1.-DETA*DDX2/2)*DSQR((CB2+CB23)/(1.+25*DDX2/2))
 SLOPP = 1.017
 DISP = .045
 JMIN = -1000.
 JMAX = 1000.
 0087
 0088
 0089
 0090
 0091
 0092
 0093
 0094
 0095
 0096
 0097
 0098
 0099
 0100
 0101
 0102
 0103
 0104
 0105
 0106
 0107
 0108
 0109
 0110
 0111
 0112
 0113
 0114
 0115
 0116
 0117
 0118
 0119
 0120

```

0121      IP (EIPP,LT,-.06) GO TO 3
0122      BETA2 = BCNST2*(-J2-.5)/DSORT (J2**2+J2+.333333)
0123      FFTA4 = FFTA2*DIPP
0124      RETA1 = FFTA1**2*DIPP
0125      KCONST = SIGEPP*(BETA1)*(1.+BETA1*BETA1)/(1.+BETA1*BETA1)
0126      XCUR = -KCONST*(1.-KINP)/(BETA1-BETA1)/(1.+BETA1*BETA1)
0127      YCUR = -YCUR*(1.-KINP)
0128      YCUR1 = YCUR
0129      YCUR2 = (BCNST1+2.*DIPP)/BCNST2
0130      CMIN = (BCNST1+2.*DIPP-BCNST1)/BCNST2
0131      CMAX = (2.*DIPP-BCNST1)/BCNST2
0132      IP (DARS(CMIN).LT.1.) JMIN = -.5-CHIN/DSORT (12.*(1.-CHIN**2))
0133      IP (DARS(CMAX).LT.1.) JMAX = -.5-CHIN/DSORT (12.*(1.-CHIN**2))
0134      IP (J2.LT.JMIN) GO TO 5
0135      IP (J2.GT.JMAX) GO TO 6
0136      C1 = RETA1/BCNST1
0137      J1 = -.5-C1/DSORT (12.*(1.-C1**2))
0138      YY(1) = XCUR/PITCH-J1*YCUR1-J2*YCUR2
0139      IP (YY(1).LT.-SLOPE*DISP2/JMIN) YY(1) = -SLOPE*DISP2/JMIN
0140      GO TO 12
0141      5 YY(1) = SLOPE*(J2-JMIN-DISP)
0142      GO TO 12
0143      6 YY(1) = SLOPE*(J2-JMAX+DISP)
0144      GO TO 12
0145      3 BETA1 = BCNST1*(-J1+.5)/DSORT (J1**2-J1+.333333)
0146      RETA1 = RETA1*DIPP
0147      BETA2 = BETA1**2*DIPP
0148      KCONST = SIGEPP*(BETA1)*(1.+BETA1*BETA1)/(1.+BETA1*BETA1)
0149      XCUR = -KCONST*(1.-KINP)/(BETA1-BETA1)/(1.+BETA1*BETA1)
0150      YCUR = -KCONST*(1.-KINP)
0151      YCUR1 = YCUR
0152      YCUR2 = (BCNST2-2.*DIPP)/BCNST1
0153      CMIN = (BCNST2-2.*DIPP-BCNST1)/BCNST1
0154      CMAX = (-BCNST2-2.*DIPP)/BCNST1
0155      IP (DARS(CMIN).LT.1.) JMIN = -.5-CHIN/DSORT (12.*(1.-CHIN**2))
0156      IP (DARS(CMAX).LT.1.) JMAX = -.5-CHIN/DSORT (12.*(1.-CHIN**2))
0157      IP (J1.LT.JMIN) GO TO 7
0158      IP (J1.GT.JMAX) GO TO 8
0159      C2 = RETA2/BCNST2
0160      J2 = -.5-C2/DSORT (12.*(1.-C2**2))
0161      YY(1) = XCUR/PITCH-J1*YCUR1-J2*YCUR2
0162      IP (YY(1).LT.-SLOPE*DISP1/JMIN) YY(1) = -SLOPE*DISP1/JMIN
0163      GO TO 12
0164      7 YY(1) = SLOPE*(J1-JMIN-DISP)
0165      GO TO 12
0166      8 YY(1) = SLOPE*(J1-JMIN+DISP)
0167      12 TENDP=2.*GAY(3.*DULTA**2/(1.+BPS*PHI*HTAS0)
0168      S / (1.+RETB**2))
0169      TPA2=TPMP*(V1BT22-V1BT22)/(V0**2*PHI*HTAS0)
0170      S * (1.-DEEP(-THETA3*/V1))
0171      S * (1.-DEEP(-THETA3*/V1))
0172      S * (1.-DEAP(-THETA1/V1)) * (1.-DEAP(-THETA2/V2))**2

```

FORTRAN IV 31 RELEASE 2.0 PCNS DATE = 78053 20/41/49

```

0171      TPNP=TEA1-TEA2-TEA3
0172      LNPQ = U*XI**2/(3.*V*U*DELTA*NU*(1.+EPS*PHI*ETASO))
0173      LRATF = U/(RATE(TP)*NPSTAR**2*(1.+PHI*(PHI+2.)*ETASO))
0174      G = (TE1*RF-T)/(TE-T)*S*DSORT((1.-K-R5)**2*BEТАV**2)-DSORT((1.-
$ 9-R5)**2*BEТАC**2)
0175      GSTAR = (TE1*RF-T)/(TE-T)*S*DSORT((1.-R5)**2*BEТАV**2)-G
0176      LAMBDI = 4./A1*LNRC/LRATF*(1.-ETASO)/(1.+PHI*(PHI+2.)*ETASO)
0177      PHINEW = (G+GSTAR+LAMBDI)*(NE/NESTAR)**2/(GSTAR+LAMBDI)
0178      NEU1 = NEU1/LRATF*(1.-NE/NESTAR)**2*(1.-3.*ETASO)/(1.+
$ PHI*(PHI+.)*ETASO)
0179      NEU12=NUA1*VIBTP2*VIBTP2*DAREA/(K*TE*XI*TAU22)
0180      $ +(VIBTP3-VIBTP3)*DATER/(K*TE*XI*TAU3E)
0181      TENVW = TE1NP/(1.+NEU1/(1.+DELTA/(2.*XI)*NU*NE*NU*DARE
$ *(1.+EPS*PHI*ETASO)))
0182      IP (TENVW,LT,0.) TENVW = 1.806
0183      IP (TE0,LT,1.05*T) TENVW = 1.5*T
0184      IP (TE0,GT,10000.) TENVW = 1.5*T
0185      YY(2) = TE-TENVW
0186      YY(3) = PHI-NU NEW
0187      IP (IPNNT,NU,2) RETURN
0188      WRTF (NO,200) BETA1,TE PHI,NESTAR,NU,DELTA,RS,RS,
$ 2PS,RETAC,BETA1,BETA2,BETA2,J1,
$ J2,SIGMA,SIGEFF,TE1NU,LNRC, RATE,G,GSTAR,
$ YY(1),YY(2),YY(3),T1,T2,T3,E1,E2,
$ P1,NEU1,TEA1,TEA2,TEA3,KCONST,ACUR,YCUR,
$ VIBTP2,VIBTP3
0189      200 FORMAT(1X,10 (1P8D16.6,/,2X))
0190      RETURN
      END

```

```

SUBROUTINE DIFPP2Q(DERIVS,X,Y,DY,NDIM,N,EPS,ITYPE,AUX,IER)
  IMPLICIT PEAL*8 (A-H,O-Z)
  DIMENSION V(NDIM),DY(NDIM),AUX(NDIM,7),EPS(NDIM)

  IER = 0
  IP (ITYPE,GT,2) GO TO 1
  IP (ITYPE,LE,1) GO TO 2
  DO 3 J1 = 2,ITYPE
  3 = ITYPE+2-J1
  DO 3 I = 1,NDIM
  3 AUX (I,J+2) = AUX (I,J+1)
  2 DC 4 I = 1,NDIM
  AUX (I,1) = H*D(Y,I)
  4 Y(I) = Y(I) + .5*AUX (I,1)
  X = X+.5*H
  CALL DERIVS (X,Y,DY)
  DC 5 I = 1,NDIM
  AUX (I,2) = H*D(Y,I)
  5 Y(I) = Y(I) + .5*(AUX (I,2) - AUX (I,1))
  CALL DERIVS (X,Y,DY)
  DO 6 I = 1,NDIM
  AUX (I,3) = H*D(Y,I)
  6 Y(I) = Y(I) -.5*AUX (I,2) + AUX (I,3)
  X = X+.5*H
  CALL DERIVS (X,Y,DY)
  DC 7 I = 1,NDIM
  7 Y(I) = Y(I) - AUX (I,3) + (AUX (I,1) + 2.*AUX (I,2) + 2.*AUX (I,3) + H*D(Y,I))/6.
  CALL DERIVS (X,Y,DY)
  DC 8 J = 1,NDIM
  8 AUX (I,J) = DY(I)
  IP (ITYPE,GE,1) ITYPE2 = ITYPE+1
  RETURN
  1 X = X+H
  ICOUNT = 1
  DO 9 I = 1,NDIM
  9 AUX (I,0) = Y(I) + H*(1901./720.*AUX (I,3) - 1367./360.*AUX (I,4))
  $ + 109./30.*AUX (I,5) - 637./360.*AUX (I,6) + 251./720.*AUX (I,7)
  CALL DERIVS (X,AUX,DY)
  DO 10 I = 1,NDIM
  DO 10 J1 = 3,6
  J = 9-J1
  10 AUX (I,J+1) = AUX (I,J)
  16 DO 11 I = 1,NDIM
  AUX (I,3) = DY(I)
  11 AUX (I,2) = Y(I) + H*(251./720.*AUX (I,J) + 323./360.*AUX (I,4) -
  $ 11./720.*AUX (I,5) + 53./360.*AUX (I,6) - 19./720.*AUX (I,7))
  DC 12 I = 1,NDIM
  12 CONTINUE
  IP (DARS (AUX (I,1) - AUX (I,2)) .GT. EPS (I)) GO TO 13
  GO TO 18
  13 IP (ICOUNT,LT,10) GO TO 16
  16 IER = 1
  RETURN
  14 ICOUNT = ICOUNT+1

```

PROTRAN IV G1 RELEASE 2.0 DIPPEQ
0052 1052 DATE = 78053 20/01/89
0053 DO 15 I = 1,NDIN
0054 15 AUX(I,1) = AUX(I,2)
0055 CALL DPRIVS(X,AUX,DT)
0056 DO 19 I = 1,NDIN
0057 19 DY(I) = .5*(DY(I)+AUX(I,3))
0058 GO TO 16
0059 DO 17 I = 1,NDIN
0060 17 Y(I) = AUX(I,2)
0061 RETURN
END

POSTMAN IV G1 RELPASE 2.0

SEARCH DATE = 78053 20/41/79

```
ROUTINE SEARCH(PCNS,NN,M1,X,Y,DX,ACC,INMAX,ISCN,GRAD,EA)
IMPLICIT REAL*8 (A-H,O-Z)
DIMENSION X(MNN),Y(MNN),DX(MNN),ACC(MNN),GRAD(MNN,MNN),A(MNN,M1)
COMMON/PLA5/ICAH,IPNT
COMMON/STEP/ISTEP
NN=NN
IPP = 0
10007
      IP (N,LP,0) GC TO 25
      IP (N+1,LP,0) GO TO 25
      IP (INMAX,LP,0) GC TO 25
      PG 1 I = 1,N
      IP (ACC(I),LE,0.) GO TO 25
1  CONTINUE
      DO 26 I = 1,N
26  A(I,1) = DX(I)
      ICOUNT = 1
      ISCALE=0
      DC 2 IPCN = 1,N
      S = 1.
      DO 3 ITRY = 1,INMAX
      IP (ITRY,LP,1) GO TO 4
      IP (ICOUNT,LE,INMAX) GO TO 4
      IPP = 1
      RPUTN
4  DO 69 I=1,NN
      69  YOLD(I)=A(I,M1)
      41 CALL PCNS(X,I,A(I,M1))
      DO 16 I=1,N
      16  YOLD(I)=A(I,M1)
      IP (ITRY,EO,1) GO TO 182
      TST(I)=YOLD(I)*A(I,M1)
      TST=TRST(I)
      IP (TRST(I),GT,0.) GO TO 181
      ISCALE=1
      GC TO 182
      181 ISCALE=0
      182 IP (ICOUNT,LE,INMAX-10) GO TO 24
      VPUTF(6, 200) IPCN
      WRITE(6,201) (X(I),I=1,N)
      WRITE(6,201) (A(I,M1),I=1,N)
      200 FORMAT (// 1X,T4)
      201 POUT(1X,1P7D17.7)
      24  DO 6 I = 1,N
      XHOLD = X(I)
      X(I) = X(I) + A(I,2)
      CALL PCNS(X,A)
      X(I) = XHOLD
      DO 6 J = 1,N
      6  GRAD(I,J) = (A(J,1)-A(J,M1))/A(I,2)
      217 IP (IPCN,GT,1) GC TO 7
      217 GR2 = 0.
      DO 8 I = 1,N
      8  GR2 = GR2+GRAD(I,1)**2
      0053
```

PORTA IV 31 RELEASE 2.0 SEARCH DATE = 78053 20/41/69
 0054 IF (GR2.NE.0.) GO TO 15
 0055 IPR = 2
 0056 RETURN
 15 SCALE = 0.
 DC9 I = 1,N
 A(I,J) = (Y(I)-A(I,N1))*GRAD(I,J)/GR2
 S = DABS(A(I,1)/DX(I))
 IP (S.GT.SCALE) SCALE = S
 9 CONTINUE
 GO TO 10
 7 DO 5 J = 1,IPCN
 DO 20 I = 1,N
 20 E(I,J) = GRAD(I,J)
 IP (J.PQ.1) GC TO 5
 DC 21 K = 2,J
 I = K-1
 DC7 = 0.
 ESO = 0.
 DO 22 L = 1,N
 DOF = DOT*E(I,J)*E(L,J)
 22 ESO = ESO+DOF
 DC 23 L = 1,N
 23 E(I,J) = E(L,J)-DOT*E(L,I)/ESQ
 K CONTINUE
 DO 11 I = 1,N
 DO 12 J = 1,N
 A(I,J) = 0.
 IP (J.GT.IPCN) GO TO 13
 IP (I.GT.IPCN) GO TO 13
 DO 19 K=1,N
 19 A(I,J) = A(I,J)+GRAD(K,I)*E(K,J)
 GO TO 12
 13 IP (I.PO.J) A(I,J) = 1.
 12 CONTINUE
 11 A(I,N1) Y(I)-A(I,N1)
 CALL ELIM(N,N1,A)
 IP (N.NP.0) GC TO 14
 IER = 2
 RETURN
 14 SCALE = 0.
 DO 16 I = 1,N
 A(I,1) = 0.
 DO 17 J = 1,IPCN
 17 A(I,J) = A(I,1)+A(J,N1)*E(I,J)
 S = DABS(A(I,1)/DX(I))
 IP (S.GT.SCALE) SCALE = S
 16 CONTINUE
 10 IPLAG = 0
 S = 1.
 DO 230 I=1,IPCN
 1 IP (DABS(A(I,N1)).GE.10.) IFLAG=1
 230 CONTINUE
 231 IP (SCALE.GR.1.) GO TO 23

FORTRAN IV G1 REL1PAGE 2.0 SEARCH DATE = 70053 20/41/49

```

0107      S = SCALE
0108      SCALP = 1.
0109      23 DO 19 I = 1,N
0110      IP (DABS (A(I,1)) *GP, ACC(I)) IFLAG = 1
0111      X(I) = X(I) + A(I,1) /SCALP
0112      IP (A(I,1) *PC0, ) A(I,1) = -1.
0113      18 A(I,2) = -A(I,1) /DABS (A(I,1)) *DX(I)*S
0114      IP (IPRNT,NE,2) GO TO 666
0115      WRITE (6,200) IPCN
0116      WRITE (6,201) (A(I,1),I=1,N)
0117      WRITE (6,201) (GRAD(I,1),I=1,N)
0118      CONTINUE
0119      ICOUNT = ICOUNT+1
0120      IP (IPRAG, EQ,0) GC TO 2
0121      3 CONTINUE
0122      IEP = 1
0123      RETURN
0124      2 CONTINUE
0125      RETURN
0126      25 IEP = 3
0127      RETURN
0128      END
  
```


POSTPAN IV 31 RELEASE 2.0 ELIM DATE = 78053 20/41/69

0038 C 0 FOR ONE OF THE MATRIX DIMENSIONS

0039 0 4 M = 0

0040 A(1,1) = 0.

0040 RETURN

C SINCE THE MATRIX IS SQUARE, THE PURPOSE OF THIS ROUTINE IS TO
C EVALUATE THE DETERMINANT. BACK SUBSTITUTION IS NOT NECESSARY.

C MULTIPLYING ONE OF THE DIAGONAL ELEMENTS BY ISWAP CORRECTS THE
C SIGN. THE DETERMINANT IS NOW THE PRODUCT OF THE DIAGONAL
C ELEMENTS, AND IS RETURNED IN A(1,1)

10 A(1,1) = A(1,1)*ISWAP

0042 DO 13 I = 2,M

0043 13 A(1,I) = A(1,I)*A(I,1)

0044 RETURN

0045 END

```

PORTRAN IV G1 RELEASE 2.0           INPUT           DATE = 76053
C001
C002      SUBROUTINE INPUT(MG,MS,VI,THI,THE,LNOZ,LCHAN,TS,T00,P00,NEO,
$      PTA500,DMAX)
C003      IMPLICIT REAL*8 (A-H,O-Z)
C004      DIMENSION HEADER(80)
C005      READ(M,100) LNOZ,LCHAN,NEO
C006      COMMON/DEVICE/ NI, NO
C007      THIS SUBROUTINE READS IN THE CARD DATA, TRANSFERS IT TO THE MAIN PROGRAM
C008      AND PRINTS IT ON THE OUTPUT, AND
C009      READ(M,100) (HEADER(I),I=1,80)
C010      WRITE(M,200) (HEADER(I),I=1,80)
C011      READ(M,100) (HEADER(I),I=1,80)
C012      READ(M,100) MG,MS,VI
C013      WRITE(M,202) THI,THE,LNOZ,LCHAN
C014      READ(M,105) TS,T00,P00
C015      WRITE(M,205) TS,T00,P00
C016      P00 = P0C41.0133E05
C017      READ(M,106) NEO,ETA500,DMAX
C018      WRITE(M,206) NEO,ETA500,DMAX
C019      103  FORMAT(90A1)
C020      101  FORMAT(1PF9.0)
C021      102  FORMAT(1PF9.0)
C022      105  FORMAT(1PF9.0)
C023      106  FORMAT(1PF9.0)
C024      201  FORMAT(1X,90A1)
C025      201  FORMAT(//,1X,'THE GAS',/5X,'NGAS = ',PF7.2,'/5X,'NSEED =
$      ,PF7.2,'/5X,'UPSTREAM CONDITIONS',/5X,'SEED FRACTION',/5X,'
$      ,PF2.,'VOLTS')
C026      202  FORMAT(//,1X,'THE CHANNEL',/5X,'INSULATOR THICKNESS = ',1PD10.3,
$      ,METERS',/5X,'ELECTRODE THICKNESS = ',D10.3,' METERS',/5X,
$      ,PF2.,' METERS LENGTH = ',OPPF7.4,' METERS')
C027      205  FORMAT(//,1X,'UPSTREAM STAGNATION TEMP = ',PF6.1,' KELVIN',/5X,
$      ,PF6.3,' ATM')
C028      206  FORMAT(//,1X,'THE ANALYSIS',/5X,'NB AT CHANNEL ENTRANCE = ',
$      1PD13.5,'/5X,'ETA50 AT CHANNEL ENTRANCE = ',OPPF9.0,'/5X,
$      ,PF2.,'MAX INCREMENT SIZE = ',1PD13.5,' METERS',//)
C029
C030

```

```

PORTRAY IV G1 RELEASE 2.0          OG          DATE = 78053    20/4/1989

0001      FUNCTION OG(TE)
0002          REAL*8 OG,TE
0003          OG = 6.25D-20
0004          RETURN
0005          END

0001      FUNCTION OS(TE)
0002          REAL*8 OS,TE
0003          OS = 2.2D-16
0004          RETURN
0005          END

0001      FUNCTION RATE(TE)
0002          REAL*8 RATE,TE
0003          RATE = 2.29D-34*(1100./TE)**4.5
0004          RETURN
0005          END

0001      SUBROUTINE RAYER(X,DAREA)
0002          IMPLICIT REAL*8 (A-H,O-Z)
0003          CFRA = 1.8D-03*X**.6
0004          DAPR = A(X)-PERIN(X)*DELTA
0005          RETURN
0006          END

0001      FUNCTION A(X)
0002          REAL*8 A,X
0003          A=2.205D-03+0.023426*X
0004          I = (X,CF,0.05) A=0.0033764+5.6033D-03*(X-0.05)
0005          RETURN
0006          END

0001      FUNCTION H(X)
0002          REAL*8 H,B,A,X
0003          H=.5422
0004          H=(X)/B
0005          RETURN
0006          END

```

```

FORTRAN IV G1 RELEASE 2.0           PERIM           DATE = 76053      20/41/69
0001                                     FUNCTION PERIM(X)
0002           REAL*8 PERIM,X
0003           PERIM=1.0926+0.08642*X
0004           IF (X.GT.-0.05) PERIM=1.0959+0.02068*X
0005           RETURN
0006           END

0001                                     FUNCTION B(X)
0002           REAL*8 B,X
0003           B=0.0
0004           RETURN
0005           END

0001                                     FUNCTION POWER(X)
0002           REAL*8 X,VOLUME,POWER
0003           POWER = 0.
0004           IF (X.GT.-.05) RETURN
0005           VOLUME=0.82D-04
0006           POWER=30.5D03/VOLUME
0007           RETURN
0008           END

0001                                     FUNCTION VE(X)
0002           REAL*8 VP,X
0003           VP=(-48.46*X+109.8)/10.0
0004           RETURN
0005           END

0001           SUBROUTINE LOAD(U,KINP)
0002           IMPLICIT REAL*8(A-H,O-Z)
0003           REAL*8 LM02,LCHAN,MASS,KINP
0004           COMMON/CHAN/ TH1,TH2,LM02,LCHAN,MASS
0005           PITCH = TH1+TH2
0006           VLOAD = 0.
0007           KINP = (VLOAD+VE(X)) / (U*B(X)*H(X))
0008           RETURN
0009           END

```

PORTMAN IV G1 RELIFASE 2.0 OUTPUT DATE = 78053 20/41/49
 SUBROUTINE OUTPUT(X)
 IMPLICIT REAL*8 (A-H,O-Z)
 REAL*8 KINF,KOLD,KCOPR,KNEY,NE,NESTAR,NEUA,NEUA1,NEO,M,I,J,
 \$ LAMBD0,NUG,NUS,NUL,NUR,LRG,LRATE,LAMBD1,KCONST,J1,J2,JL,
 \$ LNOZ,LCHAN,MASS
 REAL*8 NUL,NU2,NU3,NUC02,NUU2
 QFAL8 JMIN,JMAX
 CCNMCN/DERLVS/ D1,D2,D3,D4
 COMMON/CHAN/ THI,THE,LNOZ,LCHAN,MASS
 COMMON/CHAN/ THI,THE,LNOZ,LCHAN,MASS
 COMMON/ALLELS/ X1,PO,P,TO,T,V,M,U,DARE,M,NEUA,NEUA1,NE,NESTAR,
 \$ TE,TEIRP,EPB,PHL,ETPSO,ALPHA,XI,DO,LAHED,CE,WIG,WUS,WUL,WU,
 \$ DELTA,R,R,RETAC,BETA,BETAA,BTAA,BCNST1,BCNST2,BET1,
 \$ BFTA2,J1,J2,KCONST,KINF,JL,Z0,TNGNT,S,SIGMA,SIGAV,SIGEFF,
 \$ LNRG,IRATE,G,GSTAR,LAMBD1,I,PLOSS,KCORR,ETAP,LOAD,
 \$ XCUB,CUR,YCUR,1,DEFF
 COMMON/PLAIS/ ICHAN,FRNT
 COMMON/DEVICE/ VI,NO
 COMMON/TEPS/ T2,T3,THETA1,THETA2,THETA3,HPL,NEUA2,NU2,NU1,
 \$ COMMON/LASR/TAICO2,NO01,NO02,NO03,NO04,NO05,NO06,NO07,NO08,NO09
 \$ COMMON/VERBS/ VIBT22,VIBT33,VIBT34,VIBT35,VIBT36,VIBT37,VIBT38,TAU2E,TAU3E,AU2E
 \$ COMMON/SIGNAL/COLRAT,WJ,WC,ZIN,ZUL,ZLI,GIN
 COMMON/DIG/DHDY,CMIN,CMAX,JMIN,JMAX,C2,PITCH,DV1,DV2
 COMMON/KNOW/TRA1,TEA2,TEA3,TAUK3H,TAU3C,RELRA,TAU3RL,
 \$ DV1RL,D5,D6,C1,CD160,DMAX,CB21,CB22,CB23,
 \$ A18,A2R,A3R,A4R,A5R,A6R,A7R,A8R,A9R,B1R,B2R,B3R,B4R,B5R,B6R,
 \$ B7R,B8R,B9R
 COMMON/REFLAX/ T1,P1,P2,AUPI,AUE2,D7,VIBT11,VIBT22,VIBT27,
 \$ DV2T,DV1T,DV12,TU1H,TU1C,DV12,DV31,DG31,DG32,DG33,DG111,DG112,DG12,DG13,
 \$ COMMON/JULY/CAVAD,CAVL,DG31,DG32,DG33,DG111,DG112,DG12,DG13,
 \$ DG3TOT,DG17TOT,ALPH1,ALPH2,BIPL1,BIPL2,AE12DU,AE1DU,DE12DU,
 \$ UFL1A,AE3DU,AE3DU,ALPH1P,ALPH2P,BLPH1P,BLPH2P
 COMMON/OSCILL/CAVGN,CAVPO,DISULCAVEFF,PODEN,TOTPOV,
 \$ DV1P,EPFP,FPFL,EPPO,EPFMHD,EPFPOT,TOFP,POBPF,
 \$ EPFPUR,EPKER,TOTDIS,REP1,REP2,EPFLOC,EPFLAL
 \$ IP (ICHAR(PV)) GO TO 1
 CLOUD = -JL*CNRA(X)*(THE*THE)/H(X)
 WRITE (NO,200) X,PO,TC,INFLA,ETASO,P,T,U,M,
 \$ HE,NESTAR,TE,TEIN,EPB,PHI,NU,DELTA,
 \$ RETAC,BETA,RETAV,RETAP,RTAA,BCNST1,BCNST2,J1,
 \$ J2,SIGMA,SIGAV,SIGEFF,LNRG,LRATE,JI,CHR,
 \$ I,KINF,KCOPR,G,GSER,LARRD,LOAD,LOAD,
 \$ DIPP,DIDY,BETA2,BCNST1,BCNST2,CMIN,CMAX,JMIN,
 \$ JMAX,C1,PITCH,DV2P,DV2E,DV2Z,DV3RL,DS,D6,
 \$ TEA1,TEA2,TEA3,TAU3H,TAU3C,RELRA,TAU3RL,TAU3E,
 \$ TAU2E,TAU2H,P,CB21,CB22,CB23,A5R,A6R,A7R,
 \$ A8R,A9R,A18,A2B,A1R,A4R,B1R,A2R,
 \$ B3R,B4R,A5R,B6R,B7R,B8R,B9R,NUC02,
 \$ DV1T,DV12D,TAU1HP,TAVIC
 WRITE (NO,200) T1,T2,T3,E1,E2,E3,AUE1,AUE2,AUE3
 WRITE (NO,200) GAIN,ZUL,ZLI,ZIN,COLRAT,WC,WJ
 WRITE (6,200) CAVRAD,CAVL,DG3TOT,EG1TOT,ALPH2P,BLPH1P,
 \$ BLPH2P,AP3DU
 WRITE (NO,200) CAVPO,TOTPOV,DISJUL,TOTPOV,PODEN,DV3E,

```

0027      0028      0029      0030      0031
 0937AN 4 1  RELEASE 2.0      OUTPUT      DATE = 78053      20/61/49
      S      EPP,EPPL,EPPOPT,EPPLLOC,EPPTUN,EPPEHD,EPPTOT,EPVFL,EPVKE
      RETURN
      1  WRITE (NO,200) X,P0,T,P,T,U,N,D1,D2,
      $  T1,T2,T3,E1,E2,E3,DV1,DV2,DV3,
      $  GAN,ZUL,ZLL,ZIN,CONRAUT,N,ABJ,TAUKJN,
      $  TAUKJC,RELRAAT,VIH,VISIT2,TAUH2,DTAII,DV12,
      $  D5,D7,VIBT51,VIBT52,VIBT53,VIBT54,VIBT55,
      200  PORTAT (/,1K,1PD15.5,10/,1K,1PD15.5)
      END

```

REFERENCES

1. Kerrebrock, J.L., and Draper, J.S., "Nonequilibrium MHD Generator with Molecular Gases," AIAA Paper 70-41 (1970).
2. Draper, J.S., and Kerrebrock, J.L., "Molecular Behavior in Nonequilibrium MHD Generators," 5th Int. Conf. on MHD Elec. Power Gen., Munich (1971).
3. Mnatsakanyan, A. Kh., "Electron Energy Balance in Inert Gas-Alkali Metal-Nitrogen Mixtures," High Temperature 7, 353 (May 1969).
4. Lowenstein, A., "Physical Processes in a Magnetohydrodynamic Laser," Ph.D Thesis, MIT Department of Aeronautics and Astronautics (February 1974).
5. Shaw, J.F., "Effects of Nonelastic Collisions in Partially Ionized Gases," SU-IPR Rept. #254, Stanford, CA (1968).
6. Brown, R.T., Hall, R.J., and Nighan, W.L., "Laser Excitation Using a Nonequilibrium MHD Generator," United Aircraft Research Lab. Report, East Hartford, CT (1969).
7. Nighan, W.L., Brown, R.T., and Hall, R.J., "Laser Excitation Using a Nonequilibrium MHD Generator," AIAA Paper 71-67 (1971).
8. Bullis, R.H., Churchill, T.L., Nighan, W.L., et al., "Investigation of the Feasibility of a Magnetohydrodynamic Laser," Report #N921308-4, United Aircraft Research Lab., East Hartford, CT (May 1974).
9. Zauderer, B., Tate, E., and Marston, C.H., "CO₂ MHD Laser, Analysis, Design and Shock Tunnel Experiments," 14th Symp. on Eng. Aspects of MHD, Tullahoma, Tennessee (1973).
10. Zauderer, B., Tate, E., and Marston, C.H., "Investigation of High Power MHD Gas Lasers," General Electric Space Sciences Lab. Report, Philadelphia, PA (1974).
11. Biberman, L.M., Vorobjev, V.S., Ivanov, R.S., et al., "Some Results of MHD Laser Investigation," 16th Symp. on Eng. Aspects of MHD, Pittsburgh, PA (1977).
12. Sharma, S., Private communication (August 1977).
13. Rosa, R.J., Magnetohydrodynamic Energy Conversion, McGraw-Hill, New York, NY (1968), p 35.

REFERENCES (Cont.)

14. Lowke, J.J., Phelps, A.V., and Irwin, B.W., "Predicted Electron Transport Coefficients and Operating Characteristics of $\text{CO}_2 - \text{N}_2 - \text{He}$ Laser Mixtures," *J. App. Phys.* 44, 10, 4664 (1973).
15. Solbes, A., "Study of Non-Equilibrium MHD Generator Flows with Strong Interaction," Final Report for NSF PSK0488-00, (June 1974).
16. Cole, J.A., "A Numerical Study of Non-Equilibrium MHD Generators," S.M. Thesis, M.I.T. Department of Aeronautics and Astronautics (May 1976).
17. Herzberg, G., Molecular Spectra and Molecular Structure II, Van Nostrand, New York, N.Y. (1945).
18. Hake, R.D., and Phelps, A.V., "Momentum - Transfer and Inelastic Collision Cross Sections for Electrons in O_2^+ , CO , and CO_2 ," *Phys. Rev.* 158, 1, 70 (June 1967).
19. Schulz, G.J., and Boness, M.J.W., "Vibrational Excitation of CO_2 by Electron Impact," *Phys. Rev. Letters* 21, 15, 1031 (1968).
20. Nighan, W.L., "Electron Energy Distributions and Collision Rates in Electrically Excited N_2^+ , CO , and CO_2 ," *Phys. Rev. A* 2, 5, 1989 (Nov. 1970).
21. Claydon, C.R., Segal, G.A., and Taylor, H.S., *J. Chem. Phys.* 52, 3387 (1970).
22. Anderson, J.D., Jr., and Winkler, E.M., "High Temperature Aerodynamics with Electromagnetic Radiation," *Proc. IEEE* 59, 651 (April 1971).
23. Anderson, J.D., Jr., Introduction to Gasdynamic Lasers, Academic Press, New York, NY (1976).
24. Statz, H., Tang, C.L., and Koster, G.F., "Transition Probabilities between Laser States in Carbon Dioxide," *J. App. Phys.* 37, 11, 4278 (Oct 1966).
25. Schappert, G.T., "Rotational Relaxation Effects in Short-pulse CO_2 Amplifiers," *Appl. Phys. Lett.* 23, 6, 319 (1973).
26. Schwartz, R.M., Slawsky, Z.I., and Herzfeld, K.F., "Calculation of Vibrational Relaxation Times in Gases," *J. Chem. Phys.* 20, 1591 (1952).

REFERENCES (Cont.)

27. Yariv, A., Introduction to Optical Electronics, Holt, Rinehart, and Winston, New York, NY (1971).
28. Glowacki, W.J., and Plummer, M.J., "Theoretical Investigation of the CO Supersonic Electric Discharge Laser," AIAA Paper 73-623 (1973).
29. Parma, C.C., "Study of the M.I.T. Non-Equilibrium MHD Generator Experiments," S.M. Thesis, M.I.T. Department of Aeronautics and Astronautics (May 1974).
30. Liepmann, H.W., and Roshko, A., Elements of Gasdynamics, Wiley, New York, NY (1957).
31. Shapiro, A.H., The Dynamics and Thermodynamics of Compressible Fluid Flow, Ronald, New York, NY (1953).
32. Kerrebrock, J.L., "Nonequilibrium Ionization Due to Electron Heating: I. Theory," AIAA J. 2, 6, 1072 (June 1964).
33. Solbes, A., "Instabilities in Non-Equilibrium MHD Plasmas, A Review," AIAA Paper 70-40 (1970).
34. Hinnov, E., and Hirschberg, J.G., "Electron-Ion Recombination in Dense Plasmas," Phys. Rev. 125, 3, 795 (1962).
35. McGregor, D.D., Mitchner, M., and Shaw, J.F., "Ionization Rate Calculations for Preionizers," AIAA J. 8, 5, 908 (May 1970).
36. Lin, S.C., Resler, E.L., and Kantrowitz, A.R., "Electrical Conductivity of Highly Ionized Argon Produced by Shock Waves," J. App. Phys. 26, 95 (1955).
37. Craggs, J.D., and Massey, H.S.W., "Collisions of Electrons with Molecules," Handbuch der Physik, 37/1, 1959 (314 - 315).
38. Draper, J.S., "Nonequilibrium Magnetohydrodynamic Generators with Molecular Addition," Ph.D. Thesis, MIT Department of Aeronautics and Astronautics (January 1971).
39. Solbes, A. "Quasi-Linear Plane Wave Study of Electro-thermal Instabilities," SM-107/26, 4th Int. Conf. on MHD Elec. Power Gen., Warsaw (1968).
40. Gerry, E.F., and Leonard, D.A., "Measurement of $10.6 \mu\text{CO}_2$ Laser Transition Probability and Optical Broadening Cross Sections," Appl. Phys. Lett 8, 9, 227 (May 1966).

REFERENCES (Cont.)

41. Burch, D.E., Gryvnak, D.A., and Williams, D., "Total Absorptance of Carbon Dioxide in the Infrared," *Appl. Opt.* 1, 759 (October 1962).
42. Christenson, C.P., Freed, C., and Haus, H.A., "Gain Saturation and Diffusion in CO_2 Lasers," *IEEE J. Quant. Electron.* QE-5, 276 (June 1969).
43. Lyon, D.L., "Collisional Relaxation Mechanisms Governing Operation of High-Pressure CO_2 Lasers," Ph.D. Thesis, MIT Department of Electrical Engineering (Sept. 1972).
44. Cheo, P.K., and Abrams, R.L., "Rotational Relaxation Rate of CO_2 Laser Levels," *Appl. Phys. Lett.* 14, 2, 47 (Jan 1969).
45. Granek, H., "Cross-Relaxation in the Doppler Profiles of J-Levels And between J-Levels of the 00^01 and 10^00 Vibrational States in CO_2 ," Ph.D Thesis, MIT Department of Electrical Engineering (May 1971).
46. Stark, E.E., Jr., "Generation And Amplification of Short Laser Pulses," Ph.D. Thesis, MIT Department of Electrical Engineering (September 1972).
47. Rosser, W.A., Jr., Wood, A.D., and Gerry, E.T., "Deactivation of Vibrationally Excited Carbon Dioxide (ν_3) by Collisions with Carbon Dioxide or with Nitrogen," *J. Chem. Phys.* 50, 4996 (June 1969).
48. Rosser, W.A., Jr., and Gerry, E.T., "De-excitation of Vibrationally Excited CO_2 (ν_3) by Collisions with He, O_2 , and H_2O ," *J. Chem. Phys.* 51, 2286 (December 1969).
49. Rosser, W.A., Jr., Hoag, E., and Gerry, E.T., "Relaxation of Excess Populations in the Lower Laser Level CO_2 (100)," *J. Chem. Phys.* 57, 10, 4153 (November 1972).
50. Rhodes, C.K., Kelly, M.J., and Javan, A., "Collisional Relaxation of the 10^00 State in Pure CO_2 ," *J. Chem. Phys.* 48, 5730 (June 1968).
51. Taylor, R.L., and Bitterman, S., "Survey of Vibrational Relaxation Data for Processes Important in the $\text{CO}_2 - \text{N}_2$ Laser System," *Rev. Mod. Phys.* 41, 26 (January 1969).

REFERENCES (Cont.)

52. Christiansen, W.H., and Greenfield, E., "Analysis of A Collisionally Induced Dipole Laser," *Appl. Phys. Lett.* 23, 11, 623 (December 1973).
53. Nighan, W.L., Wiegand, W.J., Fowler, M.C., and Bullis, R.H., "Investigation of the Plasma Properties of High Energy Gas Discharge Lasers," Rept. #K-920833-5, United Aircraft Research Lab., East Hartford, CT (June 1971).
54. Murray, E.R., Jr., "Vibrational Non-Equilibrium in Carbon Dioxide Electric Discharge Lasers," *SU-IPR Rept. #562*, Stanford, CA (1974).
55. Judd, O.P., "The Effect of Gas Mixture on the Electron Kinetics in the Electrical CO_2 Gas Laser," *J. App. Phys.* 45, 10, 4572 (October 1974).
56. Sharma, R.D., "Kinetics of Equilibration of 1388 cm^{-1} Vibrational Level of CO_2 ," *J. Chem. Phys.* 49, 5195 (December 1968).
57. Carbone, R.J., and Witteman, W.J., "Vibrational Energy Transfer in CO_2 under Laser Conditions with and without Water Vapor," *IEEE J. Quant. Electron.* QE-5, 442 (September 1969).
58. Seeber, K.N., "Radiative and Collisional Transitions between Coupled Vibrational Modes of CO_2 ," *J. Chem. Phys.* 55, 10, 5077 (November 1971).
59. Bulthuis, K., and Ponsen, G.J., "On the Relaxation of the Lower Laser Level of CO_2 ," *Chem. Phys. Lett.* 14, 5, 613 (1972).
60. Bulthuis, K., "Laser Power and Vibrational Energy Transfer in CO_2 Lasers," *J. Chem. Phys.* 58, 12, 5786 (June 1973).
61. Jacobs, R.R., Pettipiece, K.J., and Thomas, S.J., "Rate Constants for the CO_2 $02^0 - 10^0$ Relaxation", *Phys. Rev. A* 11, 1, 54 (January 1975).
62. Stark, E.E., "Measurement of the 100-020 Relaxation Rate in CO_2 ," *Appl. Phys. Lett.* 23, 6, 335 (September 1973).
63. Murray, E.R., Kruger, C.H., and Mitchner, M., "Vibrational Non-Equilibrium in Carbon Dioxide Electric Discharge Lasers," *J. Chem. Phys.* 62, 2, 388 (January 1975).

REFERENCES (Cont.)

64. DeTemple, T.A., Suhre, D.R., and Coleman, P.D., "Relaxation Rates of Lower Laser Levels in CO₂," *Appl. Phys. Lett.* 22, 8, 349 (April 1973).
65. Reilly, J., "High Power Electric Discharge Lasers (EDLs)," *Astronautics and Aeronautics* 13, 352 (March 1975).
66. Christiansen, W.H., and Tsongas, G.A., "Gain Kinetics of CO₂ Gasdynamic Laser Mixtures at High Pressure," *Phys. Fluids* 14, 12 (December 1971).
67. Simons, G.A., "Decay of a Boundary-Layer Induced Shock," *AIAA J.* 9, 1417 (July 1971).
68. Simons, G.A., "The Effect of Boundary Layers on GDL Medium Homogeneity," *AIAA Paper 72-709* (1972).
69. Sutton, G.W., "Effect of Turbulent Fluctuations in an Optically Active Fluid Medium," *AIAA J.* 7, 9, 1737 (Sept. 1969).
70. Milora, S.L., "Non-Linear Plane Wave Studies of Electro-thermal Instabilities," S.M. Thesis, M.I.T. Department of Aeronautics and Astronautics (Sept 1968).
71. Grove, R.E., "An Experimental Study of the Effects of Molecules in Nonequilibrium MHD Plasmas," S.M. Thesis, M.I.T. Department of Aeronautics and Astronautics, (Sept 1971).

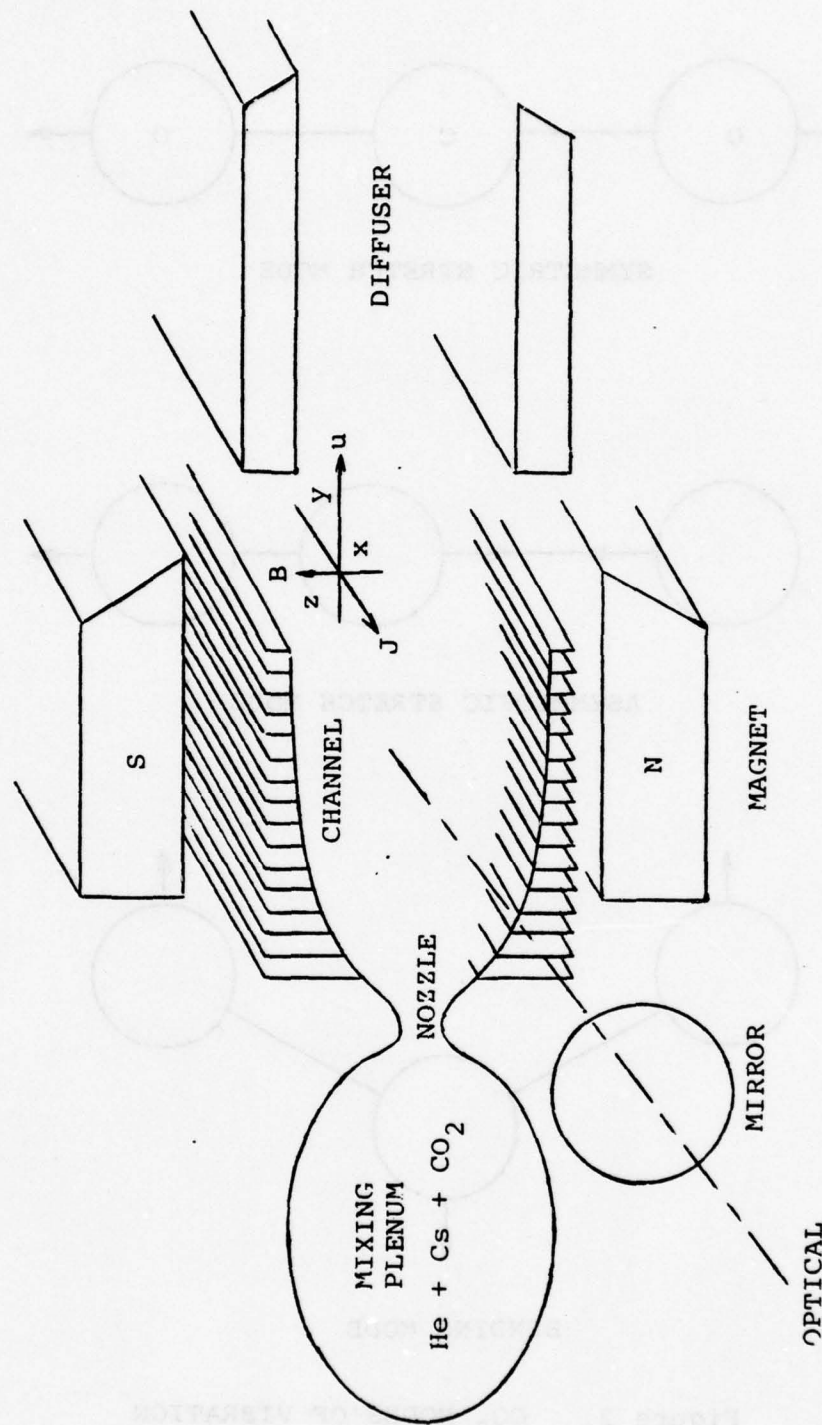
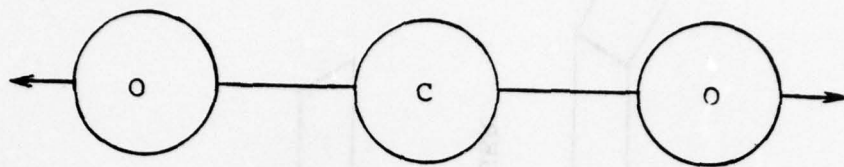
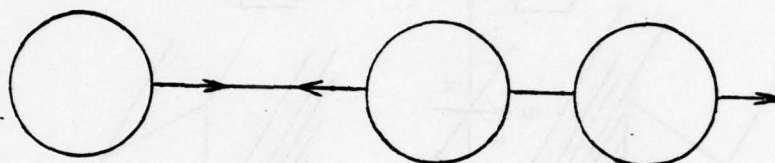


Figure 1. SCHEMATIC OF MHD LASER CONFIGURATION
(After Ref. 7)

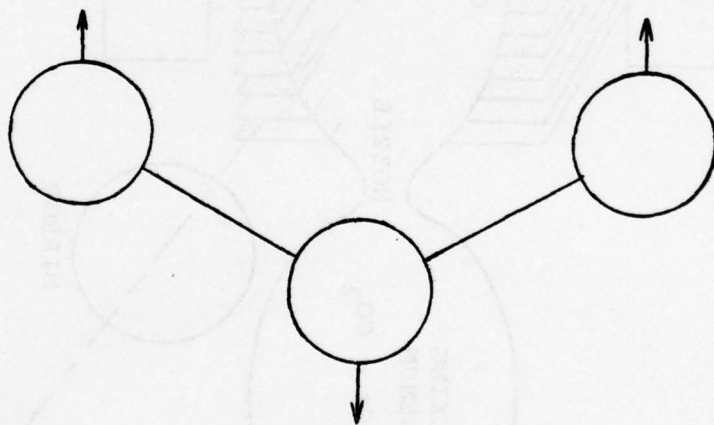
Figure 1.



SYMMETRIC STRETCH MODE



ASYMMETRIC STRETCH MODE



BENDING MODE

Figure 2. CO_2 MODES OF VIBRATION

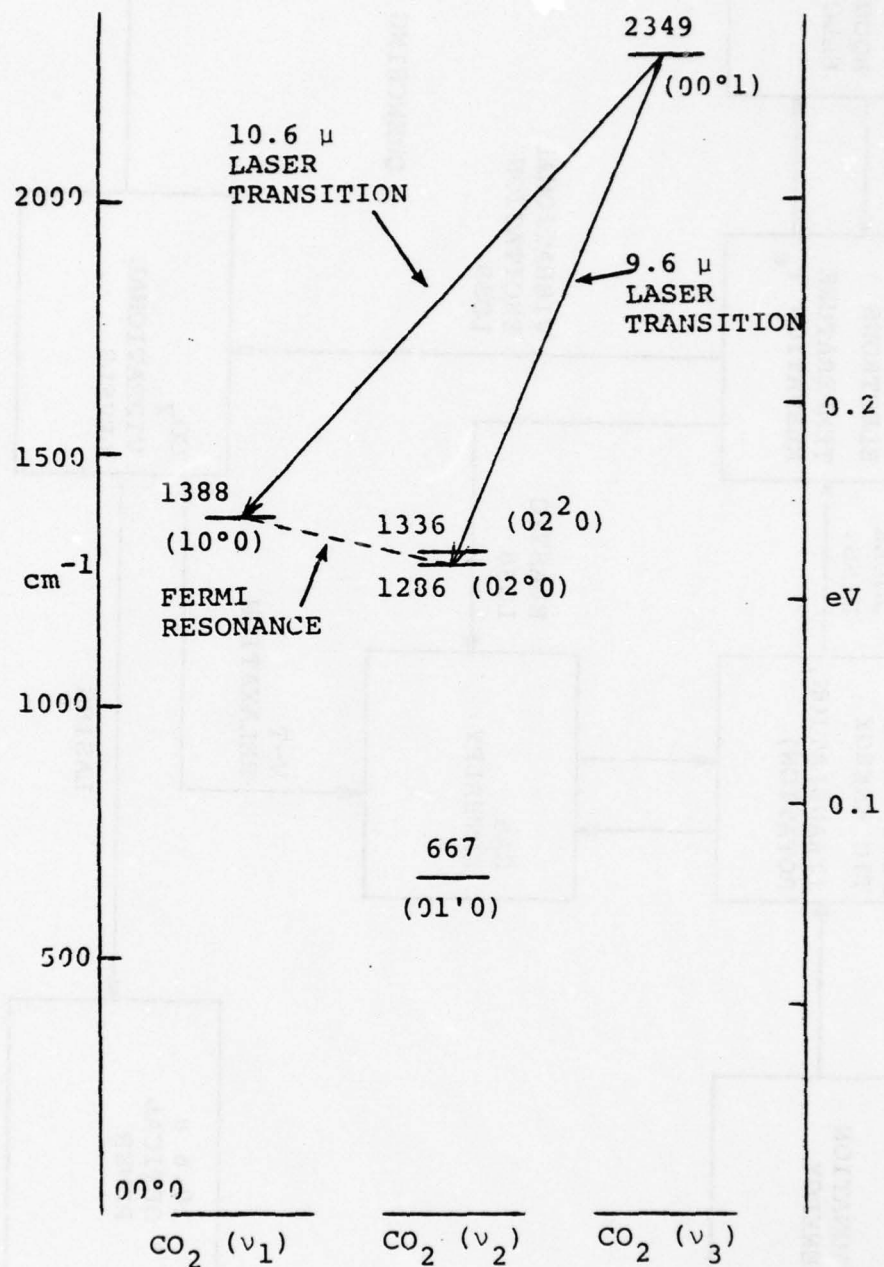


Figure 3. CO_2 ENERGY LEVEL DIAGRAM.

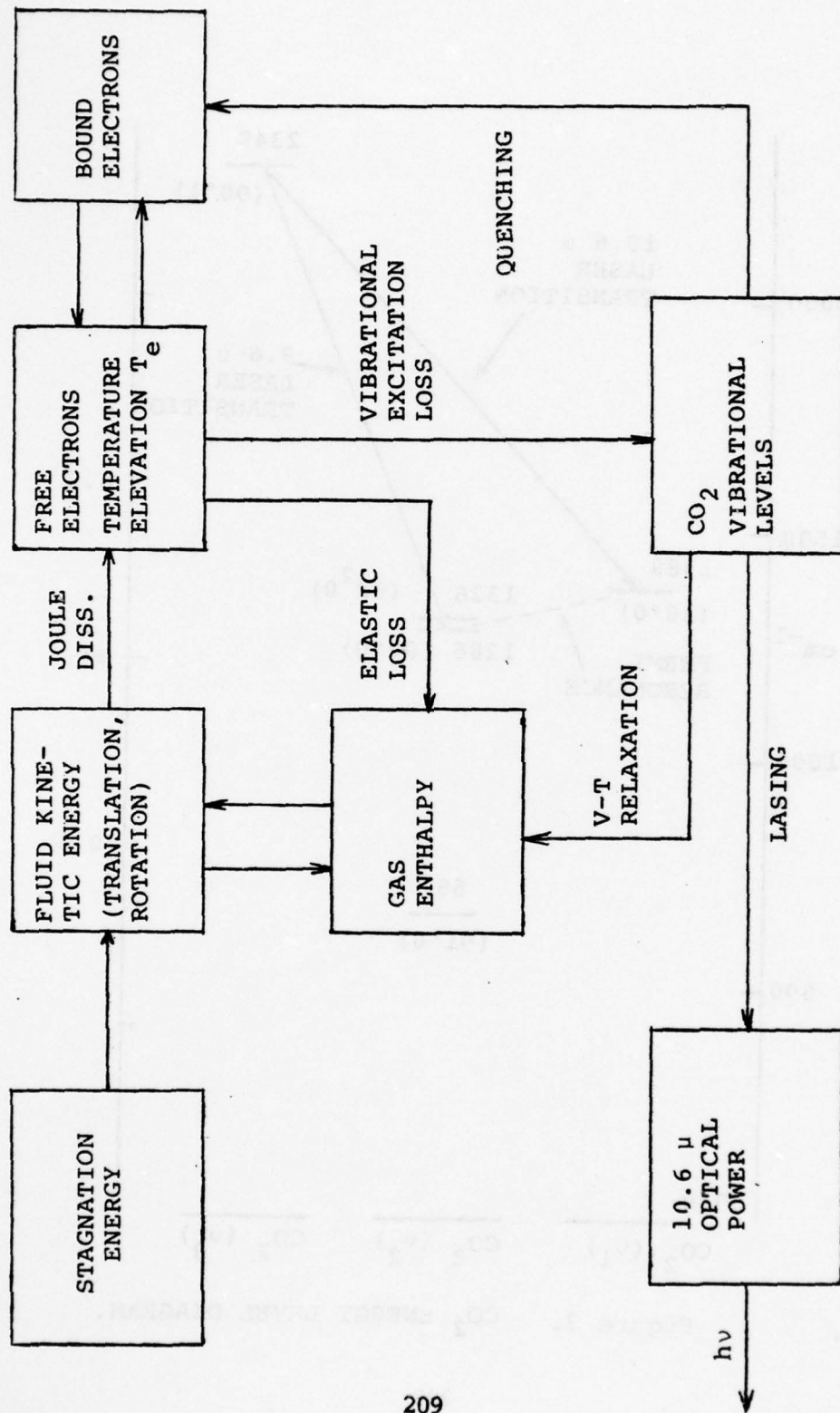
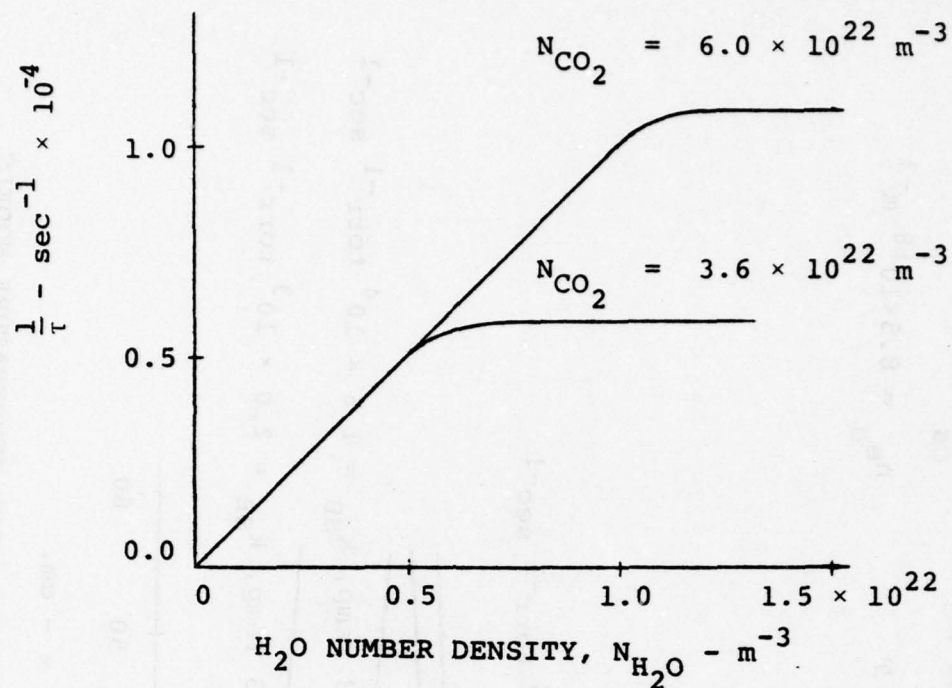
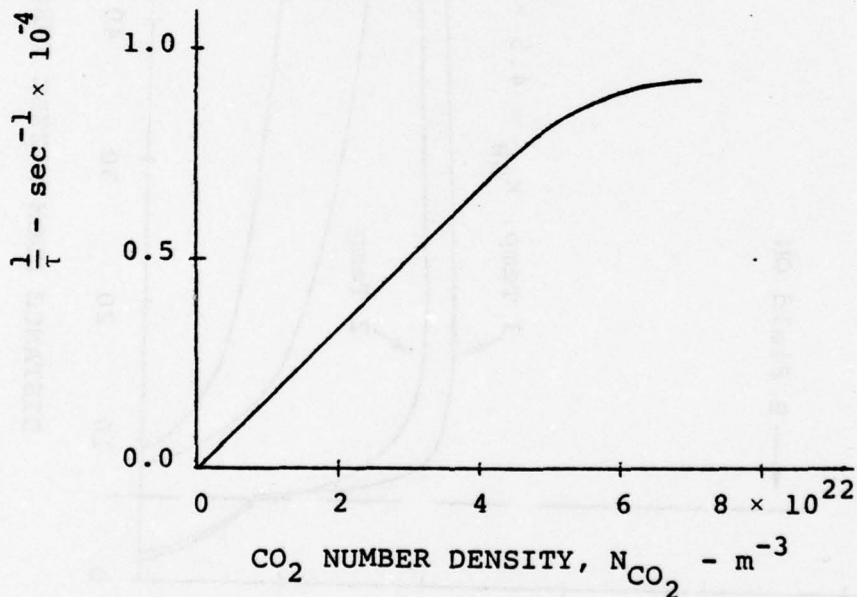


Figure 4. RELATIONSHIP OF PHYSICAL PROCESSES IN AN MHD LASER.

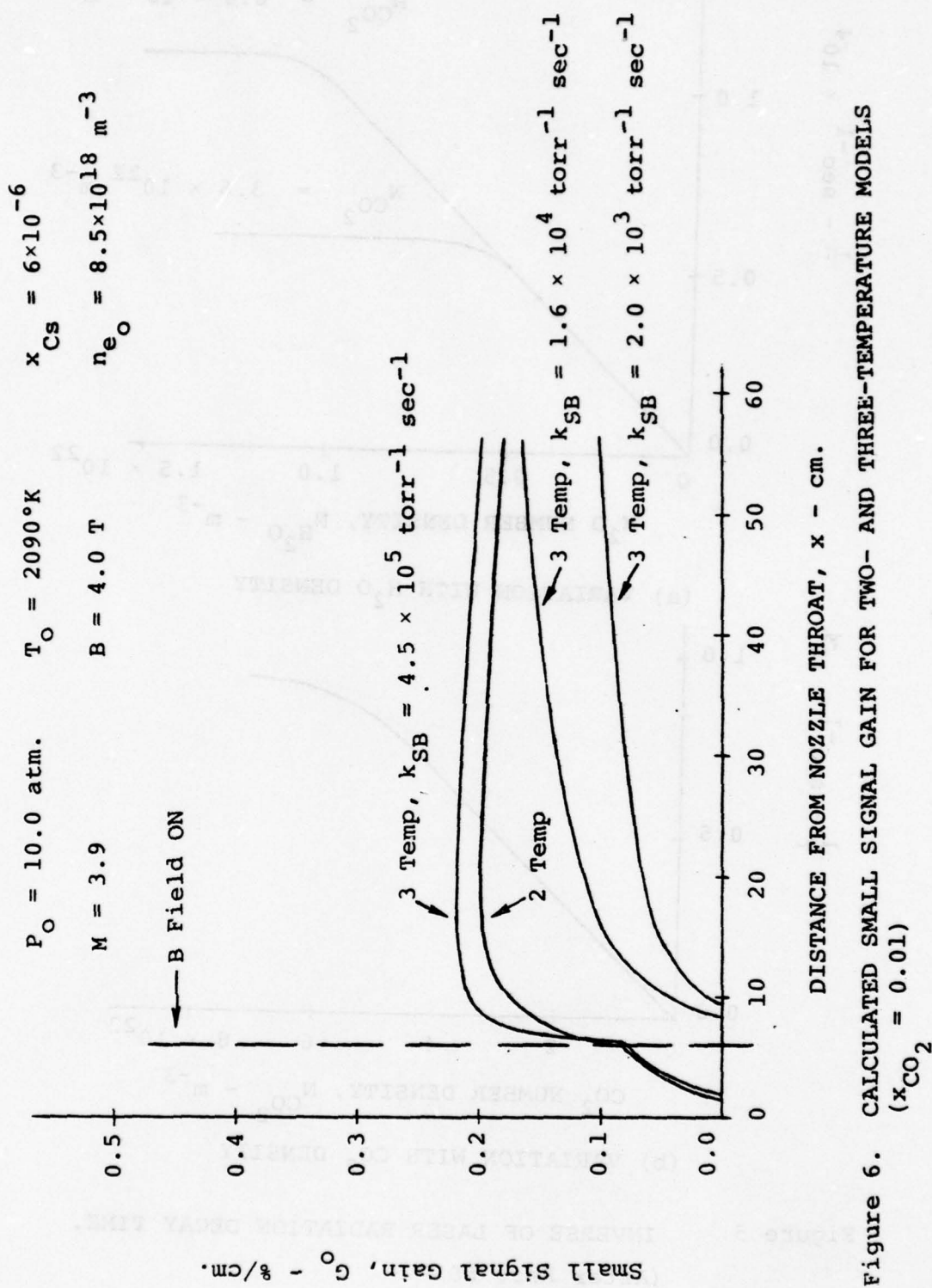


(a) VARIATION WITH H_2O DENSITY



(b) VARIATION WITH CO_2 DENSITY

Figure 5. INVERSE OF LASER RADIATION DECAY TIME.
(After Ref. 60)



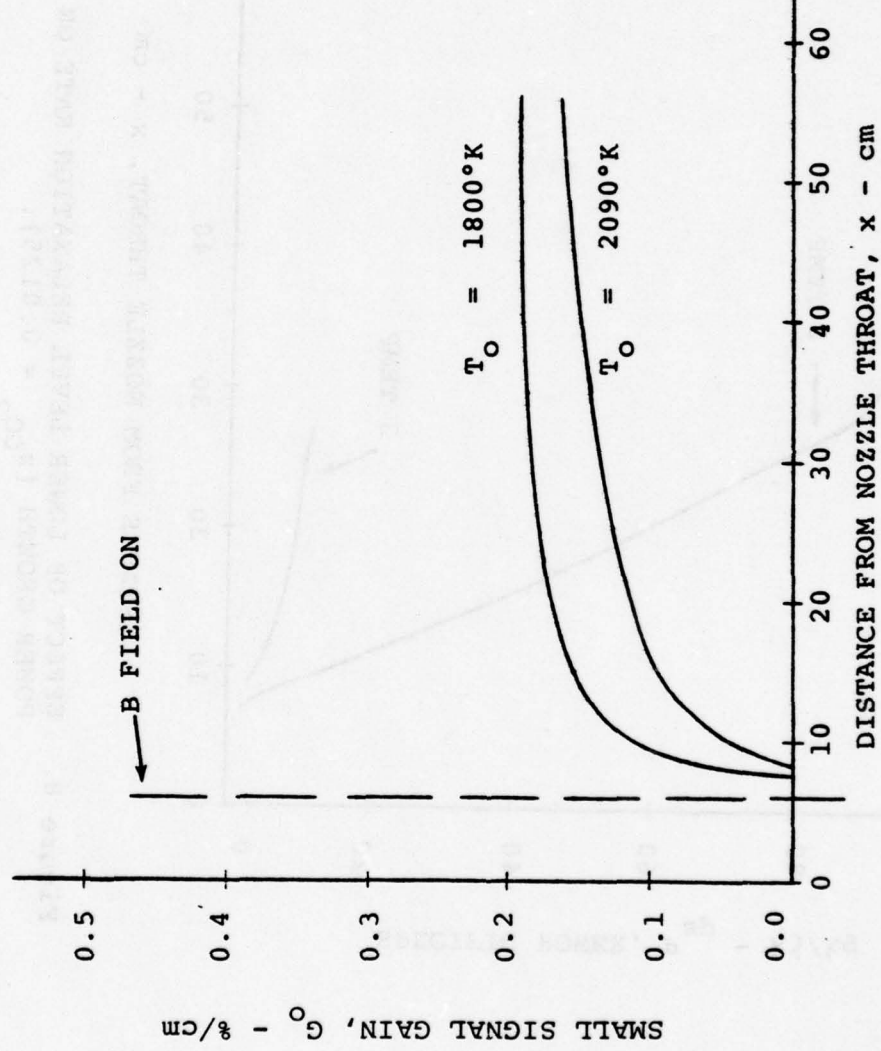


Figure 7. EFFECT OF INITIAL STAGNATION TEMPERATURE ON CALCULATED SMALL SIGNAL GAIN.

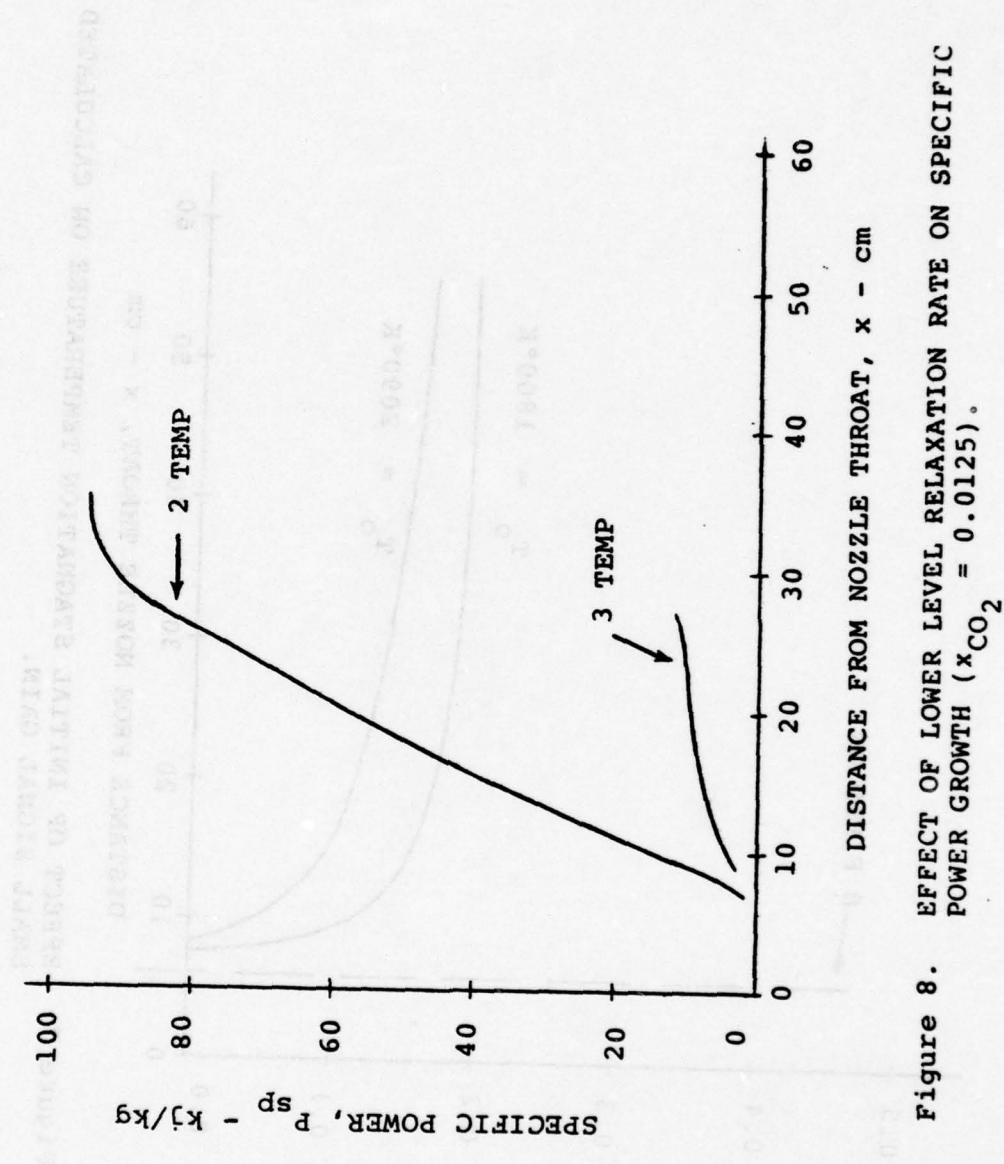


Figure 8. EFFECT OF LOWER LEVEL RELAXATION RATE ON SPECIFIC POWER GROWTH ($x_{CO_2} = 0.0125$).

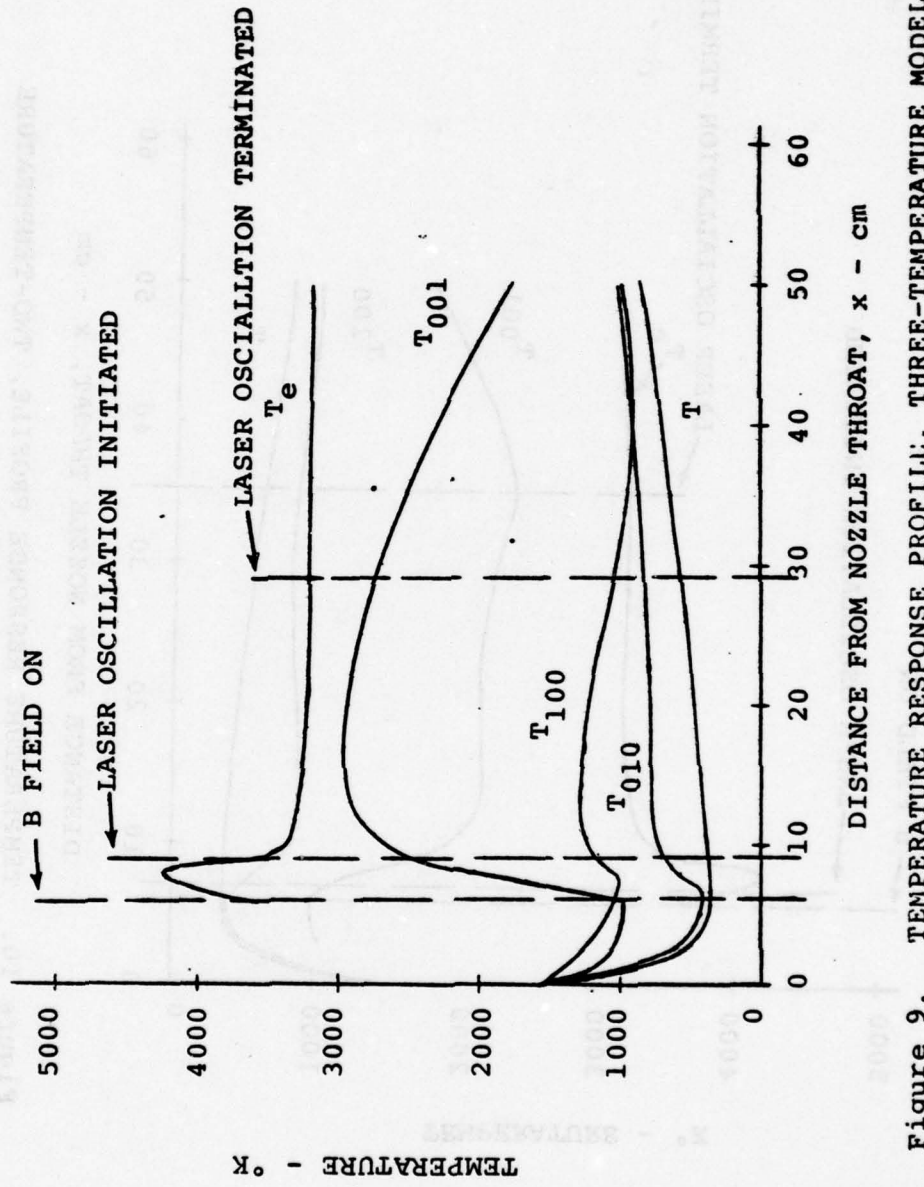


Figure 9. TEMPERATURE RESPONSE PROFILE, THREE-TEMPERATURE MODEL
 $(x_{CO_2} = 0.0125, k_{SB} = 3.3 \times 10^4 \text{ torr}^{-1} \text{ sec}^{-1})$.

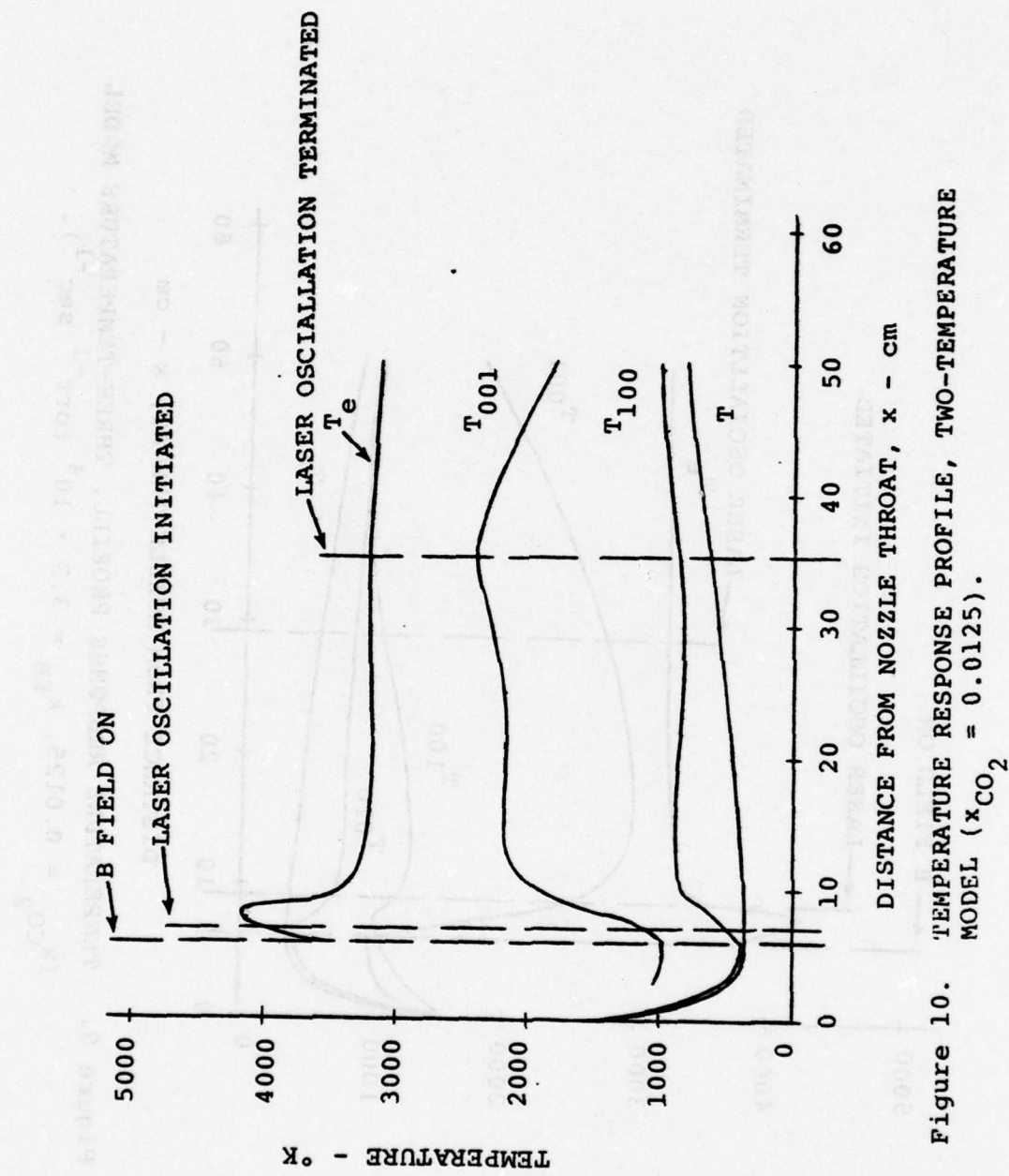


Figure 10. TEMPERATURE RESPONSE PROFILE, TWO-TEMPERATURE MODEL ($x_{CO_2} = 0.0125$).

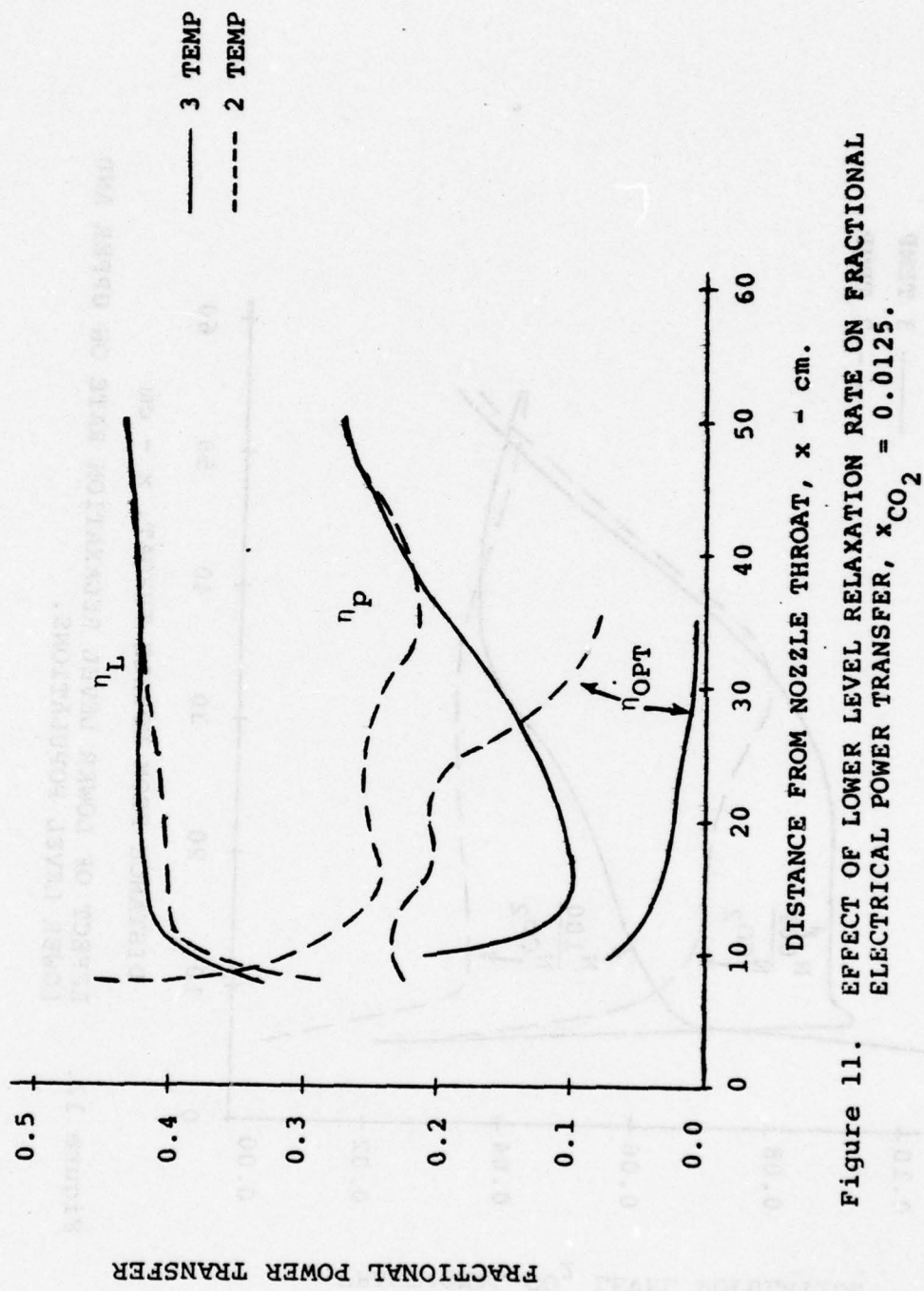


Figure 11. EFFECT OF LOWER LEVEL RELAXATION RATE ON FRACTIONAL ELECTRICAL POWER TRANSFER, $x_{CO_2} = 0.0125$.

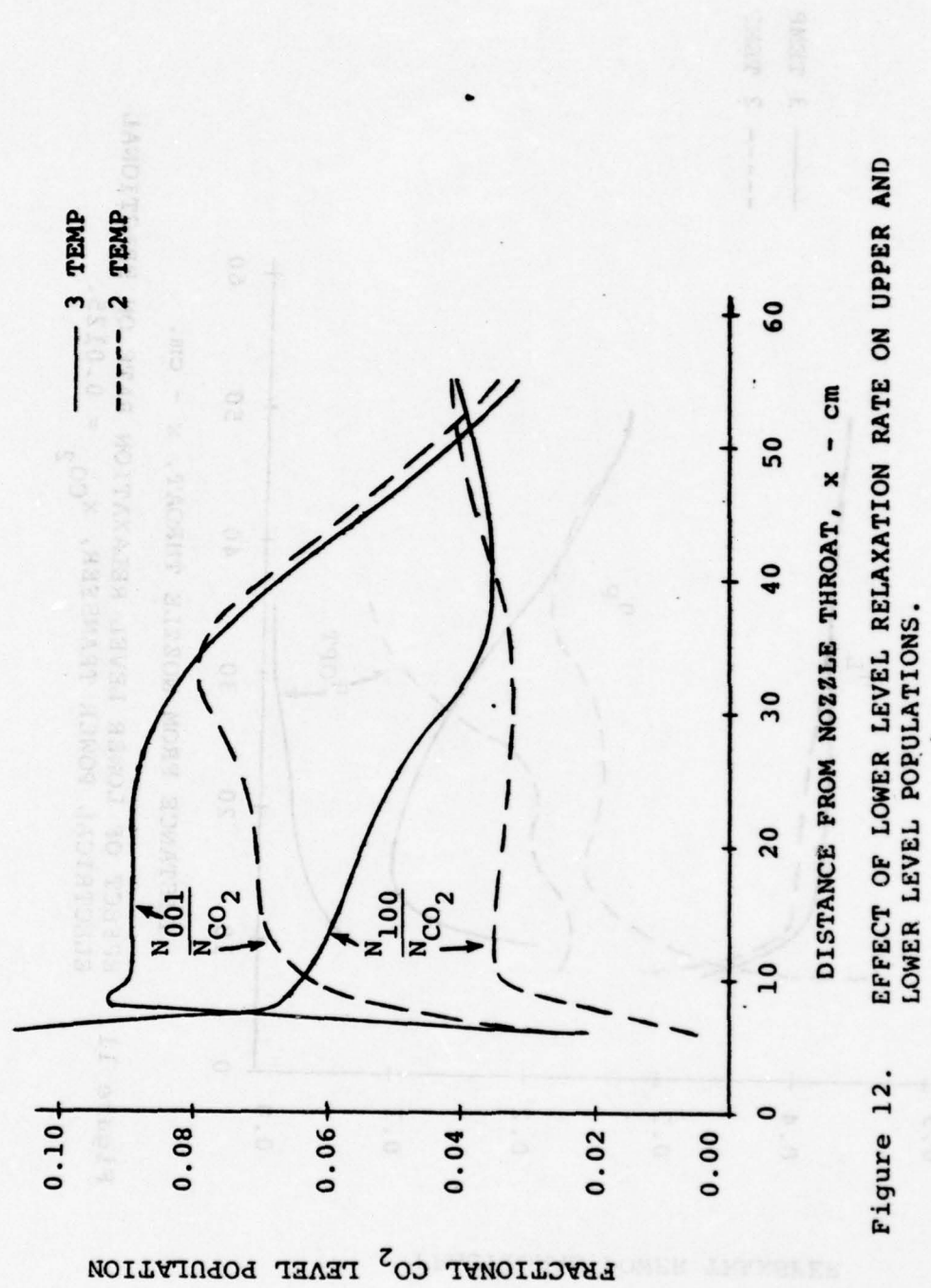


Figure 12. EFFECT OF LOWER LEVEL RELAXATION RATE ON UPPER AND LOWER LEVEL POPULATIONS.

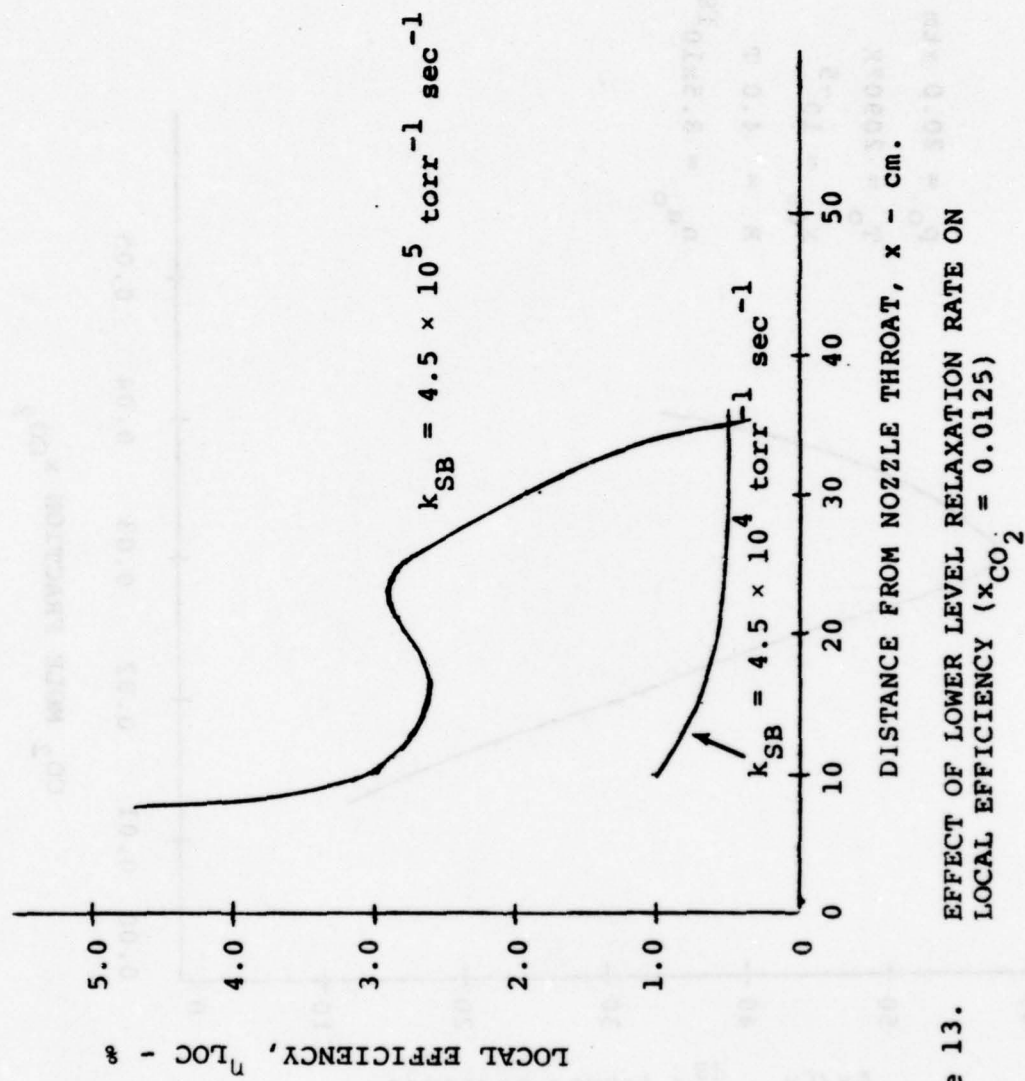


Figure 13.
EFFECT OF LOWER LEVEL RELAXATION RATE ON
LOCAL EFFICIENCY ($x_{CO_2} = 0.0125$)

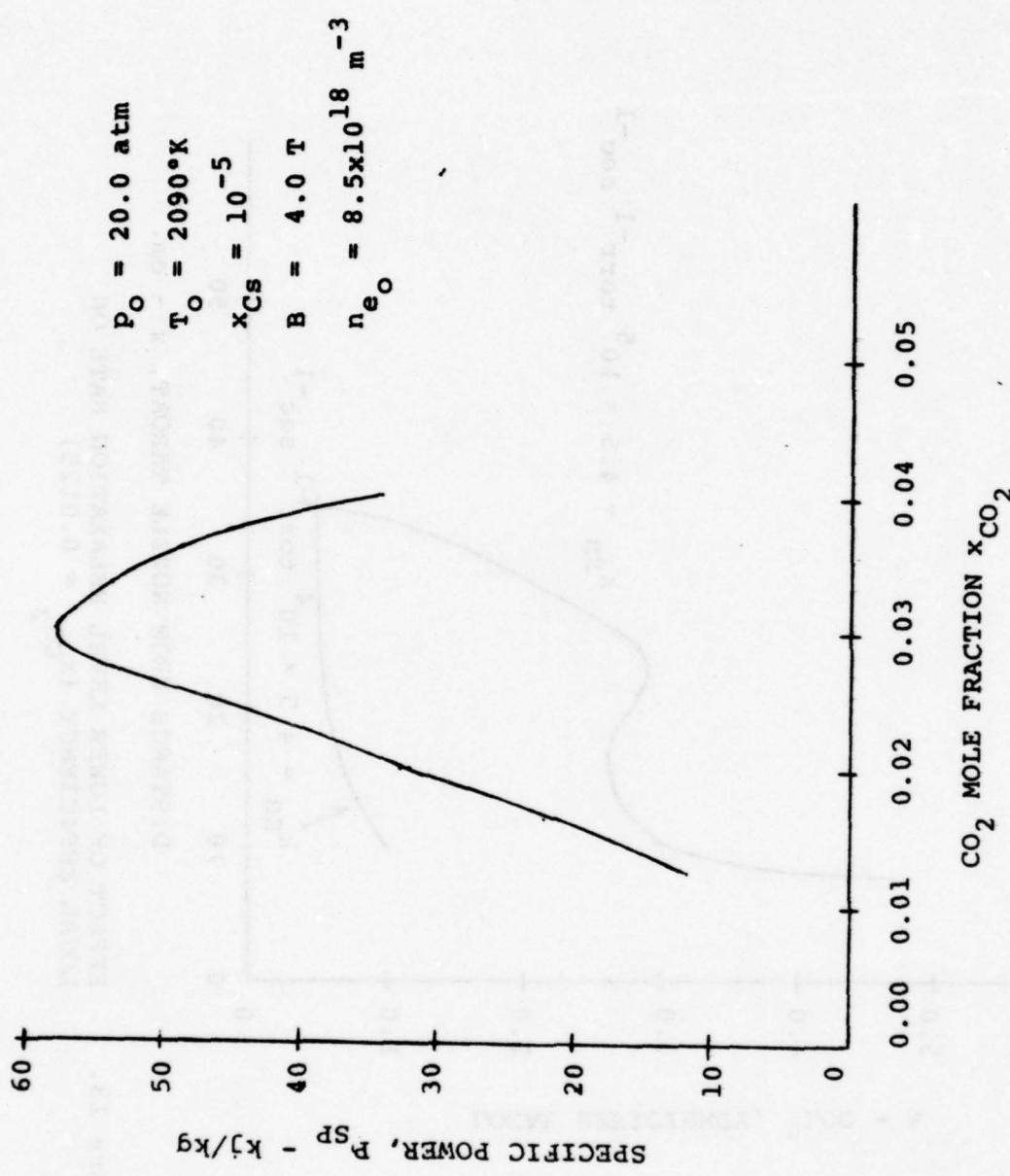


Figure 14. EFFECT OF CO_2 CONCENTRATION ON OPTICAL OUTPUT ($M = 4$)

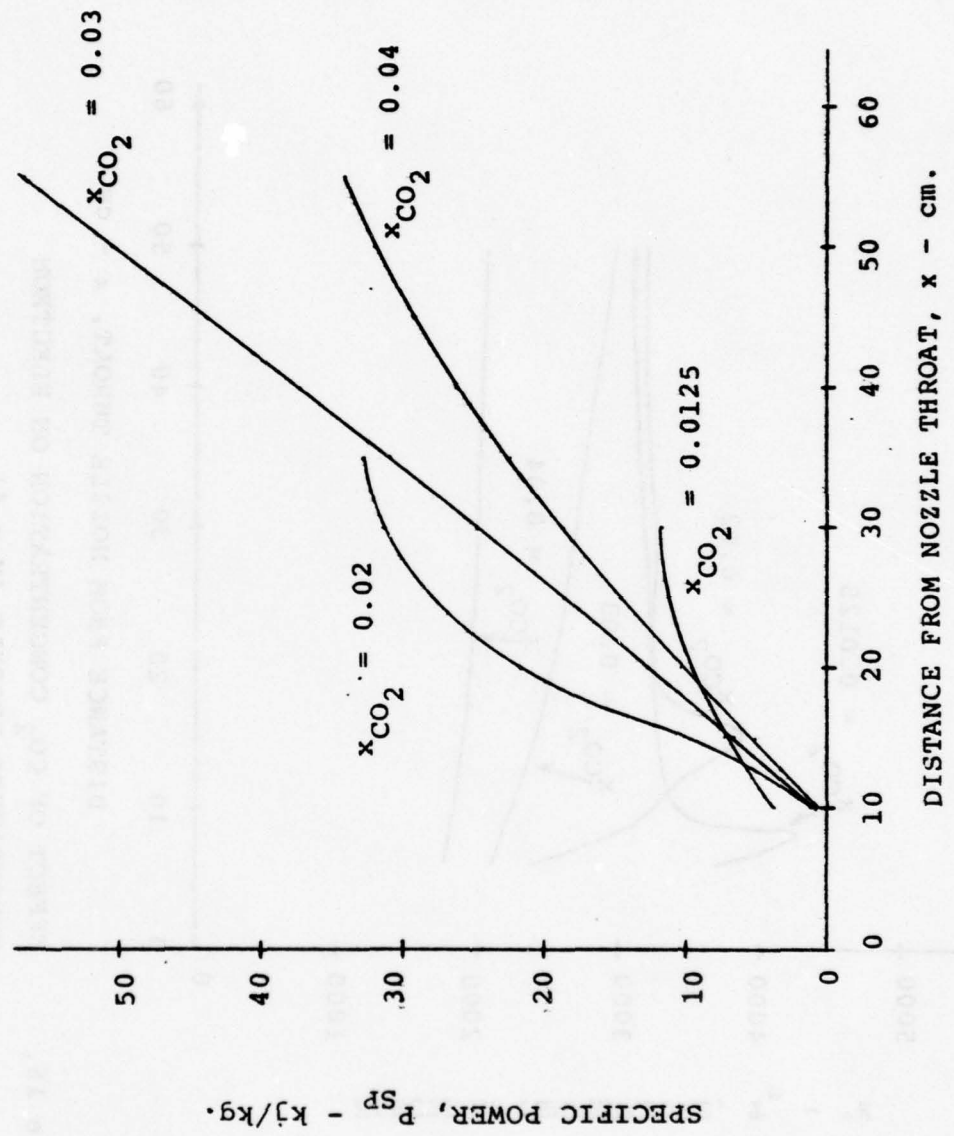


Figure 15.

EFFECT OF CO_2 CONCENTRATION ON SPECIFIC POWER GROWTH.

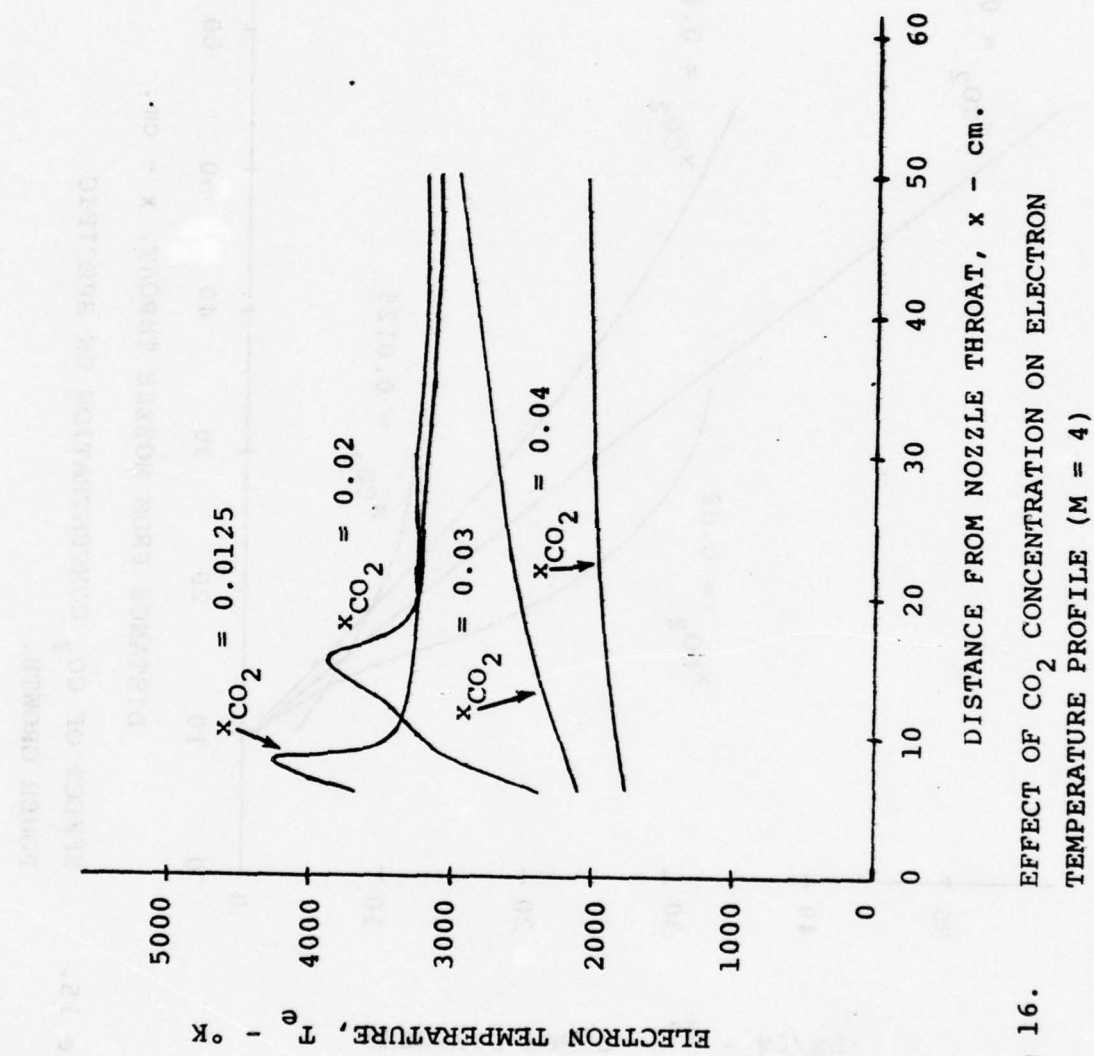


Figure 16.

EFFECT OF CO_2 CONCENTRATION ON ELECTRON
TEMPERATURE PROFILE ($M = 4$)

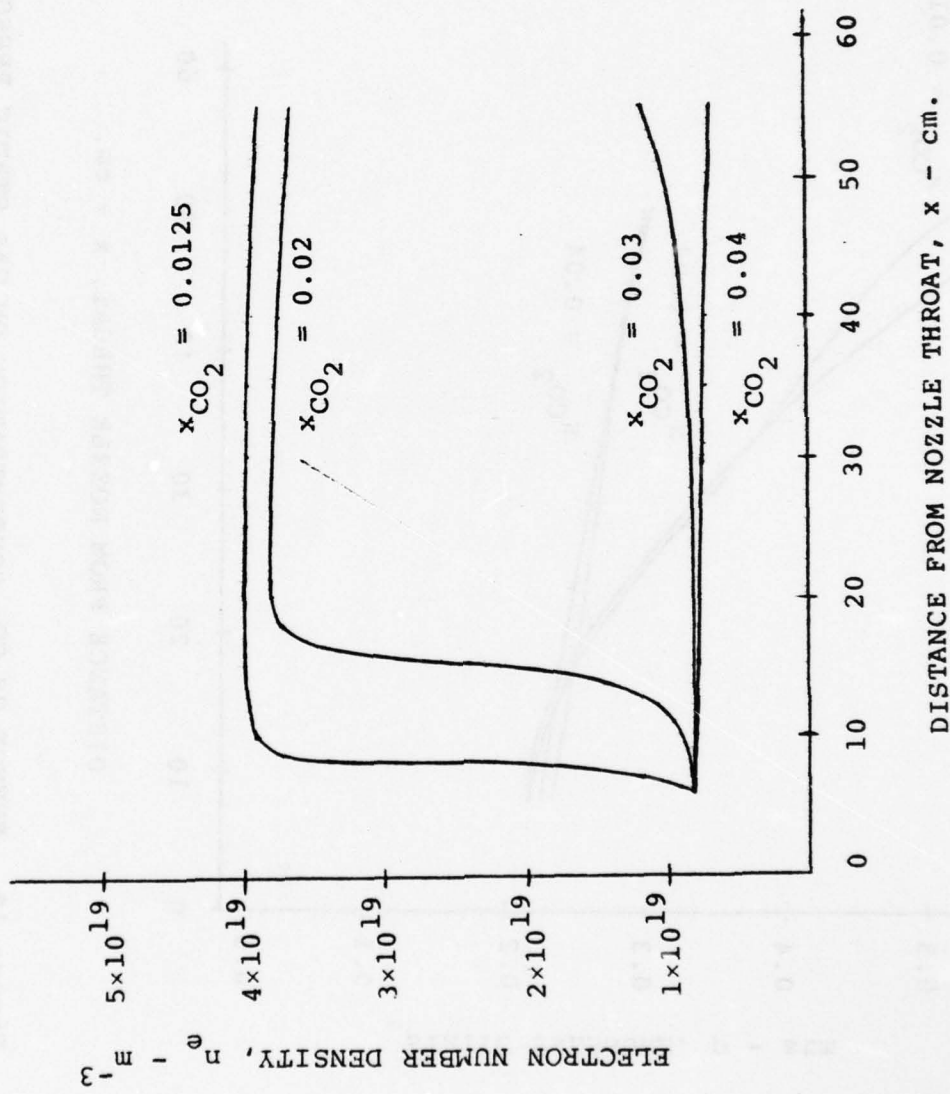


Figure 17. EFFECT OF CO_2 CONCENTRATION ON ELECTRON NUMBER DENSITY ($M = 4$)

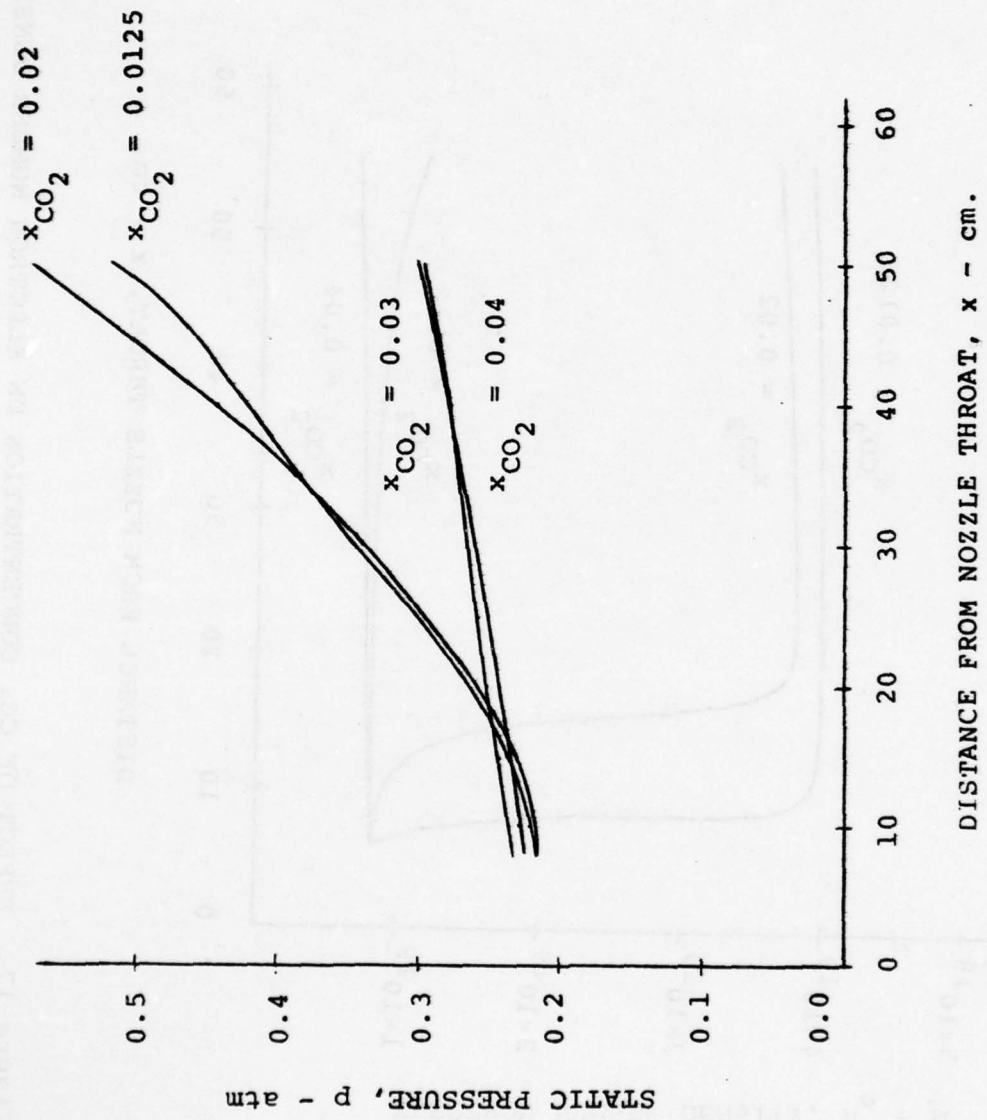


Figure 18. EFFECT OF CO_2 CONCENTRATION ON GAS STATIC PRESSURE ($M = 4$)

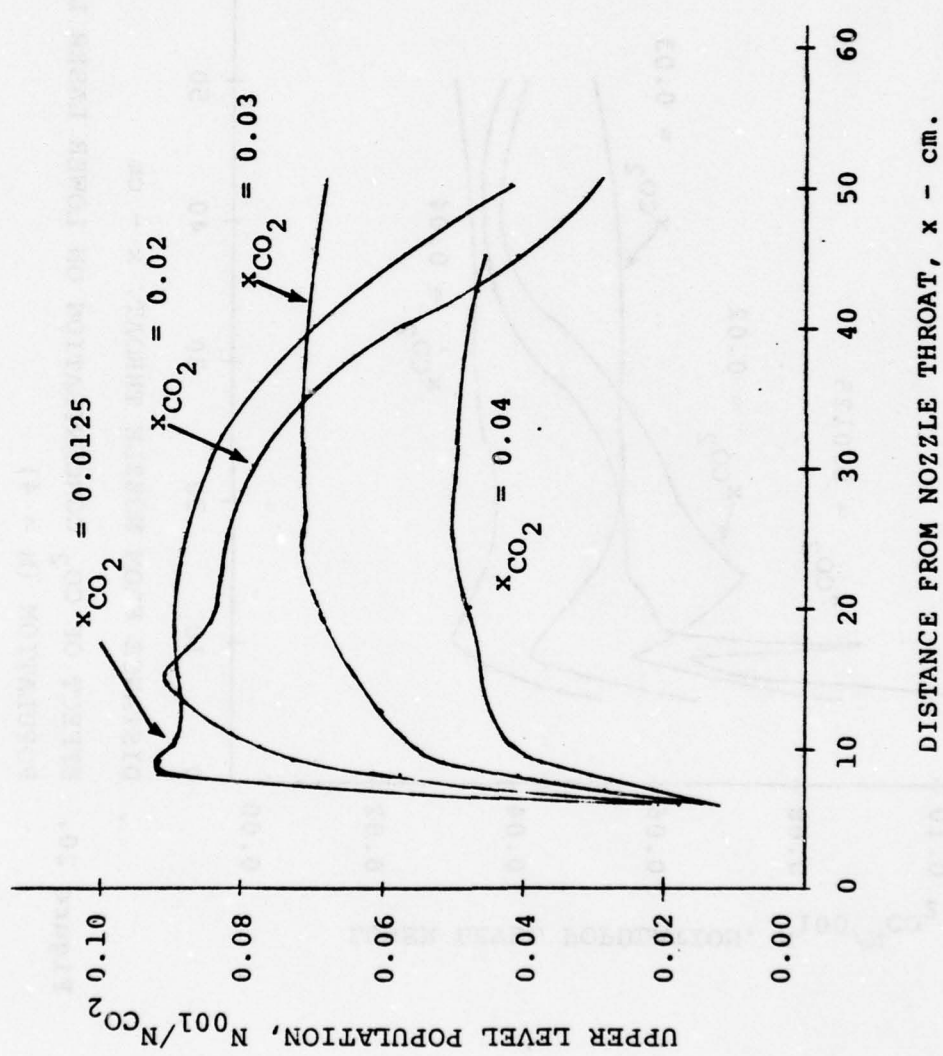


Figure 19. EFFECT OF CO_2 CONCENTRATION ON UPPER LEVEL POPULATION ($M = 4$).

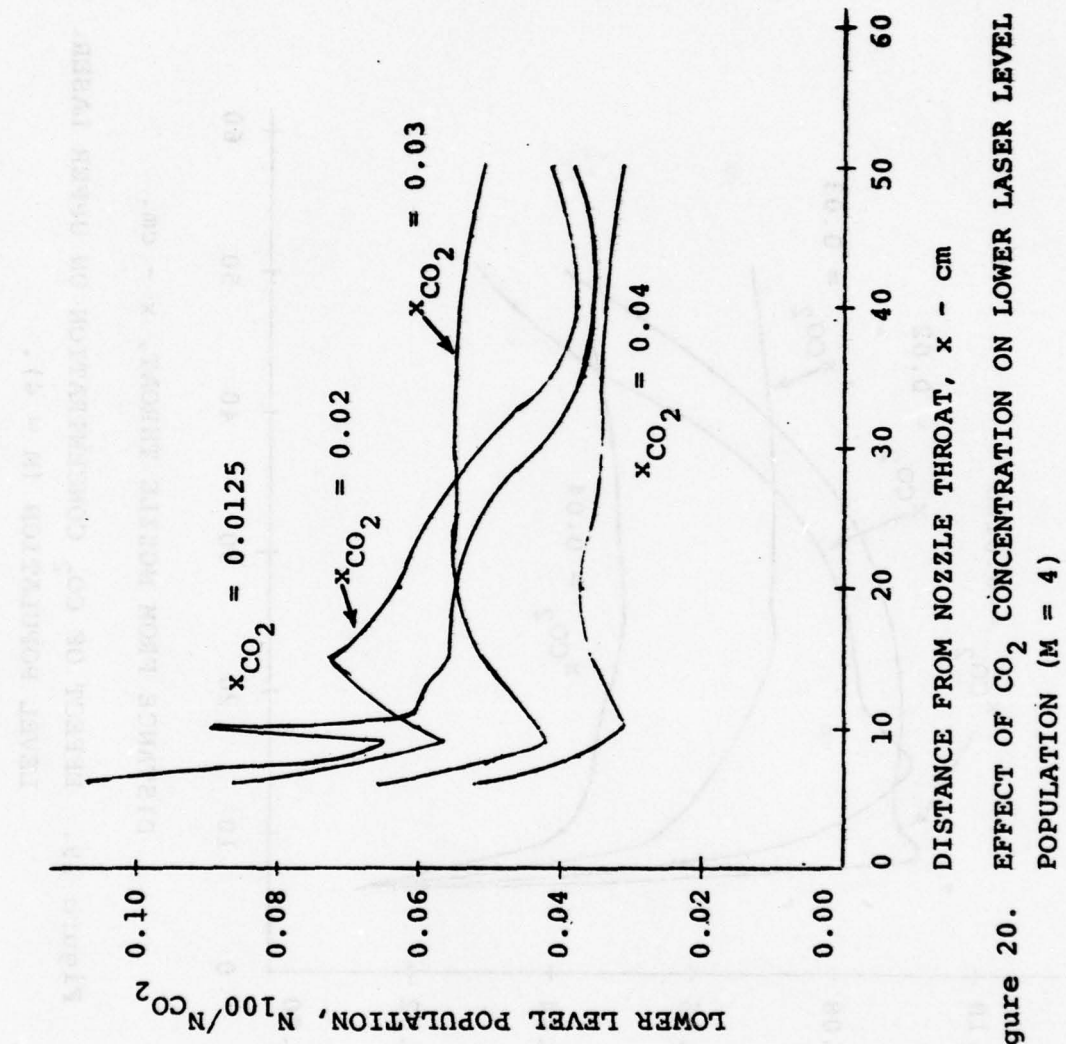


Figure 20. EFFECT OF CO₂ CONCENTRATION ON LOWER LASER LEVEL POPULATION (M = 4)

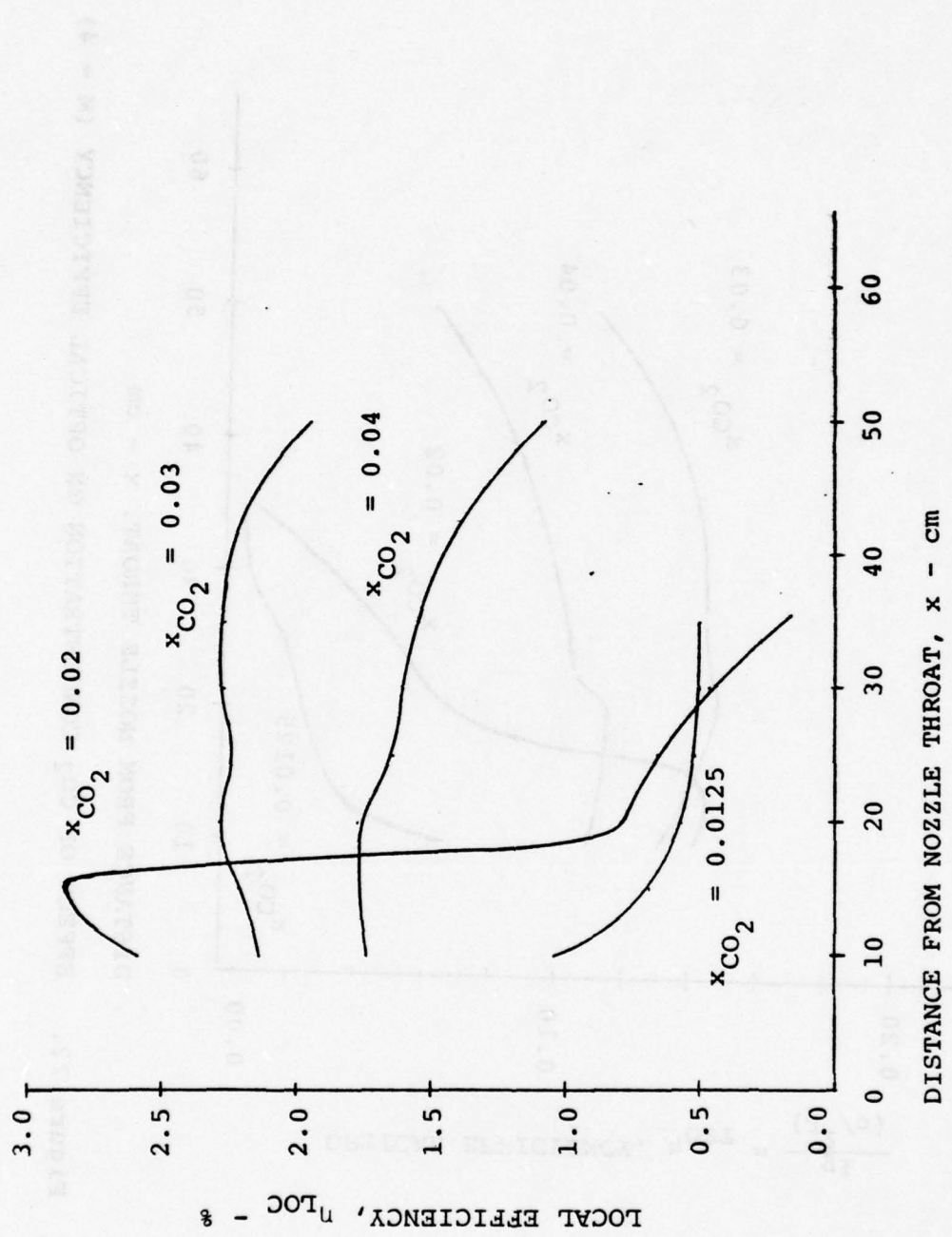


Figure 21. EFFECT OF CO_2 CONCENTRATION ON LOCAL EFFICIENCY ($M = 4$)

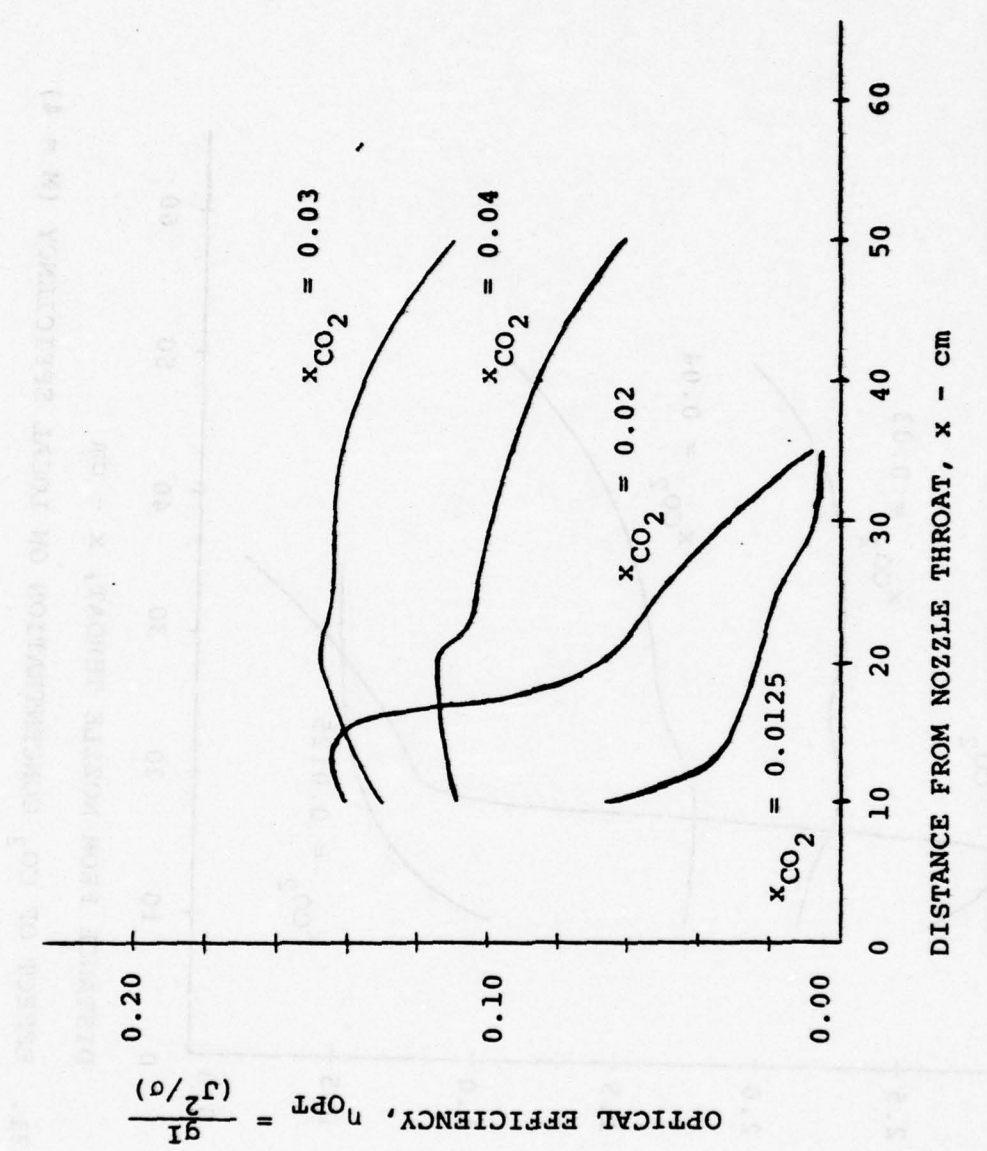


Figure 22. EFFECT OF CO_2 CONCENTRATION ON OPTICAL EFFICIENCY ($M = 4$)

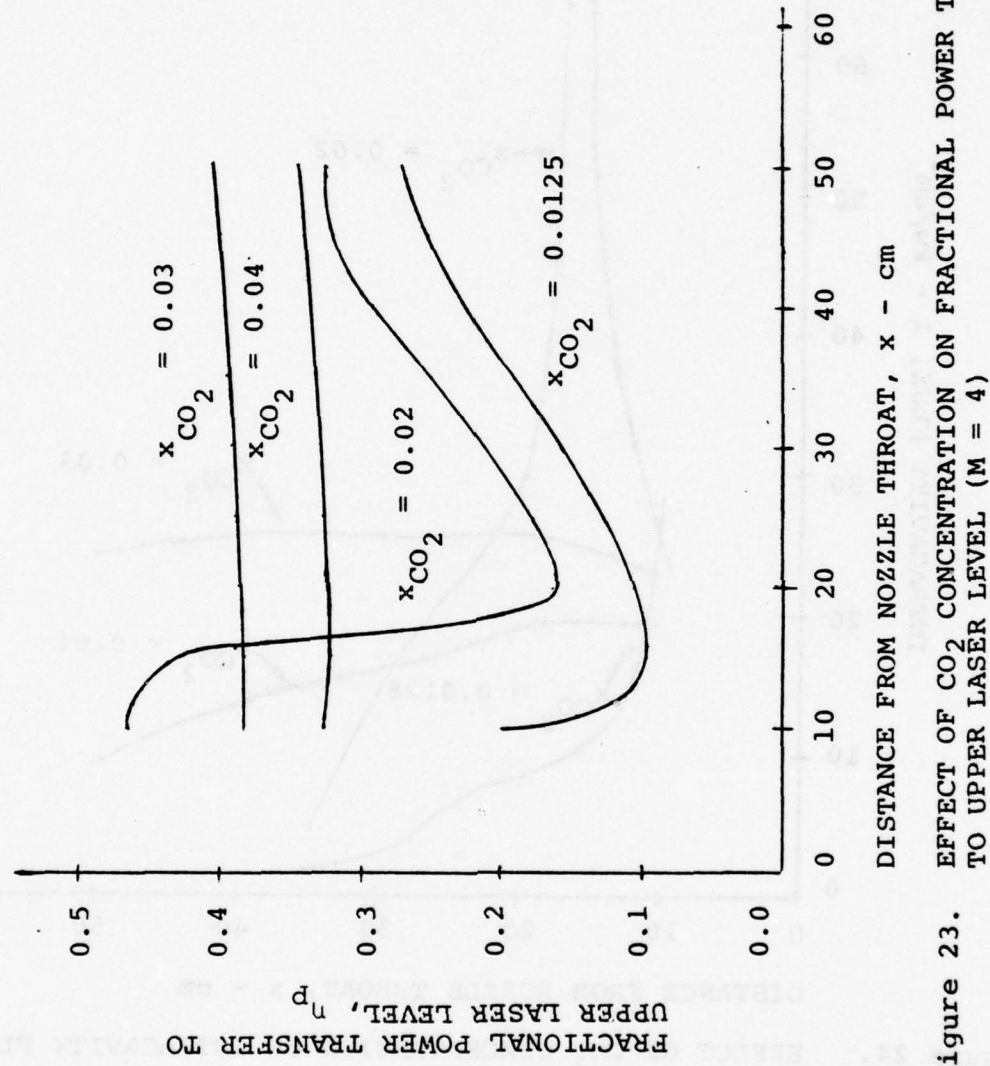


Figure 23. EFFECT OF CO_2 CONCENTRATION ON FRACTIONAL POWER TRANSFER TO UPPER LASER LEVEL ($M = 4$)

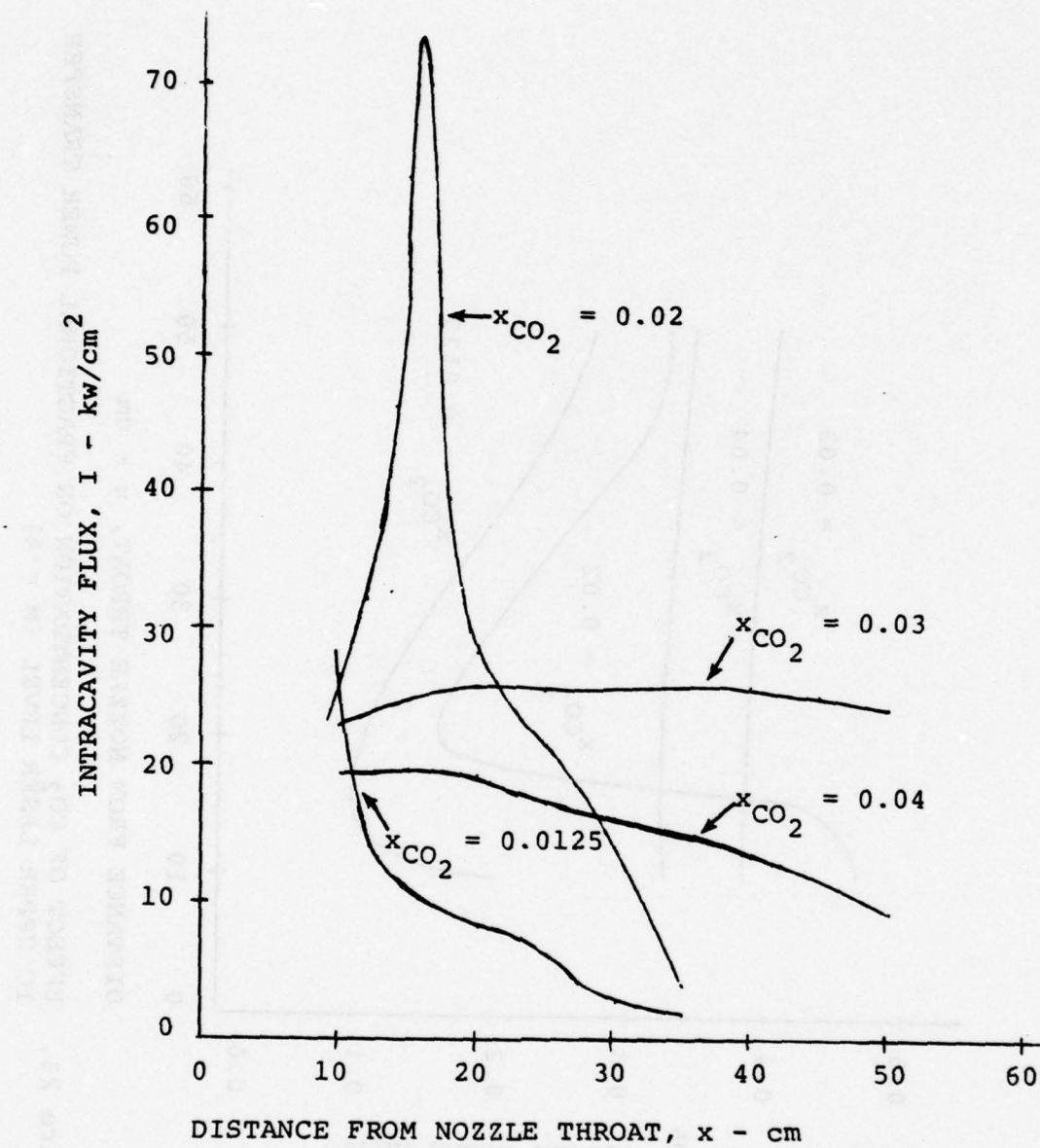


Figure 24. EFFECT OF CO_2 CONCENTRATION ON INTRACAVITY FLUX DEVELOPMENT ($M = 4$)

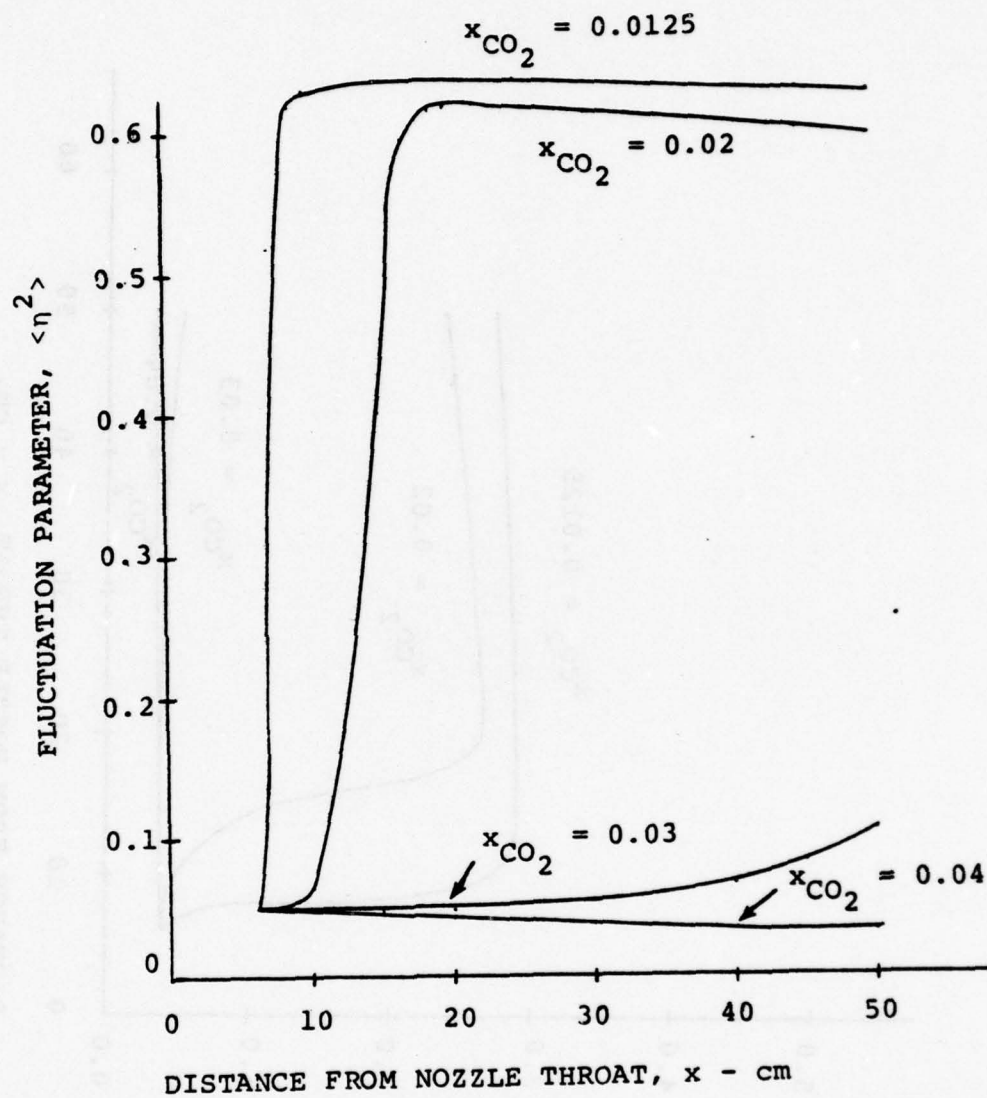


Figure 25. EFFECT OF CO_2 CONCENTRATION ON FLUCTUATION PARAMETER GROWTH ($M = 4$)

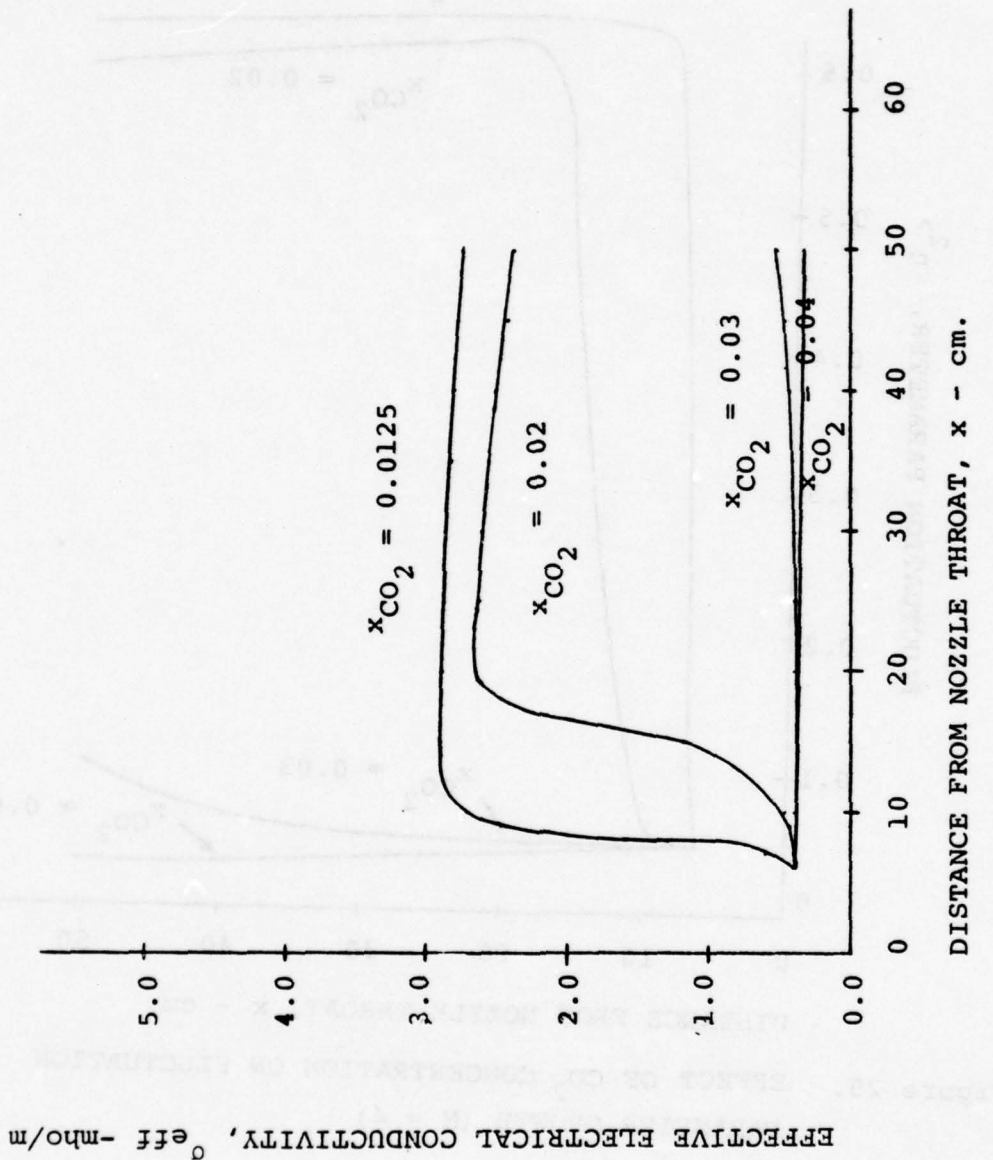


Figure 26. EFFECT OF CO_2 CONCENTRATION ON EFFECTIVE CONDUCTIVITY OF PLASMA

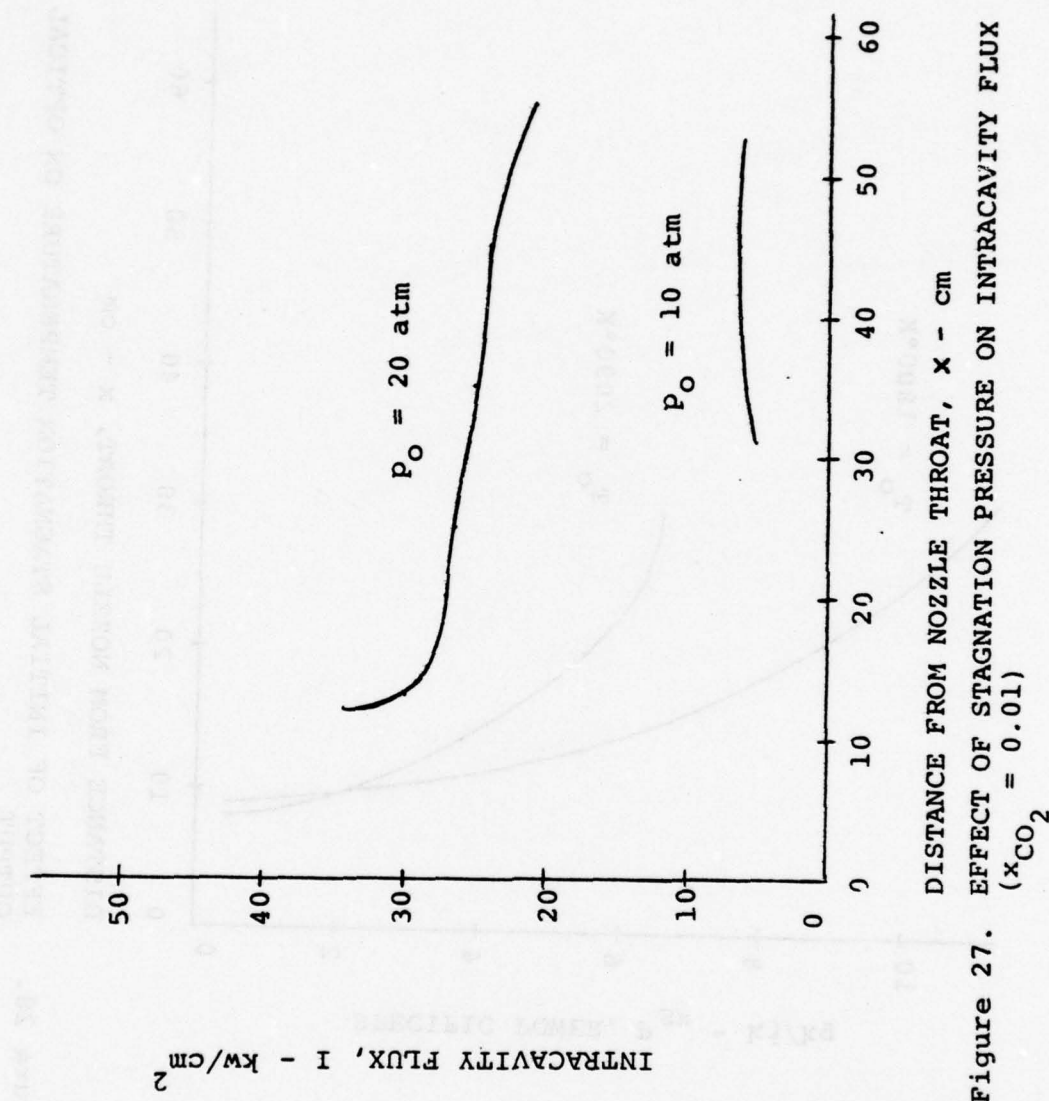


Figure 27. EFFECT OF STAGNATION PRESSURE ON INTRACAVITY FLUX
 $(x_{\text{CO}_2} = 0.01)$

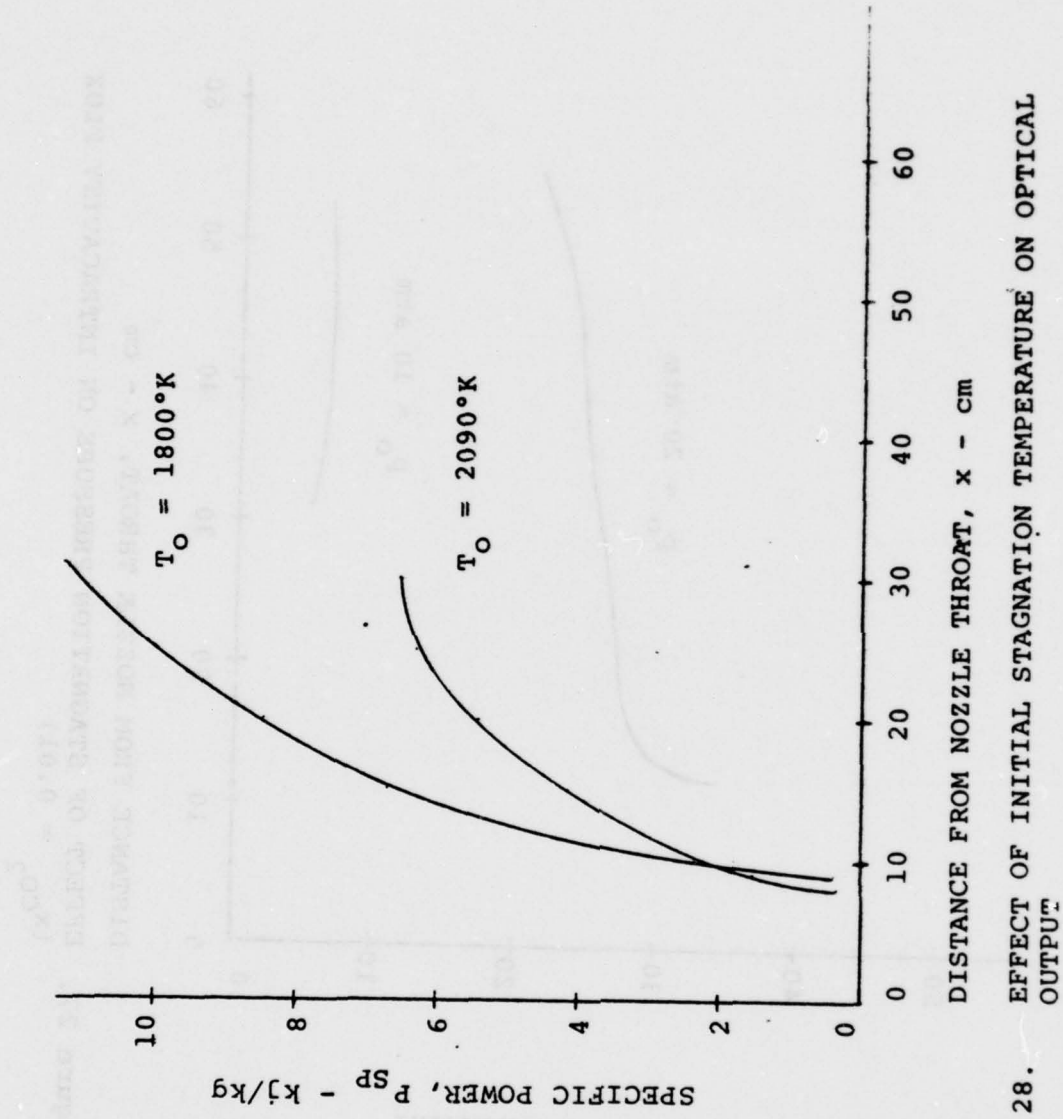


Figure 28. EFFECT OF INITIAL STAGNATION TEMPERATURE ON OPTICAL OUTPUT

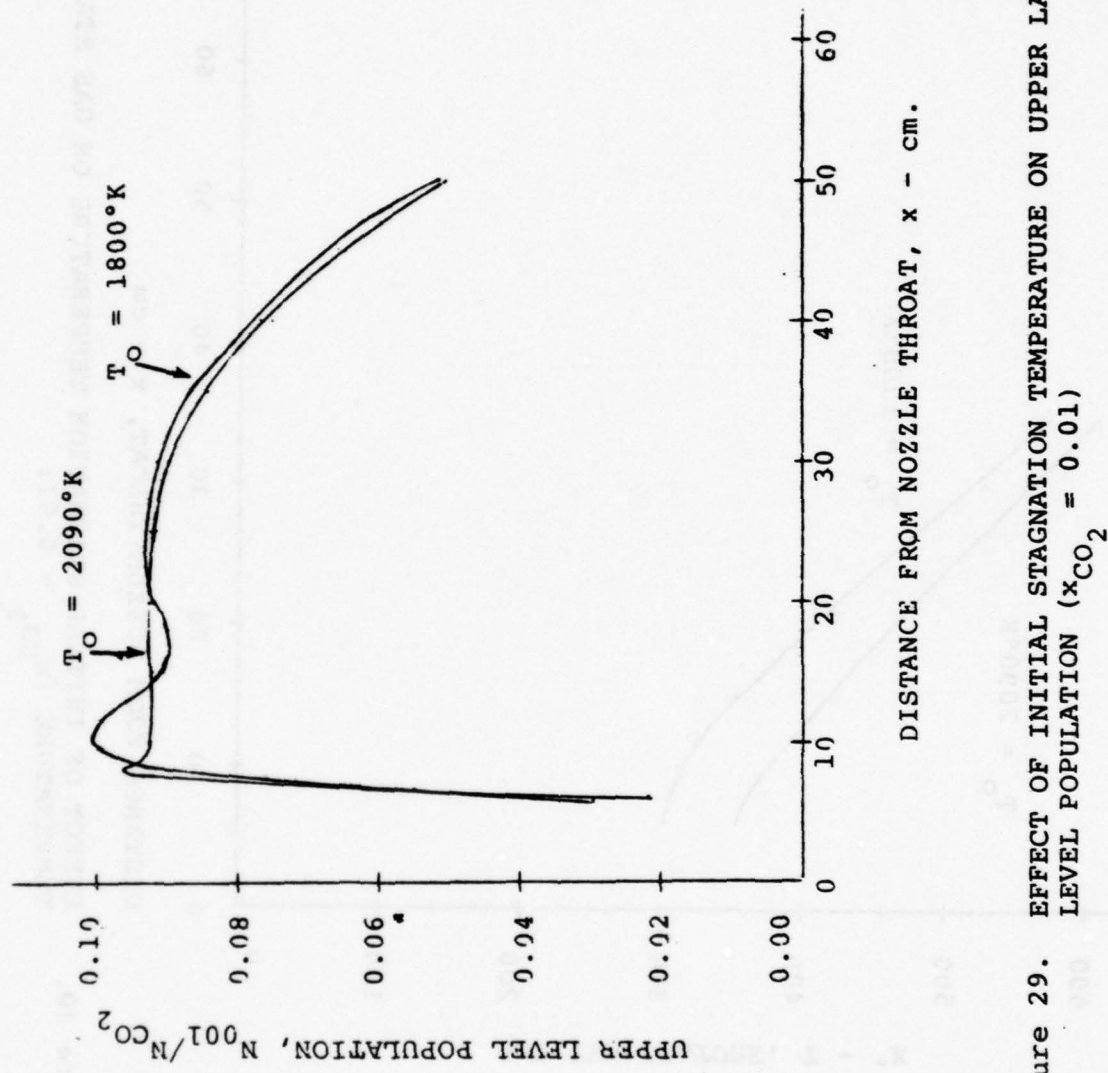


Figure 29. EFFECT OF INITIAL STAGNATION TEMPERATURE ON UPPER LASER LEVEL POPULATION ($x_{CO_2} = 0.01$)

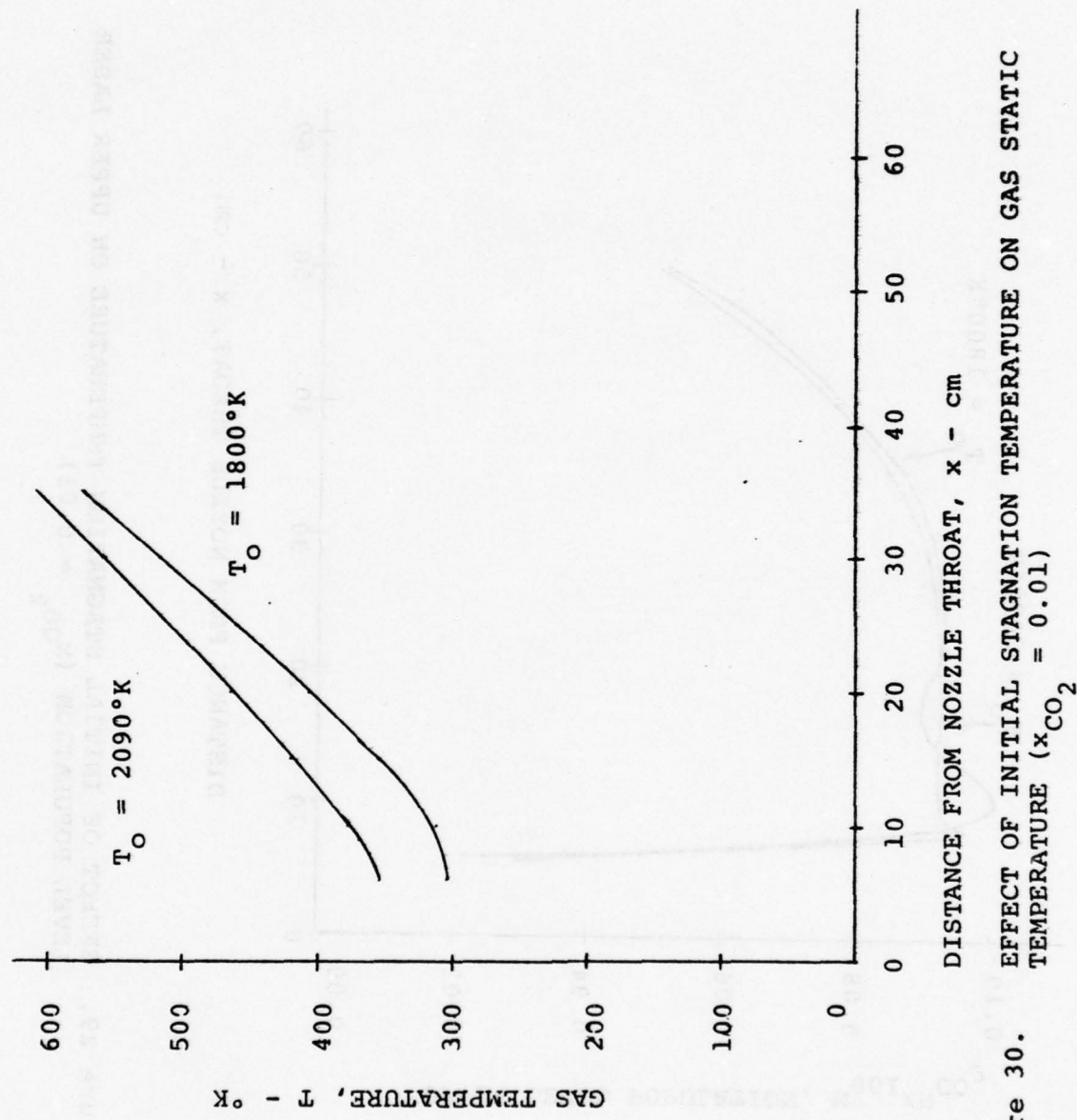


Figure 30. EFFECT OF INITIAL STAGNATION TEMPERATURE ON GAS STATIC TEMPERATURE ($x_{\text{CO}_2} = 0.01$)

235

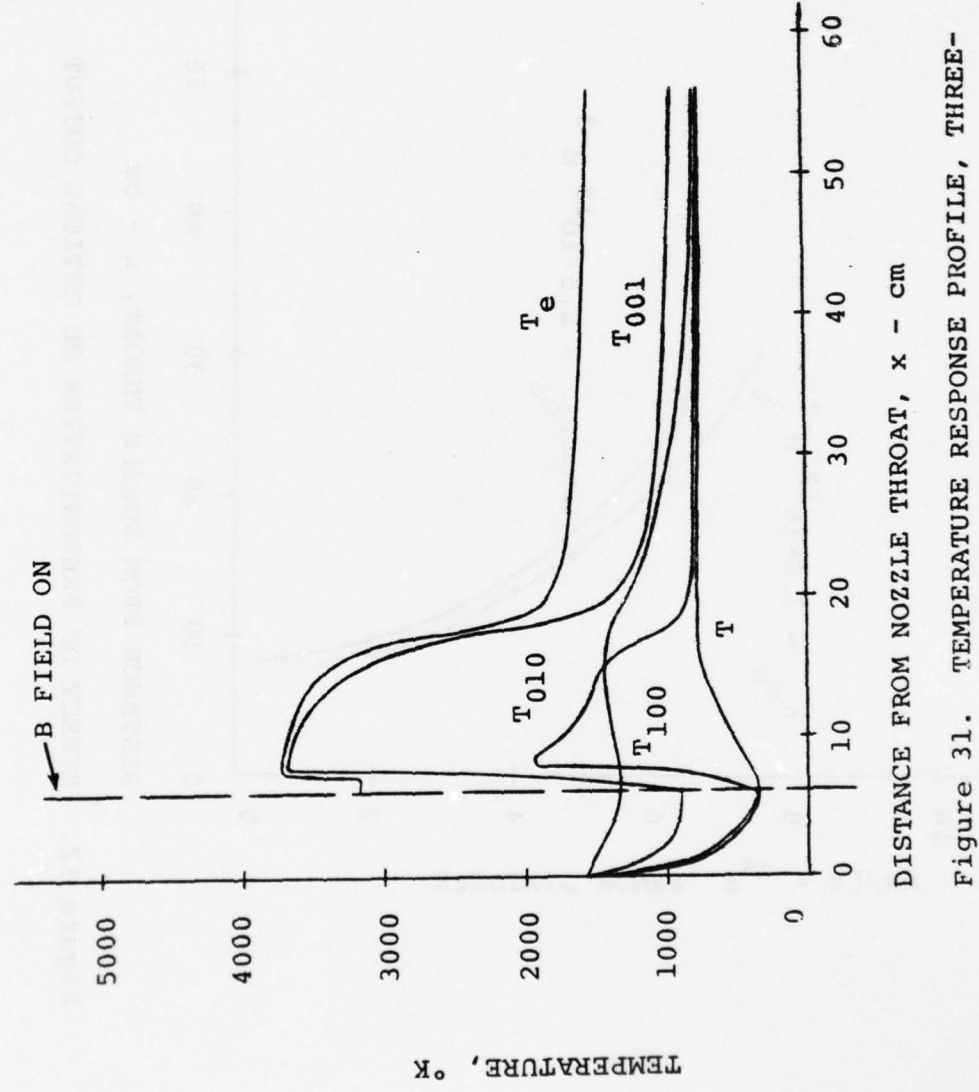


Figure 31. TEMPERATURE RESPONSE PROFILE, THREE-TEMPERATURE MODEL

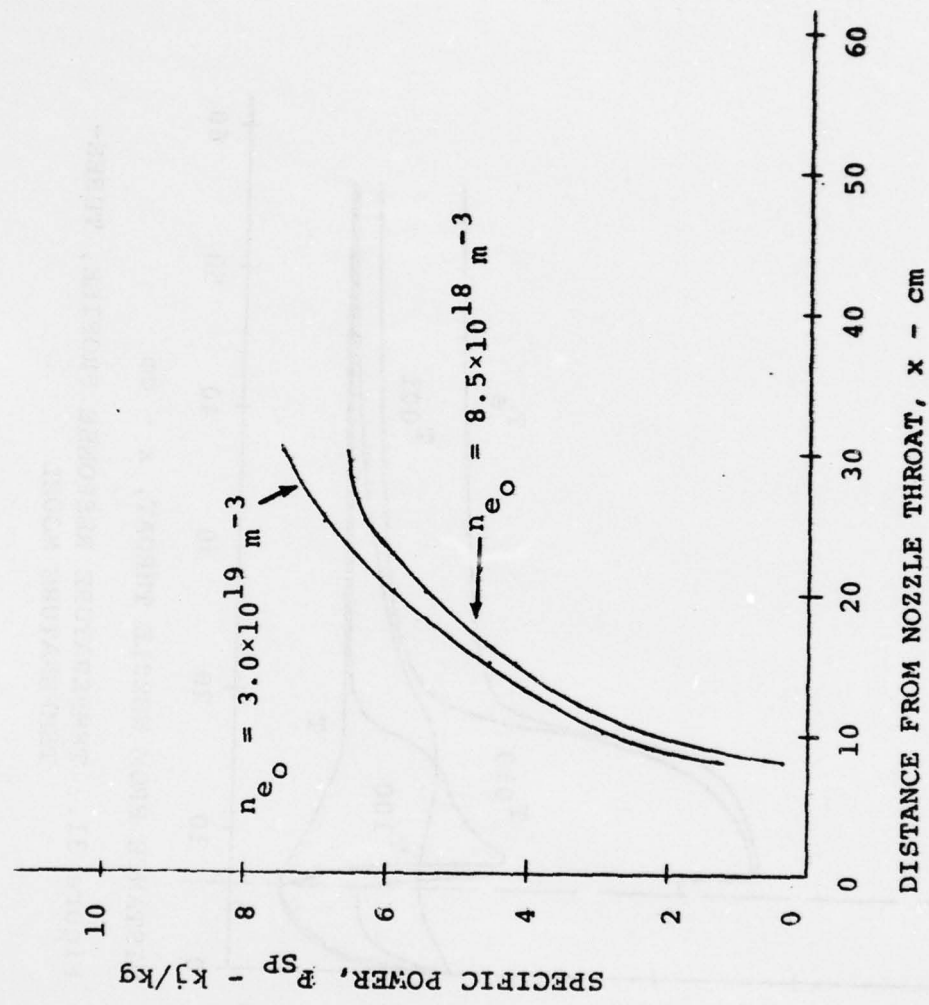


Figure 32. EFFECT OF PREIONIZATION ON OPTICAL OUTPUT

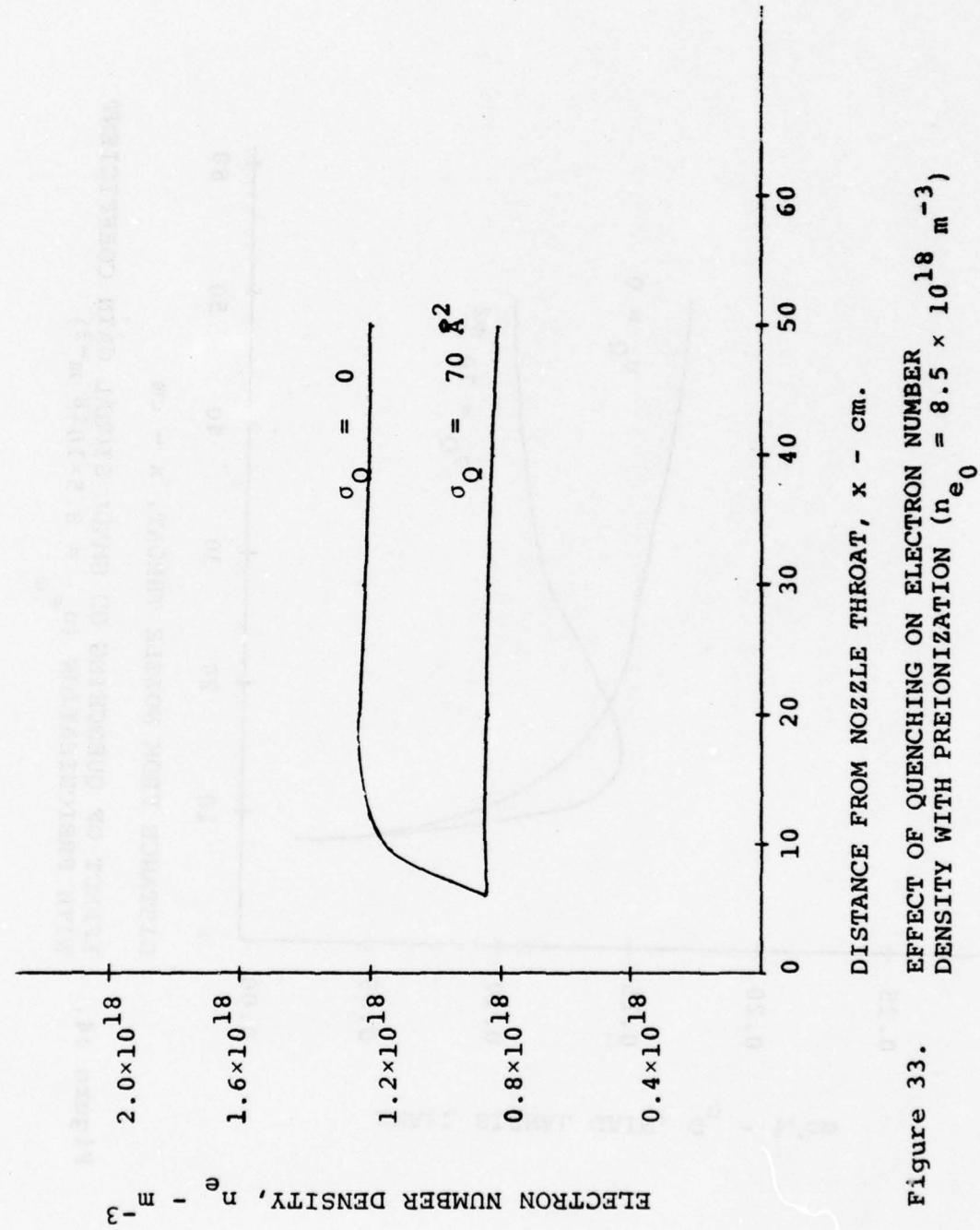


Figure 33.
EFFECT OF QUENCHING ON ELECTRON NUMBER
DENSITY WITH PREIONIZATION ($n_{e0} = 8.5 \times 10^{18} m^{-3}$)

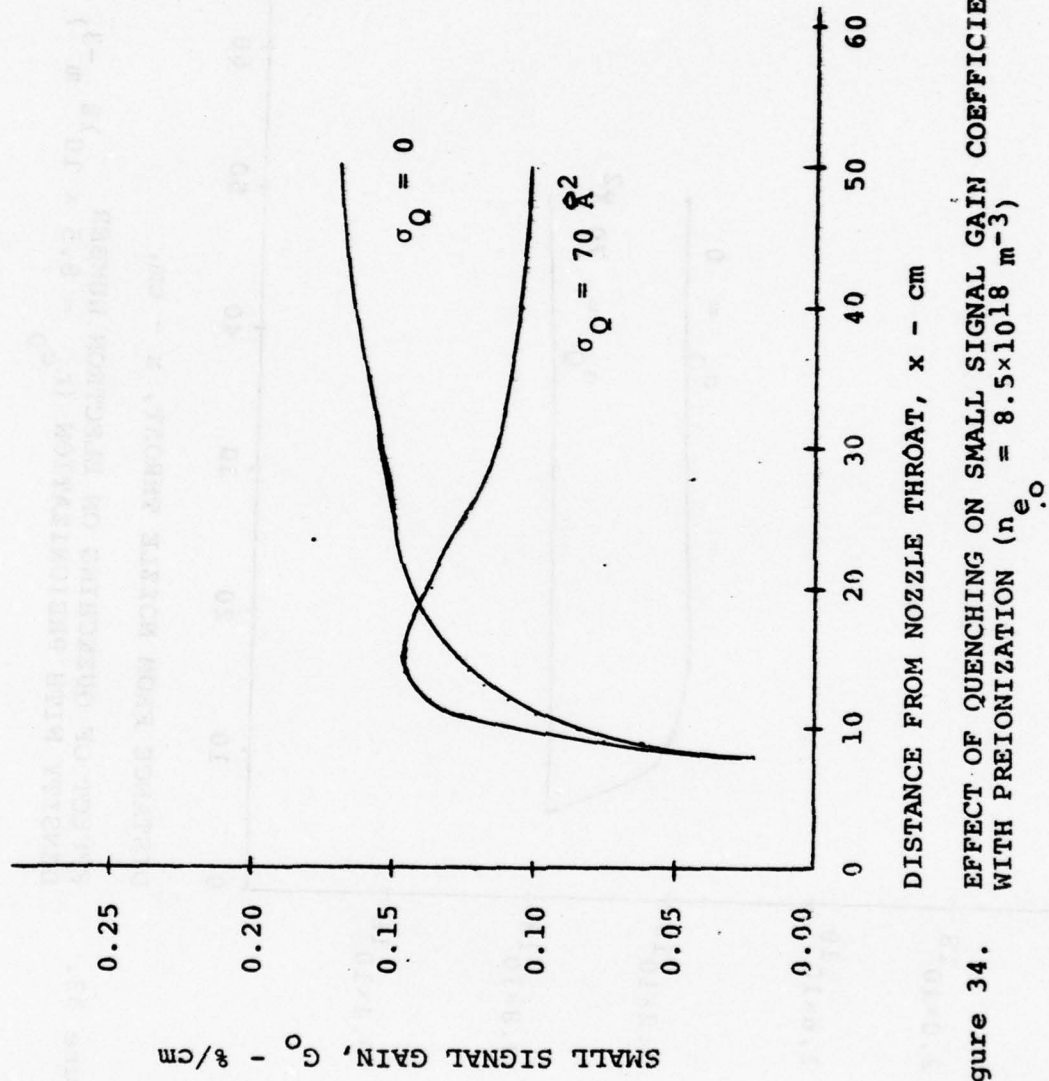


Figure 34. EFFECT OF QUENCHING ON SMALL SIGNAL GAIN COEFFICIENT WITH PREIONIZATION ($n_{e_0} = 8.5 \times 10^{18} \text{ m}^{-3}$)

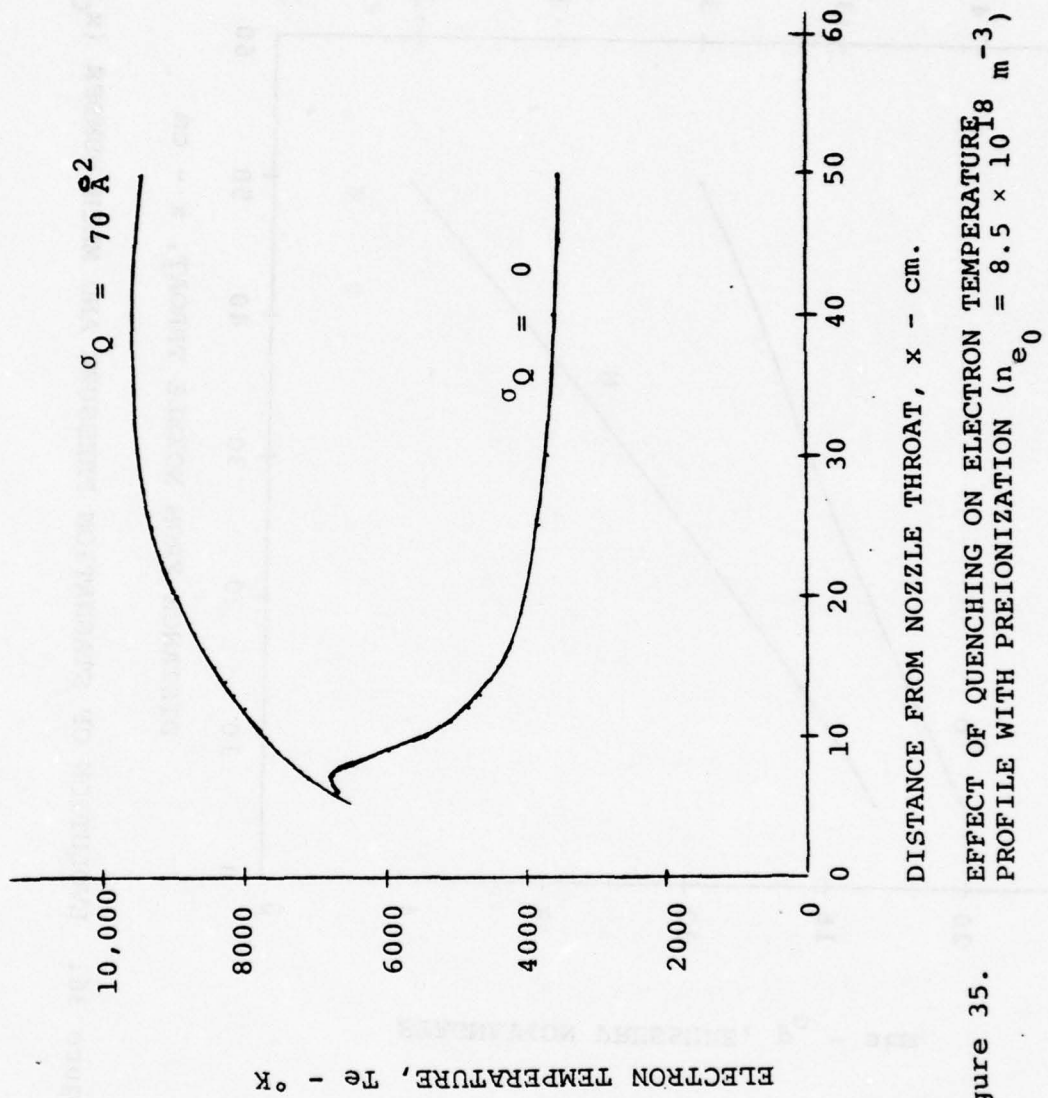


Figure 35. EFFECT OF QUENCHING ON ELECTRON TEMPERATURE ($n_{e_0} = 8.5 \times 10^{18} \text{ m}^{-3}$) PROFILE WITH PREIONIZATION

Figure 35.

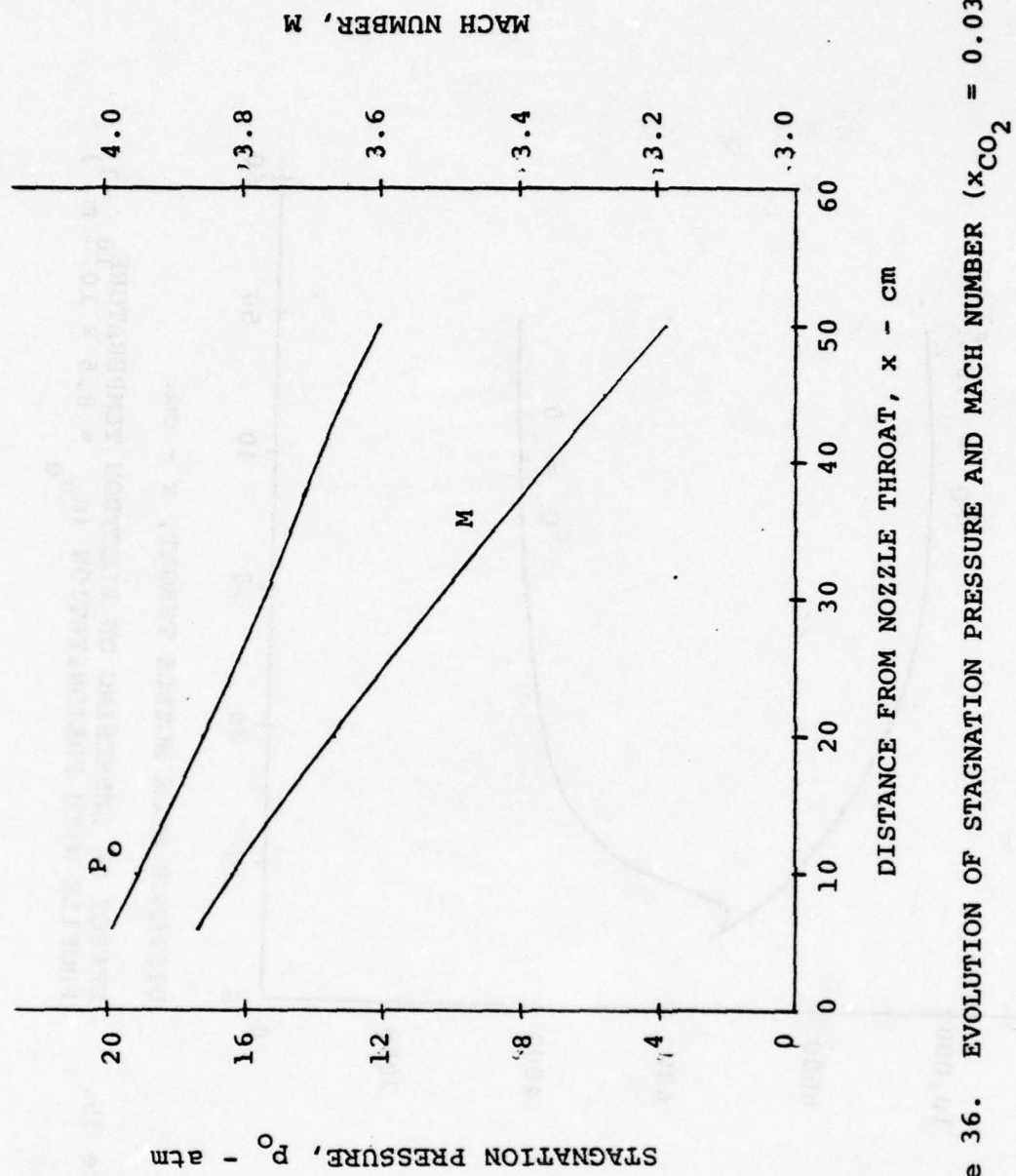


Figure 36. EVOLUTION OF STAGNATION PRESSURE AND MACH NUMBER ($x_{CO_2} = 0.03$)

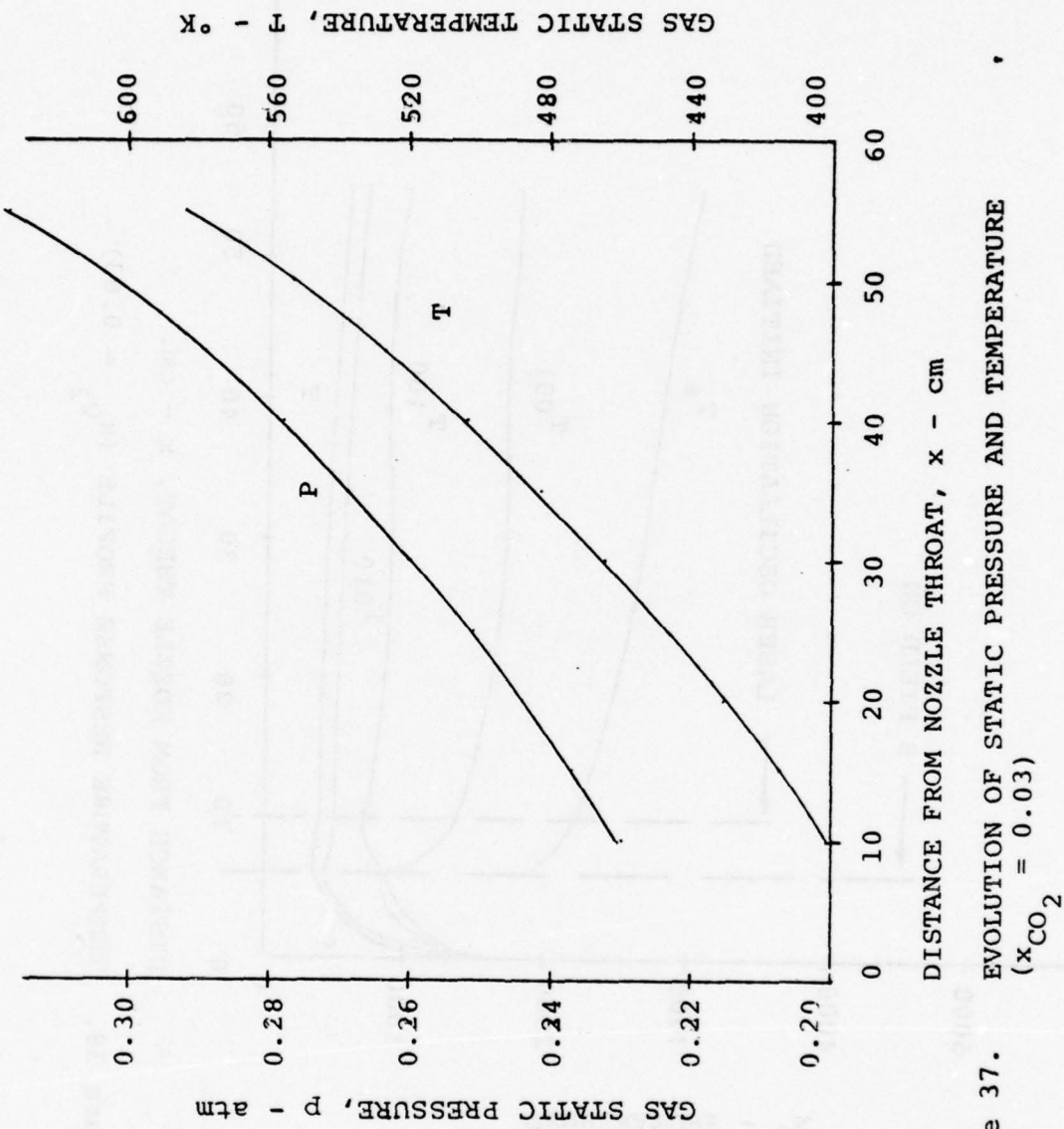


Figure 37.

EVOLUTION OF STATIC PRESSURE AND TEMPERATURE
 $(x_{CO_2} = 0.03)$

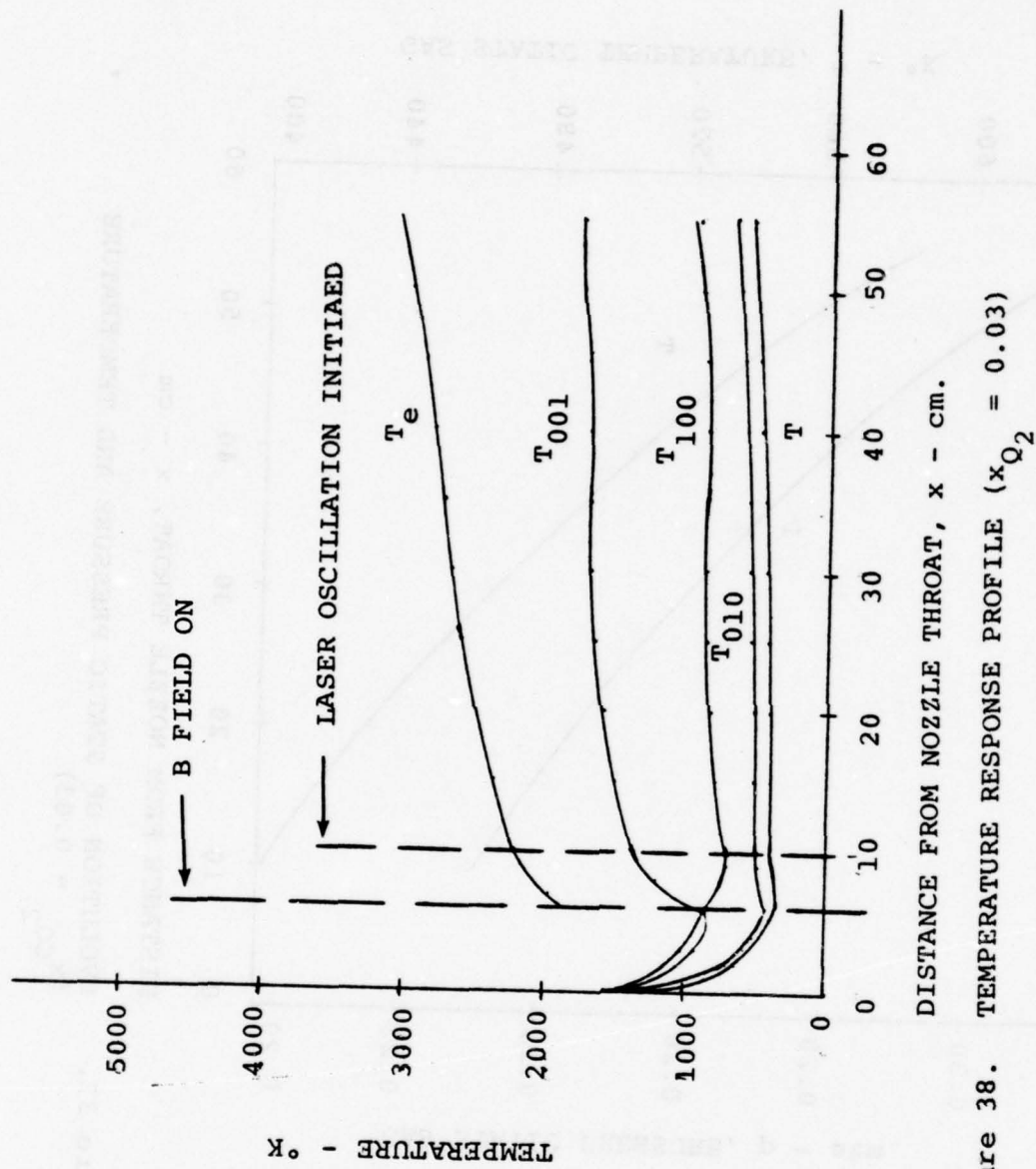


Figure 38. TEMPERATURE RESPONSE PROFILE ($x_{Q_2} = 0.03$)

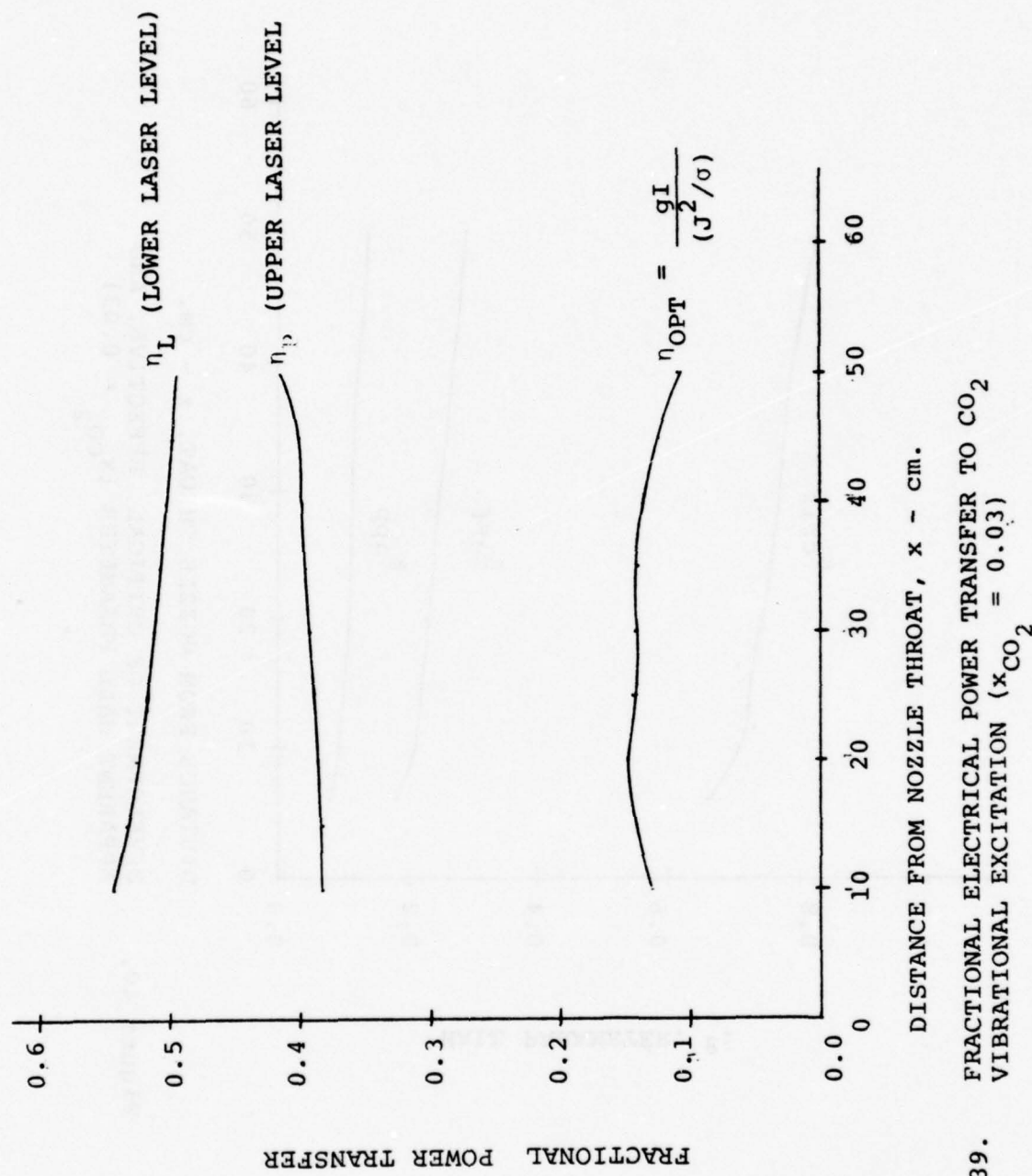


Figure 39.

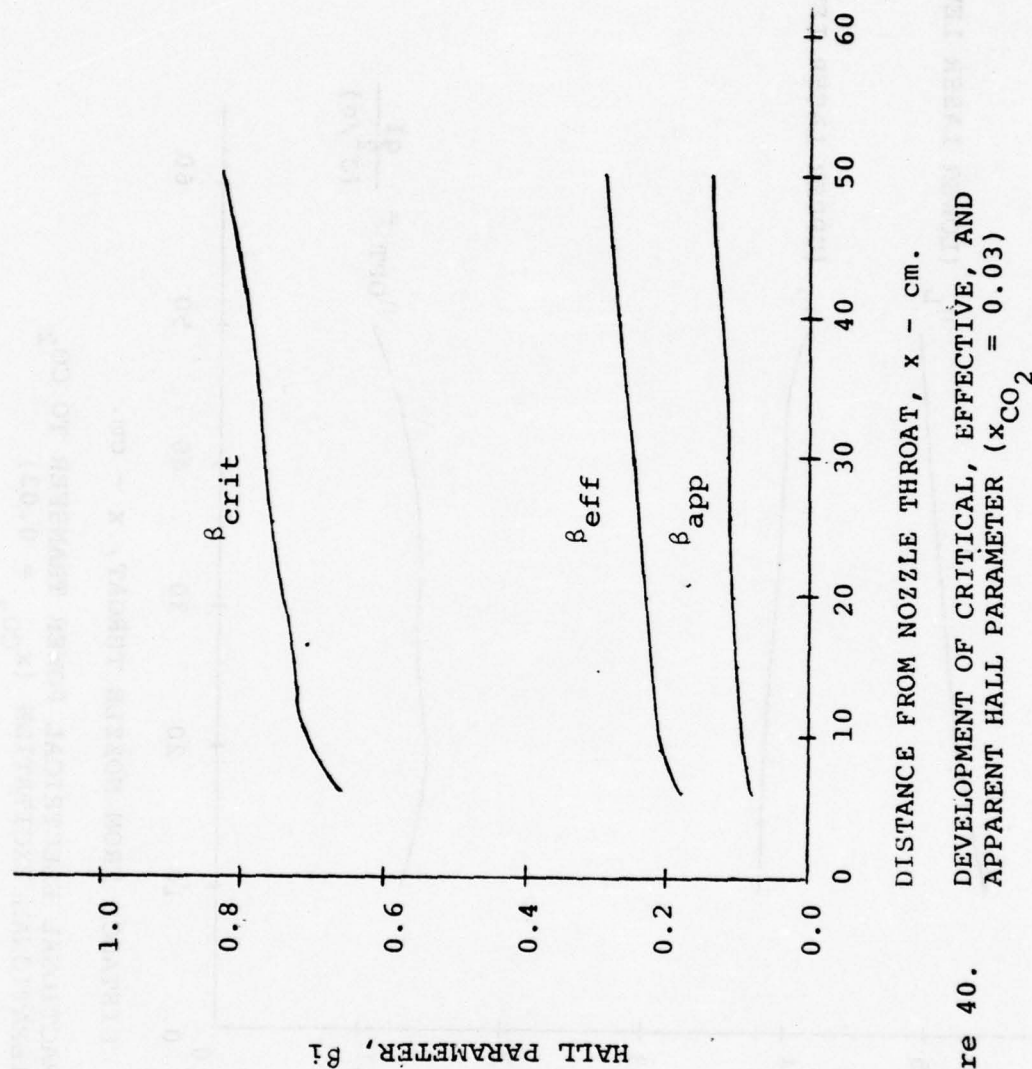


Figure 40.

DEVELOPMENT OF CRITICAL, EFFECTIVE, AND APPARENT HALL PARAMETER ($x_{\text{CO}_2} = 0.03$)

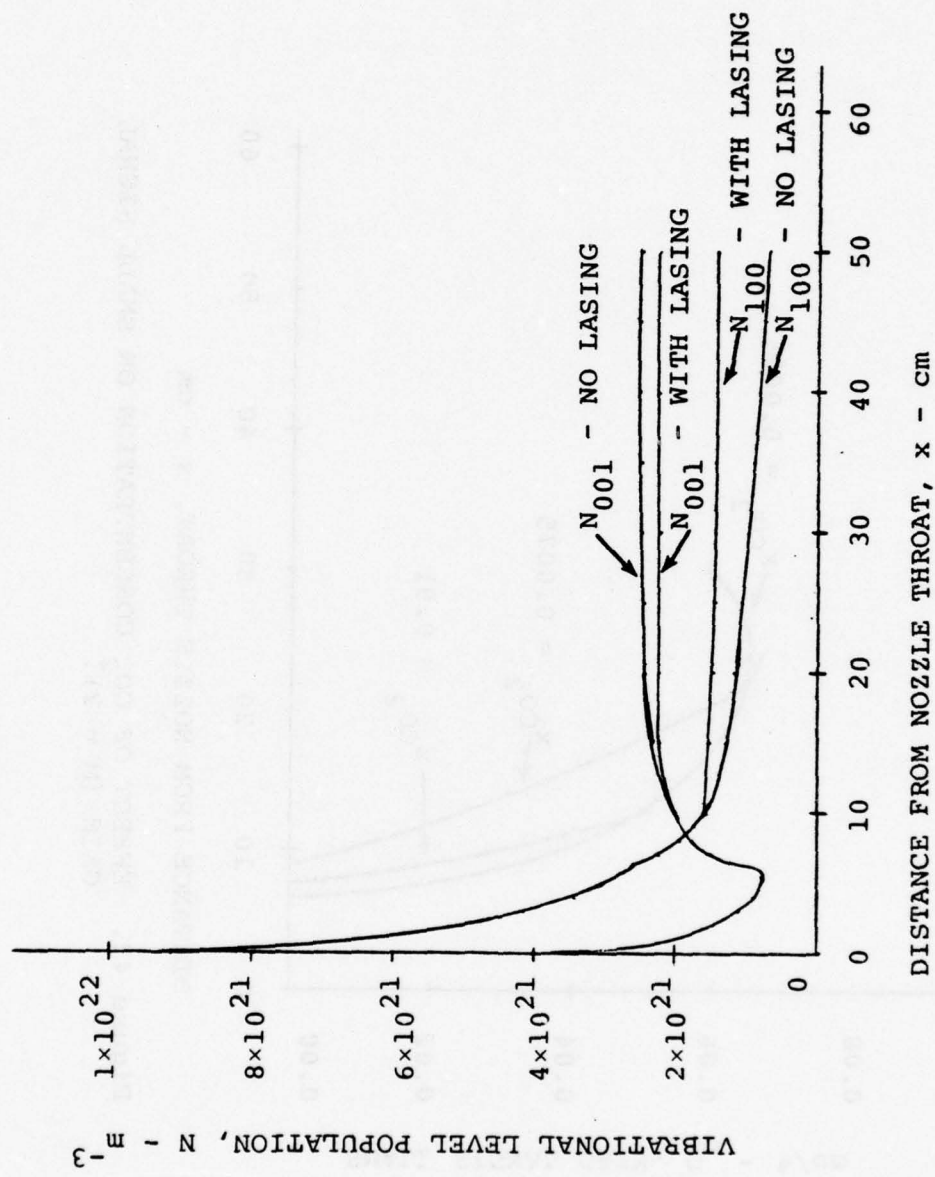


Figure 41. EFFECT OF LASING ON UPPER AND LOWER LEVEL POPULATIONS

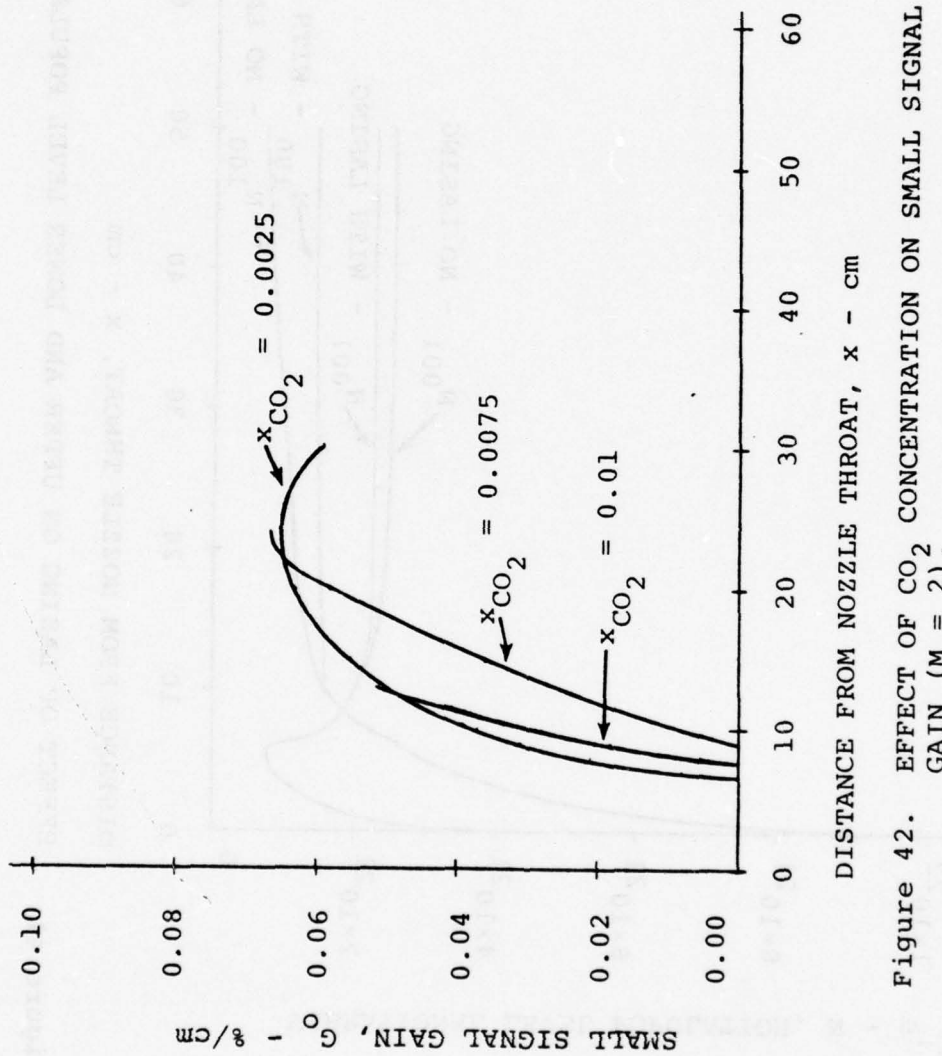


Figure 42. EFFECT OF CO_2 CONCENTRATION ON SMALL SIGNAL GAIN ($M = 2$).

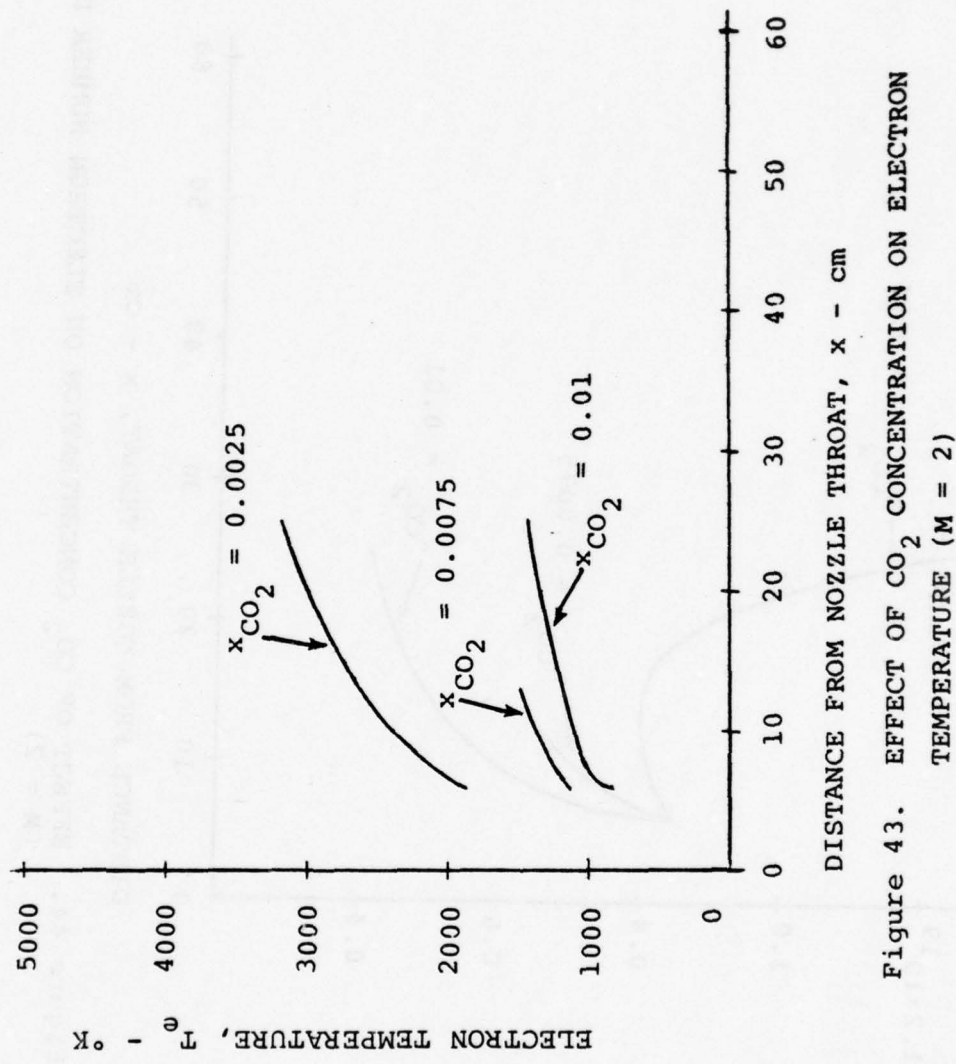


Figure 43. EFFECT OF CO_2 CONCENTRATION ON ELECTRON TEMPERATURE ($M = 2$)

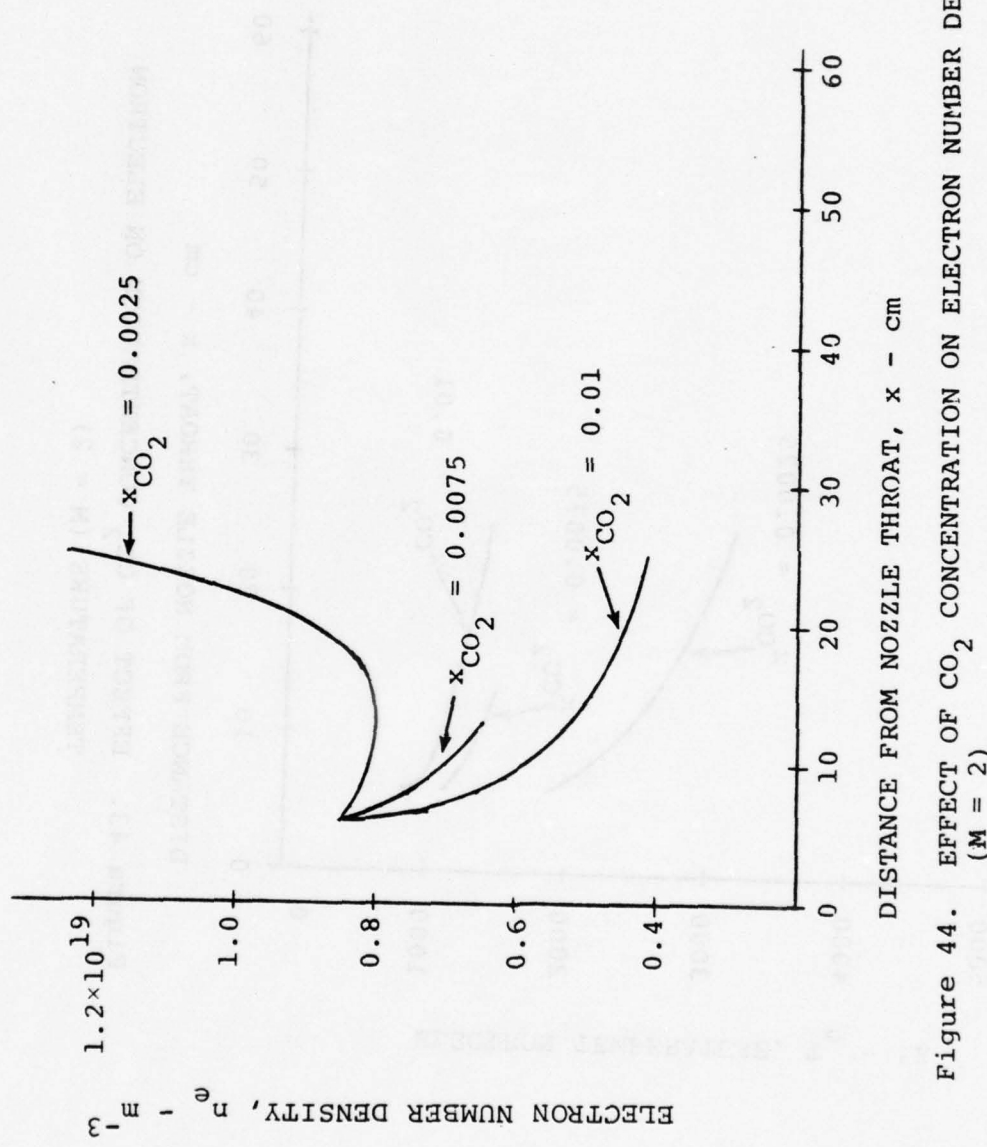


Figure 44. EFFECT OF CO_2 CONCENTRATION ON ELECTRON NUMBER DENSITY
($M = 2$)

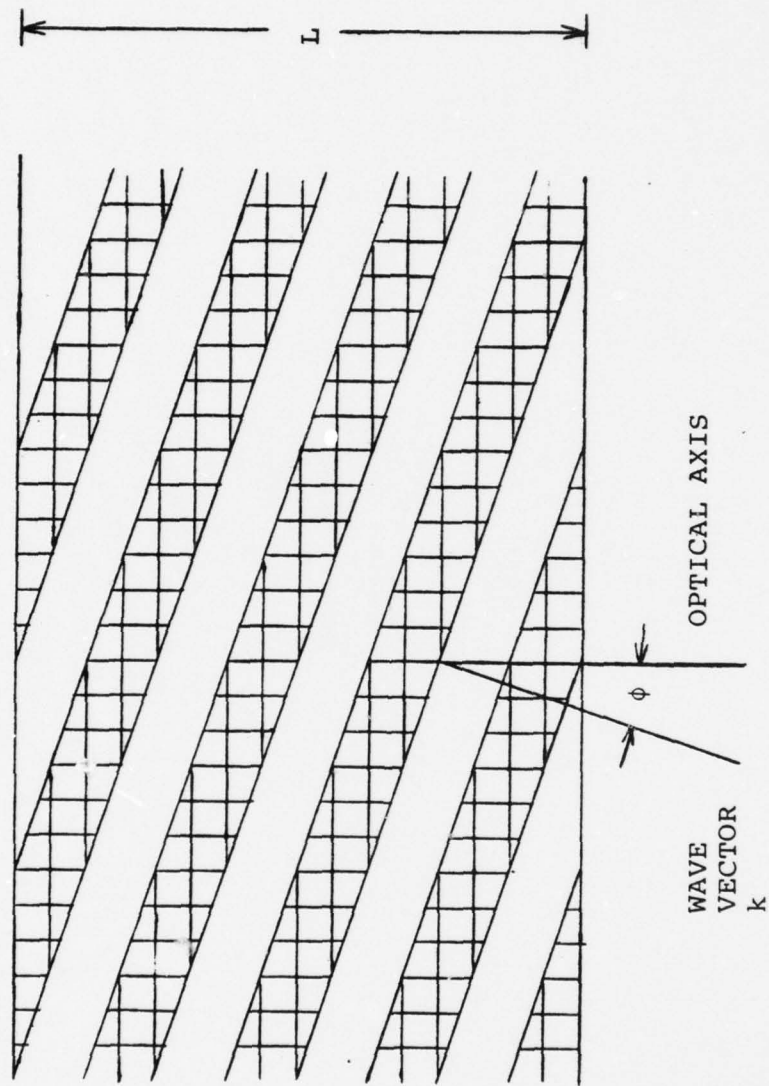


Figure 45. ORIENTATION OF ELECTROTHERMAL WAVE STRIATIONS

PART III

EXPERIMENTAL INVESTIGATION OF THE PHYSICAL PROCESSES
IN A MAGNETOHYDRODYNAMIC LASER

LIST OF SYMBOLS

a	optical depth
a_1, a_2	mirror absorption coefficient
A	geometric area
A^*	nozzle throat area
A_{ji}	Einstein coefficient for transition from j level to i level.
\bar{B}	magnetic induction
B_v	Einstein coefficient for alkali $7P_{3/2} - 6S_{1/2}$ transition
c	speed of light
\bar{c}_{ij}	relation collision velocity between species i and j, averaged over the distribution function.
\bar{E}	electric field in gas frame
E_j	Energy density of j th vibrational level of CO_2 molecule
f_j	mole fraction of 'j' species
$g(v)$	line shape function
h	Plank's constant
I	optical intensity
I_0	output intensity
I_s	saturation optical intensity
I_v	intensity per unit wave length
J	rotational quantum number
\bar{J}	electric current density
J_x, J_y	x,y components of current density vector

k	Boltzmann constant
k_{i-j}	kinetic rate constant
k_{Total}	thermalization rate constant of CO_2 molecules with other neutral species
k_v	absorption coefficient of frequency v
$k_{\text{Rotational}}$	rate constant for thermalization of rotational levels in a given vibrational state
L	optical cavity length
m_e	mass of electron
m_H	mass of 'H' heavy neutral particle
\dot{m}	mass flow rate
M_j	molecular weight of 'j' species
n	index of refraction
n_{CO_2}	CO_2 number density
n_{He}	He number density
n_e	electron number density
N_1, N_{100}	lower laser level population
N_2, N_{001}	upper laser level population
p	pressure
p_0	stagnation pressure
P_0	optical output power
Q_i	cross section
r_1, r_2	mirror reflectivities
R_1, R_2	pumping rate of lower, upper laser levels

s ratio of effective to average conductivity
 t_1, t_2 mirror transmission coefficients
 T gas static temperature
 T_e electron temperature
 T_{rot} rotational temperature
 v gas velocity
 x axial coordinate
 y transverse coordinate in electric field and optical axis
direction
 z transverse coordinate in magnetic field direction

GREEK SYMBOLS

α	optical gain
α_0	small signal gain
β	Hall parameter
$\langle \beta \rangle$	average Hall parameter
β_{app}	apparent Hall parameter
β_{crit}	critical Hall parameter
β_{eff}	effective Hall parameter
δ	loss parameter
δ_{CO_2}	inelastic loss parameter for CO_2
λ	wave length
ν	frequency
ν_0	laser transition frequency at line center
ν_j	characteristic vibrational frequency of 'j' vibration level
ν_e	collision frequency
$\Delta\nu$	broadened line width
ν_e	electron collision frequency
ρ	gas density
σ	electrical conductivity
$\langle \sigma \rangle$	average conductivity
σ_{app}	apparent conductivity
σ_{eff}	effective conductivity
σ_j	collision cross section
$\tau_{e,j}$	relaxation time due to 'j' species
τ_{rad}	spontaneous decay time
τ_{spont}	

LIST OF FIGURES

<u>Figure</u>		<u>Page No.</u>
2.1	CO ₂ Energy Level Diagram	85
2.2	Electron Cross Section for Vibrational Excitation of CO ₂ Molecules from Ref. 7	86
3.1	Gas Flow System	87
3.2	Quartz Discharge Tube	88
3.3	End Flange	89
3.4	Discharge Current Pulse	90
3.5	Magnet Cross Section	91
3.6	Magnetic Field Distribution in Discharge Region	92
3.7	Magnetic Current Pulse	93
3.8	Cs Diagnostic System	94
3.9	Cs Absorption Diagnostics Calibration Experiment	95
3.10	Calibration Curve for Cs Absorption Diagnostics	96
3.11	Typical Scope Trace of Pressure Pulse (Top Solid Curve) and Cs Absorption Diagnostics (Chopped Curve)	97
3.12	Arrangement To Measure Optical Gain - (Schematic)	98
3.13	Gain Measurement	99
3.14	Sequence of Events During a Test	100
4.1	Measurement of Signal to Noise Ratio	101
4.2	Current Probe Calibration	102
4.3	Typical Scope Traces	103
4.4	Gain and Current Density Time History	104
4.5	Gain and Current Density (Exp. 4120)	105

LIST OF FIGURES (cont'd)

<u>Figure</u>		<u>Page No.</u>
4.6	Transient Behavior of Gain	106
4.7	Laser Gain vs Seed Mole Fraction; $B = 0$	107
4.8	Gain vs CO_2 Concentration	108
4.9	Gain and Current Density (Exp. 4163)	109
4.10	Gain and Current Density (Exp. 3050)	110
4.11	Gain vs B Field	111
4.12	Laser Gain vs Cs Mole Fraction; $B \neq 0$	112
4.13	Gain vs Average Hall Parameter	113
4.14	Gain vs Current Density, $f_{\text{CO}_2} = 0.74\%$, $f_{\text{Cs}} = 10^{-5}$ $p = 42.0 \text{ Torr}$	114
4.15	Gain vs Current Density	115
4.16	Dependence of Gain on Electrical Conductivity	116
4.17	Gain vs $f_{\text{CO}_2}/f_{\text{Cs}}$ Ratio	117
4.18	Lower Laser Level Deactivation	118
4.19	Gain Saturation Test	119
5.1	Increase in Electron Temperature During the Experiment	120
6.1	Laser Output and Saturation Intensity	121
6.2	Specific Power of Various Laser Systems	122
6.3	Schematic of MHD Laser Configuration	123

LIST OF TABLES

	<u>Page No.</u>
1. Relaxation Rate for Various Energy Transfer Processes	81
2. Summary of Reported Values of $\text{CO}_2(10^00)$ - $\text{CO}_2(01^10)$	82
Relaxation Rates	
3. Summary of Reported Values of $\text{CO}_2(10^00)$ - $\text{CO}_2(20^00)$	83
Relaxation Rates	
4. Important Features of Other Investigations	84

I. INTRODUCTION

1.1 MHD Laser Concept

The MHD laser is a non-equilibrium MHD generator in which the electron gas, one of the constituents of its characteristic two temperature plasma, is used to produce a population inversion in a molecular additive, such as CO_2 . The Joule dissipation, which maintains the electron temperature well above that of the carrier gas, is a measure of the pumping power of the laser, and can be as large as 500 watts/cm³, which suggests the possibility of very high lasing power densities.

The device has several appealing features. As the electric power generated by the MHD process is delivered locally to the molecular gas, entirely within the flow, there is no need to take high electrical power out of the source, and in turn put it back into a gas discharge. This eliminates many uncertainties stemming from power conditioning and from electrode phenomena inherent to electric discharge lasers. Further, the high speed flow which appears to be essential for the removal of waste heat in high power lasers is an intrinsic feature of the MHD laser. The process for inversion production being essentially local, there is a chance of achieving more uniform gain, hence better beam quality than in externally excited devices. Unlike gasdynamic laser, the inversion may be extended to a much larger length along the

flow providing more active volume for power extraction, and hence higher output power per unit of mass flow, ($> 12 \text{ KJ/kg}$).

The overall efficiency of MHD lasers as a device capable of converting thermal energy into optical energy has been placed by many estimates (7.12) between 2-3%, much higher than that of even second generation gasdynamic lasers. This value is competitive even with the $\sim 10\%$ efficiency of electrical to optical conversion of gas discharge lasers (high power $> 50 \text{ KW}$), when the efficiency of the electrical power system (thermal to electrical conversion and power conditioning) is taken into account.

Due to the above mentioned attractive features of MHD lasers several feasible studies have been undertaken over a period of almost a decade, but with controversial results.

1.2 Review of Previous Work

Successful operation of a non-equilibrium MHD generator depends upon minimizing electronic energy losses to the working fluid, which has therefore usually been selected from the monatomic gases. When molecules are added to the fluid for laser operation, a significant fraction of electronic energy is lost to the internal storage modes of the former, for example the loss factor δ for CO_2 is about 5000.0 compared to the loss factor of 2.0 for He. Thus the addition of molecular species could impair the non-equilibrium heating of electrons. Since a selective excitation of laser levels is imperative for creation of an inversion, which in turn in the case of MHD lasers depends upon

the properties of the electron gas, a question is raised whether the non-equilibrium generator can serve as an effective laser pumping source.

In 1969 effects of molecular additives (CO, N₂) on non-equilibrium generator performance were studied by Kerrebrock and Draper¹⁻² using the MIT experimental generator. Excitation of vibrational levels to near equilibrium with the electron gas was achieved. In an He + Cs + CO plasma, CO ($\delta=460$) mole fractions up to 0.2% did not make any noticeable change in the collisional losses and at electron temperatures above 2200°K $T_{vib.}$ to T_e was achieved. As the mole fraction of the molecular gas was increased, the inelastic losses became effective and, as expected, a drop in electron temperature was observed, however, the equilibration of $T_{vib.}$ to T_e were achieved even at mole fraction of 1%, provided the electron temperatures were close to 3000°K. With proper estimates of achievable electron temperature, the molecular mole fraction which may be permitted to be injected into a non-equilibrium generator without degrading its performance may be extrapolated to values as large as a few percent.

In years to follow several theoretical and experimental investigations were conducted. First experimental studies were performed at the United Aircraft Research Laboratories.⁶⁻⁸ In a supersonic MHD channel (velocity ~ 3000 m/sec) small signal gains up to $0.15\%cm^{-1}$ were measured, but efforts to extract optical power from an oscillator were inconclusive. It was mentioned that due to probably the decomposition of insulating material at high temperatures, the inversion was poisoned by foreign

organic compounds, and laser oscillations of even He + Ne mixture were not realized. The analytical model produced by the group assumed a fully turbulent plasma with respect to ionization instabilities. Also, the model utilized the CO_2 relaxation data available in 1970. It predicted that approximately 20% of the Joule dissipation power could be converted into optical power, with an overall thermal to optical conversion efficiency of about 5%.

Zauderer et al at the General Electric Company measured a relatively high small signal gain exceeding $0.2\% \text{cm}^{-1}$ using a mixture composed of 78% He, 18% Ar, and 4% CO_2 with either 3-5% Xe or 0.1% Cs. In these experiments external voltage augmentation was required to maintain the discharge. The author claimed that for the laser to work the CO_2 mole fraction must be much larger than the Cs mole fraction, if most of the CO_2 population were to be kept unreacted with Cs. However, the ratio $f_{\text{CO}_2}/f_{\text{Cs}}$ was only 40 compared to $\sim 3 \times 10^3$ as value quoted by other investigators.⁵⁻¹² A light scattering measurement showed that the Cs concentration dropped by a factor of 5 to 7 due to CO_2 -Cs chemical reaction. No efforts to extract laser power were made.

In 1977 Biberman¹¹ et al. at the Institute of High Temperatures of the USSR Academy of Sciences reported the results of both experimental and theoretical investigations of MHD lasers. A short-circuited segmented MHD channel with constant cross section was used in the experimental study and was operated in pulsed-mode. In a 4.0 tesla magnetic field self-sustained discharge was maintained in a laser mixture of 1% CO_2 + 0.001% Cs

in He at a pressure of 15 torr. In the MHD induced discharge mode laser oscillations were established and a laser power density of 10 KJ/kg was recorded. With the estimate of losses in the salt Brewster windows (due to pollution by Cs - CO) placed at \sim 20%, the small signal gain was computed to be $\sim 0.3\% \text{cm}^{-1}$. Laser oscillations were not recorded in every experiment due to deterioration of the windows, and to avoid this problem the investigators substituted Xe as the seed and ran the tests in a supersonic channel. The discharge in this case was not self-sustained and an external voltage was required. The small signal gain was measured to be $0.35\% \text{cm}^{-1}$ (3% Xe and 6% CO_2) with power density falling in the same range as before (10kW/kg/sec).

In theoretical work of Biberman et al. it was assumed that, due to the Fermi-resonance, a strong coupling between the symmetric stretch mode and the bending mode existed. Based on the model gain and intracavity laser intensity was calculated, from which, if extrapolated, value of the saturation intensity at 125 torr pressure (1.4% CO_2) is found to be 6kW/cm^2 .

At MIT over a period from 1969 to 1978 various aspects of MHD lasers were studied by several investigators.^{4,12,71} Lowenstein⁴ while constructing a theoretical model of MHD laser plasmas investigated the effect of quenching of excited Cs atoms by CO_2 molecules on the laser performance. Mnatsakanyan³ studied this quenching phenomenon for an N_2 , A_2 and Cs plasma. His results indicate that a molecular mole fraction of less than one percent can be responsible for severe depopulation of the

excited bound states and hence cause a sharp decrease in the electron number density. Extending the work of Mnatsakanyan and Shaw,⁵ Lowenstein made an effort to calculate the effects of collisions with CO₂ on the bound state populations of Cs. The inelastic losses due to CO₂ - Cs encounters tend to disturb the bound electron equilibrium distribution and the magnitude of this perturbation can be obtained by comparing the rate of depopulation of the first excited states of Cs by CO₂ - Cs collisions with the rate of excitation of the first state by electrons. The balance between the depopulation rate and the excitation rate determines the number density of electrons. The "quenching section" which is required to compute the rate of depopulation of the first state by encounter with CO₂ molecules has never been measured. In his calculation Lowenstein assumed a value of 70 Å² which is very close to the value for Cs - N₂ quenching. The analysis indicated upper limit of allowable CO₂ mole fraction in the MHD laser $n_{CO_2}/n_e \leq 100$. He predicted that at a Cs mole fraction of 0.001% the maximum small signal gain (0.02%cm⁻¹) would occur at a CO₂ mole fraction of 0.22%, and at the electron temperature of 3200°K 7% of Joule dissipation may be converted into laser radiation.

Another aspect which was investigated by Lowenstein concerns the evolution of ionization instabilities in an MHD laser plasma. The study concluded that the radiation field does not have any significant effect on the instability, however, the latter's influence on the radiation field may lead to a serious problem of non-uniformities in the direction

transverse to the optical axis. However, since he assumes a constant temperature and pressure along the flow, and therefore his solution corresponds to conditions which would prevail at a single station along an MHD channel, the conclusion about the evolution of non-uniformities along the flow direction does not make much sense.

The important features of these studies have been summarized in Table 4. The results from the three investigations ^{4,7,10} which were available in 1974 when this experimental investigation was undertaken at MIT presented a very controversial picture:

1) Recommended Cs mole fraction for the successful operation of an MHD laser varied by 2 orders of magnitude, from 10^{-3} to 10^{-5} . Both experimental studies ^{7,10} indicated loss of atomic Cs due to its chemical interaction with CO_2 , whose nature and resultant products is to date not very much researched. Lowenstein's conclusions regarding the quenching phenomenon called for another look at the physics of the laser. Finally, it was speculated that the discrepancy in the Cs mole fraction could be due to poor diagnostics.

2) Nighan ⁷ et al. calculated that large values of gain ($\sim 0.5\text{-}1\%\text{cm}^{-1}$) can be produced, however, during the experimental investigation it was measured to be only $0.05\text{-}0.15\%\text{cm}^{-1}$. Zauderer ^{9,10} measured a value of $0.2\%\text{cm}^{-1}$.

3) CO_2 mole fractions allowed ranged from 1-4%, which were in direct violation of the theory proposed by Lowenstein.

At this point it was felt that a better understanding of MHD laser physics was required and accordingly the present investigation was undertaken. This dissertation describes the results of the experimental investigation. The results of the analytical study conducted by Walter are described in Ref. 12, and will be mentioned frequently in forthcoming sections.

1.3 Summary of Results and Discussion

In the present study a different approach to the experimental investigations of MHD laser was taken. Since the physical phenomena in such a device might be exceedingly complex, as the kinetic and thermochemical complexity of molecules excitation is added to the already intricate behavior of the electrothermally unstable non-equilibrium plasma, a pulsed experiment simulating the kinetic situation of an MHD laser was designed, which allowed us to uncouple the fluid dynamics and bulk plasma phenomena. A further advantage of the pulsed technique is that the very complex kinetic processes which occur in the plasma as it flows downstream in the actual laser, are displayed as a transient in the pulsed experiment, vastly simplifying the diagnostic problem.

The experiment is designed to measure the small signal gain in MHD laser plasmas. By varying the applied electric field and changing the composition of the mixture (He+Cs+CO₂) a wide spectrum of kinetic conditions were achieved.

The small signal gain measured ranged from 0.06%cm⁻¹ to 0.3%cm⁻¹ arriving at the following optimum conditions for laser operation:

1) The optimum value for Cs mole fraction is determined to be 1.4×10^{-5} . It is concluded that operation at laser values would lead to very unstable inversion with the gain fluctuating by very large amount ($\pm 30\%$). However, at values higher than 10^{-5} , the small signal gain is very insensitive to the variations in f_{Cs} , a 10% increase would drop the gain only by $\sim 5\%$.

2) There is an optimum value for the current density for each particular gas mixture establishing a certain amount of Joule dissipation. In order to achieve favorable conditions the non-dimensional parameter $(T_e - T_g)/T_g$ should be kept around 9.0. The electron temperature determined by this parameter in conjunction with the Cs mole fraction would provide the required electron number density.

3) It has been observed that as the turbulence in the plasma grows higher values of gain are achieved, saturating at approximately at $0.32\% \text{cm}^{-1}$, the maximum gain value recorded during this study. In his numerical study Walter¹² discovered a behavior similar to this, wherein at low CO_2 mole fractions ($\sim 1-2\%$), very rapid growth of ionization instabilities was observed, the fluctuation parameter $\langle \eta^2 \rangle$ reached an asymptotic value of 0.5 from a modest value of 0.05 within a distance of 10cm as the mixture moved downstream with a velocity of 4300.0 m/sec. During this growth period very large values of intra-cavity laser flux were computed, however, when $\langle \eta^2 \rangle$ leveled off to the value 0.5 lasing stopped. The spread of the peak inversion was in the order of 2.0cm ($\tau = 2 \times 10^{-2} / 4300 = 4.6 \mu\text{sec}$). Interestingly enough in the experimental

study the $0.32\% \text{ cm}^{-1}$ gain did not last more than $4.0 \mu\text{sec}$. It seems that in order to achieve longer lasting inversion, a more stable plasma would be a better choice, such achieved probably by increasing the CO_2 mole fraction.

4) Based on the measured values of small signal gain and approximate evaluation of saturation intensity using the results of Walter's analysis an estimate of extractable laser power has been made. The computed value for specific power at 3% CO_2 is 32 KJ/kg .

5) By monitoring the absorption of the laser signal in the after-glow the relaxation rate of the lower laser level by CO_2 molecules has been measured to be $3.3 \times 10^7 \text{ atm}^{-1} \text{ sec}^{-1}$. This value matches the figure calculated by Seeber⁵⁸ and is in close agreement with the measurement performed by Bulthuis.^{59,60} Since the relaxation of the $\text{CO}_2(01'0)$ made by He is much faster than by $\text{CO}_2(000)$, there is no doubt that the measured rate is for the $\text{CO}_2(100^0)-\text{CO}_2(01'0)$ process. The exact pathways of the relaxation mechanism are still a matter of serious discussion.

6) The pulsed technique has enabled us to measure the rate of $\text{Cs}-\text{CO}_2$ interaction, the cross section for which has been found to be in the range of $1.3 \times 10^{-24} \text{ m}^2$ to $4.6 \times 10^{-24} \text{ m}^2$ (400°K). A simple calculation shows that at a pressure of 0.1 atm in a mixture with 3% CO_2 the loss of metallic Cs due to this chemical reaction would be less than 1% (in a one meter long cavity).

Consistent gain measurements and preliminary power extraction calculations strongly suggest that construction of a high power MHD laser is feasible. The measurement of relaxation rates of lower laser level and the fact that the rates are in agreement with the results from several other investigations certify the reliability of the data.

II. PHYSICS OF CO₂ LASERS

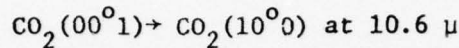
MHD lasers are characterized by relatively high electron number densities (10^{19} - 10^{20} m^{-3}) and low average energies (0.2 - 0.4 eV), in contrast with the conditions in electric discharge lasers in which typical values of these parameters are in the ranges 10^{15} - 10^{16} m^{-3} and 1-2 eV respectively. Low energy electrons of MHD lasers are most suitable for excitation of vibrational modes of a molecular species. CO₂ molecules have been a better choice as the laser medium for several reasons: (1) high quantum efficiency (~41%), (2) energy transfer to the upper laser level, CO₂(00⁰1), by electrons with energies ~0.3 is several times larger than to the bending mode CO₂(01¹0), and (3) He, the basic carrier gas acts as an effective coolant, selectively relaxing the lower laser level. In the following section we will review the properties of CO₂ molecules and the available data on excitation and relaxation rates of various vibrational modes of the molecule.

2.1 CO₂ Molecular Kinetics

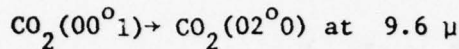
CO₂ is a linear triatomic symmetric molecule with three normal modes of vibration, v_1^{17} (symmetric stretch mode, fundamental frequency = 1337 cm^{-1}), v_2 (doubly degenerate bending mode, fundamental frequency = 667 cm^{-1}), v_3 (asymmetric stretch mode, fundamental frequency = 2349 cm^{-1}). The laser transitions involve the lowest vibrational levels, namely $v_3 - v_1$ and $v_3 - 2v_2$, therefore the modes may be modeled as harmonic oscillators (Fig. 2.1), as far as the laser kinetics is concerned. For every

vibrational level there exists a set of rotation levels, but with slightly different spacing for the different vibrational levels.

Two prominent laser transitions have been observed in CO_2 molecules:



and



where $\text{CO}_2(00^01)$, $\text{CO}_2(10^00)$ and $\text{CO}_2(02^00)$ are the first excited state of the asymmetric stretch mode, the first excited state of the symmetric mode and the second excited state of the bending mode, respectively.

Laser oscillation always starts on the 10.6μ transitions, because the gain is slightly higher on these transitions than on 9.6μ transitions, unless frequency selection devices are used in the cavity. Since both groups of transitions share the population of the same upper level (00^01) , the competition effect among the 9.6μ and the 10.6μ transitions precludes the operation of the 9.6μ transitions. Probably for the same reason the laser kinetics of 10.6μ transitions is extensively researched and studied. In the present study we will confine ourselves to this laser band as far as the experiments are concerned, for the sake of simplicity, and then discuss the 9.6μ transitions.

Each transition band has two branches: P (transition from J rotational level to $J+1$) and R (transition from J to $J-1$). From the expression for gain

$$\alpha_{2,J+1,J \pm 1} = \left[N_{2,J} - N_{1,J \pm 1} \frac{g_J}{g_{J+1}} \right] \frac{\lambda^2 g(v)}{4\pi n^2 (t_{\text{spont}})_{2,J \pm 1,J \pm 1}} \quad (2.1)$$

* This matter will be further discussed in Chap. 5.

It can be seen that for the P branch the ratio of degeneracies g_J/g_{J+1} is less than 1.0, as $g_J = 2J+1$, the reverse is true for the R branch.

This suggests that a P transition may oscillate even with partial ($N_2 < N_1$) inversion (above some J_{\min}).

The rotational population density $N_{i,J}$ ($i=1,2$) is

$$N_{i,J} = \frac{N_i g_J \exp(-E_{i,J}/k T_{\text{rot}})}{\sum_J g_J \exp(-E_{i,J}/k T_{\text{rot}})} \quad (2.2)$$

so that N_i is the population density of i^{th} vibrational state. The energy separation between two adjacent rotational levels increases as we go to higher rotational J values. However, even up to very high rotational levels the energy separation between the rotational levels is still smaller than or comparable to the thermal energy. Since the rotational relaxation rate is several orders of magnitude faster than the intermode vibrational transfer rate, even under excitation conditions, $^8 T_{\text{rot}}$, which represents the thermal energy of the vibrational state, may be assumed equal to temperature T describing the translational kinetic energy of the molecules.

Equation (2.2) suggests that in either case, whether inversion between the vibrational states exists or not, the relative population of one of the rotational levels would be higher than that of other levels (in the same vibrational state), thus when inversion is created, the laser oscillation starts on only one (at most only on a few) rotational transitions. It has been experienced that at room temperature P(20) is the line which starts to lase first and as long as the thermalization of rotational levels is rapid enough the lasing is maintained at P(20). Some other strong lasing lines are P(18) and P(22).

2.2 Electron Excitation in a MHD Laser

N_2 molecules are one of the main constituents in electric discharge and gasdynamic lasers because of their energy storage capability. They cannot decay to the ground state because of zero permanent dipole moment without any collisional relaxation. The first excited state of the molecule which is in resonance with the laser upper level, $CO_2(00^01)$, ($\Delta E \sim 18 \text{ cm}^{-1}$), can excite a ground level CO_2 molecule to $CO_2(00^01)$ at a rapid rate of $1.4 \times 10^7 \text{ atm}^{-1} \text{ sec}^{-1}$. The equilibrium between N_2 ($v=1$) and $CO_2(00^01)$ states, in effect, increases the effective lifetime of $CO_2(00^01)$, the upper laser level.

At an electron energy of $\sim 2.0 \text{ eV}$, which is typical of electric discharge lasers, the effective cross section for vibrational excitation of N_2 is about 6.0 times larger than that for $CO_2(00^01)$.⁷¹ However, for electron temperatures in the range $2500\text{--}4000^\circ\text{K}$, the rate for N_2 is one to two orders of magnitude less than that for $CO_2(00^01)$.⁶ Thus, in MHD lasers, N_2 would not be particularly useful, even if we risk the overloading of the nonequilibrium plasma by injecting another molecular species other than CO_2 , into it.

It was mentioned in Chapter 1 that a nonequilibrium generator is used as the electron source, and for laser operation CO_2 is added to the flowing gas. In order to maximize the Joule dissipation, which is required for effective electron heating, the generator is short circuited. A Faraday generator seems to be the logical choice for an MHD laser, as it is capable of high local efficiencies in the short-circuited mode.

It has been predicted⁷ that high MHD interactions are possible when the electron number density is greater than $5 \times 10^{18} \text{ m}^{-3}$, which has a positive effect on the pumping power of the device. However, an upper limit exists for the electron number density, beyond which the excitation of the bending and symmetric modes becomes significant. As the cross sections are electron temperature dependent, this limit would also be a function of T_e , and, n_e in effect, will depend upon the Cs mole fraction. For $f_{\text{Cs}} = 10^{-5}$ Lowenstein⁴ places the limit at 10^{19} m^{-3} .

As the power output from a laser cavity is almost proportional to the mixture static pressure, it would be advisable to operate an MHD laser at relatively higher pressure (say $\sim 0.25 \text{ atm}$).¹² At this pressure the gain profile $g(v)$ is homogeneously broadened:

$$g(v) = \frac{\Delta v}{2\pi[(v_0 - v)^2 + (\frac{\Delta v}{2})^2]} \quad (2.3)$$

where

$$\Delta v = \Delta v_D + \sum_i \frac{1}{\pi \tau_i} \quad (2.4)$$

For this case the saturated gain is

$$\alpha = \frac{\alpha_0}{1 + I/I_s} \quad (2.5)$$

where α_0 and I_s are the small signal gain and the saturation intensity respectively.

2.2.1 Nonequilibrium Generator with Molecular Additives

The process of electron heating due to Joule dissipation has been extensively studied.^{32,15} In essence the magnitude of electron energy is determined by the balance between the energy gain by mechanisms like acceleration in an electric field, recombination in a nozzle by a three body process, and the energy loss by mechanisms like elastic collisional losses, radiation losses and heat diffusion losses. Neglecting the radiation¹⁵ and the heat diffusion¹⁵ losses and considering the energy gain only by acceleration in an electric field we can write the energy equation for electrons:

$$\frac{\partial}{\partial t} [n_e (eV_i + \frac{3}{2} kT_e)] + \nabla \cdot [n_e (eV_i + \frac{3}{2} kT_e) \bar{V}_e] + n_e kT_e \nabla \cdot \bar{V}_e = \frac{J^2}{\sigma} - \sum_s \Delta \epsilon_s \quad (2.6)$$

On the right hand side the first term is the Joule dissipation and the second term is the loss due to collisional processes. The term on the left hand side represents the temporal variations of the electron-gas energy (potential and thermal), their convective flux and the pressure work. At high magnetic fields, which would be required for successful operation of MHD lasers, the plasma becomes unsteady and non-uniform^{33,39} leading to an increased Joule dissipation and to a saturation of the "effective" conductivity. Solbes³⁹ developed a quasilinear averaging technique to account for these "ionization instabilities". Growth of these instabilities occurs when the Hall parameter, β , defined as

$$\beta = \frac{e B}{m_e v_e} \quad (2.7)$$

exceeds a limit, conveniently called the critical Hall parameter, β_{crit} . The parameter β_{crit} is a unique property of the plasma and depends on the type of seed, plasma constituents, the degree of ionization, and the gas temperature.* For plasmas typical of MHD lasers, this value has been found to be ≤ 1 . The ratio of effective conductivity and spatial average conductivity, $\sigma_{\text{eff}}/\langle\sigma\rangle$ could drop to a value as low as 0.1. Oliver et al.⁷² have shown that electrothermally induced eddy currents tend to develop together with a strong current density over the insulating wall.

When a molecular species is added to the nonequilibrium plasma,^{1,2} damping of the ionization instabilities is observed. Draper points out that the time of electron temperature relaxation is increased:

$$\frac{\tau}{\tau^*} = 1 + 2 \left[\frac{n_{\text{CO}_2}}{n_{\text{He}}} \right] \left[\frac{n_{\text{He}}}{n_e} \right] \left[\frac{kT_e}{eV_i} \right]^2 \quad (2.8)$$

where τ and τ^* are the electron temperature relaxation times with and without molecules.

Molecular addition enhances the loss term, $\sum_s \Delta \epsilon_s$, in the energy equation (2.6), due to added inelastic losses. From the cross-section data for vibrational excitation of CO_2 by electrons we know that excitation of $\text{CO}_2^0(001)$ and $\text{CO}_2^1(010)$ levels are dominant, however due to the stimulated transition (10.6μ), the molecules are continuously transferred to the $\text{CO}_2^0(100)$ level. Further, it will be seen in the next section that the

*A detail description and analytical expression for β_{crit} can be found in Ref. 39.

relaxation processes tend to populate various levels of the bending mode. Thus a complete redistribution of the population amongst the vibrational levels takes place. Under these conditions the inelastic loss factor δ_{CO_2} , which in "swarm" experiments has been measured to be ~ 5000 , does not remain constant, in fact decreases. This indicates that the plasma in an MHD laser consists of several "gases", each describable by a temperature of its own.

2.3 Relaxation Processes

As the molecules are pumped to the desired excited state in order to create an inversion, they also lose energy by way of "relaxation processes". These processes may or may not be favorable to the creation of inversion depending upon whether they relax the lower or upper laser level. In gas lasers the relaxation may occur by three different mechanisms: (1) radiative decay, (2) collisional loss, and (3) diffusion out of the active area.

In CO_2 lasers the relaxation rates due to radiative decay and diffusion are very slow, at least by 3 orders of magnitude.^{24,40,41,42} For this reason we will examine only the collisional relaxation in detail.

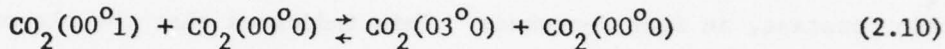
There are various units in which the relaxation rates are expressed. In this study we use the unit $atm^{-1} sec^{-1}$. A relaxation time can be defined:

$$\frac{1}{\tau_e} = \frac{1}{kp} \quad (2.9)$$

where k is the relaxation rate and p the pressure of the relaxing agent.

2.3.1 Relaxation Rates of the Upper Laser Level

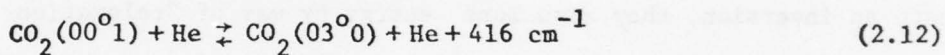
As is required for an efficient laser operation, the relaxation rates for $\text{CO}_2(00^01)$, the upper laser level, are very slow. For relaxation by $\text{CO}_2 - \text{CO}_2$ encounters:



The rate at a temperature of 400°K is measured to be⁴⁷

$$k_{\text{CO}_2(00^01)-\text{CO}_2} = 2.8 \times 10^5 \text{ atm}^{-1} \text{ sec}^{-1} \quad (2.11)$$

For the process:



The rate for $T = 300^{\circ}\text{K}$ is:

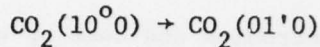
$$k_{\text{CO}_2(00^01)-\text{He}} = 6.8 \times 10^4 \text{ atm}^{-1} \text{ sec}^{-1} \quad (2.13)$$

It can be seen that although this process is slow, it populates the third level of the bending mode. Also, for a gas mixture typical of MHD lasers, 3% CO_2 + 0.001% Cs + ~97% He, most of the relaxation will be performed by He, in contrast to electric discharge lasers.

2.3.2 Relaxation Rate of the Lower Laser Level

Although since 1966 at least ten experiments have been performed, as yet neither the basic mechanism of the process is known nor any universally acceptable data on the rates is available. Most confusion arises from the existence of Fermi resonance between 10^00 level and doubly degenerate 02^00 level of the bending mode.

For the relaxation process:



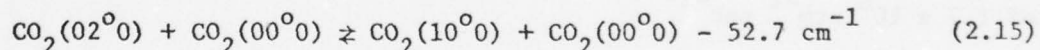
the rate constants reported range from $7.6 \times 10^5 \text{ atm}^{-1} \text{ sec}^{-1}$ to $3.4 \times 10^8 \text{ atm}^{-1} \text{ sec}^{-1}$. Collisions between $\text{CO}_2(10^00)$ and He are believed to play almost no role in this process,⁴⁹ at least they were not measurable.

There are several schools of thought on the mechanism of this relaxation process. Experimental measurements of rate of the Fermi resonance has been claimed by many investigators. Stark⁶² performed a series of experiments, using a 1.6μ beam to disturb the equilibrium between the two levels and then monitor the absorption of a 10.6μ beam. He reported a rate value as:

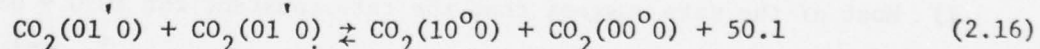
$$k_{10^00 - 02^00} = 1.4 \times 10^5 [p_{\text{CO}_2} + 0.046 p_{\text{N}_2} + 0.054 p_{\text{He}}] \quad (2.14)$$

Rhodes et al.⁵⁰ and Jacobs et al.⁶¹ reported this rate constant to be $7.6 \times 10^8 \text{ atm}^{-1} \text{ sec}^{-1}$ and $2.3 \times 10^8 \text{ atm}^{-1} \text{ sec}^{-1}$ respectively (see Table 3).

Rhodes et al. in their 1968 experiment observed two more absorption rates, the faster of these two were attributed to process like



and



and based on this measurement a relaxation rate constant for $\text{CO}_2(10^00)$ was reported as $3.4 \times 10^8 \text{ atm}^{-1} \text{ sec}^{-1}$. The third rate was ignored.

AD-A068 190

MASSACHUSETTS INST OF TECH CAMBRIDGE GAS TURBINE AND--ETC F/G 20/5
FUNDAMENTAL MECHANISMS OF NONEQUILIBRIUM MHD LASING PHENOMENA. (U)
DEC 78 J L KERREBROCK

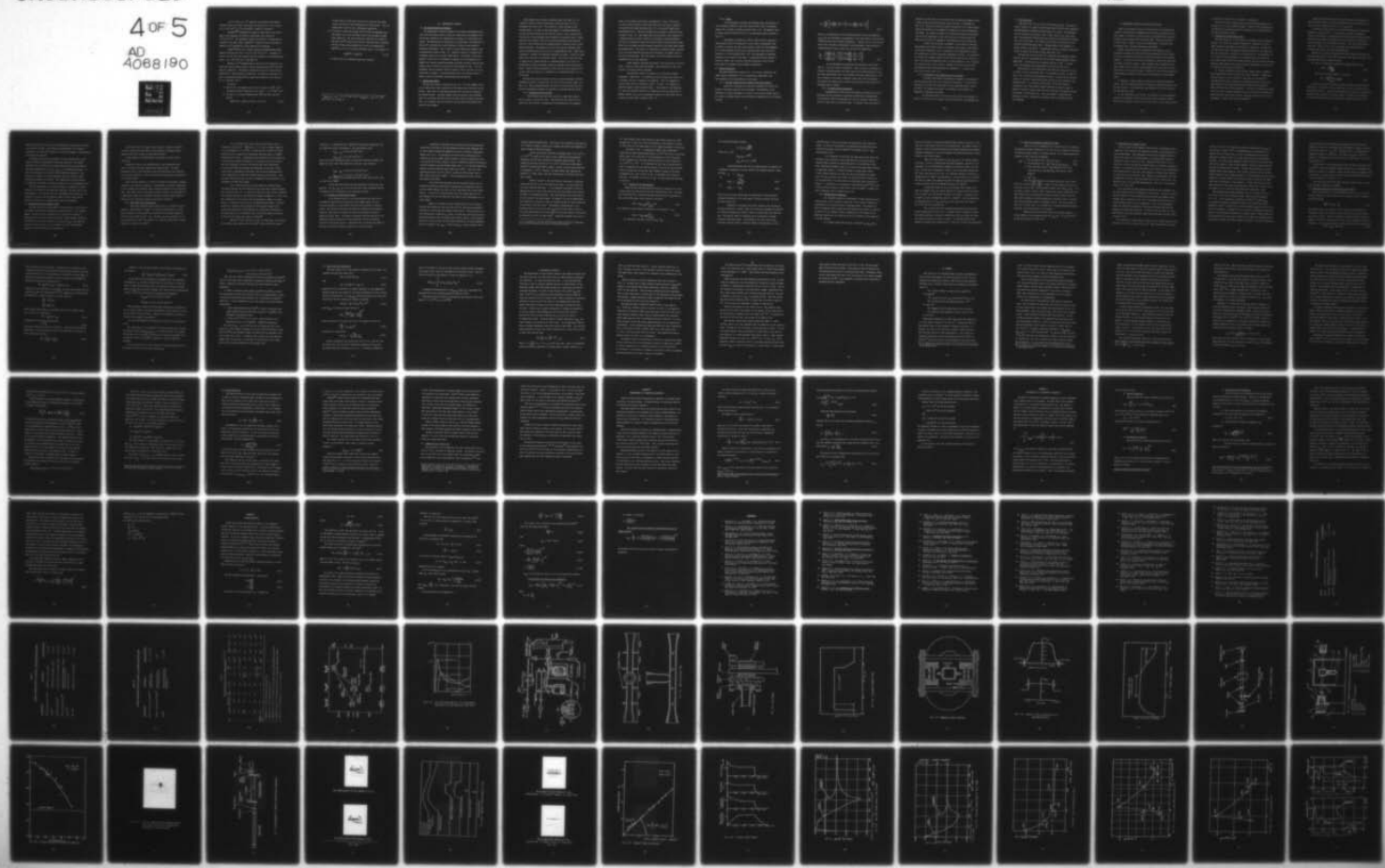
F44620-76-C-0067

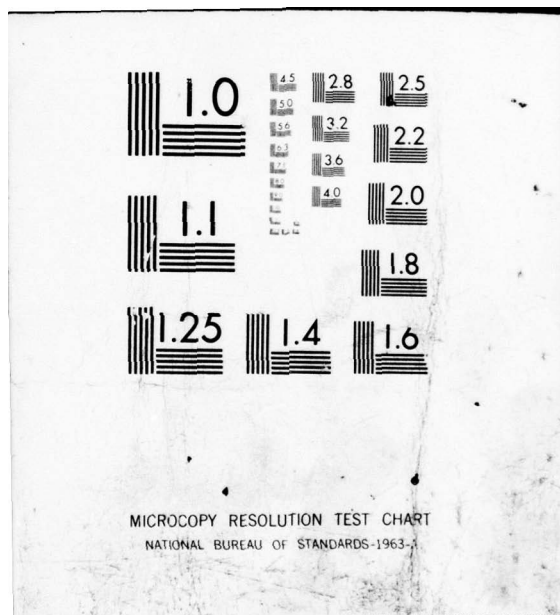
UNCLASSIFIED

4 OF 5
AD
A068190

AFOSR-TR-79-0506

NL





In 1974 Jacobs et al.⁶¹ repeated the experiment with smaller saturating pulse and faster electronics and came up with a rate constant of $2.5 \times 10^7 \text{ atm}^{-1} \text{ sec}^{-1}$ for $\text{CO}_2(10^00) \rightarrow \text{CO}_2(01^10)$ relaxation.

Bulthuis^{59,60} monitored the decay of laser power in the after-glow of the discharge and reported a bottleneck rate constant of $\sim 10^7 \text{ atm}^{-1} \text{ sec}^{-1}$. His experiment seems more realistic in predicting the relaxation rate $[\text{CO}_2(10^00), \text{CO}_2(02^00)] \rightarrow \text{CO}_2(01^10)$ since he used H_2O to deplete the 01^10 population, before shorting the discharge.

Seeber⁵⁸ based on his modified Schwartz-Slawsky-Herzfeld (SSH) theory calculates the value to be $3.3 \times 10^7 \text{ atm}^{-1} \text{ sec}^{-1}$. In Chapter IV we will see that this rate constant has been measured in this investigation and is $\sim 3.3 \times 10^7 \text{ atm}^{-1} \text{ sec}^{-1}$ (see Table 2).

Murray et al.⁵⁴ measured gain at 10.6μ and 9.6μ transitions and found that they are almost equal, a strong coupling between 10^00 and 02^00 would not explain it. Theoretical calculations based on strong coupling predicted 40 - 50% more gain at 10.6μ band. By adjusting the figures such that a correlation between would be found they predicted a rate constant of $1.7 \times 10^6 \text{ atm}^{-1} \text{ sec}^{-1}$.

To sum up:

- 1) Most of the data suggest that the rate constant for $10^00 \rightarrow 01^10$ relaxation would be somewhere in the range $1 - 3 \times 10^7 \text{ atm}^{-1} \text{ sec}^{-1}$.
- 2) If there is a strong coupling between 10^00 and 02^00 , then the process

$$[10^00, 02^00] + (00^00) \rightleftharpoons 2(01^10) + 50.1 \text{ cm}^{-1} \quad (2.17)$$

is most likely to take place and both the 10.6μ and 9.6μ bands would be governed by this bottleneck rate in MHD lasers. Also the bending mode would not have a Boltzmann equilibrium.

3) If there is a weak link between 10^00 and 02^00 and depending upon the pathway one of the two bands would be more suitable for MHD laser operation. The reason being that $CO_2(01^0)$ is relaxed by He^* much faster⁵¹ than by CO_2 and hence under MHD laser conditions (97% He, 3% CO_2) the bottleneck rate is not the relaxation of $CO_2(01^0)$, as it is in electric discharge lasers. For example, if



is faster than 9.6μ operation would more suitable.

* $k_{CO_2(01^00) - CO_2} = 1.8 \times 10^5 \text{ atm}^{-1} \text{ sec}^{-1}$; $k_{CO_2(01^00) - He} = 2.7 \times 10^6 \text{ atm}^{-1} \text{ sec}^{-1}$ at $T = 400^\circ \text{ K}$.

III. EXPERIMENTAL APPARATUS

3.1 The Pulsed Simulation Technique

The experimental facility utilized in the present investigation simulates the flow-induced electric field of an MHD laser by an applied field and thereby eliminates the complexities and expense of a high speed flow system. The experiments are conducted in a pulsed mode, the advantages of which will be pointed out in the sections to follow as each system is described individually. The sequence of events which occur during a test is schematically shown in Fig. 3.14. Helium is stored in a heated flask containing copper wool wet with liquid Cesium. By opening a fast-acting pneumatic valve the Cs + He mixture is allowed to flow through the test chamber into vacuum, giving the pressure transient sketched; simultaneously another valve is opened to allow CO₂ to flow through the tube. At a predetermined time the magnetic field is turned on and the shutter to the CO₂ probe laser is opened. A few milliseconds after, the electric field is pulsed to pass a prescribed current through the gas mixture.

3.2 Pulsed Flow System

The gas flow system is sketched in Fig. 3.1. The test chamber is fed by two separate gas lines carrying a Cs + He mixture pipe line and a CO₂ + He mixture. Both lines are simultaneously opened to the tube by activating two solenoid valves. The pipe lengths (from the valves to the discharge tube) are so matched that both the gas mixtures reach the tube at the same time, so no chemical reaction between Cs and CO₂ takes place before they reach the test chamber.

The stainless steel vessel containing copper wool (Fig. 3.1) is flushed by liquid Cs before conducting a series of tests, so as to thoroughly wet the Cu wool. The liquid Cs is then returned to the storage vessel. In order to keep the system at a uniform temperature, an oven was built around the pot with the Cu wool. Also, the pipe line from the pot to the discharge tube is heated by electrical tapes. During operation the pneumatic valve 10 is actuated allowing the He saturated with Cs to flow through the test chamber giving a pressure pulse of about 700 milliseconds. The temperature of the oven and the stainless steel tube is monitored and kept constant at a predetermined value. Under these conditions a reliable and repeatable seeding is provided. After the copper wool is wet the valve 5 is securely closed. The valves 1 and 9 are used to charge the Cs vessel with He to a desired pressure, and valve 9 is closed before firing the pressure pulse by suddenly opening the pneumatic valve. Valves 3 and 8 are normally closed, and are used to evacuate the Cs pots, when the liquid Cs is required to be transferred from or to one of the pots.

The $\text{CO}_2 + \text{He}$ mixture is passed to the test section through a 0.394 mm choked hole, which is situated near the inlet in the tube (see insert A in Fig. 3.1). This microhole prevents the flow of Cs + He into the CO_2 line and also determines the amount of CO_2 which is injected into the plasma.

3.2.1 Discharge Tube and Circuit

The discharge tube (the test section) is made from a quartz one inch square cross-section pipe. This dimension was chosen so as to ensure that wall effects (recombination and deexcitation) are negligibl

small at the pressure level under investigation: $\sim 50.0 - 70.0$ torr). A conical quartz fitting is fused onto each end of the pipe to provide O-ring seals and flange mounting (Fig. 3.2), the overall length being approximately 40 cm. The end fitting butts up against an electrode block as shown in Fig. 3.3. Each block holds ten electrodes, each connected to a separate ballast resistor ($\sim 100 \Omega$) to encourage a uniform discharge. The tube is terminated at each end by brass bellows and adjustable flanges which serve as window and mirror mounts required for multipass small signal gain measurements. The bellows are supported by aluminum stands, insulated so as to prevent external shorting of the discharge, the middle point of the tube being grounded. The "tee" shape of the tube provides an easily accessible port for gas injection.

Eight tungsten electrodes are fused to the side walls of the tube, which, being in contact with the plasma, allow monitoring of the axial as well as transverse (Hall) voltages.

The discharge circuit is powered by a 66 μ F capacitor-bank chargeable to 4000 volts. Two ignitrons are used as high power relays, one to initiate and one to terminate the discharge. They are triggered by current pulses from two thyratrons, which, in turn, are triggered by amplified signals from the oscilloscopes. The duration of the discharge, i.e. the time difference between the triggering of the two ignitrons, is usually 200-350 μ sec, and is adjustable by means of a time delay circuit. A typical current pulse is shown in Fig. 3.4.

3.2.2 Magnet

An electromagnet surrounds the discharge tube, and consists of two rectangular Helmholtz coils, each with 8 turns of No. 10 insulated copper wire, resting on aluminum channels (Fig. 3.5). The magnetic field is nearly uniform ($\pm 0.3\%$) over most of the discharge region as shown in Fig. 3.6.

The magnet is powered by a 500 μF , 3000 V bank of capacitors interconnected with 55 μH inductors so as to form a transmission line. A resistor in series with the magnet allows to match the load impedance to the line impedance thus giving an approximately square pulse for a duration of 2-3 milliseconds (Fig. 3.7). The experiment is performed during the flat portion of the pulse. An ignitron-thyatron system is used as a switch, and a pick-up coil and integrating circuit allows monitoring of the magnet current during an experiment.

3.3 Plasma Diagnostics

The plasma diagnostics consists of: (1) electron temperature and number density measurement, (2) Cs concentration measurement, and (3) estimation of CO concentration in the plasma.

3.3.1 Electron Temperature and Number Density Measurements

During the discharge some electrons recombine with cesium ions giving continuum radiation from the plasma. The intensity of the radiation at a given wavelength is related to the electron number density, the cesium ion number density, and the electron temperature by the following relation:

$$I_v \propto \frac{n_e^2}{T_e^{3/2}} \left[\exp\left(\frac{hc}{kT_e} (\lambda_{6P}^{-1} - \lambda^{-1})\right) + 2.22 \exp\left(\frac{hc}{kT_e} (\lambda_{5D}^{-1} - \lambda^{-1})\right) \right] \quad (3.1)$$

where I_v is proportional to the continuum radiation from the plasma and $\lambda_{6P,5D}$ are the wavelengths corresponding to the lower levels of the electron transitions from the continuum (Appendix A). From Eq. (3.1) it can be seen that if the radiation is monitored at two wavelengths, then the ratio of intensities may be used to calculate the electron temperature:

$$\frac{I_{v1}}{I_{v2}} \propto \frac{\exp\left(\frac{hc}{kT_e} (\lambda_{6P}^{-1} - \lambda_1^{-1})\right) + 2.22 \exp\left(\frac{hc}{kT_e} (\lambda_{5D}^{-1} - \lambda_1^{-1})\right)}{\exp\left(\frac{hc}{kT_e} (\lambda_{6P}^{-1} - \lambda_2^{-1})\right) + 2.22 \exp\left(\frac{hc}{kT_e} (\lambda_{5D}^{-1} - \lambda_2^{-1})\right)} \quad (3.2)$$

In the experiment the radiation was monitored at 4904 Å and 4285 Å. A spectral lamp GE 6.6A/T4Q/1CL - 200 W was used to calibrate the radiation recording system, the fiber optics and the photomultiplier tubes. The fiber optics bundle has a cross-section (optically sensitive) of 1 cm² and is capable of recording a radiation field from a 120° solid angle. The location the fibers are so chosen that the entire 1-inch width of the discharge tube is covered.

3.3.2 Cs Concentration Measurement

Determination of the actual concentration of metallic Cs in the discharge has been especially troublesome in MHD laser investigations. In the present study the measurement was done by resonance absorption at 4550 Å of light from a Cs spectral lamp. To minimize noise and record a

reference on each scope trace the light from the lamp was chopped at about 15 kHz, giving many periods during a gas flow pulse, as sketched in Fig. 3.13. During this pulse the lamp was powered by a D.C. power supply; during idle periods it was powered by a regular A.C. source designed for such lamps. The change in height of the pulse gives directly the absorption by the Cs population in the tube, and since the record spans the whole gas flow time, any fogging of the discharge tube can be detected.

In Fig. 3.8 the optical arrangement of the system is sketched. The housing of the lamp is heated to maintain the Cs vapor in the lamp at a particular temperature, which corresponds to the temperature at which the calibration of the Cs absorption measurement was done. For calibration two quarts test chambers sealed off with 60 torr and 120 torr of He were used. The set-up is sketched in Fig. 3.9 (see Appendix B). The calibration curve shown in Fig. 3.10 is used to estimate the Cs mole fraction from the absorption data recorded during the experiments. A typical scope trace can be seen in Fig. 3.11.

3.3.3 Estimation of CO Concentration in the Plasma

In earlier experiments⁵ with MHD laser plasmas it was suspected that CO_2 dissociates to CO and O_2 during the discharge. To confirm this, radiation at the 5052 Å triplet band of CO was monitored using a filter at 5050 Å. To estimate the amount of CO present in the plasma, the diagnostics system was calibrated.

As mentioned before, the Hall and axial fields were measured by probes in contact with the plasma, which were fused into the discharge tube.

3.4 CO₂ Probe Laser

The probe laser is a CW electric discharge CO₂ laser. The optical cavity consists of a spherical gold-plated mirror (R~10 m) and a germanium semi-transparent (T=10%) mirror placed about 1.5 m apart. The discharge section is made of pyrex glass, water cooled, and has two, one at each end, flat germanium windows which are coated with antireflection coating (10.6 μ) on both sides. The flowing laser system is powered by a well filtered 50 kW-50 mA power supply. The gas mixture used comprises of 16% N₂, 14% CO₂, and 70% He. An adjustable orifice is placed in the laser cavity to operate the system in TEM₀₀ mode (Fig. 3.12).

The detection system consists of a liquid N₂ cooled HgCdTe infrared detector and a low noise-high gain (40 dB) small signal amplifier (Perry Model 603). The detector has a sensitive area of 1.0 mm². A typical scope trace showing a gain measurement can be seen in Fig. 3.13.

Three Tektronix 555 oscilloscopes with multi-trace plug-ins are used to record the data on Polaroid film. The sequence of events, as shown in Fig. 3.14, is initiated by throwing one switch. At first the two solenoid valves are activated, opening the Cs+He and CO₂+He flow systems to the discharge tube. At a time when the pressure in the tube reaches a preselected value (the delayed trigger mechanism of scopes is used to adjust the timing) trigger pulses are sent to activate the magnet and open the shutter to the CW CO₂ laser. After the magnet is stabilized the discharge is fired. Sometimes a preionizer pulse is required to start the discharge.

IV. EXPERIMENTAL RESULTS AND ANALYSIS OF THE DATA

After the experimental set-up was test-proven to be reliable and capable of reproducing the gasdynamic and electrical conditions in the test chamber consistently, several series of experiments were conducted during the period August 1976 to February 1978. This was carried out in three steps: Signal to noise ratio measurements, calibration and preliminary tests, and gain measurement experiments.

Before proceeding with the experimental investigation, it was necessary to measure the noise level and the magnitude of other errors, if any, in the diagnostic and data acquisition systems of the designed facility. A series of test runs was conducted to record the noise level in various electrical signals. Radio frequency noise transmitted from high current cables of magnet and discharge circuit was found to be the main source of the electrical noise. However, by use of proper insulation and grounding the signal to noise ratio was increased to an acceptable level.

a) Figure 4.1 shows absence of noise in the laser gain detection system. Here the discharge was fired through a Cs seeded He plasma, without CO_2 injection. The experiments were conducted in two sets; without and with magnetic field.

b) The calibration curve in Fig. 4.2 indicates a linear dependence between the discharge current and the probe current integrator output. Even when the magnetic field is on, the noise level, at the current values

of interest (0.2 amp/cm^2 to 1.0 amp/cm^2) is negligible.

The data have been carefully read from Polaroid photographs to an accuracy of $\pm 0.1 \text{ mm}$ in measured lengths. However, while presenting the recorded data in graphical form this uncertainty in the measured values has been accordingly plotted.

4.1 Calibration and Preliminary Tests

For data reduction, it was required to calibrate various diagnostic systems. The theory and technical approach for calibration of the Cs light absorption measurement are discussed in Appendix A. In Fig. A-1, the calibration curve, relating the measured absorption of Cs lamp light and the concentration of metallic Cs, has been shown. In absorption, as it is read from the photographs, can be measured with an accuracy of $\pm 2\%$, which, when reduced to Cs number density, does not exceed $\pm 10\%$ mark. Electron number density and CO number density measurements were the other two systems which required calibration.

a) For the calibration of the electron number density, diagnostic system experiments named the 1000 series, were conducted. Several pre-selected values of current density in the range of 0.20 amp/cm^2 to 1.00 amp/cm^2 were passed through a Cs seeded He plasma and, along with other parameters, Cs bound-free continuum radiation was measured at $4904 \pm 50 \text{ \AA}$ and $4285 \pm 50 \text{ \AA}$ wavelengths. In order to minimize the calibration error other relevant parameters, such as axial electrical field, gas mixture pressure and Cs mole fraction, were kept constant for one set of experiments. Several such sets were conducted.

Using the basic equations governing an MHD plasma (see Appendix C), electron number density and electron temperature were analytically calculated from the recorded data (i.e. E_x , J , f_{Cs} and p).

A theoretical expression for the spectral emission of Cs free-bound radiation is given in Ref. 73 and has been discussed in Appendix A. Using this expression a relationship was found between the electron number density and the radiation emitted from a unit volume of the plasma in a unit solid angle in a unit frequency interval. Two fiber optic bundles, each with a field of view of 30° half angle, were calibrated with a standard light source, GE lamp 6.6A/T4Q/ICL-200 W.

Finally, the constants relating the electron number density (and the electron temperature) and the photo-multiplier tube output were found, and were henceforth used to reduce the data.

b) Gain in a medium with homogenous broadening saturates as:

$$\alpha(v) = \frac{\alpha_0(v)}{1 + \frac{I(v)}{I_s(v)}} \quad (4.1)$$

where the saturation intensity is given by

$$I_s(v) = \frac{4\pi\eta^2 hv}{(t_2/t_{\text{spont}}) \lambda^2 g(v)} \quad (4.2)$$

In order to measure the unsaturated gain, otherwise called the small signal gain, the intensity of the probe laser has to be far less than the saturation intensity. A series of experiments was conducted to ensure this, the probe laser intensity was varied between the values of 3.0 watts/cm^2 and 50.0 watts/cm^2 and gain was measured for a given plasma (Fig. 4.19).

Within the limits of errors due to the diagnostic system, gain was found to be constant ($\pm 10\%$). For actual gain measurements, the laser was operated at ~ 6.0 watts/cm² intensity, a value low enough for safe operation of the Hg Cd Te detector.

Consistent laser gain measurements have been achieved over a wide range of conditions appropriate to MHD laser operation. The plasma conditions were controlled and systematically varied by maintaining the five basic parameters (B , J_x , f_{Cs} , f_{CO_2} , p) to predetermined values. In order to investigate the effects of each individual parameter on the population inversion, all other parameters were kept constant, while varying the parameter in question. The temperature of the gas mixture was computed to be 400°K, a quantity constant in all the experimental runs.

All the experiments were carefully planned to illuminate the basic kinetics of inversion in CO₂ under MHD conditions, the main task of this investigation. To facilitate this the experiments were divided into two categories; without, and with magnetic field, thereby isolating the effects of turbulence in the MHD plasma from other phenomena.

4.2 Measurements without Magnetic Field

The laser gain data without magnetic field provides a good record of collisional excitation and relaxation of CO₂ molecules in a Cs seeded He plasma. Details of these processes will be discussed in chapter 5. Keeping the total static pressure in the test chamber between 33.30 torr and 70.00 torr, for various values of J_x , f_{Cs} and f_{CO_2} , laser gain was measured as shown in Fig. 4.4 as a function of time. The principal features of this time history of the gain are:

a) The gain rises in a time of about 10 ms to a value of 0.1cm^{-1} , is nearly constant for some 100 ms, then decreases, becoming strongly negative before the current is terminated at 330 ms.

b) The negative gain (absorption) then relaxes on about a 500 μs time scale.

During the course of our investigation, it was established that Fig. 4.4 describes the gain behavior only qualitatively. The time required for gain to peak and then convert into absorption were different for each run, and hence so were the excitation and deactivation frequencies of the laser levels.

Since the data obtained is a result of careful and systematic scanning through all the relevant parameters, a large number of possible combinations of laser pumping and relaxation rates have been achieved in this investigation. Thus almost all the information needed to predict the performance of an MHD laser plasma can be extracted from these results without detailed analysis of the individual processes favoring the inversion.

4.2.1 Small Signal Gain Measurements

Under some conditions small signal gain up to 0.3cm^{-1} has been measured. Maximum gain of 0.3cm^{-1} was recorded in experiment No. 4120. Current density of 0.382 amp/cm^2 was applied to an He plasma composed of 0.93% CO_2 and 0.0015% Cs (Fig. 4.5). The gain rises very rapidly, in 2 μs , stays constant at 0.3cm^{-1} for another 4 μs and then slowly falls, turning negative to a value of -0.22cm^{-1} .

In a real MHD laser cavity, where the gas mixture may be flowing at a velocity of ~ 3000 m/sec ($\sim M = 3.0$), a channel length of 12 mm (3×10^6 mm/sec $\times 4 \times 10^{-6}$ sec = 12 mm) would be available for power extraction with a capability of generating zero power gain of $0.3\% \text{cm}^{-1}$ along the laser cavity. Depending upon the dimensions of the channel and on the electrical power dissipation, a 12 mm long optical cavity may or may not be adequate to extract the desired laser power efficiently. In each case of MHD laser design, the dimensions of the laser cavity, output mirror transmission coefficient, and the nozzle dimensions have to be compromised to achieve the required resultsnt power output. Here the matter has been pointed out only to demonstrate the usefulness of the information for MHD laser design.

For a clearer picture the entire spectrum of measured gain was plotted against the time during which the peak value remained constant and is shown in Fig. 4.5. It can be seen that for a gain value of $0.09\% \text{cm}^{-1}$ the transient behavior of the inversion literally disappears ($\tau = 300 \mu \text{sec}$). The consequences of this result will be discussed in chapter 5 in more detail. It should be noted that the flowing MHD plasma (Mach = 3.0) will travel 0.9 m along the nozzle length and will provide enough room to extract huge laser power, while keeping the transmission coefficient of the output mirrors at a relatively lower value (which might be dictated by the lower zero power gain value of $0.09\% \text{cm}^{-1}$).

Walter,¹² in his analytical study of an MHD plasma, has arrived at an average small signal gain of $0.07\% \text{cm}^{-1}$, which yields laser power

densities of $\sim 1.8 \times 10^6$ W/m³ and $\sim 60 \times 10^6$ W/m³ using three temperature and two temperature models respectively. The deactivation rates:

$$k_{100 - CO_2} = 8.8 \times 10^5 \text{ atm}^{-1} \text{ sec}^{-1}$$

$$k_{100 - He} = 4.8 \times 10^4 \text{ atm}^{-1} \text{ sec}^{-1}$$

used in his three temperature model, as published by Murray, Mitchner and Kruger are much slower than measured in this work, (see section 4).

$$k_{100 - CO_2} = (3 \pm 0.3) \times 10^7 \text{ atm}^{-1} \text{ sec}^{-1}$$

$$k_{100 - He} = (7.5 \pm 0.5) \times 10^4 \text{ atm}^{-1} \text{ sec}^{-1}$$

This suggests that average extractable laser power can be close to a few tens of MW/m³.

As has been said before the main parameters effecting the laser gain are: J_x , f_{Cs} , f_{CO_2} ($B = 0$ in this section), their individual effects on inversion will be discussed in the following sections.

4.2.2 Effects of Cesium Concentration

It is believed that with CO_2 concentrations less than 1% in a Cs seeded He plasma the free electrons of the plasma remain, for all practical purposes, in saha balance with the bound electrons of metallic cesium. CO_2 molecules along with absorbing the translational energies of electrons, also quench the excited Cs atoms thus creating a source of additional energy drain. The degree of departure from Saha balance of the ionization process depends on the gas composition and the collisional activity of the various species. Quenching tends to decrease the number of electrons lowering the pumping capability of the laser plasma.

According to published cross sectional data electron-molecule vibrational excitation of the CO_2 asymmetric stretch mode dominates that of other models (bending and symmetric stretch) at electron temperatures higher than 0.3 ev. The population inversion thus created grows with increase in electron number density (and/or in electron temperature) only to an extent for several reasons. Even for a Maxwellian energy distribution, electron population having energies higher than ~ 1.5 ev becomes significant enough to directly pump the lower laser level ($10^0 0$). Also due to the simultaneous growth at $01' 0$, which is coupled to $10^0 0$ stronger than to $00^0 1$, tends to get more crowded. Its poor deactivation by He and CO_2 intensifies this effect.

It is clear from the above that the inversion process can be optimized by properly selecting the average electron temperature and the electron number density, and this, in fact, prescribes the Cs seed number density. It need not be mentioned here that the optimum value for f_{Cs} thus obtained will not be unique for the value of CO_2 concentration in the lower plasma.

Figure 4.7 provides a better understanding of this situation. The data are divided into sets such that each set represented experiments conducted at a particular and constant seed fraction. From all these sets each representing a different f_{Cs} value, the peak gain values were selected and plotted against their respective seed fraction values. This technique allows us to find for each set that unique combination of other independent relevant parameters ($J_x, f_{\text{CO}_2}, p, B=0$), while f_{Cs} is kept constant, which

produces maximum pumping power. This search, when carried out for each set in an identical manner, enables us to examine the physics and importance of proper seeding of MHD laser plasma.

As the Cs seed mole fraction is increased from $\sim 8.0 \times 10^{-6}$ to $1.4 \times 10^{-5}^*$, a rapid rise in gain is seen, indicating strong positive dependence of 001^0 level excitation on electron number density. The optimum Cs seed mole fraction of 1.4×10^{-5} at which the record gain of $0.32\% \text{cm}^{-1}$ was measured, seems to almost coincide with the value predicted by Lowenstein ($\sim 10^{-5}$). However, the small signal gain computed was $0.02\% \text{cm}^{-1}$, 15 times lower, with CO_2 concentration of 0.22% (in this work $\text{CO}_2 = 0.93\%$).

Further increase in the seed fraction causes gain to decrease slower than the rise on the left side of the curve. As can be seen from the cross sectional data (Fig.) for electronic excitation of 10^0 the pumping rate of the lower laser level will rise very slowly with increase in number of available electrons. Thus overcrowding of this level may be the sole cause of the drop in gain. In chapter 5 it will be demonstrated that quenching of excited Cs atoms can severely poison the laser plasma and a steep drop in gain may result. The degree of poisoning due to the quenching effect is set by the ratio n_{CO_2}/n_e and there exists a limit on its value beyond which the actual number of electrons present in the plasma is depressed far below the Saha value⁵. Lowenstein estimates this value to

* It is needless to say that the absolute values of n_e will be misleading here, as the experiments were done at different pressures.

be ≈ 100 , however, this study indicates a much higher value ($\sim 3 \times 10^3$). Consequences of this result will be discussed in the sections to follow. At this stage we will simply deal with the engineering aspect of the laser.

The graph in Fig. 4.7 immediately suggest than an MHD laser operating with seed concentrations below 1.4×10^{-5} will not be a practical device, gain is too sensitive to the fluctuations in fcs in that zone. The data suggests that seed mole fraction should be in the vicinity of 1.4×10^{-5} to 2×10^{-5} . It is important at this time to mention that in order to compensate per the loss of metallic Cs due to CO_2 and Cs interaction one might have to seed the laser plasma in excess of the above recommended value, and an error, if any, is desirable in the positive direction. An estimate of the rate of CO_2 - Cs interaction has been made in section 4.

4.2.3 Effects of CO_2 Concentration

Using the data reduction method discussed in section 4.3.4 a plot of gain versus CO_2 concentration has been obtained (Fig. 4.8). The laser gain coefficient for a pressure broadened profile which is applicable in this case of MHD laser, may be written in the form:

$$\alpha(v) = \Delta N_{\text{CO}_2} \frac{\lambda^2}{8\pi n^2 t_{\text{spont}}} g(v) \quad (4.3)$$

For simplicity considering the equation at the resonance $v = v_0$:

$$\alpha(v_0) = \Delta N_{\text{CO}_2} \frac{\lambda^2}{8\pi n^2 t_{\text{spont}}} \quad (4.4)$$

As normalized line shape function $g(v_0) = \frac{1}{\Delta v}$.

For pressure broadened profiles:

$$\Delta v = \sum_s N_s \sigma_s \sqrt{\frac{8kT}{\pi \mu s}}$$

Values for σ_s are:

$$\sigma_{CO_2-CO_2} \approx 10^{-8} m^2$$

$$\sigma_{CO_2-He} \approx 0.3 \times 10^{-8} m^2$$

Calculations show that for CO_2 concentrations of interest the broadening is dominated by the He, which is the dominant species. Hence we write:

$$\Delta v \propto \frac{N_{He+CO_2}}{N_{He+CO_2}}$$

or,

$$\alpha(v_0) \propto \frac{\Delta N_{CO_2}}{N_{He+CO_2}} \quad (4.5)$$

or,

$$\alpha(v_0) \propto \Delta f_{CO_2} \quad (4.6)$$

Thus we see that small signal gain is proportional to the population inversion normalized to the total number of neutral species, and hence the plot in Fig. 4.8.

Initially, as expected, gain rises linearly, with increase in molecular population. However, gain after reaching a maximum of $0.32\%/\text{cm}^{-1}$ at 0.93% CO_2 concentration starts to drop at a much slower rate than the rise. The adverse effect on inversion may be attributed to already discussed following reasons: overcrowding of the laser lower level, increased inelastic losses of electron energy to CO_2 molecules, as the

relative number of the latter grows, and quenching of the excited Cs atoms. In spite of overloading of the nonequilibrium MHD interaction, inversion providing a gain of 0.09cm^{-1} is achieved, even at a CO_2 concentration of 3%.

It is important to note that for high laser output power, CO_2 population made available to the plasma should be as large as may be allowed without sinking the unsaturated gain to an unacceptable level. Also, recalling the graph in Fig. 4.6, it can be seen that laser operation at lower gain values ($\sim 0.1\text{cm}^{-1}$) provides a longer useful cavity. A laser design enthusiast can very well see that although the optimum value for CO_2 concentration is 0.93%, for efficient power extraction it will be much higher, the limit being the bottle-neck effect discussed in chapter 2. According to the theoretical study done by Walter¹² this value is 3%, at which he predicts a gain value close to 0.1cm^{-1} , a figure very much in agreement with the graph in Fig. 4.8.

4.2.4 Optimum Current Densities

As a variable during the investigation current density has been representative of the electrical properties of the plasma in question by simulating the $\underline{U} \times \underline{B}$ induced field of flowing systems. The qualitative effect of magnetic field on gain has been discussed in section 4.4, however the picture is not complete without consideration of the effect of its magnitude coupled with flow velocity \underline{U} , which is implicit in the magnitude of current density.

In a flowing system both \underline{U} and \underline{B} , along with f_{Cs} , f_{CO_2} and p ,

have to be defined to create any desired plasma condition, however, in our case the current density serves as the closing link. The number density of electrons, their distribution function and average temperature are uniquely defined, consequently so are the excitation and deactivation rates of laser levels by the current density.

When, for fixed values of f_{Cs} , f_{CO_2} and p , the current density is varied, a value is reached where the gain is maximum. Results of such experiments for two different gas mixtures are plotted in Figs. 4.14 and 4.15. For the set of experiments of Fig. 4.14 the seed mole fraction was 10^{-5} with a CO_2 fraction of 0.74%. At a constant pressure of 42.00 torr, maximum gain of $0.10\%cm^{-1}$ was recorded at a current density of 0.4 amp/cm^2 . The curve is almost cone symmetrical about the maximum, gain disappears at current densities below 0.22 amp/cm^2 and above 0.50 amp/cm^2 .

On the other hand, in Fig. 4.15 the gain rises rapidly from seed to $0.125\%cm^{-1}$ when the current density is increased from 0.25 amp/cm^2 to 0.3 amp/cm^2 , and with further increase in the latter, although it falls it tends to reach an asymptotic value of $0.05\%cm^{-1}$. The main difference in these data sets is in f_{Cs} and f_{CO_2} , in this case (Fig. 4.15 being 6.0×10^{-5} and 2.47% respectively.

For a clearer view the corresponding conductivities have been plotted against gain in Fig. 4.16. At higher values of CO_2 mole fraction the plasma stabilizes, increase in conductivity does not effect the inversion severely and decay in gain is slower. As concluded before, laser operation at higher CO_2 concentrations ($\sim 2\%$) will be stable and predictable.

4.2.5 Effect of Quenching of Excited Cs Atoms

When the rate of relaxation of the excited state of Cs atoms by CO_2 molecules becomes comparable to the rate of its excitation by electrons, the electron number density is severely reduced. For a simple qualitative analysis we make following assumptions:

and 1. The excitation rate = $N_{\text{Cs}} N_e \bar{C}_e Q_{e-\text{Cs}}$ (4.7)

2. The Quenching rate = $N_{\text{Cs}}^* n_{\text{CO}_2} \bar{C}_{\text{Cs}-\text{CO}_2} Q_{\text{CO}_2-\text{Cs}}$ (4.8)

3. The vibrational levels of CO_2 molecules act in such a way that an average quenching cross section can be defined.

4. $N_{\text{Cs}}^* \approx N_e$

Then the effectiveness of the quenching process can be represented by the ratio $\frac{n_{\text{CO}_2}}{n_{\text{Cs}}} = \frac{f_{\text{CO}_2}}{f_{\text{Cs}}}$. In Fig. 4.17 the dependence of gain on this ratio can be seen. Gain increases linearly with $\log(f_{\text{CO}_2}/f_{\text{Cs}})$. Until the latter reaches a value of 700, a steep drop in gain follows that point. Shaw⁵ reports that the depression of electron number density below the Saha value is gradual, as the quenching rate increases, and at a critical value electron number density is severely reduced. The drop in gain in Fig. 4.17 is linear and it is concluded that, though quenching has become important, the critical point is not reached.

Taking $0.1\% \text{cm}^{-1}$ as the lower limit for desirable value of $f_{\text{CO}_2}/f_{\text{Cs}}$, we find 1800 to be the allowable value for $f_{\text{CO}_2}/f_{\text{Cs}}$. For $f_{\text{Cs}} = 2.0 \times 10^{-5}$, the CO_2 mole fraction is then 3.5%.

4.3 Experiments with Magnetic Field

The data taken without magnetic field provide a comprehensive knowledge about the excitation and relaxation processes of CO_2 molecules in a univorm MHD plasma. Gain measurements were made with magnetic field to observe the effects of non-uniformities. Two typical gain curves are presented in Fig. 4.9 and Fig. 4.10. During the first $10-15 \mu \text{ sec}$, a steep rise is seen, and then the inversion tends to follow an oscillatory pattern. It is believed that the Lorentz force, which in our configuration acts perpendicular to the laser beam, generates a pressure wave carrying the excitation out of the probe area. Taking the sound speed in the tube as 1000 m/sec we find a full wave period in the 2.54 cm tube of $25 \mu \text{ sec}$, which is close to the observed average period. The ratio $J \times B/p$ ranges from 1.5 m^{-1} to 0.3 m^{-1} .

It is concluded that the peak gain recorded in such experiments are the values which would be realizable in a flow system. The data so obtained has been reduced to find a relationship between gain and magnetic field strength and is presented in Fig. 4.11. The graphs have been plotted for three different values of CO_2 concentration. With increasing magnetic field, the effective dissipation in the plasma increases and hence the pumping, and consequently the gain. It will be seen from Fig. 4.11 that gain decreases with CO_2 population, which seems consistent with the result of section 4.2.3.

As an exercise in consistency of results a plot of gain versus Cs mole fraction (for $B \neq 0$) is shown in Fig. 4.12. When compared with the graph

in Fig. 4.7 (for $B = 0$) it should be noted the optimum value for f_{Cs} , in both cases, is close to 10^{-5} . The measured gain, in this section, is smaller than its value in Fig. 4.7 for a corresponding seed fraction, especially at higher values of $J \times B/p$, when the pressure wave becomes stronger. In a flow system designed for MHD interaction the Lorentz force vector acts opposite to the pressure gradient causing the motion and does not have any similar effect on gain. (In fact the inversion in a poorly designed nozzle system might not have a uniform profile, but due to other effects which will not be discussed here.) The gain measured in this section represents the lower limit for the particular case in question and higher values may be achievable in real practice. In this work however we will limit ourselves to the data in hand and simply remark that at state of the art fields of 4 to 5 tesla the gain would be of respectable value.

The measured apparent Hall parameter falls in the range of 0.45 to 0.67, close to the value reported by other experimental investigators (4, 7, 11). In the analytical calculation of Walter,¹² in which β_{app} is computed by the model originated by Solbes¹⁵ and Parma²⁹ and later modified by Cole,¹⁶ a value of 0.1 has been reported ($f_{CO_2} = 3\%$; $B = 4.0$ tesla). Since this parameter is dependent on the electrode and insulator design and growth of electrothermal instabilities at higher magnetic fields realization of optimized Hall recovery may be difficult in an MHD laser (quantitatively the results of Parma's and Cole's models for high $\langle \beta \rangle \geq 10$ may be questioned).

The non-uniformities in an MHD plasma profoundly influence electron temperature elevation and average joule dissipation of energy in the gas.

In the limit when $\langle\beta\rangle > \beta_{\text{crit}}^{33}$ a "turbulent state" is reached with an anomalous increase in resistivity. The value of $\sigma_{\text{eff}}/\langle\sigma\rangle$, which is a measure of "turbulence", has been found to be on the order of ~ 0.2 , with β_{eff} closed to 0.5.

As the value of $\langle\beta\rangle$ increases, gain rises and reaches the peak value of 0.3cm^{-1} , which interestingly enough coincides with the maximum value measured in absence of a magnet \times field. The peak value with magnetic field was reached at a lower CO_2 mole fraction (0.74% vs 0.94%) and lasted only 4 μsec as compared to 10 μsec ($B = 0$).

It has been postulated that high turbulence somehow tends to create more favorable condition for pumping.

4.4 Relaxation Rates for the Lower Laser Level ($10^0 0$)

While the discharge is on, the vibrational levels of CO_2 are pumped and the population of any level can, in its simplest form, be computed by the rate equation:

$$\frac{d}{dt}(N) = W_p N_0 - \frac{N}{\tau_e} \quad (4.9)$$

where $\frac{1}{\tau_e}$ represents the depletion of the population in question by collisional relaxation, excitation out of the level by electron impact, and radiative decay. When the discharge is short-circuited, electronic pumping of the level ceases and the system in time approaches an equilibrium state. The transient behavior of the population can be described as:

$$N(t) = N_{\text{equ.}} \exp(-t/\tau_e) \quad 4.10)$$

For our purpose the time constant τ_e hereafter will be referred as the collisional relaxation time constant, as the radiative decay of the lower and upper laser levels of CO_2 molecules is relatively very slow (chap. 2). The decay of population inversion in the afterglow of the discharge in simplified notation can be expressed as:

$$\Delta N = N_{20} \exp(-t/\tau_{e2}) - N_{10} \exp(-t/\tau_{e1}) \quad (4.11)$$

where 2 and 1 are subscripts for the upper and lower laser levels. The time constant τ_{e2} has very large values,^{47,48} for example, for a 97% He + 3% CO_2 gas mixture at a typical pressure of 50 torr, they are:

$$\tau_{e2}^{\text{He}} = 230 \text{ } \mu\text{sec}$$

$$\tau_{e2}^{\text{CO}_2} = 1852 \text{ } \mu\text{sec}$$

Thus, without introducing any appreciable error in the analysis (<5%)

Eq. (4.12) can be rewritten as:

$$\Delta N = -N_{10} \exp(-t/\tau_{e1}) \quad (4.13)$$

A relaxation rate constant is defined as:

$$k = \frac{1}{\tau_p} \quad (4.14)$$

and usually expressed in units of $\text{atm}^{-1} \text{sec}^{-1}$. Since both the He and CO_2 participate in the deactivation process, the relaxation time constant τ_e can be split into two parts:

$$\frac{1}{\tau_e} = \frac{1}{\tau_{e,\text{He}}} + \frac{1}{\tau_{e,\text{CO}_2}} \quad (4.15)$$

Using Eq. (4.9) and simple algebra, the following relationship can be obtained:

$$\frac{1}{\tau_e^p} = k_{CO_2-He} + f_{CO_2} (k_{CO_2-CO_2} - k_{CO_2-He}) \quad (4.16)$$

As the small signal gain measures the magnitude of the population difference ΔN , τ_e is easily obtained from the data (Fig. 4.5; note the decay of laser beam absorption after the discharge is short-circuited). Values of $\frac{1}{\tau_e^p}$ have been plotted against their respective CO_2 concentrations in Fig. 4.18 and the following rate constants were determined:

$$k_{CO_2-He} = (7.5 \pm 0.5) \times 10^4 \text{ atm}^{-1} \text{ sec}^{-1}$$

$$k_{CO_2-CO_2} = (3.3 \pm 0.3) \times 10^7 \text{ atm}^{-1} \text{ sec}^{-1}$$

The mechanism of symmetric stretch mode relaxation by CO_2 molecules is very complex (chap. 2) and this investigation cannot identify the individual pathways of deactivation. However, the following facts allow us to make some reasonable speculations:

(1) The system measures the slowest rate and hence the "bottleneck" rates.

(2) Deactivation of the $CO_2(01^00)$ level by He is one order of magnitude faster than by CO_2 ($k_{CO_2(01^00)-He} = 4.0 \times 10^6 \text{ atm}^{-1} \text{ sec}^{-1}$ at $T = 400^\circ K$) and the major role of CO_2 - CO_2 collisions is to bring the $CO_2(10^00)$ level to $CO_2(01^00)$ either via $CO_2(10^00) \rightarrow CO_2(02^00)$ or $CO_2(10^00) \rightarrow CO_2(01^00)$ transfers.

It is concluded that the rate measured for CO_2 - CO_2 relaxation is the bottleneck rate for the lower level deactivation:

$$k_{CO_2(10^00)-CO_2(01^00)} = (3.3 \pm 0.3) \times 10^7 \text{ atm}^{-1} \text{ sec}^{-1}$$

$$= (4.3 \pm 0.4) \times 10^4 \text{ torr}^{-1} \text{ sec}^{-1}$$

This rate very closely coincides with the rate calculated by Seeber⁵⁸ and is of the same order of magnitude as reported by Bulthuis and Ponsen.⁵⁹ Table 2 compares the reported rates with the value measured in this experiment.

In Table 3 relaxation rates between $CO_2(10^00)-CO_2(02^00)$ are listed.

The investigators believe that all the levels in the bending mode do exist in Boltzmann equilibrium and bottleneck rate is determined by $CO_2(02^00)$ population. A close examination of the rates tempts us to make following speculations:

1. If the explanation given by Stark⁶² is correct, then there must exist another process, slower than $CO_2(10^00) - CO_2(02^00)$, which determines the bottleneck rate.
2. If the other^{61,63} rates are correct, then, definitely, the bottleneck exists at the $CO_2(10^00) - CO_2(02^00)$ equilibrium.

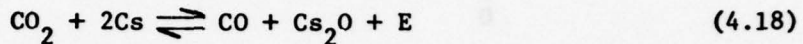
The value of $k_{CO_2 - He}$ is very low for the relaxation rate of the lower laser level (except according to the value reported by Rosser, Hoag, and Gerry,⁴⁹ and interestingly enough, coincides with the relaxation rate for the upper laser level. It would be wise to leave this rate with the comment that it represents a slow process of deactivation by the atoms, and $CO_2 - CO_2$ collisions establish the "bottleneck rate".

4.5 Rate of Cs - CO₂ Interaction

The exact nature of Cs + CO₂ chemical interaction is not known. Two possible reactions have been cited:



and



Reaction (4.18) is believed to be weakly exothermic at room temperature. Without going into the details of the reaction mechanism, we will estimate the rate of interaction. Let Q_{CS-CO₂} be the cross-section for this interaction such that the frequency of chemical encounters

$$v_{\text{Cs-CO}_2} = n_{\text{CO}_2} Q_{\text{Cs-CO}_2} \bar{c}_{\text{CO}_2} \text{ sec}^{-1} \quad (4.19)$$

where \bar{c}_{CO_2} is the mean velocity defined as

$$\bar{c}_{\text{CO}_2} = \left[\frac{8kT}{\pi} \left(\frac{1}{M_{\text{CO}_2}} + \frac{1}{M_{\text{Cs}}} \right) \right]^{1/2}$$

Thus the fraction of Cs atoms lost due to the chemical reaction is:

$$\frac{\Delta n_{\text{Cs}}}{n_{\text{Cs}}} = v_{\text{Cs-CO}_2} \text{ sec}^{-1} \quad (4.20)$$

and hence the cross-section

$$Q_{\text{Cs-CO}_2} = \frac{\Delta n_{\text{Cs}}}{n_{\text{Cs}} n_{\text{CO}_2} \bar{c}_{\text{CO}_2}} \quad (4.21)$$

Several experiments were conducted in sets of two: one with, and one without CO₂, and from the Cs absorption diagnostics the n_{CS} was determined using the calibration curve 3.10. It should be remembered

that in the absence of CO_2 the Cs mole fraction remains constant throughout the pressure pulse, which is confirmed by the absorption curve. From the two curve we get the time history of total Cs atoms lost, i.e.

$$(\Delta n_{\text{Cs}})_{\text{tot}} = \int_0^t n_{\text{Cs}} n_{\text{CO}_2} \sigma_{\text{Cs-CO}_2} \bar{c}_{\text{CO}_2} dt \quad (4.22)$$

A numerical differentiation of $(\Delta n_{\text{Cs}})_{\text{tot}}$ gives Δn_{Cs} , from which the cross-section can be calculated using the equation (4.21).

From several sets of data the cross-section was computed to be in the range of 1.3×10^{-24} to $4.6 \times 10^{-24} \text{ m}^2$.

V. DISCUSSION OF RESULTS

The measurements of axial electric field by two probes in contact with the plasma show that the conductivity does not remain constant throughout the experiment. Its value increases with time. It has been mentioned from time to time in previous chapters that due to redistribution of CO_2 molecules amongst their vibrational levels due to excitation and various relaxation processes, the value of the inelastic loss factor δ_{CO_2} goes down. Walter¹² in his analytical three temperature study has observed that this reduction may be as large as 50%. While reviewing the relaxation processes we have seen that the levels in the bending mode relax much slower than would be required to attain a Boltzmann distribution within the mode. In that case it would be inaccurate to assign one temperature to all the levels of the bending mode. 02^00 , 01^10 and 03^20 should be described by three different temperatures, and one would require a "5 temperature" model. One would expect a drastic reduction in δ_{CO_2} , and hence increase in conductivity if this occurs. In the experiment, however, there is another phenomenon, which may cause the same effect. The electron energy equation if written for static conditions, i.e. if the fluid velocity is zero, will take the form:

$$\left(\frac{3}{2} + \frac{\epsilon_1}{kT_e}\right) kT_e \frac{\partial n_e}{\partial t} = \frac{J^2}{\sigma} - \sum_s \epsilon_s \quad (5.1)$$

where $\epsilon_s = \delta_s \frac{m_e}{m_s} \frac{3}{2} (T_e - T) n_e v_e$ is the loss term. Since J is maintained constant during the experiment, one would expect a gradual change in n_e .

(and T_e coupled with Saha equation). Further analysis shows that, in fact, a gradual evolution of the ionization process towards full ionization takes place, which results in an increase in the conductivity of the plasma.

Typical increase in electron temperature with time is shown in Fig. 5.1. We know that at higher electron number densities ($n_e/n_{He} > 10^{-5}$) pumping of the bending mode becomes significant, which has a negative effect on the inversion. This has been confirmed during the experiment, since in most cases where a positive gain in the beginning of the discharge was recorded, a gradual decrease in gain is observed, and toward the end of the discharge the gain turns into absorption.

The numerical model of Walter¹² predicts gains in the range of 0.1 - 0.15% ($T_0 = 2090^\circ K$), however he points out that if the stagnation temperature is lowered to $1800^\circ K$ gain may reach a value of 0.21%, and it seems perfectly plausible that if T_0 is reduced further the calculated small signal gain may rise to the measured value of $0.3\% \text{ cm}^{-1}$. It is not clear, however, how low the static temperature has to be to achieve such an inversion. In the calculations using $T_0 = 2090^\circ K$, the static temperature falls to the range of $400^\circ K$ to $600^\circ K$, then, due to the Lorentz force, it rises as the fluid moves along the nozzle. This temperature range is slightly higher than that of the experiments.

Furthermore, Walter's calculations are based on a constant Mach number channel, which may not be an advantageous design for an MHD laser, probably a constant temperature or a compromise between the two may be better. At this point it is difficult to speculate, only after a series of numerical calculations would one be able to draw any conclusions.

The Russian group,¹¹ by extrapolating from the losses in the cavity, came to the conclusion that a small signal gain of $0.3\%/\text{cm}^{-1}$ was achieved in the experiments ($T = 400^\circ\text{K}$), which equals the value measured in this investigation.

Walter concludes that the optimum CO_2 mole fraction is 3%. In this study the maximum gain has been measured at 1% CO_2 and, as will be shown in Chapter 6, maximum power extraction will not occur at 1% CO_2 . The output intensity is dependent on one more factor, namely, saturation intensity, whose value increases with increasing CO_2 mole fraction. The gain is measured to decrease as f_{CO_2} is increased from 1%. Thus the optimum CO_2 mole fraction definitely will be larger than 1% and may be equal to 3%. A power extraction experiment is needed to confirm this.

The fact that Walter did not account for $\text{Cs} - \text{CO}_2$ chemical interaction does not effect the validity of his results, as the cross-section for the reaction is measured to be very small $\sim 10^{-24} \text{ m}^2$. At pressures on the order of 0.25 atm only a few percent of Cs would be lost.

The electron temperatures measured range from 3300°K to 4500°K (1% CO_2), which is in close agreement with the prediction of the numerical study. The same is true for values at other CO_2 mole fractions. The electron number density, when scaled down by a factor equal to the ratio of the pressures, is in good agreement with Walter's values. Under optimum conditions (1% CO_2) the value is $6 \times 10^{18} \text{ m}^{-3}$ ($p = 60$ torr, $f_{\text{Cs}} = 10^{-5}$). Lowenstein, while studying the effect of quenching computed an upper limit for ratio $n_{\text{CO}_2}/n_e \lesssim 100$ to be allowed into a laser cavity. In the present

study typical values have been on the order of $\sim 10^4$, and much higher gain values have been recorded. This indicates that his estimate for the quenching cross-section is unrealistically high. Furthermore, Walter in his study showed that even if the cross-section is as high as assumed by Lowenstein (70 \AA^2), in an adequately preionized fluid, losses due to quenching would be negligible.

VI. SUMMARY

With the aid of a 6 watts/cm² probe CO₂ laser (oscillating at 10.6 μ infrared wavelength) the small signal gain of He + CO₂ + Cs plasmas with compositions typical of MHD lasers has been measured. Variables used to provide a wide spectrum of pumping and relaxation rates are:

- (1) Current density J varied from 0.2 amp/cm² to 0.75 amp/cm².
- (2) CO₂ mole fraction f_{CO_2} varied from 0.74% to 4.7%.
- (3) Cs mole fraction f_{Cs} varied from 8.0×10^{-6} to 3.0×10^{-4} .
- (4) Magnetic field B varied from 0.0 to 0.68 tesla.
- (5) Mixture static pressure P varied from 33.0 torr to 70.0 torr.

Under these conditions, the small signal gain was measured to be in the range of 0.06% cm⁻¹ to 0.3% cm⁻¹. During the \sim 300 μ sec experimental time of each experiment, population inversion, in general, was found to be transient in behavior, which has been a very important feature of this investigation. Time scales for relaxation processes to attain equilibrium range from 1 μ sec to $10^* \mu$ sec,¹² in fact for most of the experiments it has been on the

* It is assumed that sufficient number of CO₂ molecules are available in the ground state.

order of 5.0^* μ sec (which has been computed based on the relaxation data measured during this study). Thus, gain (or absorption) lasting more than 5 μ sec is a result of fully developed inversion kinetics and has been regarded as valid experimental data.

Due to redistribution of the CO_2 molecule population amongst it's various vibrational levels, the average coefficient of inelastic losses changes, actually drops, sometimes enough to alter the electron number and electron temperature on the scale of 5-10 μ sec. Under these conditions one single experiment is able to provide several valid experimental gain measurements.

The time history of the gain data tells another interesting story, that the higher the gain value, the shorter the time it lasts. A graph of gain versus it's duration has been presented in Fig. 4.6. This phenomenon, apart from drop in δ_{CO_2} value may be due to another reason: severe reduction of ground state CO_2 molecules. In fact, a simple calculation based on rate equations has shown that at low CO_2 concentration ($\sim 0.9\%$ at $p = 50.0$ torr) more than 50% of the total molecular population participates in creation of a gain value of, say, $0.3\% \text{ cm}^{-1}$, requiring a population inversion of $[N_{\text{CO}_2(00^{\circ}1)} - N_{\text{CO}_2(10^{\circ}0)}] = 1.7 \times 10^{15}$ molecules/ cm^3 . In experiment 4120, at 0.94% of CO_2 mole fraction, the measured gain reached a value of $0.32\% \text{ cm}^{-1}$, but lasted only a few μ sec, and then very rapidly dropped, turning into absorption. It is concluded that the pumping power of the

* It is assumed that sufficient number of CO_2 molecules are available in the ground state.

plasma, representing the number density and the temperature of electrons, was high enough to excite the required number of CO_2 molecules, but after a few micro-seconds the supply of ground level molecules had been depleted, and the inversion could not be maintained further. Thus, if the mixture static pressure is increased and the mole fraction of CO_2 is kept at $\sim 0.9\%$, both, high pumping power and adequate supply of CO_2 molecules may be maintained and the small signal gain on the order of $0.3\% \text{ cm}^{-1}$ may be achieved. At this point it is important to note that CO_2 mole fraction is not the only nondimensional parameter which should be kept constant in order to duplicate the plasma conditions at any particular pressure, the others* will be discussed later in this section.

As the CO_2 mole fraction is increased, beyond 0.9% , gain drops, at $3\% \text{ CO}_2$ the value is $0.1\% \text{ cm}^{-1}$, and lasts for the entire duration of the discharge ($\sim 300 \mu\text{sec}$). Three different phenomena affect the inversion kinetics as the CO_2 mole fraction is increased in the plasma: (1) more molecules become available in the ground state (for excitation); (2) the inelastic "load" on the non-equilibrium regime increases; (3) relaxation of the lower laser level by CO_2 molecules (to the $01'0$ level) intensifies and finally reaches the "bottleneck", a saturation point.

In a flowing system (Mach number of 4) the plasma would move with a velocity of $0.4 \text{ cm}/\mu\text{sec}$ and travel a distance of, say, half a
 $*\langle\beta\rangle, M, \frac{\sigma_{\text{eff}}}{\langle\sigma\rangle}, \beta_{\text{app}},$ to name a few.

meter in ~ 125 μ sec. Thus the plasma conditions creating an inversion lasting more than 100 μ sec would provide enough active volume for power extraction.

The optimum Cs mole fraction has been found to be 1.4×10^{-5} . At lower values of f_{Cs} gain very sensitive to former's value, a 10% reduction in f_{Cs} causes a 30% drop in gain, whereas a similar increase ($f_{Cs, \text{opt.}} + 10\%$) does not make any significant drop in the gain value (-5%). It is common knowledge that, in practice, even a moderate accuracy ($\sim \pm 50\%$) in seeding is hard to achieve, the error margin should be set only in the positive direction (i.e. $f_{Cs} + 50\%$, for example), for reasons said before.

Although, it is known that Cs and CO_2 interact chemically, no concrete information about the nature of the resultant products or the rate of interaction is available, to date. During this investigation the cross-section for this interaction has been experimentally determined to be $1.3 \times 10^{-24} - 4.6 \times 10^{-24} \text{ m}^2$ at 400°K . Based on these data, at a pressure of 0.1 atm the characteristic time for the chemical reaction with 3% of CO_2 would be about 30 msec against the residence time of 0.17 msec of a 0.5 m cavity:

$$t_{\text{res}} = \frac{L}{u} = \frac{0.5 \text{ m}}{3000 \text{ m sec}^{-1}} = 0.17 \text{ milli sec}$$

which means that only $0.17/30 \approx 5.6 \times 10^{-3}$ fraction of the Cs number density would be lost and even with an accuracy of $f_{Cs} + 10\%$ seeding, no noticeable change in n_{Cs} will occur.

The apparent Hall parameter has been found to be in the range of 0.45 to 0.67. The average Hall parameter is computed as ranging between 1.80 and 2.60 and definitely indicates signs of turbulence. With increasing $\langle \beta \rangle$, the gain rises and achieved the recorded highest limit of $0.3\% \text{ cm}^{-1}$ even at a low CO_2 concentration of 0.74%, though, for the reasons explained above, gain does last only for 10 μsec . This suggests that the pumping power is enhanced in a turbulent MHD plasma. At low values of $\langle \beta \rangle$, the gain is close to $0.08\% \text{ cm}^{-1}$, a value predicted by Walter.¹² These results may tempt one to design a MHD laser to operate in the turbulent mode, however caution is warranted here, since a turbulent gain medium is likely to deteriorate the beam quality.

In order to duplicate the electrical conditions of this experimental study in real practice, an MHD laser should be designed to produce an induced field $\underline{u} \times \underline{B}$, at least, equal to the field E externally applied in this study. An electric field of 20v/cm has been typical. Thus for a flow velocity of 3000 m/sec (Mach number 3) we estimate the required magnetic field B to be 0.67 tesla, which is slightly higher than used in the experiments. At state-of-the-art fields of 4-5 tesla the induced field would be more than adequate.

Sometimes, the discharge character of a plasma is defined by the E/p value.⁷⁰ In the present work, on average, it is on the order of $0.5 \text{ vcm}^{-1} \text{ torr}^{-1}$ (Table 4), which would be high enough to create a

self-sustained discharge¹¹ (~ 6.0 volts cm^{-1} torr⁻¹) at higher magnetic fields, say, 4-5 tesla.

Joule dissipation is another important parameter. When written in non-dimensional form, it's analytical expression is very useful in design considerations:

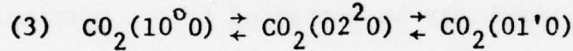
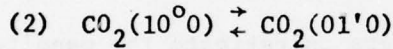
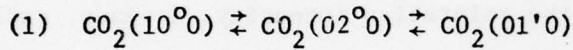
$$\frac{T_e - T_g}{T_g} = \frac{v}{3\delta'} M^2 \langle \beta \rangle^2 \frac{\sigma_{\text{eff}}}{\langle \sigma \rangle} \frac{1 + \beta_{\text{app}}^2}{1 + \beta_{\text{eff}}^2} \quad (6.1)$$

It should be noted that n_e does not directly affect the expression and Joule dissipation can be measured in terms of $\frac{T_e - T_g}{T_g}$, which in our experiments has reached values up to 9.0. For this value, substitution of other numbers, results in Mach number of 4.4, which might be a value higher than easily achievable in practice. However, as it was said before by raising $\langle \beta \rangle$, the desired dissipation can be achieved. It is interesting to note that, according to the data, the effective Joule dissipation can be achieved even at 0.5 tesla magnetic field in a 4.4 Mach number flow system, and the induced field will be on the order of the required value. In order to "ignite" the discharge a preionizer might be needed, however,

From the gain data, recorded in the after-glow of the discharge, the relaxation rate constant for the lower level by CO_2 molecules has been computed:

$$K_{\text{CO}_2(10^00)-\text{CO}_2(01^10)} = (3.3 \pm 0.3) \times 10^7 \text{ atm}^{-1} \text{ sec}^{-1}$$

This rate is equal to the value reported by Seeber,⁵⁸ who, in his modified SSM theory model, assumes that 02^00 and $01'0$ levels of the bending mode are not in thermal equilibrium. Bulthius,⁶⁰ based on his power decay measurements, reports a value very close to it ($\sim 10^7$ atm⁻¹ sec⁻¹). Since this measurement did not identify any particular pathway for the 10^00 $01'1$ relaxation process, and the published rate constants for, even, the $10^00 \rightleftharpoons 02^00$ terms resonance⁶¹⁻⁶³ are not in agreement, no speculation about the mechanism will be made. It will be sufficient to state this rate is the sum of the rates for all possible pathways:



The time constant for this process, if computed for $p = 40$ torr and $f_{\text{CO}_2} = 0.03$, comes to be $20,0 \mu\text{sec}$, which is much larger than the time constant* for $\text{CO}_2(01'0) - \text{He}^{51}$ ($\sim 4 \mu\text{sec}$), suggesting that the former process establishes the "bottleneck rate".

The value for $K_{\text{CO}_2(10^00) - \text{He}}$ relaxation process, found by extrapolation to $f_{\text{CO}_2} = 0$, is very low and falls within the error limit.

*The rate constant for this process is well researched and studied, and known with reasonable ($\pm 10\%$) accuracy.

6.1 Power Extraction

The measured gains are quite large (by MHD laser standards) and in view of the other information made available by this investigation (the rate of relaxation of the lower laser level and the rate of chemical interaction between CO_2 and Cs), we will take a fresh look at the power delivering capabilities of MHD lasers. In its simplest form, the expression for the intensity extractable from a laser cavity may be written as:

$$I_0 = P_0/A \approx 2I_s \left(\frac{\alpha_0 L}{\text{Li} + T} - 1 \right) T \quad (6.2)$$

The magnitude of I_s , the saturation intensity, depends, exclusively, on the physical properties of the laser mixture, and on its composition and static pressure. I_s lets us estimate the magnitude of the maximum laser power which may be extracted from a particular laser medium. From the expression for

$$I_s = \frac{4\pi n^2 \Delta\nu h\nu}{(t_2'/t_{\text{spont}})^2} \quad (6.3)$$

it can be seen that its value increases directly proportional to p^2 , since $\Delta\nu \propto P$ and $t_2' \propto \frac{1}{P}$. Thus the output power from a low internal loss (Li) laser cavity goes up as $\alpha_0 p^2$.

The relaxation time t_2' , in CO_2 lasers, is basically the relaxation time of the upper laser level, however, since a large number of energy levels are closely coupled with it, Christensen et al.⁴² suggest that in order to get any realistic value of the saturation intensity one should use a t_2' effective, instead of t_2' ; the discrepancy may be

as large as 2-3 orders of magnitude, since as many as 50 levels may be actively involved in competing for the inversion in the laser plasma.

Anderson²³ suggests another method for calculating the power output from a gas laser, which calls for numerical solution of the energy equations written for each vibration mode of the molecule. Such an analysis for a MHD laser cavity has been performed by Walter.¹² Walter's numerical model treats each mode individually (assuming a vibrational temperature associated with each mode) and uses the relaxation rate constants which are very close to the values measured during this investigation. For rough estimates of the laser power extractable from a MHD laser cavity, saturation intensities for various CO₂ mole fraction at a static pressure of 0.25 atm have been evaluated by extrapolating the figures made available by Walter's analysis. The results have been presented in Fig. 6.1.

For a given internal loss of the laser cavity (like absorption of power in the mirrors), there exists an optimum coupling parameter T.

$$(T)_{opt} = - Li + \sqrt{\alpha_0 L} Li \quad (6.4)$$

Using the measured small signal gain data and the computed saturation intensities, estimates of output laser intensities have been made (Fig. 6.1). It can be seen laser intensities as large as 1 KW/cm²* can be coupled-out from a MHD laser cavity, however it would be erroneous to draw any conclusions about the total power

*Cavity width L = 0.54m

output, which depends upon the length along the nozzle within which the inversion can be maintained. Walter¹² based on his numerical simulation of a MHD laser flow system points out that, although a high level of laser flux may be achieved at lower CO₂ mole fractions (say ~1% CO₂), after 5-10 cm of lasing length, the inversion is destroyed. Using these dimensions (height 2.3 cm) one gets a maximum laser output of 23.0 KW, and a power density of ~15.0 KJ/Kg.* It should be noted that the actual power would be less than this value as it assumes that the entire wall acts as a coupling mirror.

Walter, further, mentions that at $f_{Cs} = 3\%$ this "usable length" extends to the entire length of the cavity (~45 cm) and computes a power density of 60 KJ/Kg, against 30.0 KJ/Kg estimated in this study.

In Fig. 6.2 specific power of various laser systems has been compared. It can be seen that the MHD laser may have a promising future as a high power laser.

6.2 Suggestions for Future Work

The investigation has established that small signal gains of up to 0.3% cm⁻¹ may be achieved in a MHD laser plasma. The measured relaxation rate of the laser lower level suggests that the capabilities of MHD lasers might have been overestimated by other investigators⁶⁻⁸, the

*Walter used the dimensions of the MIT experimental nonequilibrium generator to calculate the gasdynamical parameters. In order to achieve a Mach number of 4 ($P_0 = 20$ atm; $T_0 = 2090^{\circ}\text{K}$) the mass flow required was $\dot{m} = 1.56$ Kg / sec.

bottom line predicted by this investigation is about 3-10 times less than previously computed. However, a close look at Fig. 6.1 would recommend the device as one of the promising competitors in the field of high power laser technology. In fact Biberman et al. measured 10KJ/Kg of specific power, which is very close to the bottom line predicted by Walter.¹²

With the new understanding of non-equilibrium plasmas and their better numerical models^{15, 16, 29} and the knowledge acquired by the numerical study of Walter and by this experimental investigation, a working model of the laser should be designed. On the design side, a better system for seeding of Cs and an appropriate location for CO₂ injection should be researched.

Further in the area of basic research the mechanism of lower laser level relation should be studied in more detail, the "bottleneck effect" which limits the magnitude of the laser power at 10.6 μ , may not affect the emission at 9.6 μ providing a possibility of high power laser operation at 9.6 μ .

The measured relaxation rate for 10⁰0 → 01¹0 process is very close to the values reported Bulthins^{59, 60} and Seeber⁵⁸ which suggests that the levels 01¹0, 02⁰0, 02²0, 03⁰0 may not be in thermal equilibrium and in order to calculate the power output more accurately, an analytical model more vigorous than the three temperature model is warranted.

APPENDIX A

MEASUREMENT OF Cs BOUND-FREE CONTINUUM

There are three possible mechanisms for emission of continuum radiation from a Cs seeded plasma: 1) Bremsstrahlung, 2) free-bound emission, 3) electron scattering by neutrals.

Free-free emission is due to an electron passing near a positive ion and being accelerated in the Coulomb field, known as Bremsstrahlung. The intensity of this type of radiation clearly depends on the product of electron and ion densities. For conditions typical of an MHD generator, Bremsstrahlung is at least 10 orders of magnitude below the free-bound emission.

Electron scattering by neutrals is a mechanism akin to Bremsstrahlung, except that the intensity depends on the product of electron and neutral densities. For a seed mole fraction of about $\sim 10^{-5}$, the electron scattering by neutrals would be more important than free-free emission by a factor of about $10^5 - 10^6$ at most. Thus, electron scattering emission is also well below the free-bound emission.

Free-bound emission is due to the capture of a free electron with a velocity, v , into a definite quantum level of the alkali metal, Cs. Any inert gas, He in this case, is considered as a buffer gas only and does not contribute to the continuum emission process. This type of radiation has been successfully used to measure electron temperature and number density. We will review the basic features of the physics involved in this process.

As a free electron of energy $1/2 \frac{m_e v^2}{2}$ interacts with an ion to occupy a certain quantum state 'j' of the ion, a photon is emitted, such that

$$h\nu = 1/2 \frac{m_e v^2}{2} + h\nu_j \quad (A.1)$$

where the ion kinetic energy has been neglected and ν is the frequency of the photon emitted.

The number of such recombinations is

$$-\frac{\partial n_e}{\partial t} = \int f_e(\vec{v}) n_I \sigma_j \vec{v} d\vec{v} \quad (A.2)$$

where σ_j is the relevant cross-section and $f_e(\vec{v})$ is the electron distribution function. Since the cross-section is expected to be isotropic and assuming that the free electrons have a Maxwellian* distribution of energy, we obtain:

$$-\frac{\partial n_e}{\partial t} = \int n_e n_I \left[\frac{m_e}{2\pi kT_e} \right]^{3/2} \exp \left(-\frac{1}{2} \frac{m_e v^2}{kT_e} \right) \sigma_j 4\pi v^2 d\vec{v} \quad (A.3)$$

Using the Einstein's coefficients we can write the expression for a number of bound-free transitions at a given frequency as (neglecting the induced emissions)

$$N_j \frac{8\pi h\nu^3}{c^3} e^{-h\nu/kT_e} B_j dv = N_j \frac{8\pi v^2}{c^2} e^{-h\nu/kT_e} \alpha_{j \rightarrow \text{free}} dv \quad (A.4)$$

here $\alpha_{j \rightarrow \text{free}}$ is the cross-section for photon emission and is given by $\alpha_{j \rightarrow \text{free}} = h\nu/c B_j$.

*For a typical MHD laser plasma with only a few percent of molecules, this is a good assumption.

The two processes described by (A.4) and (A.3) should balance exactly:

$$\begin{aligned} n_e n_I \left[\frac{m_e}{2\pi kT_e} \right]^{3/2} \exp \left(-\frac{1}{2} \frac{m_e v^2}{kT_e} \right) \sigma_j 4\pi v^2 dv \\ = \frac{N_j}{c^2} \frac{8\pi v^2}{h} e^{-hv/kT_e} \alpha_{j \rightarrow \infty} dv \end{aligned} \quad (A.5)$$

Using the Saha equation and the relation

$$\frac{dv}{dv} = \frac{m_e v}{h} \quad (A.6)$$

derived from (A.1) one gets the following relationship between $\alpha_{j \rightarrow \infty}$

and σ_j :

$$\sigma_j = \frac{h^2 v^2}{m_e^2 c^2 v^2} \frac{g_j}{g_I} \alpha_{j \rightarrow \infty} \quad (A.7)$$

g_j and g_I are the degeneracies of the state in question and the ion.

Thus the radiation energy per unit volume per unit frequency into a unit

$$\text{solid angle } J_{v_j} = \frac{c h v}{4\pi} \left. \frac{\partial n_e}{\partial t} \right|_v \quad (A.9)$$

The equation (A.8) is simplified by substitution of (A.7) and (A.3) and written in a convenient form:

$$J_{v_j} = \frac{1.5 \times 10^{-33} A_j n_e^2}{\lambda T_e^{3/2}} \exp \left[\frac{hc}{kT_e} (\lambda_j^{-1} - \lambda^{-1}) \right] \quad (A.9)$$

Here the coefficient A_j is a quantum-mechanical property of the transition state in question. In Cs two prominent transitions, namely, from continuum to 6P and 5D lower levels of the electronic transitions.

Various value for these transitions are:

$$A_j = 3.74 \times 10^{-6} \text{ for the } 6P \text{ continuum}$$

$$= 8.30 \times 10^{-6} \text{ for the } 5D \text{ continuum}$$

and

$$\lambda_j^{-1} = 19,700 \text{ cm}^{-1} \text{ for the } 6P \text{ continuum}$$

$$= 16,900 \text{ cm}^{-1} \text{ for the } 5D \text{ continuum}$$

The radiation intensity is, then, proportional to n_e^2 at each transition.

In order to determine the electron temperature one would be required to monitor the light output at two different wavelengths, and plot $\ln (J_\nu \lambda)$ against the wavelengths, the slope of the straight line would give the magnitude of T_e .

In the present study, the continuum radiation is monitored at 4904 Å and 4285 Å.

APPENDIX B

CALIBRATION OF Cs ABSORPTION DIAGNOSTICS

The method of absorption of resonant radiation is used to determine the Cs number density in the plasma. The light used for this purpose is generated by a low pressure Cesium spectral lamp. The image of a pinhole in the lamp housing is projected by two pyrex lenses through the test chamber, and the radiation that is transmitted falls on a photomultiplier tube provided by a filter to isolate the desired resonant line. The line selected is a doublet in the blue region of visible light at wavelengths 4550 \AA and 4555 \AA . The output current of the P.M. tube is then proportional to the total incident energy, which can be expressed as

$$I = \int_{-\infty}^{+\infty} I_{v_{\text{Lamp}}} (v - v_0) \exp \left[- \int_0^L k_v (v - v_0) dx \right] d(v - v_0) \quad (\text{B.1})$$

where $I_{v_{\text{Lamp}}}$ is the spectral intensity of the lamp, distributed about the central frequency v_0 , k_v is the absorption coefficient of the plasma at frequency v and at station x along the beam and L is the total optical length inside the discharge tube ($\sim 1.0''$). The total absorption coefficient $\int k_v (v) dv$ is, for a given line, is proportional to the Cesium number density, the shape of the distribution $k_v (v)$ depends on the broadening mechanisms that are present. Some of the important mechanism

will be discussed below:

1) Natural Broadening

The half width for natural broadening, $\Delta\nu_n$ is given by

$$\Delta\nu_n = \frac{e^2 v_0^2}{mc^3} f_{ji} = 9.4 \times 10^{-24} v_0^2 f_{ji} \quad (B.2)$$

For the line at 4550 Å we have $f_{ji} \equiv$ oscillator strength = 0.0174 and $v_0 = 6.59 \times 10^{14} \text{ sec}^{-1}$, thus the natural bandwidth comes to be

$$\Delta\nu_n = 7.10 \times 10^4 \text{ Hz}$$

The normalized shape of a naturally broadened line is

$$g(v)^* = \frac{1}{\pi \left[1 + \frac{2(v - v_0)}{\Delta\nu} \right]^2} \quad (B.3)$$

2) Collisional Broadening

The half-width for collisional broadening is given by

$$\Delta\nu_c = \sigma_c^2 n_g \left[\frac{8kTg}{\pi} \left(\frac{1}{M_r} + \frac{1}{M_g} \right) \right]^{1/2} \quad (B.4)$$

where σ_c is the cross section for collisional broadening between radiating and neutral atoms. The line shape is similar to that of natural broadening.

*Otherwise known as Lorentzian line shape.

3) Inter-Atomic Stark Broadening

The inter-atomic stark broadening occurs as the charged particles influence the radiating atoms. This type of broadening is as straightforward as it is for collisional or natural broadening. There are some numerical results for half-widths available for some Cs lines.

4) Due to the similarity in the nature of broadening mechanism* of the three above, broadening can be combined as:

$$\Delta v \equiv \Delta v_n + \Delta v_c + \Delta v_s \quad (B.5)$$

5) The half-width for Doppler broadening, Δv_d , is given by

$$\Delta v_d = 2v_0 \sqrt{\frac{2kTg}{M_r^2} \log 2} \quad (B.6)$$

where M_r is the mass of the radiating atoms.

The line shape of a doppler broadened medium, in normalized form is described as

$$g_D(v) = \frac{2(\log 2)}{\sqrt{\pi} \Delta v_D} \exp \left[\frac{-4(\log 2)(v - v_0)^2}{\Delta v_D^2} \right] \quad (B.7)$$

*The stark broadening is much more complex than the other two, the overall shape is inversely proportional to $(v-v_0)^{5/2}$, however the error in assuming a $(v-v_0)^{-2}$ dependence is very small.

Due to the exponential nature of the line shape, the Doppler influence on the other broadening mechanisms [Eq. (B-5)] is dominant at the line center, and in the wings of the line shape the Lorentzian shape dominates. For the present problems of determining the Cs number density ($f_{Cs} > 10^{-6}$ at $p = 50$ torr) a knowledge of the wing profile is sufficient.

When the term KvL , the optical depth, is greater than 3, the line center is completely absorbed and the ratio of incident and output intensities of the resonant radiation is proportionally to the number of radiating atoms and the number of the broadener gas atoms [see Eq. (B.4)], provided the same emitter (Lamp) is used. The line shape of lamp is again governed by the broadening mechanisms discussed before.

A precise determination of the spectral distribution of such a light source requires spectroscopic equipment with high resolving power (~ 0.01 Å), and a calculation of $I_{v_{Lamp}}$, without the knowledge of the relevant parameters (of the lamp plasma) might lead to erroneous results. Therefore, instead of relying on an assumption as to the form of the function $I_{v_{Lamp}}$ [Eq. (B.1)], a calibration experiment was devised. A schematic of the apparatus is shown in Fig. 3.9. The light of the Cs lamp is collimated by means of glass lenses and is allowed to pass through the absorption cell. The beam is then focused on a photomultiplier tube.

The temperature of the lamp gradually increased, if only air convection as a cooling process is allowed. As the variation in temperature

might change the lamp line profile, it was decided to insulate the lamp housing, and to heat it to keep the temperature constant at a desired level. The absorption cell was kept in an oven and the Cs pool stem in an oil bath to promote even heating. Several thermocouples, placed at different spots in the oven, monitored the temperatures (not shown in Fig. 3.9). To avoid condensations on the walls of the absorption cell, it was heated (in addition to the oven heating) by means of electrical tapes, and maintained the Cs pool as the coolest spot in the cell. By varying the oven temperature absorption of the Cs lamp light at various Cs mole fraction were made. The reading was corrected for the increase in He temperature by assuming a $1/\sqrt{T}$ dependence. The experiment was conducted with two absorption cells, one filled with 60.0 torr of He, the other with 120 torr.

The results were reduced in form of a master calibration curve, showing the dependence of Cs mole fraction on the fraction of light transmitted through a 60 torr He cell.

The expression used to calculate the optical depth of the absorption cell was taken from Ref. 75 which reads:

$$a = \frac{2e^2 L n_{Cs}}{\Delta v} g_j f_{j1} \exp \left[-\frac{kv_1}{KT} \right] \left(1 + \left[\frac{2(v - v_0)}{\Delta v} \right] \right)^{-1} \quad (B.8)$$

where g_j , f_{ji} , v_j are the degeneracy, the oscillator strength, and the frequency of 'j' level in Cs (i is the ground state).

For 4550 Cs line the values are:

$$g_j = 4$$

$$g_i = 2$$

$$f_{ji} = 0.0174$$

$$\Delta v \approx 3 \times 10^9 \text{ Hz}$$

$$v_j = 6.6 \times 10^{14} \text{ Hz}$$

APPENDIX C
PLASMA EQUATIONS

In MHD laser regime the electrical behavior of the plasma is governed primarily by the electron kinetics. The three equations describing the electrons in the plasma are the electron continuity equation, the electron momentum equation (Ohm's law), and the electron energy equation. In the Hall parameter range (typically larger than 3) characteristic of nonequilibrium MHD generators, the plasma is subject to ionization instabilities.^{32,33} These result in spatial and temporal nonuniformities in n_e and T_e which reduce the values of β , the Hall parameter and σ , the electrical conductivity. Solbes developed a quasi-linear averaging technique to describe the bulk plasma by calculating the effective values of σ_{eff} and β_{eff} .

Neglecting the ion slip and electron pressure gradient, the local Ohm's law can be written as:

$$\bar{J} + \bar{J} \times \bar{\beta} = [\bar{E} + \bar{u} \times \bar{B}] \quad (C.1)$$

The Hall parameter and conductivity σ are given by

$$\bar{\beta} = \frac{e\bar{B}}{m_e v_e} \quad (C.2)$$

$$\sigma = \frac{e^2 n_e}{m_e v_e} \quad (C.3)$$

The electron collision frequency v_e is computed as:

$$v_e = \sum_i v_i \quad (C.4)$$

where

$$v_i = c_i \sqrt{\frac{8kT_e}{\pi m_e}} n_i \sigma_i(T_e) \quad (C.5)$$

The summation is taken over gas atoms, seen atoms, and ions. $\sigma_i(T_e)$ is the Maxwell averaged momentum transfer cross section, while c_i depends on the force law and energy for the encounter. The appropriate values for the factors are available in plasma literature.¹³

For condition typical of plasmas under consideration the electron energy equation can be simplified to the form¹⁵

$$(ev_i + \frac{3}{2} kT_e) \left[\frac{\partial n_e}{\partial t} + \nabla \cdot (n_e \bar{u}) \right] = \frac{J^2}{\sigma} - \sum_s \Delta \epsilon_s \quad (C.6)$$

where \bar{u} is the flow velocity of the plasma, which in the present simulation experiment is zero. The loss term $\Delta \epsilon_s$ is

$$\Delta \epsilon_s = \delta_s \frac{m_e}{m_s} \frac{3}{2} k(T_e - T) n_e v_e \quad (C.7)$$

δ_s for CO_2 in the range of electron temperatures of interest is approximately 5000. However as has been discussed in previous chapters its value is not constant, as the molecular gas undergoes significant vibrational excitation in the process of creating an inversion and redistributes its population amongst its various vibrational levels. As the electron number density and electron temperature are measured in the experiment separately, in the calculations, value of δ is assumed

constant, for simplicity.

Contribution of the first term is at a very small time scale¹³ ($\sim 0.1 \mu\text{sec}$), the energy equation is simplified to a steady state solution:

$$\frac{J^2}{\sigma} = \sum_s \Delta \epsilon_s \quad (\text{C.8})$$

In the presence of ionization instabilities the equations are written in an averaged form

$$\langle \bar{J} \rangle + \langle \bar{J} \times \bar{B} \rangle = \langle (\bar{E} + \bar{u} \times \bar{B}) \rangle \quad (\text{C.9})$$

$$\langle \frac{J^2}{\sigma} \rangle \approx \langle \sum_s \Delta \epsilon_s \rangle \quad (\text{C.10})$$

or in terms of effective values of σ_{eff} and β_{eff} as:

$$\langle \bar{J} \rangle + \bar{J} \times \bar{B}_{\text{eff}} = \sigma_{\text{eff}} [\langle \bar{E} \rangle + \bar{u} \times \bar{B}] \quad (\text{C.11})$$

assuming \bar{u} and \bar{B} are constant.

For the configuration of the experimental facility (E_x - induced field, E_y - Hall field) we have,

$$\langle J_x \rangle = \sigma_{\text{eff}} \langle E_x \rangle \frac{1 + \beta_{\text{eff}} \beta_{\text{app}}}{1 + \beta_{\text{eff}}^2} \quad (\text{C.12})$$

where $\beta_{\text{app}} = \frac{\langle E_y \rangle}{\langle E_x \rangle}$ and is measured by two probes in contact with the plasma.

The energy equation is simplified to

$$\frac{\langle J \rangle^2}{\sigma_{\text{eff}}^2} \approx \sigma_{\text{eff}}^2 \langle E_x \rangle^2 \frac{1 + \beta_{\text{app}}^2}{1 + \beta_{\text{eff}}^2} \quad (\text{C.13})$$

For a plane wave structure of the nonuniformities Solbes³³ gives the following relationship

$$\frac{\sigma_{\text{eff}}}{\langle \sigma \rangle} = S \quad (\text{C.14})$$

and

$$\beta_{\text{eff}} = \langle \beta \rangle S + t(S-1) \quad (\text{C.15})$$

where

$$S = \left[\frac{(1-r)^2 + \beta_{\text{crit}}^2}{(1-r)^2 + \langle \beta \rangle^2} \right]^{1/2} \quad (\text{C.16})$$

$$t = \frac{1-r}{\langle \beta \rangle} + \left[\frac{(1-t)^2}{\langle \beta \rangle^2} + 1 \right]^{1/2} \quad (\text{C.17})$$

$$r = \frac{d \log v_e}{d \log n_e} \quad (\text{C.18})$$

β_{crit} is calculated by either of the two following relationships:

(A) Collision with Neutrals are Predominant

$$\beta_{\text{crit}} = \frac{2-\alpha}{1-\alpha} \frac{1}{X_i} \left[\frac{T_e}{T_e - T_g} + \frac{2(1-\alpha)}{1-\alpha} X_i \right]^{1/2} \left(2m + \frac{T_e}{T_e - T_g} \right)^{1/2} \quad (\text{C.19})$$

where

$$X_i = \frac{3}{2} + \frac{ev_i}{kT_e}$$

α = degree of ionization

$$m = \frac{\partial \log v_{e-N}}{\partial \log T_e}$$

(B) Coulomb Collisions Dominate the Momentum But Not the Energy Equation.

$$\beta_{crit} = \left[\left(1 + \frac{1}{2} \frac{(2-\alpha)(3T_g - T_e)}{(1-\alpha)(T_e - T_g) X_i} \right) \left(1 + \frac{1}{2} \frac{(2-\alpha)(ST_e - T_g)}{(1-\alpha)(T_e - T_g) X_i} \right) \right]^{1/2}$$

The measured values of T_e and n_e are used to compute the appropriate quantities.

REFERENCES

1. Kerrebrock, J. L., and Draper, J. S., "Nonequilibrium MHD Generator with Molecular Gases," AIAA Paper 70-41 (1970).
2. Draper, J. S., and Kerrebrock, J. L., "Molecular Behavior in Nonequilibrium MHD Generators," 5th Int. Conf. on MHD Elec. Power Gen., Munich (1971).
3. Mnatsakanyan, A. Kh., "Electron Energy Balance in Inert Gas-Alkali Metal-Nitrogen Mixtures," High Temperature 7, 353 (May 1969).
4. Lowenstein, A., "Physical Process in a Magnetohydrodynamic Laser," Ph.D. Thesis, MIT Department of Aeronautics and Astronautics (February 1974).
5. Grove, R. E., An Experimental Study of the Effects of Molecules in Nonequilibrium MHD Plasmas," S. M. Thesis, MIT Department of Aeronautics and Astronautics, (Sept. 1971).
6. Brown, R. T., Hall, R. J., and Nighan, W. L., "Laser Excitation using a Nonequilibrium MHD Generator," United Aircraft Research Lab. Report, East Hartford, CT (1969).
7. Nighan, W. L., Brown, R. T., and Hall, R. J., "Laser Excitation using a Nonequilibrium MHD Generator," AIAA Paper 71-67 (1971).
8. Bullis, R. H., Churchill, T. L., Nighan, W. L., et al., Investigation of the Feasibility of a Magnetohydrodynamic Laser,: Report #N921308-4, United Aircraft Research Lab., East Hartford, CT (May 1974).
9. Zauderer, B., Tate, E., and Marston, C. H., "CO₂ MHD Laser, Analysis, Design and Shock Tunnel Experiments," 14th Symp. on Eng. Aspects of MHD, Tullahoma, Tennessee (1973).
10. Zauderer, B., Tate, E., and Marston, C. H., "Investigation of High Power MHD Gas Lasers," General Electric Space Sciences Lab. Report, Philadelphia, PA (1974).
11. Biberman, L. M., Vorobjev, V. S., Ivanov, R. S., et al. "Some Results of MHD Laser Investigation," 16th Symp. on Eng. Aspects of MHD, Pittsburgh, PA (1977).

12. Walter, R. F., "Numerical Model of a Magnetohydrodynamic Laser," Ph.D. Thesis, MIT Department of Aeronautics and Astronautics (June 1978).
13. Rosa, R. J., Magnetohydrodynamic Energy Conversion, McGraw-Hill, New York, NY (1968), p 35.
14. Lowke, J. J., Phelps, A. V., and Irwin, B. W., "Predicted Electron Transport Coefficients and Operating Characteristics of CO_2 - N_2 - He Laser Mixtures," *J. App. Phys.* 44, 10, 4664 (1973).
15. Solbes, A., "Study of Non-Equilibrium MHD Generator Flows with Strong Interaction," Final Report for NSF PSK0488-00, (June 1974).
16. Cole, J. A., "A Numerical Study of Non-Equilibrium MHD Generators," S.M. Thesis, MIT Department of Aeronautics and Astronautics (May 1976).
17. Herzberg, G., Molecular Spectra and Molecular Structure II, Van Nostrand, New York, NY (1945).
18. Hake, R. D., and Phelps, A. V., "Momentum - Transfer and Inelastic Collision Cross Sections for Electrons in O_2 , CO , and CO_2 ," *Phys. Rev.* 158, 1, 70 (June 1967).
19. Schulz, G. J., and Boness, M.J.W., "Vibrational Excitation of CO_2 by Electron Impact," *Phys. Rev. Letters* 21, 15, 1031 (1968).
20. Nighan, W. L., "Electron Energy Distributions and Collision Rates in Electrically Excited N_2 , CO , and CO_2 ," *Phys. Rev. A* 2, 5, 1989 (Nov. 1970).
21. Claydon, C. R., Segal, G. A., and Taylor, H. S., *J. Chem. Phys.* 52, 3387 (1970).
22. Anderson, J. D., Jr., and Winkler, E. M., "High Temperature Aerodynamics with Electromagnetic Radiation," *Proc. IEEE* 59, 651 (April 1971).
23. Anderson, J. D., Jr., Introduction to Gasdynamic Lasers, Academic Press, New York, NY (1976).

24. Statz, H., Tang, C. L., and Koster, G. F., "Transition Probabilities Between Laser States in Carbon Dioxide," *J. App. Phys.* 37, 11, 4278 (Oct. 1966).
25. Schappert, G. T., "Rotational Relaxation Effects in Short-pulse CO₂ Amplifiers," *Appl. Phys. Lett.* 23, 6, 319 (1973).
26. Schwartz, R. M., Slawsky, Z. I., and Herzfeld, K. F., "Calculation of Vibrational Relaxation Times in Gases," *J. Chem. Phys.* 20, 1591 (1952).
27. Yariv, A., Introduction to Optical Electronics, Holt, Rinehart, and Winston, New York, NY (1971).
28. Glowacki, W. J., and Plummer, M. J., "Theoretical Investigation of the CO Supersonic Electric Discharge Laser," *AIAA Paper 73-623* (1973).
29. Parma, C. C., "Study of the MIT Non-Equilibrium MHD Generator Experiments," *S.M. Thesis, MIT Department of Aeronautics and Astronautics* (May 1974).
30. Liepmann, H. W., and Roshko, A., Elements of Gasdynamics, Wiley, New York, NY (1957).
31. Shapiro, A. H., The Dynamics and Thermodynamics of Compressible Fluid Flow, Ronald, New York, NY (1953).
32. Kerrebrock, J. L., "Nonequilibrium Ionization Due to Electron Heating: I. Theory," *AIAA J.* 2, 6, 1072 (June 1964).
33. Solbes, A., "Instabilities in Nonequilibrium MHD Plasmas, A Review," *AIAA Paper 70-40* (1970).
35. McGregor, D. D., Mitchner, M., and Shaw, J. F., "Ionization Rate Calculations for Preionizers," *AIAA J.* 8, 5, 908 (May 1970).
36. Lin, S. C., Resler, E. L., and Kantrowitz, A. R., "Electrical Conductivity of Highly Ionized Argon Produced by Shock Waves," *J. of App. Phys.* 26, 95 (1955).
37. Craggs, J. D., and Massey, H.S.W., "Collisions of Electrons with Molecules," *Handbuch der Physik*, 37/1, 1959 (314-315).

38. Draper, J. S., "Nonequilibrium Magnetohydrodynamic Generators with Molecular Addition," Ph.D. Thesis, MIT Department of Aeronautics and Astronautics (January 1971).
39. Solbes, A. "Quasi-Linear Plane Wave Study of Electrothermal Instabilities," SM-107/26, 4th Int. Conf. on MHD Elec. Power Gen., Warsaw (1968).
40. Gerry, E. F., and Leonard, D. A., "Measurement of $10.6 \mu \text{CO}_2$ Laser Transition Probability and Optical Broadening Cross Sections," *Appl. Phys. Lett.* 8, 9, 227 (May 1966).
41. Burch, D. E. Gryvnak, D. A., and Williams, D., "Total Absorptance of Carbon Dioxide in the Infrared," *Appl. Opt.* 1, 759 (October 1962).
42. Christenson, C. P., Freed, C., and Haus, H. A., "Gain Saturation and Diffusion in CO_2 Lasers," *IEEE J. Quant. Electron.* QE-5, 276 (June 1969).
43. Lyon, D. L., "Collisional Relaxation Mechanisms Governing Operation of High-Pressure CO_2 Lasers," Ph.D. Thesis, MIT Department of Electrical Engineering (Sept. 1972).
44. Cheo, P. K., and Abrams, R. L., "Rotational Relaxation Rate of CO_2 Laser Levels," *Appl. Phys. Lett.* 14, 2, 47 (Jan 1969).
45. Granek, H., "Cross-Relaxation in the Doppler Profiles of J-Levels and between J-Levels of the 00^1 and 10^0 Vibrational States in CO_2 ," Ph.D. Thesis, MIT Department of Electrical Engineering
46. Stark, E. E., Jr., "Generation and Amplification of Short Laser Pulses," Ph.D. Thesis, MIT Department of Electrical Engineering (September 1972).
47. Rosser, W. A., Jr. Wood, A. D., and Gerry, E. T., "Deactivation of Vibrationally Excited Carbon Dioxide (CO_2) by Collisions with Carbon Dioxide or with Nitrogen," *J. Chem. Phys.* 50, 4996 (June 1969).
48. Rosser, W. A., Jr., and Gerry, E. T., "De-excitation of Vibrationally Excited CO_2 (CO_2) by Collisions with He, O_2 , and H_2O ," *J. Chem. Phys.* 51, 2286 (December 1969).

49. Rosser, W. A., Jr., Hoag, E., and Gerry, E. T., "Relaxation of Excess Populations in the Lower Laser Level $\text{CO}_2(100)$," *J. Chem. Phys.*, 57, 10, 4153 (November 1972).
50. Rhodes, C. K., Kelly, M. J., and Javan, A., "Collisional Relaxation of the $10^0 0$ State in Pure CO_2 ," *J. Chem. Phys.* 48, 5730 (June 1968).
51. Taylor, R. L., and Bitterman, S., "Survey of Vibrational Relaxation Data for Processes Important in the $\text{CO}_2 - \text{N}_2$ Laser System," *Rev. Mod. Phys.* 41, 26 (January 1969).
52. Christiansen, W. H., and Greenfield, E., "Analysis of a Collisionally Induced Dipole Laser," *Appl. Phys. Lett.* 23, 11, 623 (December 1973).
53. Nighan, W. L., Wiegand, W. J., Fowler, M. C., and Bullis, R. H., "Investigation of the Plasma Properties of High Energy Gas Discharge Lasers," Rept. #K-920833-5, United Aircraft Research Lab., East Hartford, CT (June 1971).
54. Murray, E. R., Jr., "Vibrational Non-Equilibrium in Carbon Dioxide Electric Discharge Lasers," SU-IPR Rept. #562 Stanford, CA (1974).
55. Judd, O. P., "The Effect of Gas Mixture on the Electron Kinetics in the Electrical CO_2 gas Laser," *J. App. Phys.* 45, 10, 4572 (October 1974).
56. Sharma, R. D. "Kinetics of Equilibration of 1388 cm^{-1} Vibrational Level of CO_2 ," *J. Chem. Phys.* 49, 5195 (December 1968).
57. Carbone, R. J., and Witteman, W. J., "Vibrational Energy Transfer in CO_2 Under Laser Conditions with and without Water Vapor," *IEEE J. Quant. Electron.* QE-5, 442 (September 1969).
58. Seeber, K. N., "Radiative and Collisional Transitions between Coupled Vibrational Modes of CO_2 ," *J. Chem. Phys.* 55, 10, 5077 (November 1971).
59. Bulthuis, K., and Ponsen, G. J., "On Relaxation of the Lower Laser Level of CO_2 ," *Chem. Phys. Lett.* 14, 5, 613 (1972).

60. Bulthuis, K., "Laser Power and Vibrational Energy Transfer in CO₂ Lasers," *J. Chem. Phys.* 58, 12, 5786 (June 1973).
61. Jacobs, R. R., Pettipiece, K. J., and Thomas, S. J., "Rate Constants for the CO₂ 02⁰0 - 10⁰0 Relaxation", *Phys. Rev. A* 11, 1, 54 (January 1975).
62. Stark, E. E., "Measurement of the 100-020 Relaxation Rate in CO₂," *Appl. Phys. Lett.* 23, 6, 335 (September 1973).
63. Murray, E. R., Kruger, C. H., and Mitchner, M., "Vibrational Non-Equilibrium in Carbon Dioxide Electric Discharge Lasers," *J. Chem. Phys.* 62, 2, 388 (January 1975).
64. DeTemple, T. A., Suhre, D. R., and Coleman, P. D., "Relaxation Rates of Lower Laser Levels in CO₂," *Appl. Phys. Lett.* 22, 8, 349 (April 1973).
65. Reilly, J., "High Power Electric Discharge Lasers (EDLs)," *Astronautics and Aeronautics* 13, 352 (March 1975).
66. Christiansen, W. H., and Tsongas, G. A., "Gain Kinetics of CO₂ Gasdynamic Laser Mixtures at High Pressure," *Phys. Fluids* 14, 12 (December 1971).
67. Shaw, J. F., "Effects of Nonelastic Collisions in Partially Ionized Gases," SU-IPR Rept. #254, Stanford, CA (1968).
68. Sutton, G. W., "Effect of Turbulent Fluctuations in an Optically Active Fluid Medium," *AIAA J.* 7, 9, 1737 (Sept. 1969).
69. Abrams, R. L. and Bridges, "Characteristics of Sealed-Off Wave Guide CO₂ Lasers," *IEEE J. Quant. Elect.*, QE-9, 940 (1973).
70. Cobine J. D., "Gaseous Conductors," pp 234-235, Dover Publications Inc., New York, 1958.
71. Schulz, G. J., *Phys. Rev.*, 116, 1141 (1959).
72. Oliver, D. A. et al., 8th Symp. on Engineering Aspects of MHD, Stanford, 1967, pp 104.
73. Sedrick, A. V., "Continuous Radiation Measurements of a Helium-Cesium Plasma," S.M. Thesis, MIT, September (1968).
74. Rose, D. J., Clark, Jr., Melville, Plasmas and Controlled Fusion, Wiley & Sons, New York, p. 223 (1961).
75. Lutz, M. A., "Radiation Energy Loss from a Cesium-Argon Plasma to an Infinite Plane Parallel Enclosure," Research Report #175, AVCO Everett Research Lab., Everett, MA, September (1963).

TABLE I

Relaxation Rates for Various Energy Transfer Processes

<u>Process</u>	<u>Rate (atm⁻¹ sec⁻¹)</u>
k_{Total} (Summed overall neutral species)	~ 10
k_{Rotation} (Thermalization of rotation levels in one vibrational level)	$\sim 3.8 - 7.6 \times 10^9$
$k_{\text{CO}_2} (00^01)$ (Intramode thermalization amongst asymmetric stretch mode levels)	$\sim 3 \times 10^9$

TABLE II

Summary of Report Values of $\text{CO}_2(10^00)$ - $\text{CO}_2(01^10)$ Relaxation Rates

<u>Investigators</u>	<u>Methodology</u>	<u>Rate (atm⁻¹ sec⁻¹)</u>
Rhodes, Kelley, and Javan ⁵⁰	Absorption at 10.6 μ (1968)	3.0×10^8
Seeber ⁵⁸	Calculations (SSH theory) (1971)	3.4×10^7
Bulthuis and Ponsen ⁵⁹	Power decay in the afterglow (1972)	9.9×10^6
Rosser, Hoag, and Gerry ⁴⁹	Electric pulse, measured 4.3 μ decay and gain at 10.6 μ (1972)	7.6×10^5
Bulthuis ⁶⁰	Power decay (1973)	7.7×10^6
This work	Measured gain at 10.6 μ (1978)	3.3×10^7

TABLE III
 Summary of Reported Value of $\text{CO}_2(10^00) - \text{CO}_2(02^00)$ Relaxation Rate

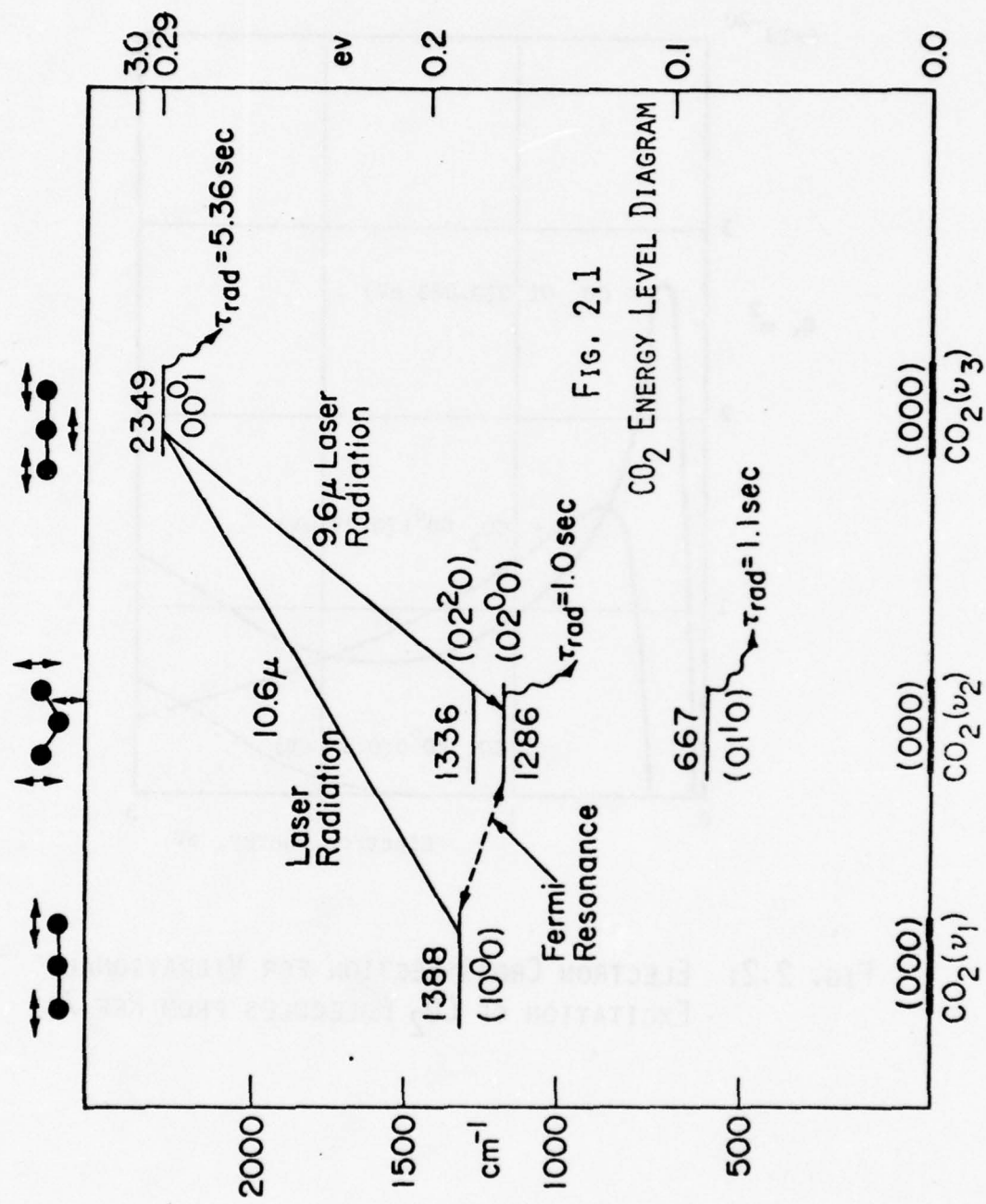
<u>Investigators</u>	<u>Methodology</u>	<u>Rate (atm⁻¹ sec⁻¹)</u>
Murray, Kruger, and Mitchner ⁶³	Experiments and Theoretical (1974)	$0.9 - 1.5 \times 10^6$
Jacobs, Pettipiece, and Thomas ⁶¹	Saturation at 10.6μ and measured gain 9.6μ	$\approx 10^7$
Stark ⁶²	Monitored gain at 10.6μ and gain at 10.6μ after saturation	1.1×10^8

TABLE IV

Important Features of Other Investigations (4,7,11,12)

Ref.	E volts/cm	E/p cm ⁻¹ torr	Mach number	T _e -T _g /T _g	<β>	$\frac{\sigma_{\text{eff}}}{\langle\sigma\rangle}$	n _e cm ⁻³	Ga ¹⁹ cm ⁻³	f _{CO₂} %	f _{CS}
1	90.0	1.18	4.7	9.0	10.0	0.1	3-4x10 ¹³	0.05- 0.15	2.0	10 ⁻⁵
2	57.3	8.30	5.0	9.6	39.0	0.05	5.8x10 ¹²	0.2	4.0	10 ⁻³
3	120- 240	6.0	3.0	13.0	1-1.5 (β _{eff})	0.8	10 ¹³	0.3	1.0	10 ⁻⁵
4	--	--	--	9.7	6.0	--	10 ¹²	0.02	0.2	10 ⁻⁵
5	174.0	1.0	4.0	9.8	0.3 (β _{eff})	0.4 (σ _{eff})	2x10 ¹³	0.8	3.0	10 ⁻⁵
PRESENT WORK	20.0	0.5	--	9.0	2.6	0.2	6x10 ¹²	0.1- 0.3	1-3	10 ⁻⁵

1. Nighan, W.L., et al⁷, United Aircraft Research Lab.
2. Zauderer, B., et al¹⁰, General Electric Co.
3. Biberman, L.M., et al¹¹, Institute of High Temperatures of USSR Academy of Sciences.
4. Lowenstein, A., et al⁴, Massachusetts Institute of Technology (Analytical Study)
5. Walter, R. F.¹², Massachusetts Institute of Technology.



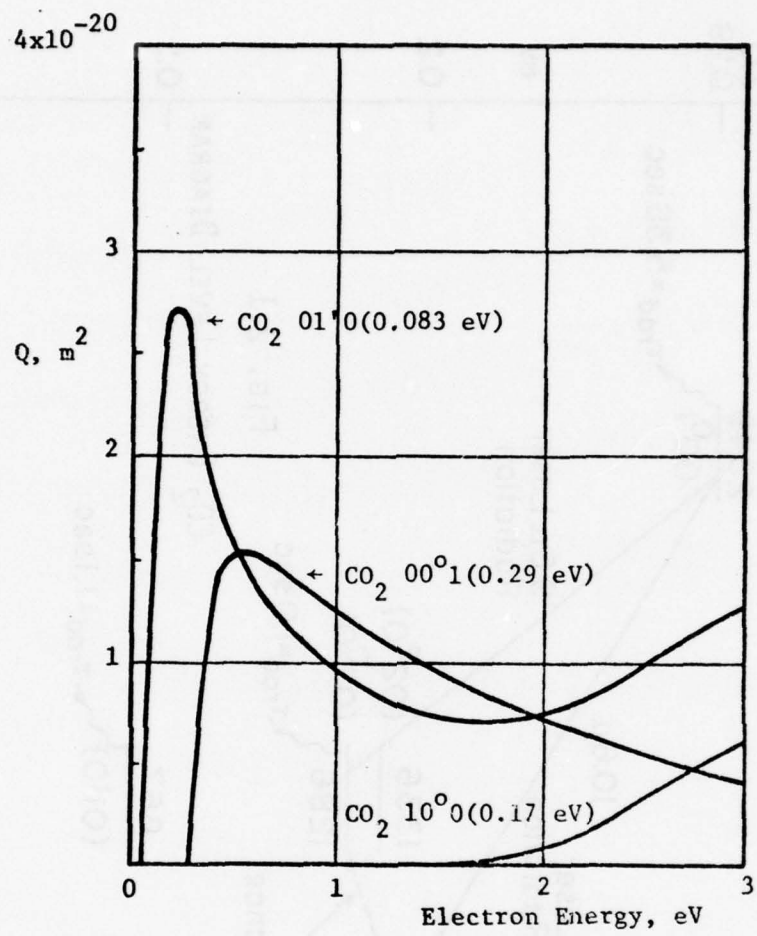


FIG. 2.2: ELECTRON CROSS SECTION FOR VIBRATIONAL EXCITATION OF CO_2 MOLECULES FROM REF.7

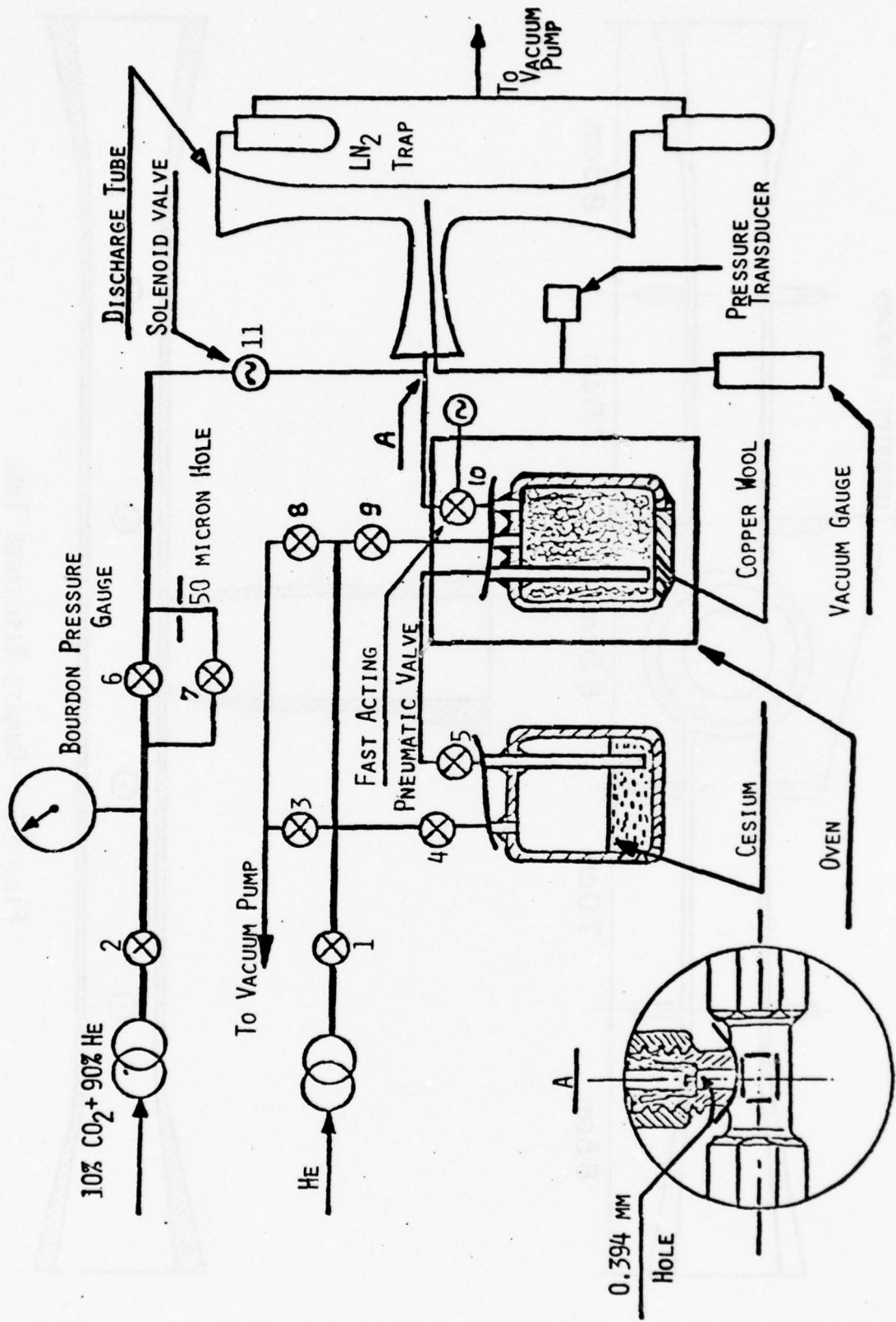


FIG. 3.1: GAS FLOW SYSTEM

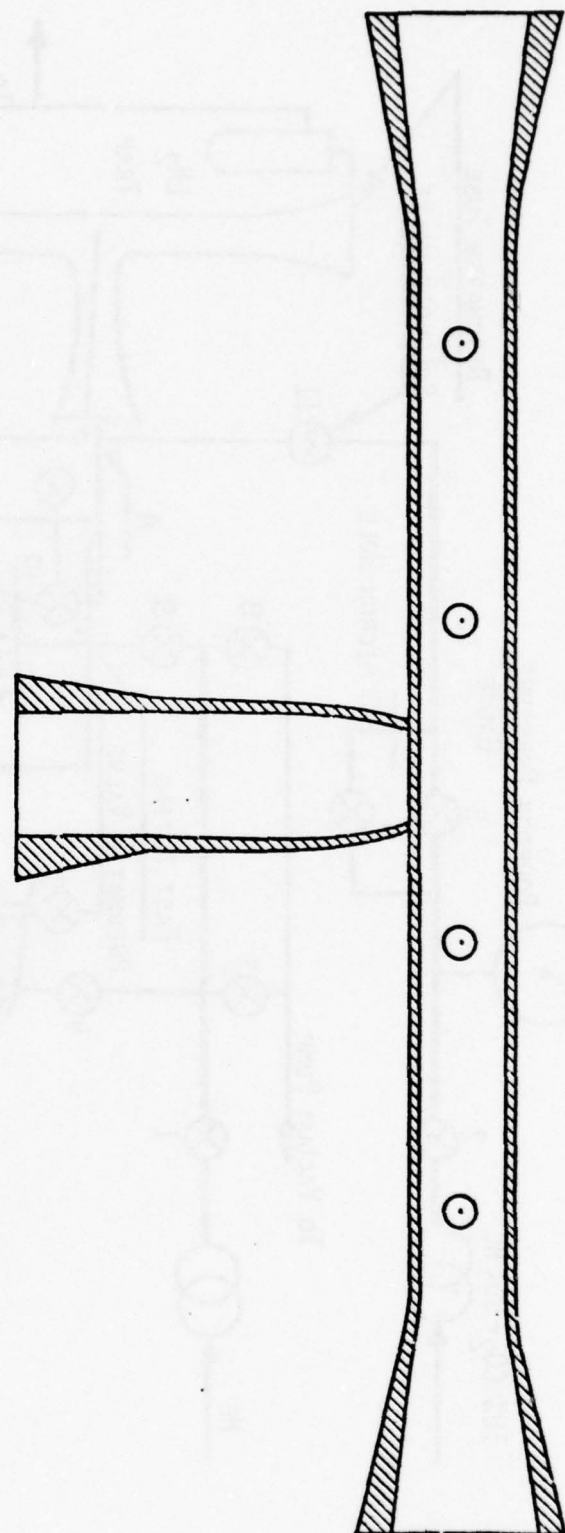
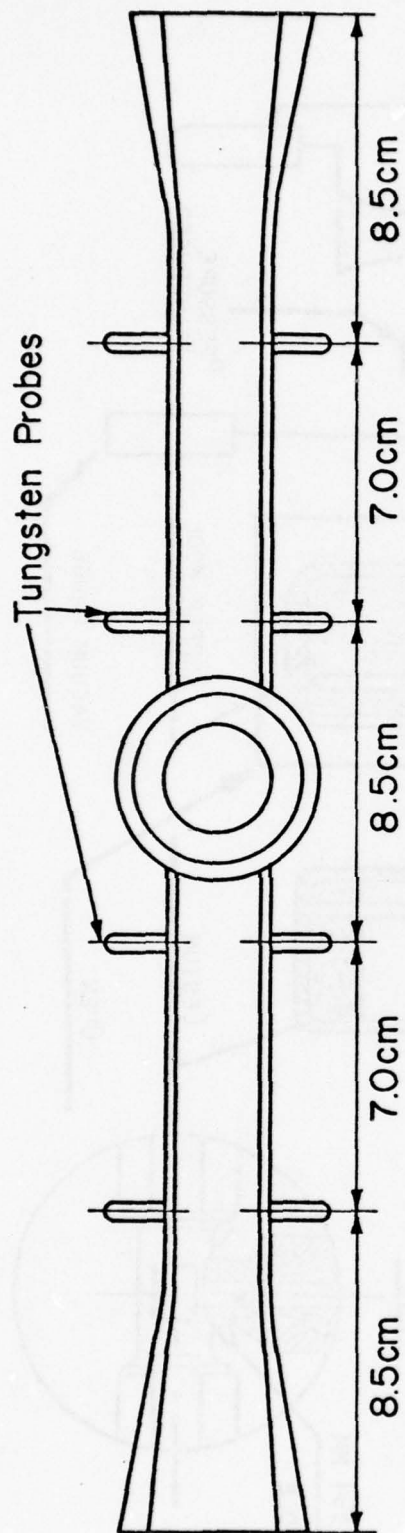


FIG. 3.2: QUARTZ DISCHARGE TUBE

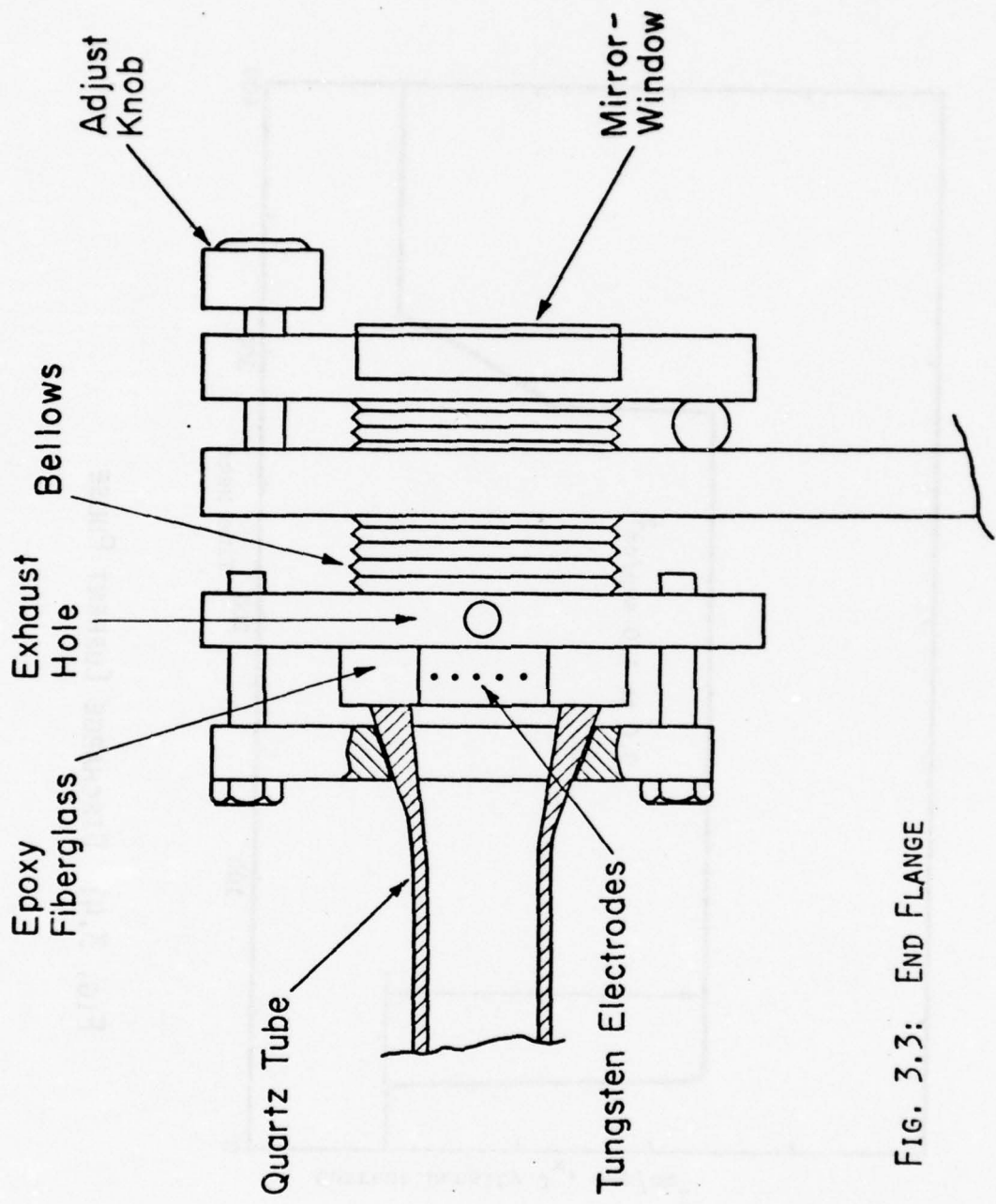


FIG. 3.3: END FLANGE

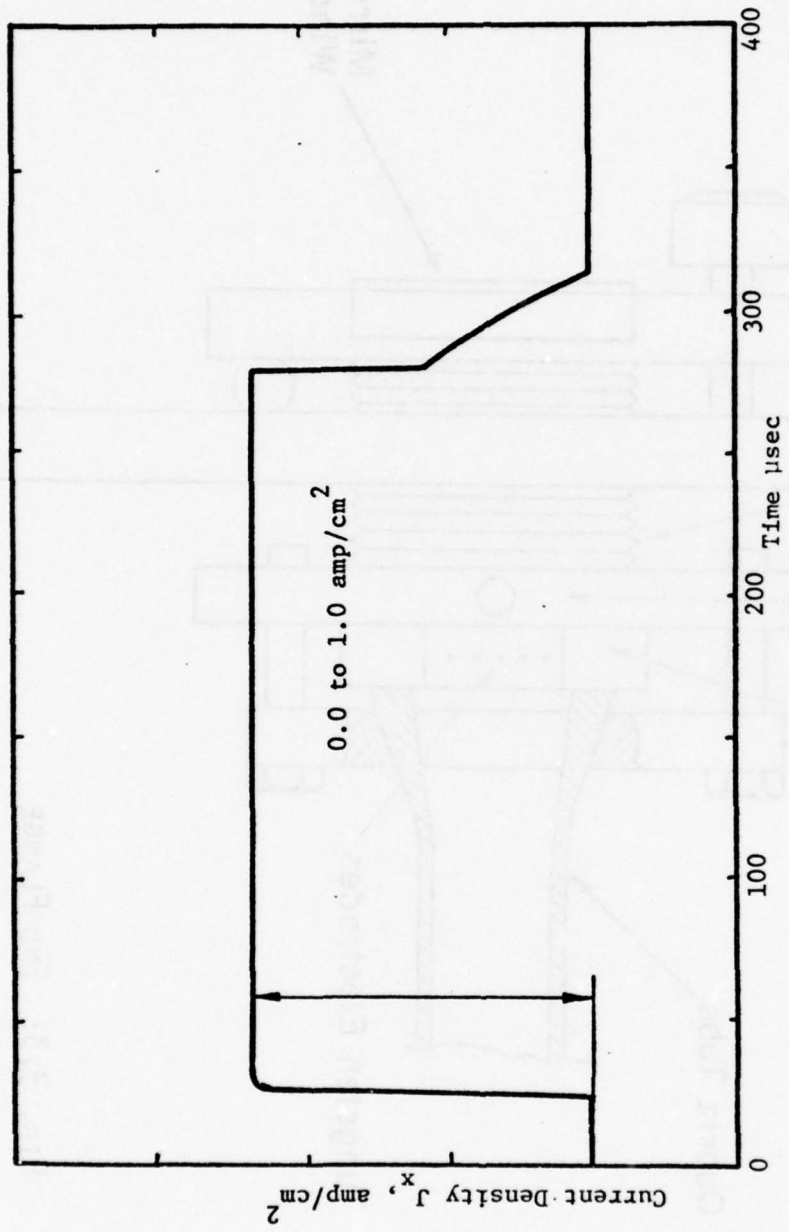


Fig. 3.4: DISCHARGE CURRENT PULSE

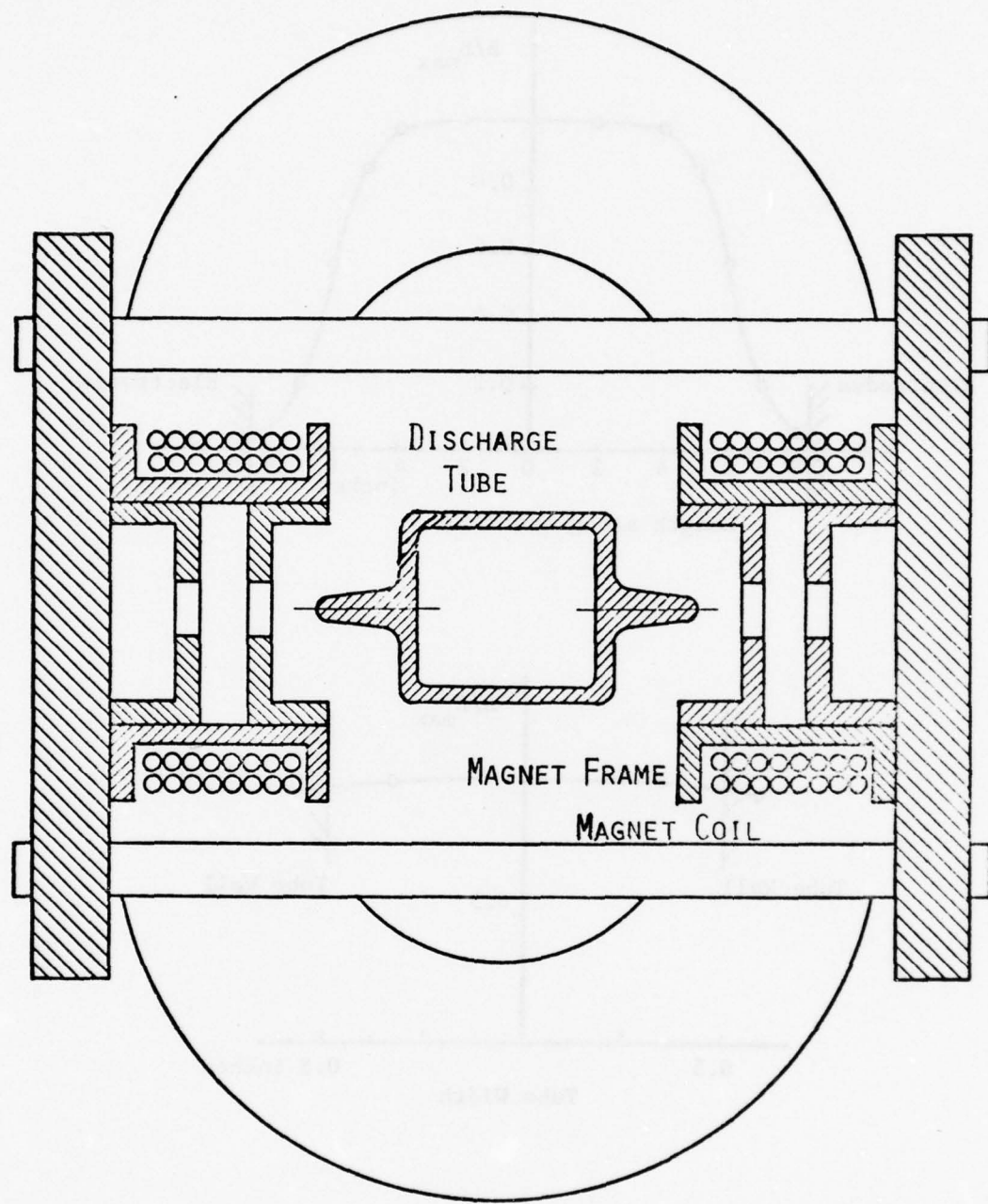


FIG. 3.5: Magnet Cross-Section

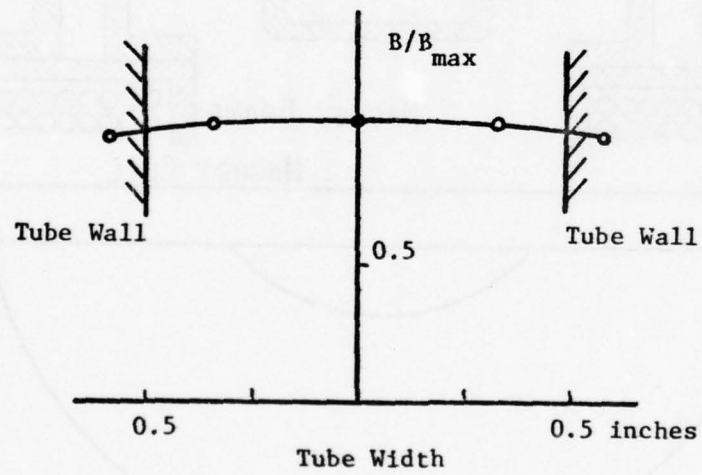
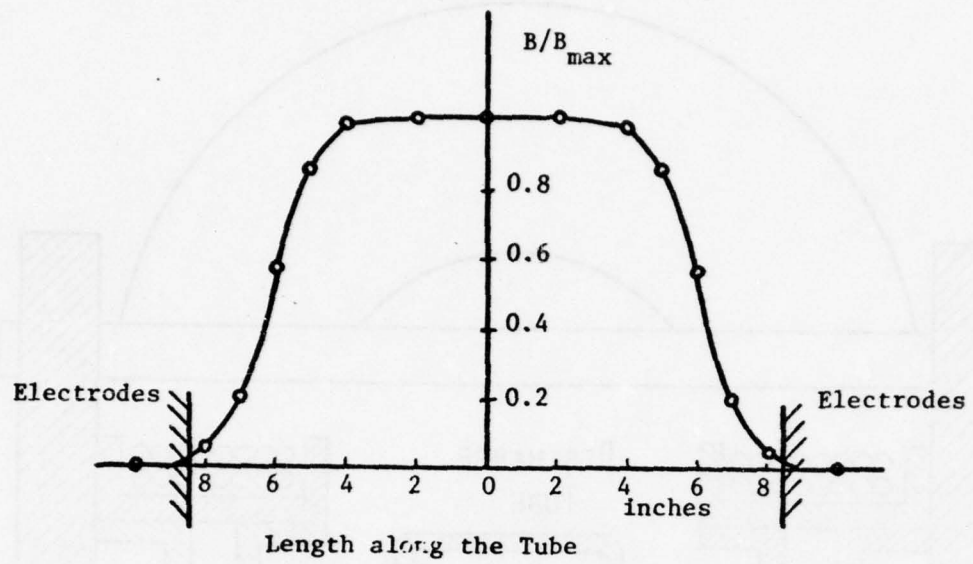


FIG. 3.6: MAGNETIC FIELD DISTRIBUTION IN DISCHARGE REGION

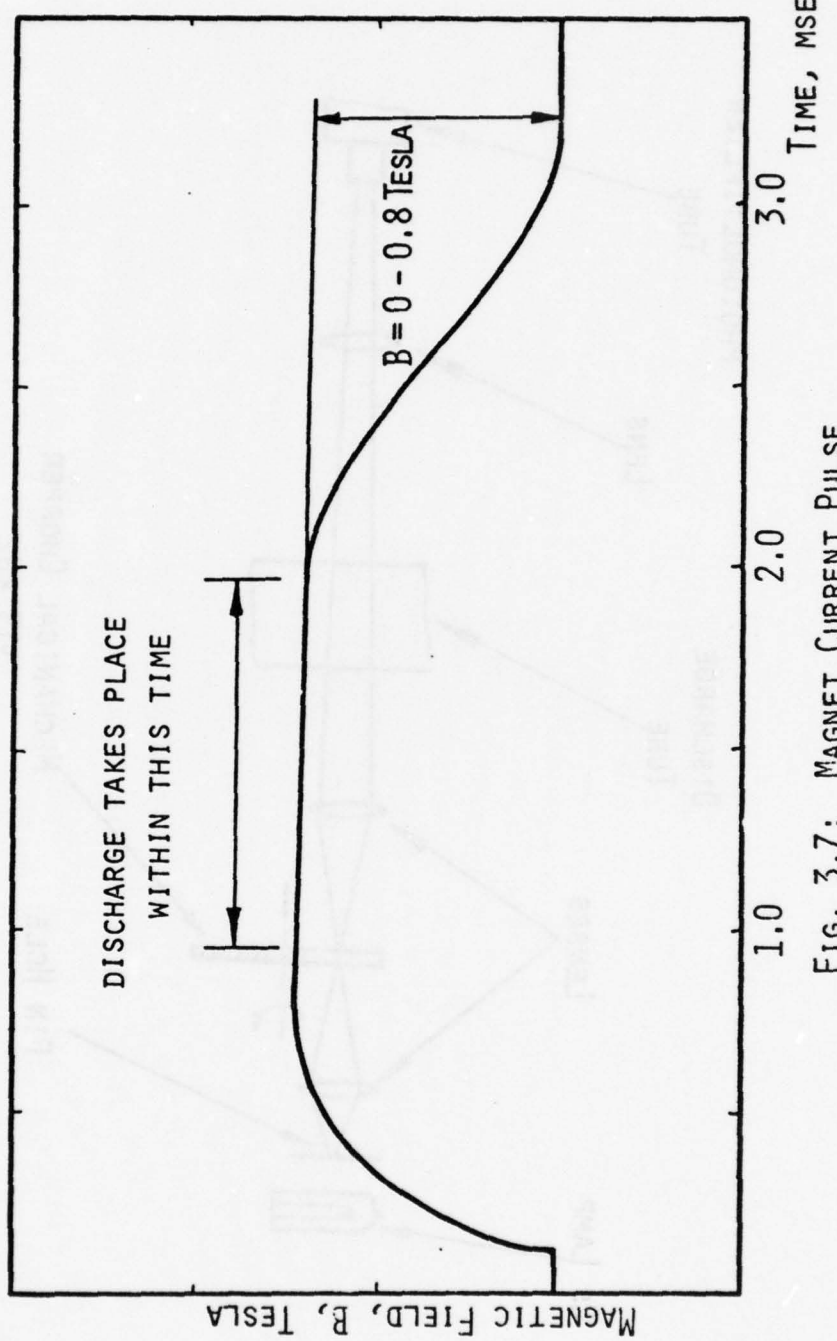


FIG. 3.7: MAGNET CURRENT PULSE

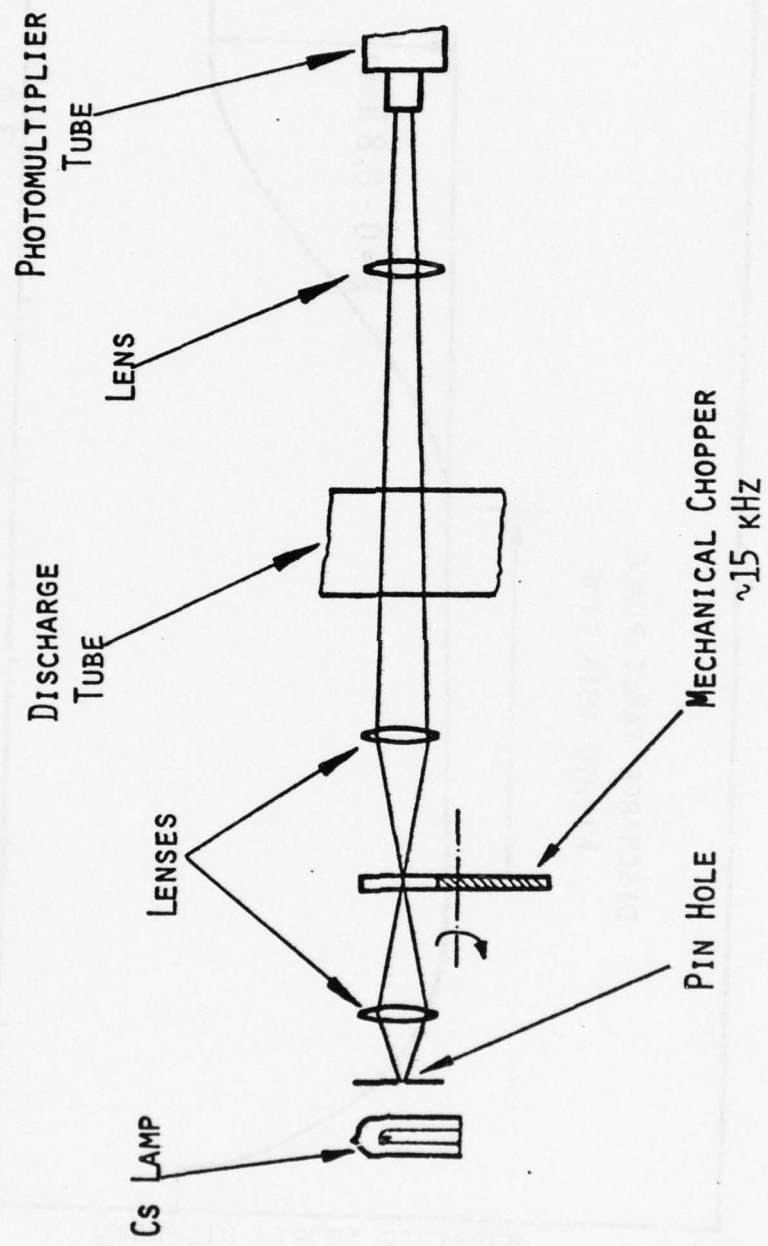


FIG. 3.8: Cs DIAGNOSTIC SYSTEM

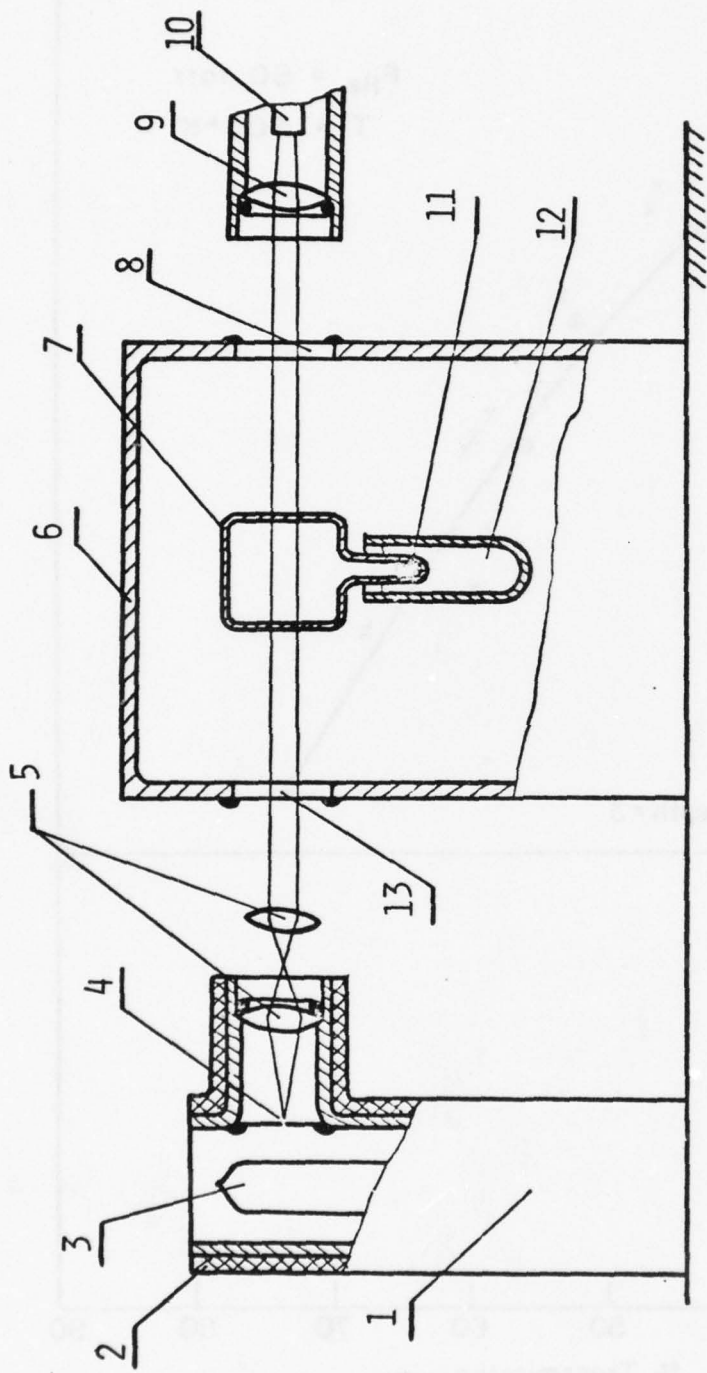


FIG. 3.9: Cs ABSORPTION DIAGNOSTICS CALIBRATION EXPERIMENT

1. LAMP HOLDER
2. HEATING TAPE & INSULATOR
3. Cs LAMP
4. PIN HOLE
5. LENSES
6. OVEN
7. TEST CHAMBER
8. QUARTZ WINDOW
9. LENS
10. PHOTOMULTIPLIER TUBE
11. Cs POOL
12. OIL BATH
13. QUARTZ WINDOW

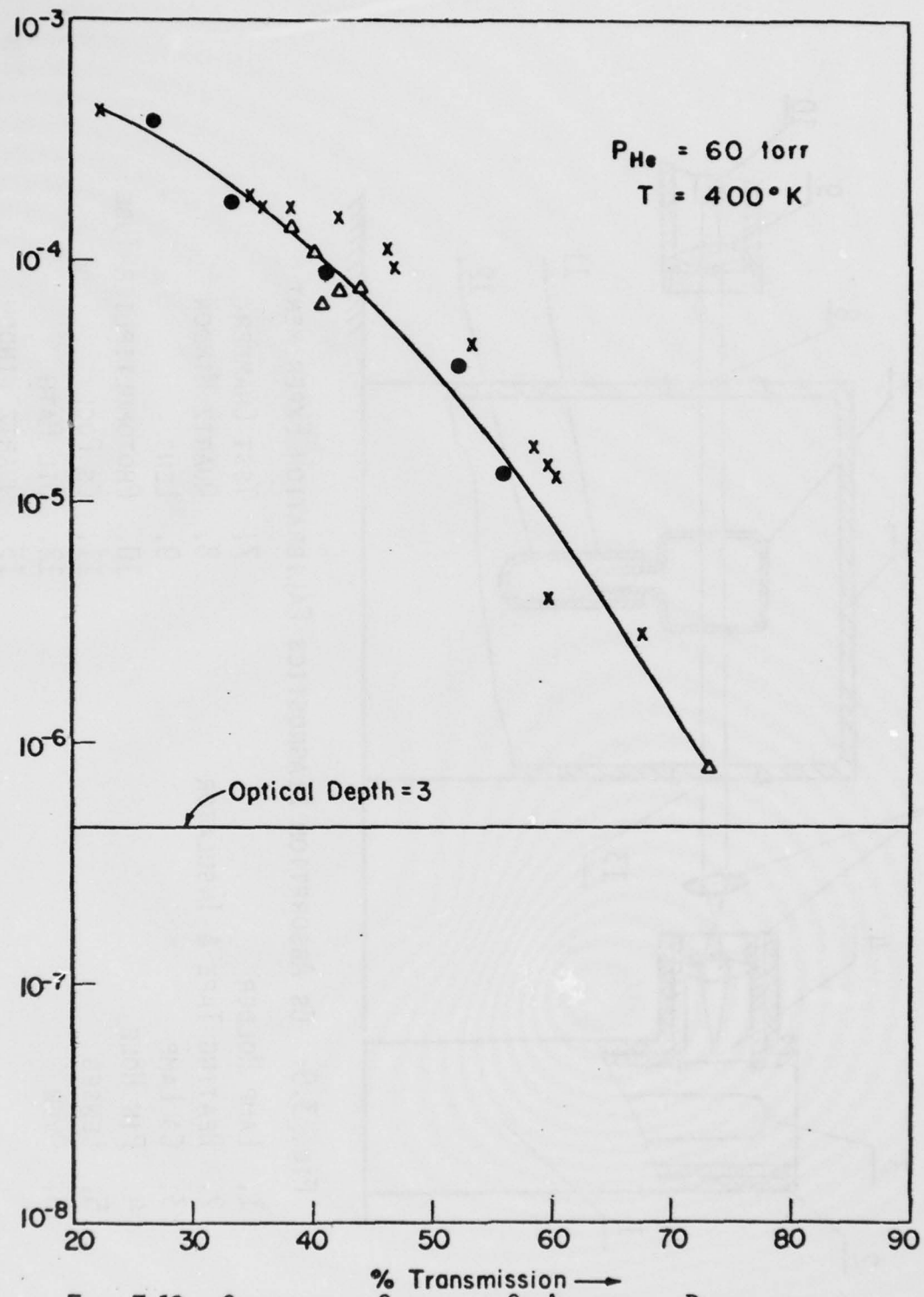


FIG. 3.10: CALIBRATION CURVE FOR Cs ABSORPTION DIAGNOSTICS

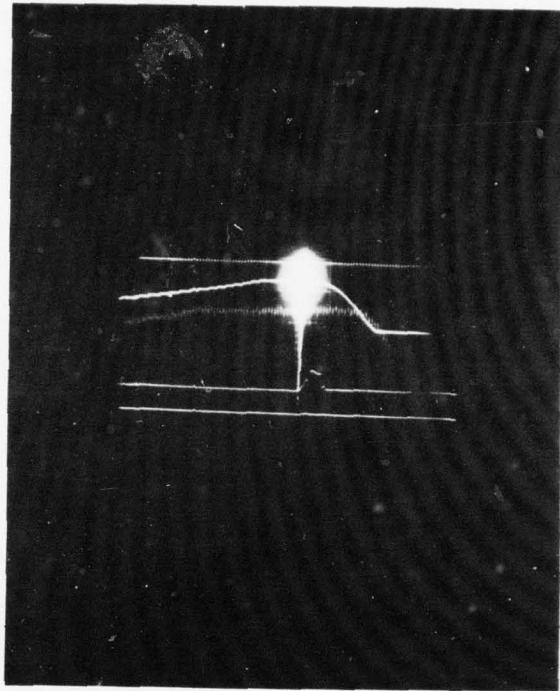


FIG. 3.11: TYPICAL SCOPE TRACE OF PRESSURE PULSE
(TOP SOLID CURVE) AND Cs ABSORPTION
DIAGNOSTICS (CHOPPED CURVE)

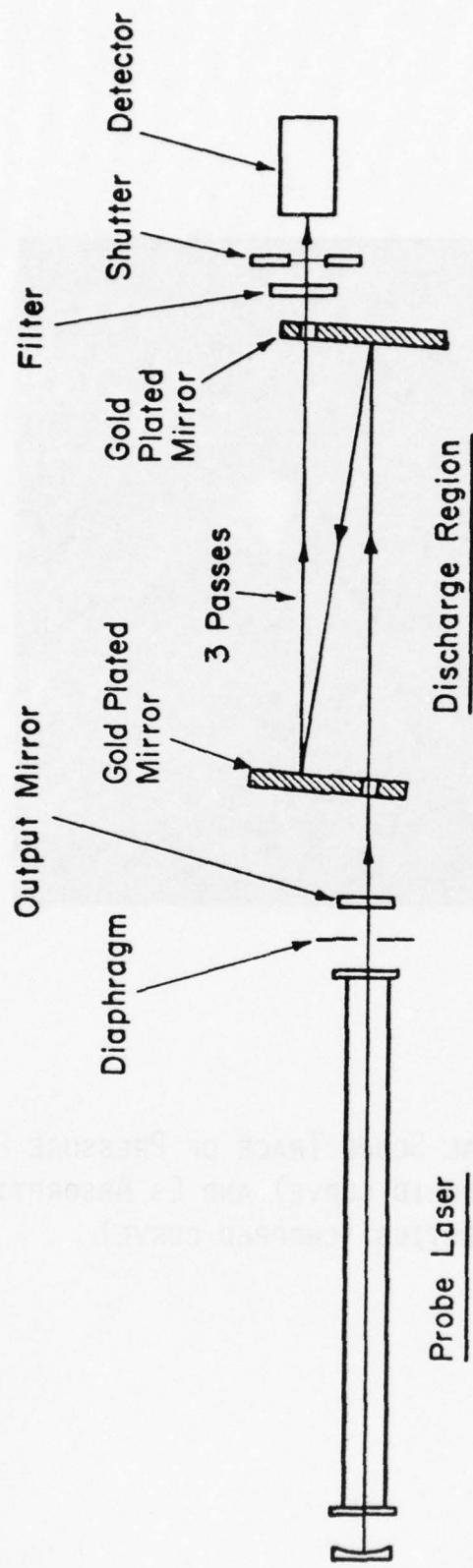
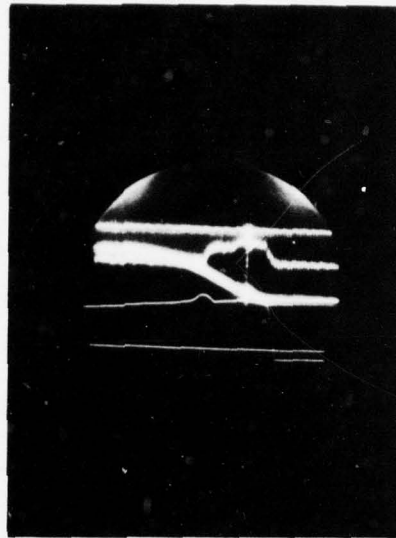
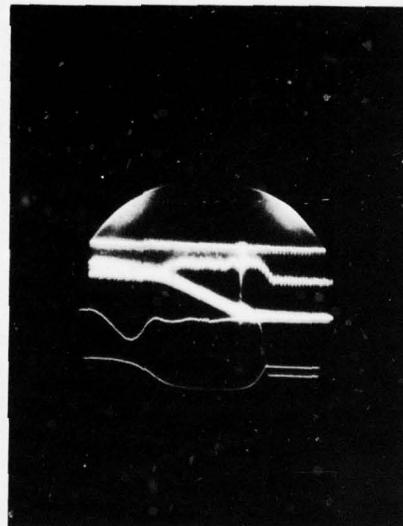


FIG. 3.12: Arrangement To Measure Optical Gain-(Schematic)



GAIN MEASUREMENT WITHOUT MAGNETIC FIELD



GAIN MEASUREMENT WITH MAGNETIC FIELD

From Bottom: 1) Magnet Pulse, 2) Laser Pulse, 3) Pressure Pulse,
4) Cs Absorption Diagnostics

FIG. 3.13

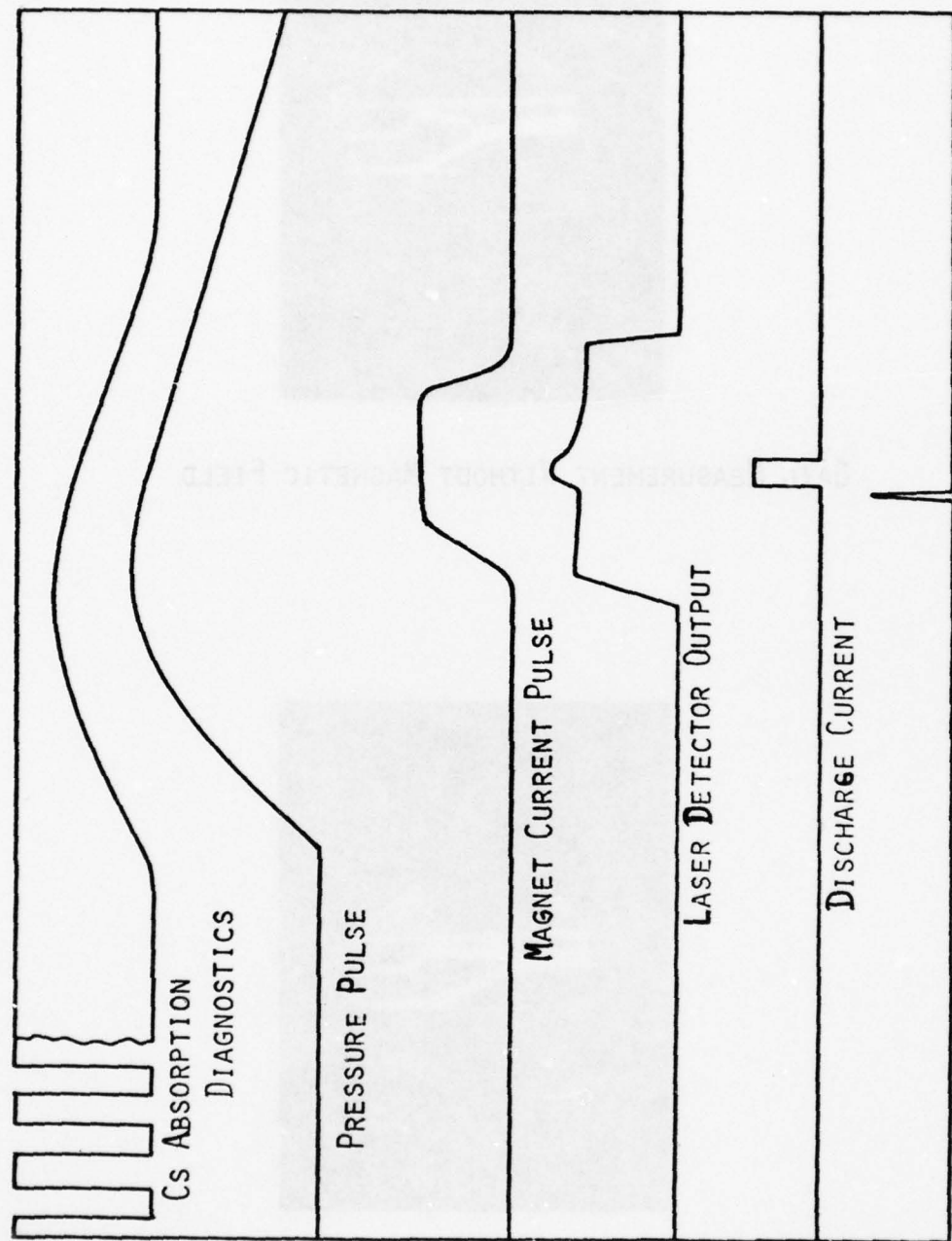
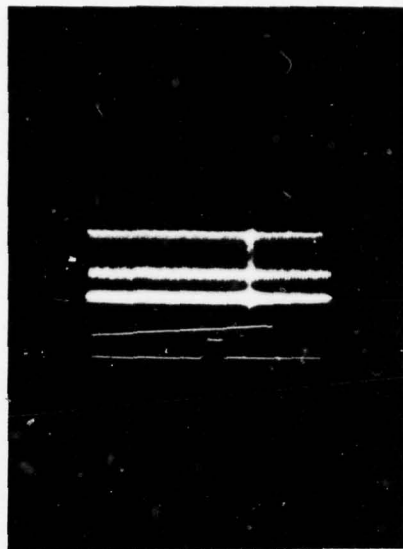
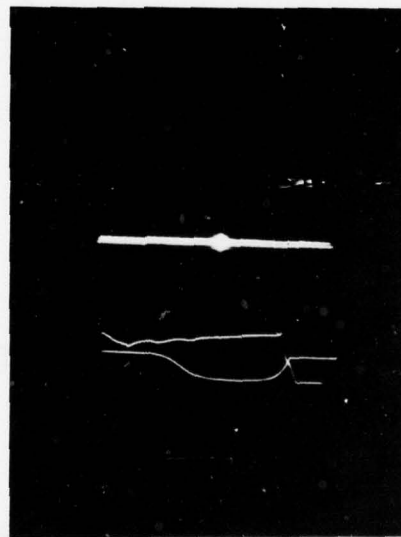


Fig. 3.14: SEQUENCE OF EVENTS DURING A TEST



MEASUREMENT WITHOUT MAGNETIC FIELD
FROM BOTTOM: 1) DISCHARGE CURRENT, 2) LASER PULSE



MEASUREMENT WITH MAGNETIC FIELD
FROM BOTTOM: 1) MAGNET PULSE, 2) LASER PULSE
FIG. 4.1

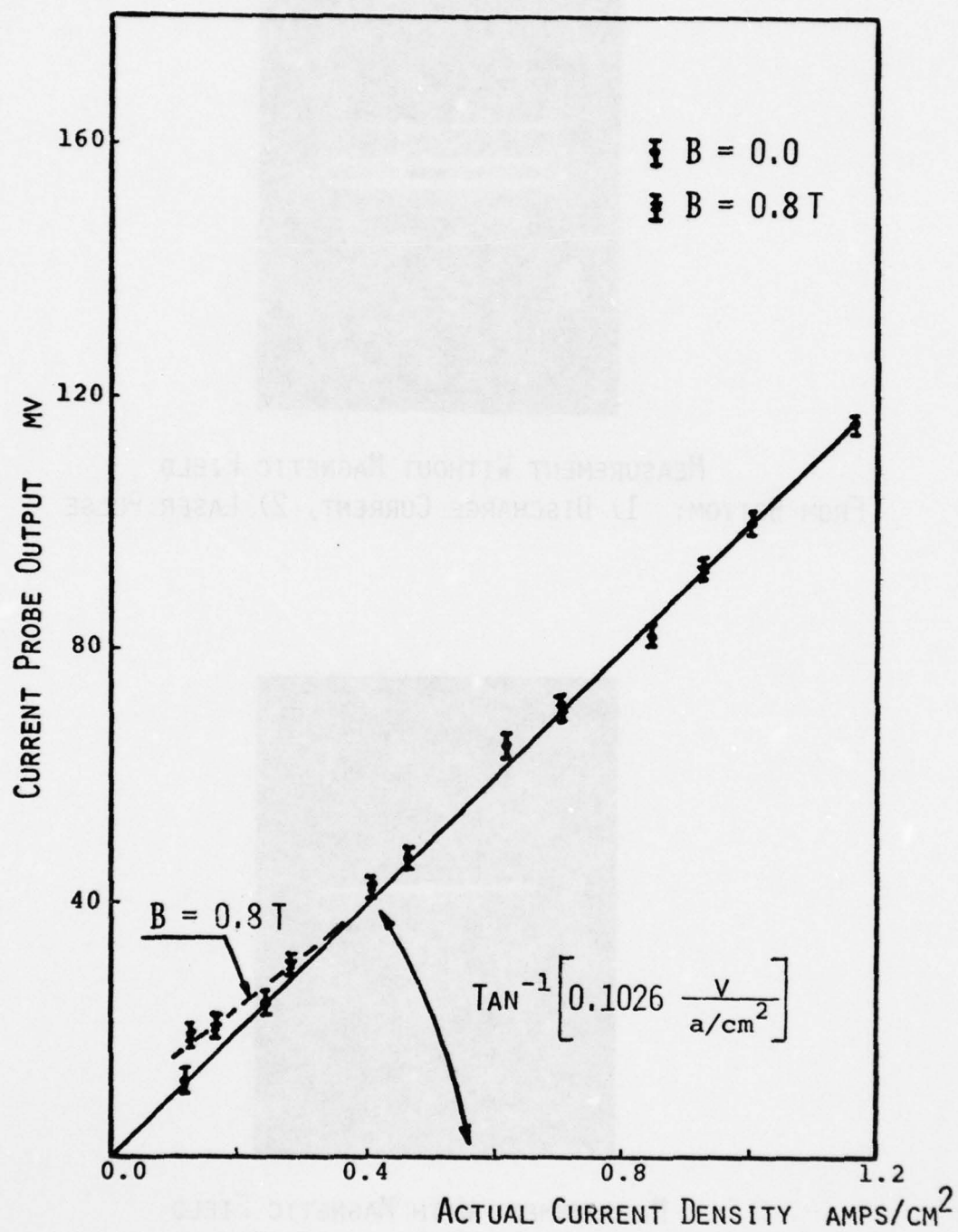


FIG. 4.2: CURRENT PROBE CALIBRATION

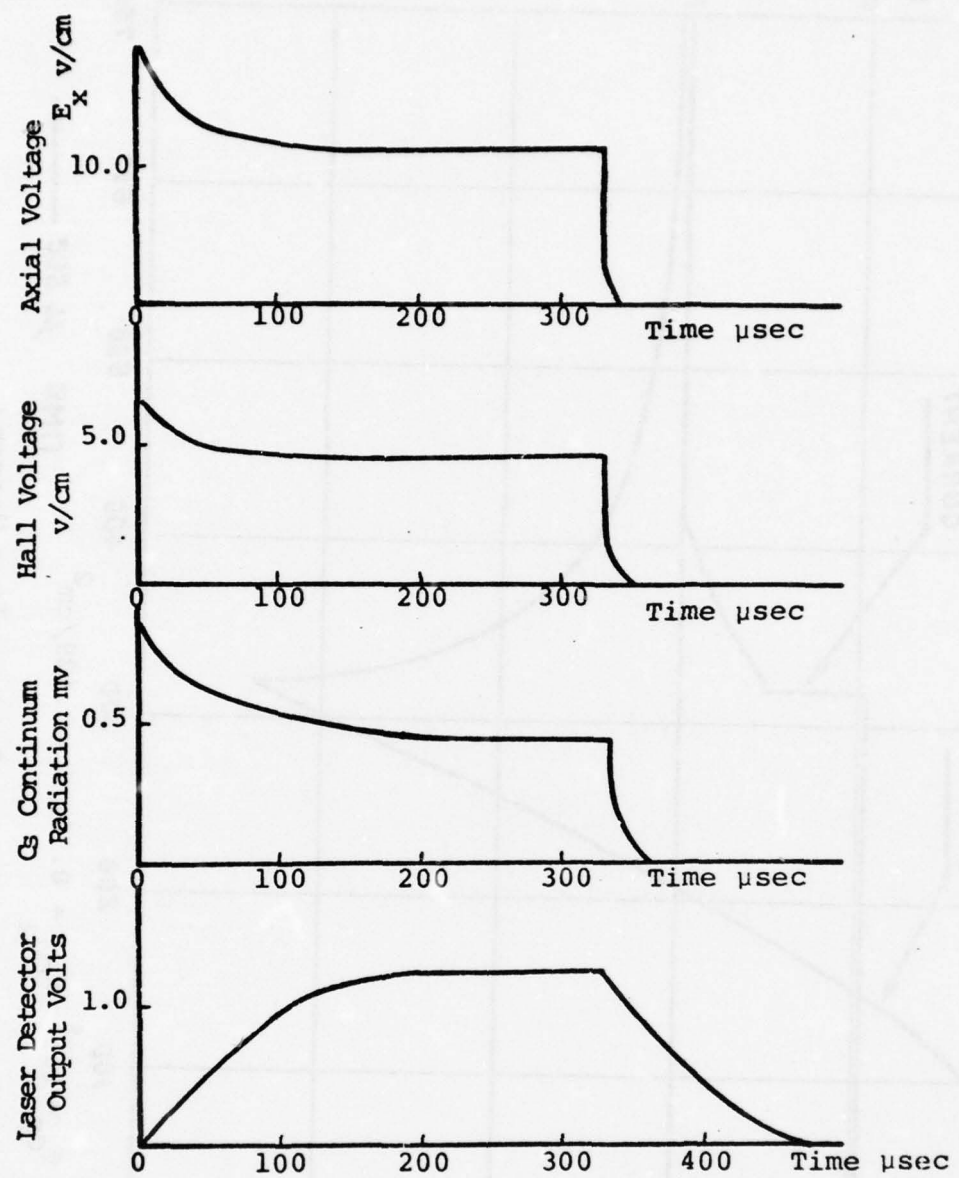


FIG. 4.3: TYPICAL SCOPE TRACES

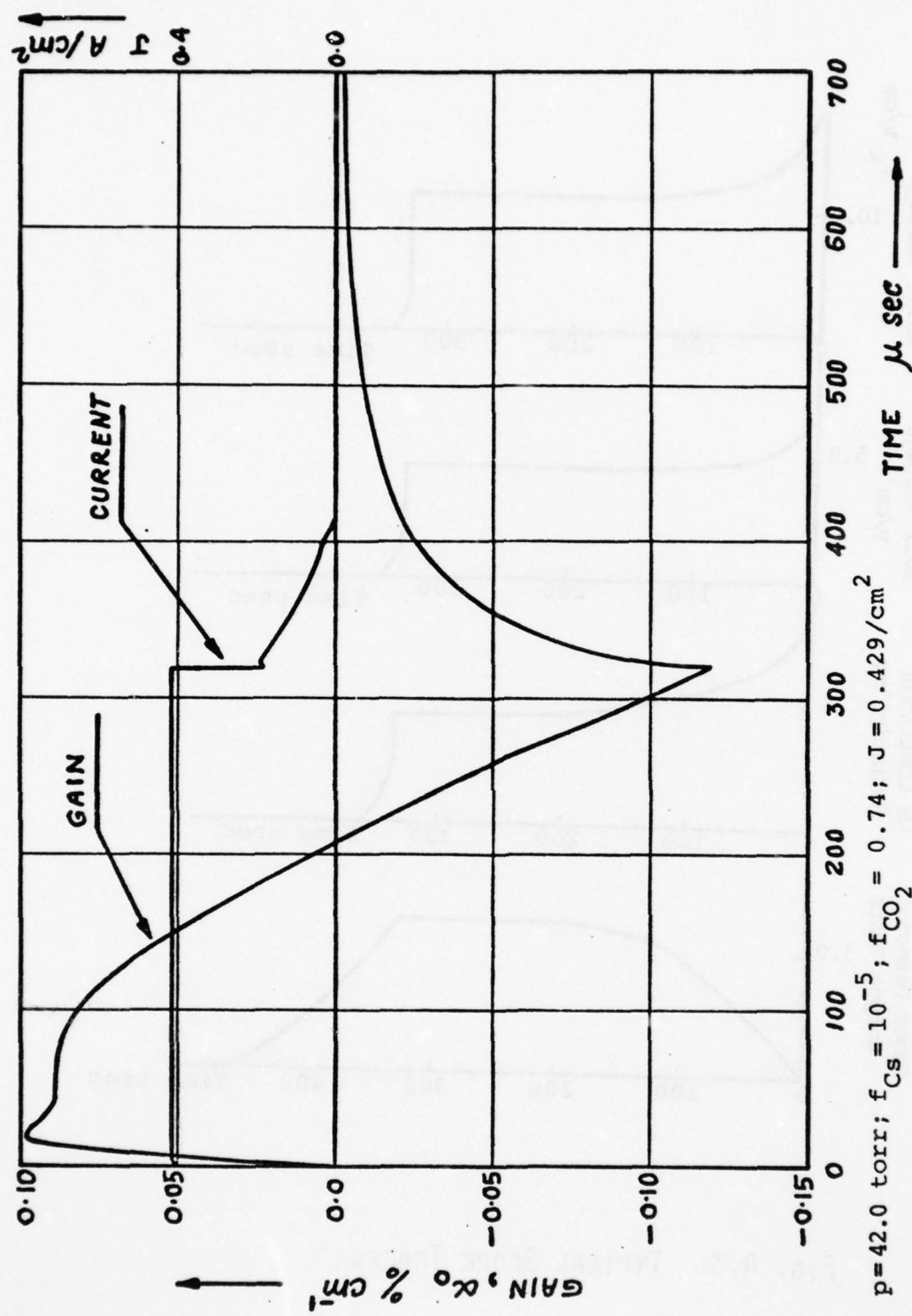


FIG. 4.4: GAIN AND CURRENT DENSITY TIME HISTORY

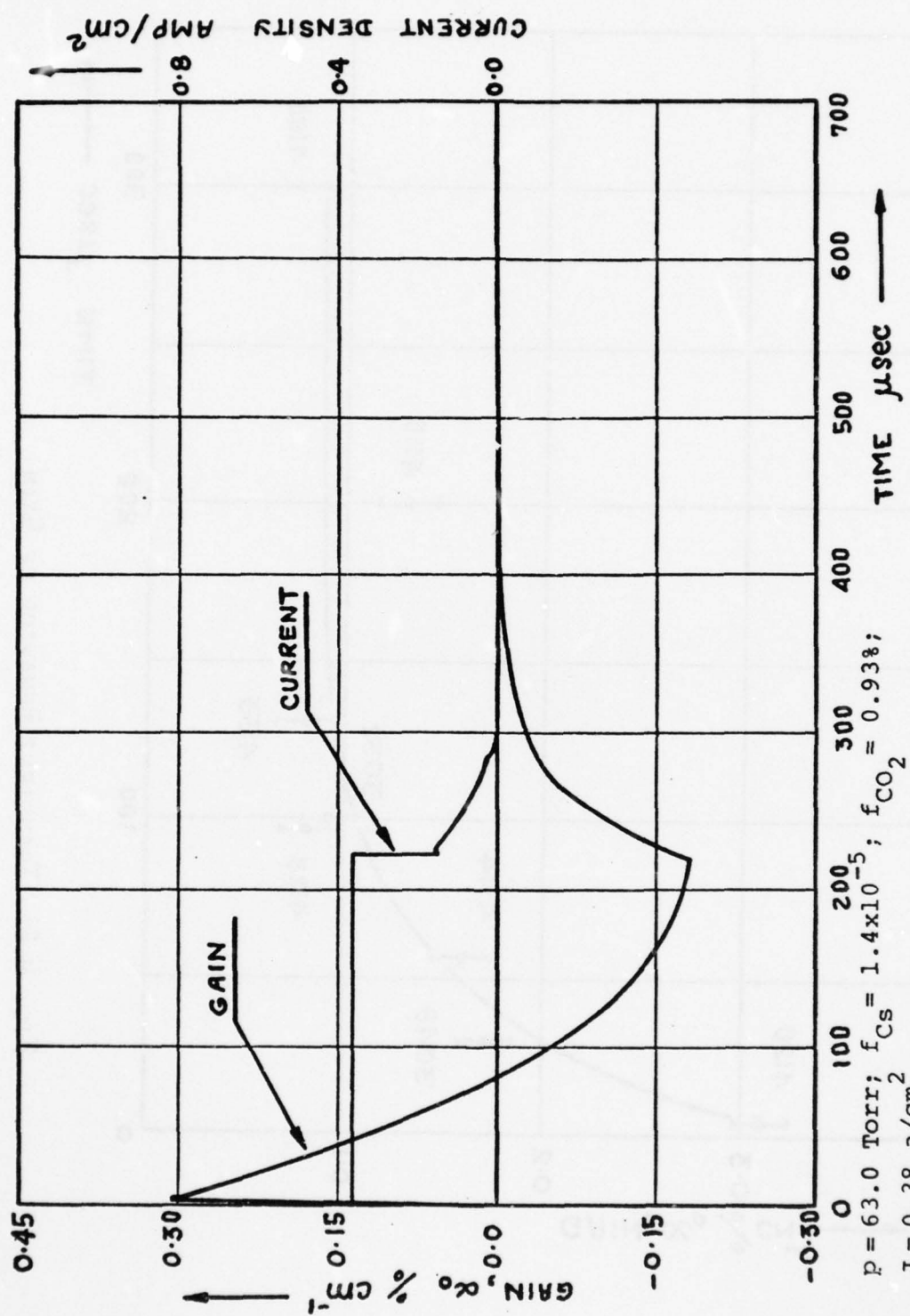


FIG. 4.5: GAIN AND CURRENT DENSITY (EXP. 4120)

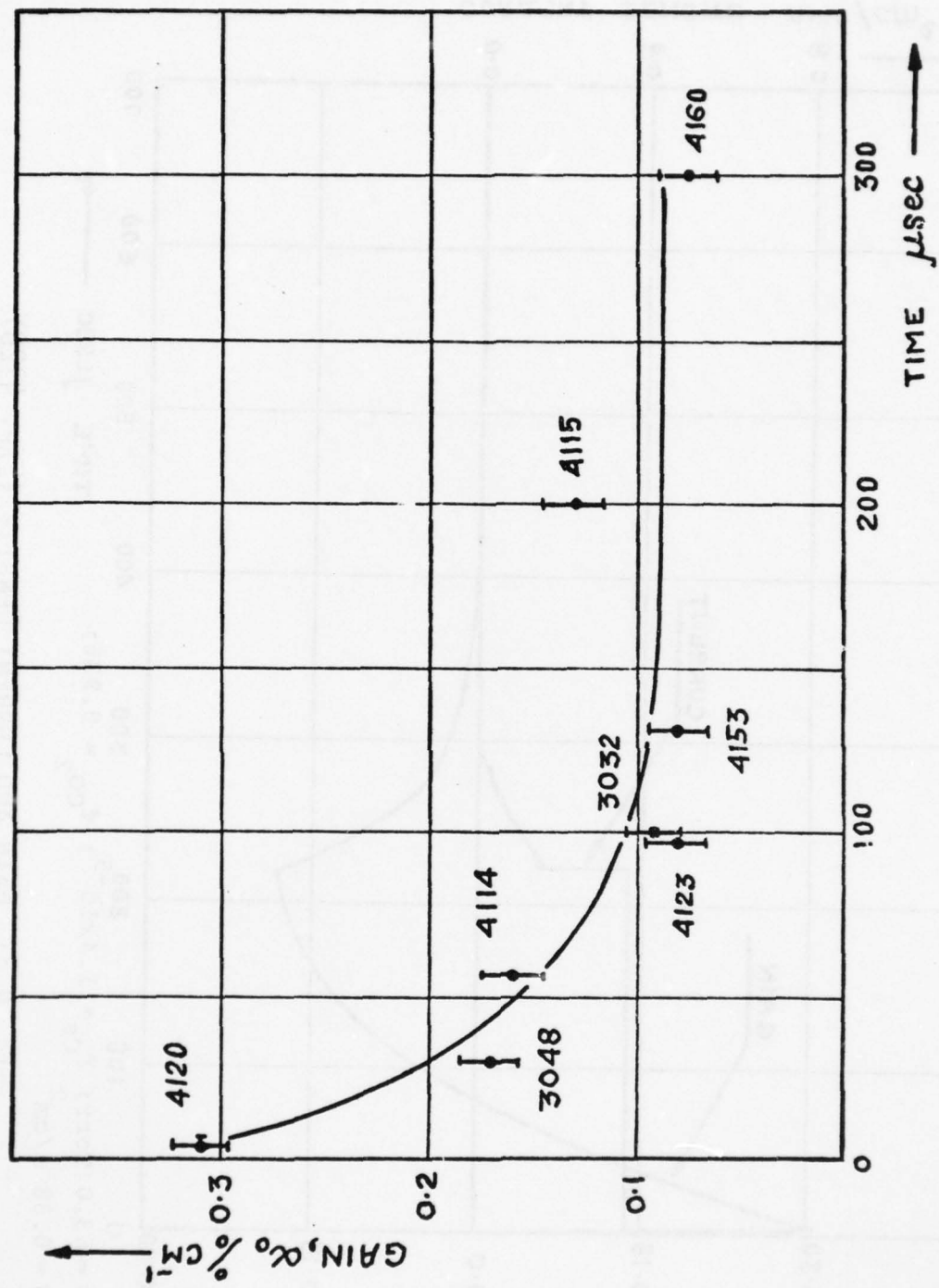


FIG. 4.6: TRANSIENT BEHAVIOR OF GAIN

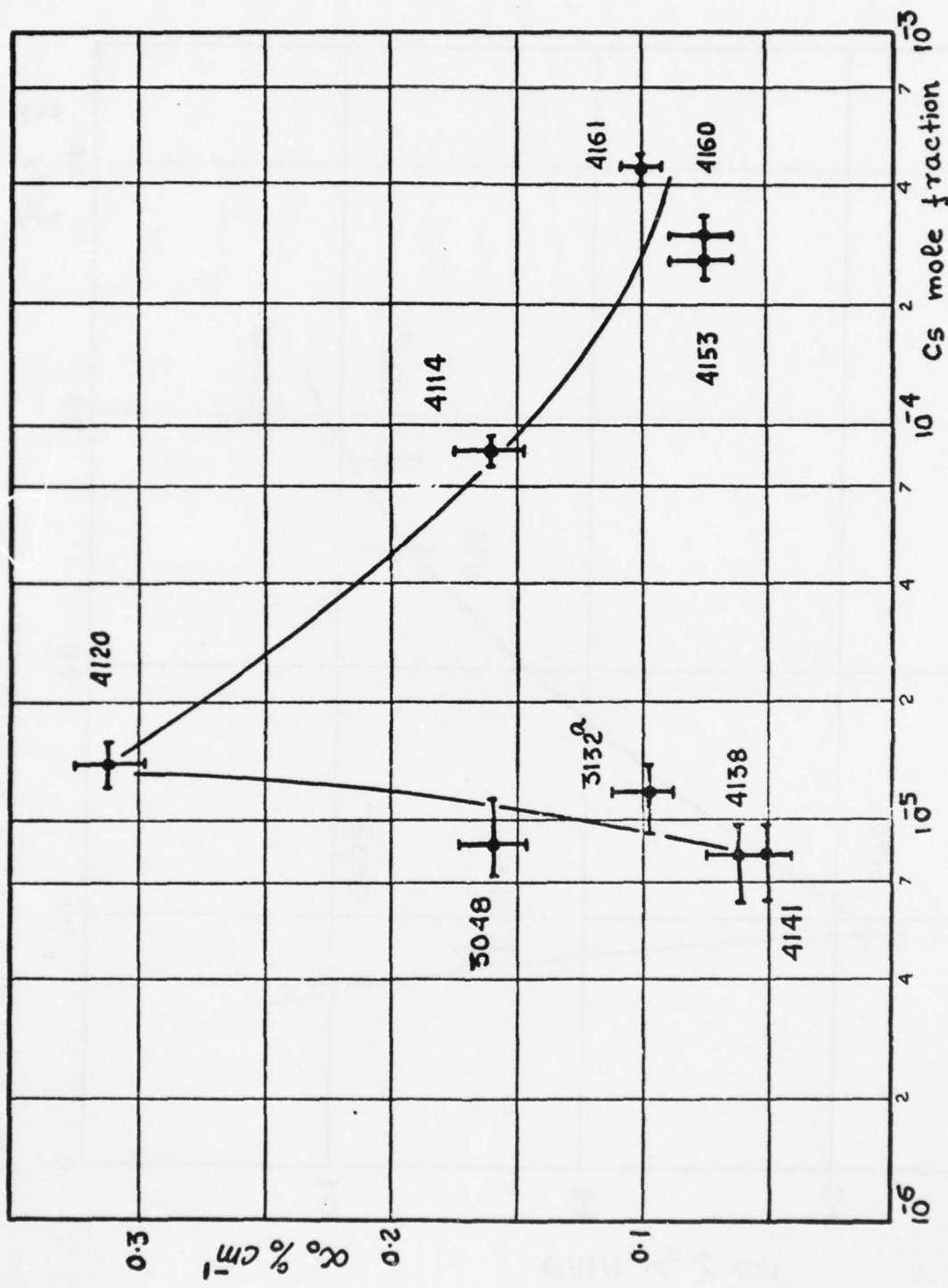


FIG. 4.7: LASER GAIN vs SEED MOLE FRACTION; $B = 0$

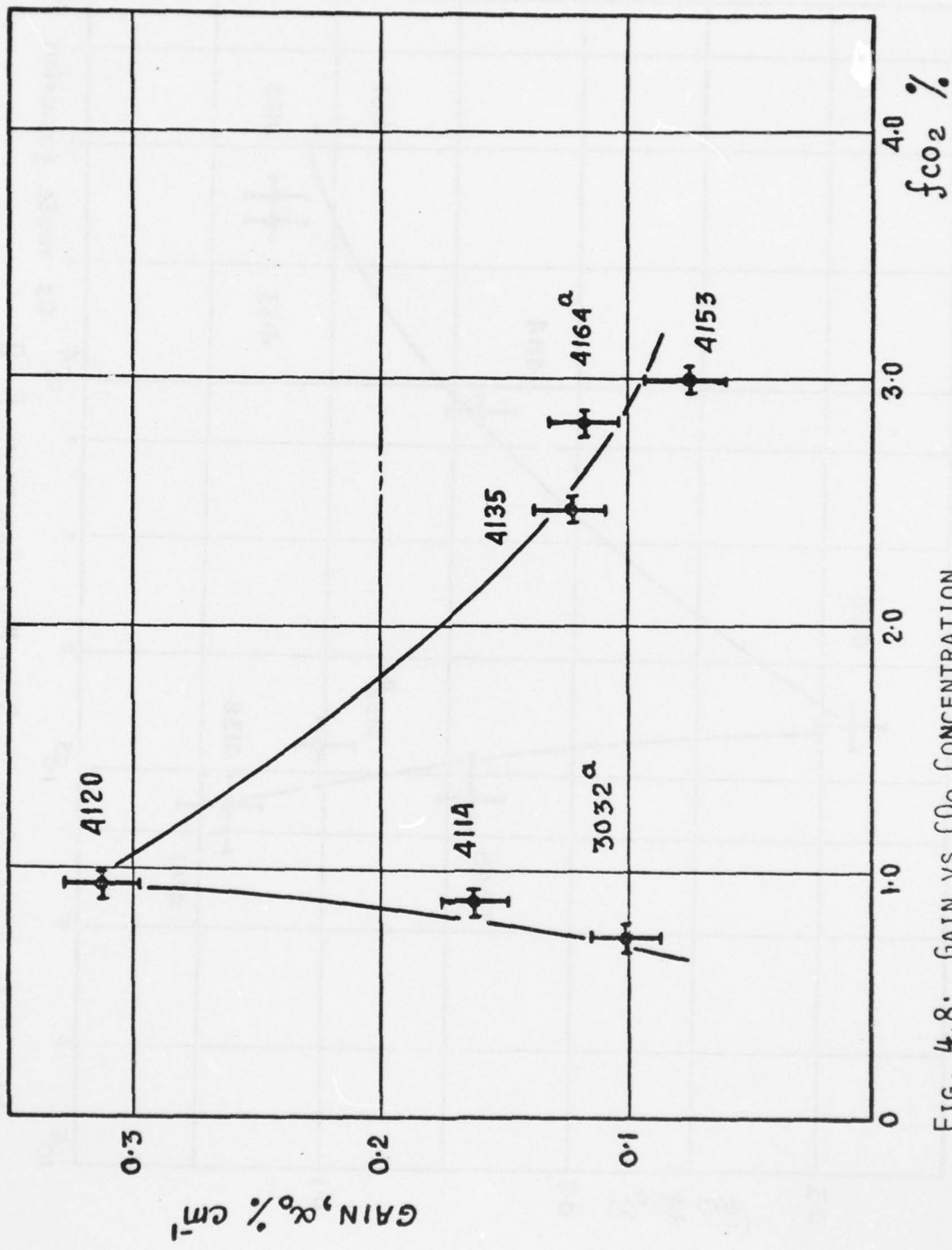
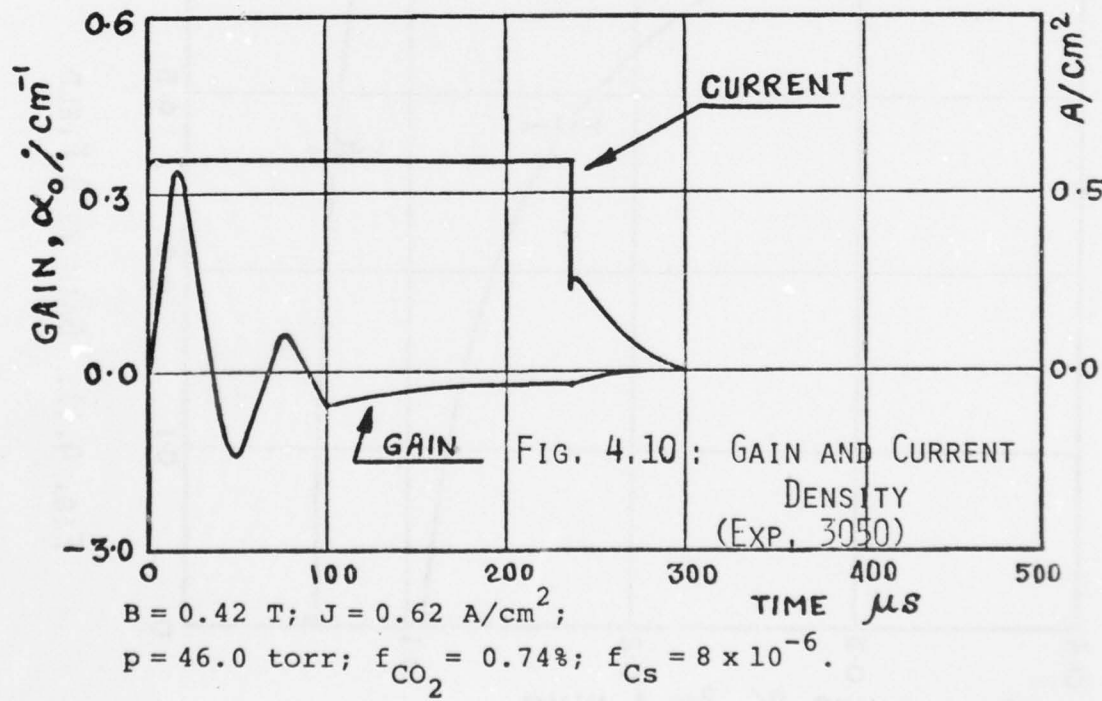
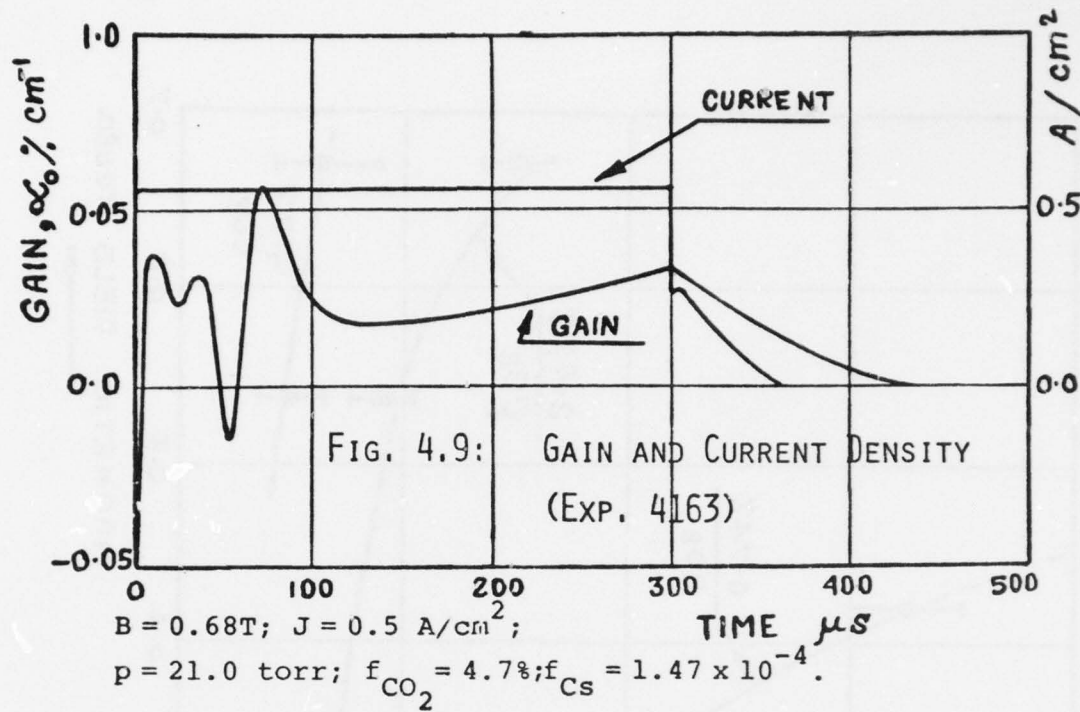


FIG. 4.8: GAIN VS CO_2 CONCENTRATION



AD-A068 190

MASSACHUSETTS INST OF TECH CAMBRIDGE GAS TURBINE AND--ETC F/G 20/5
FUNDAMENTAL MECHANISMS OF NONEQUILIBRIUM MHD LASING PHENOMENA. (U)
DEC 78 J L KERREBROCK

F44620-76-C-0067

UNCLASSIFIED

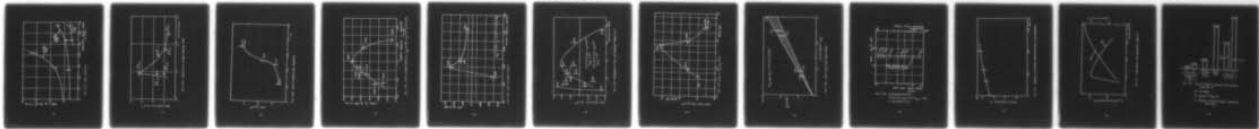
5 OF 5

AD
A068190



AFOSR-TR-79-0506

NL



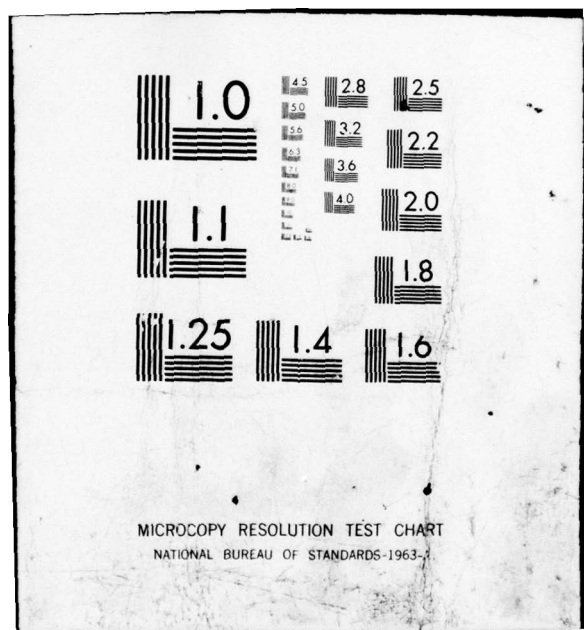
END

DATE

FILMED

7-79

DDC



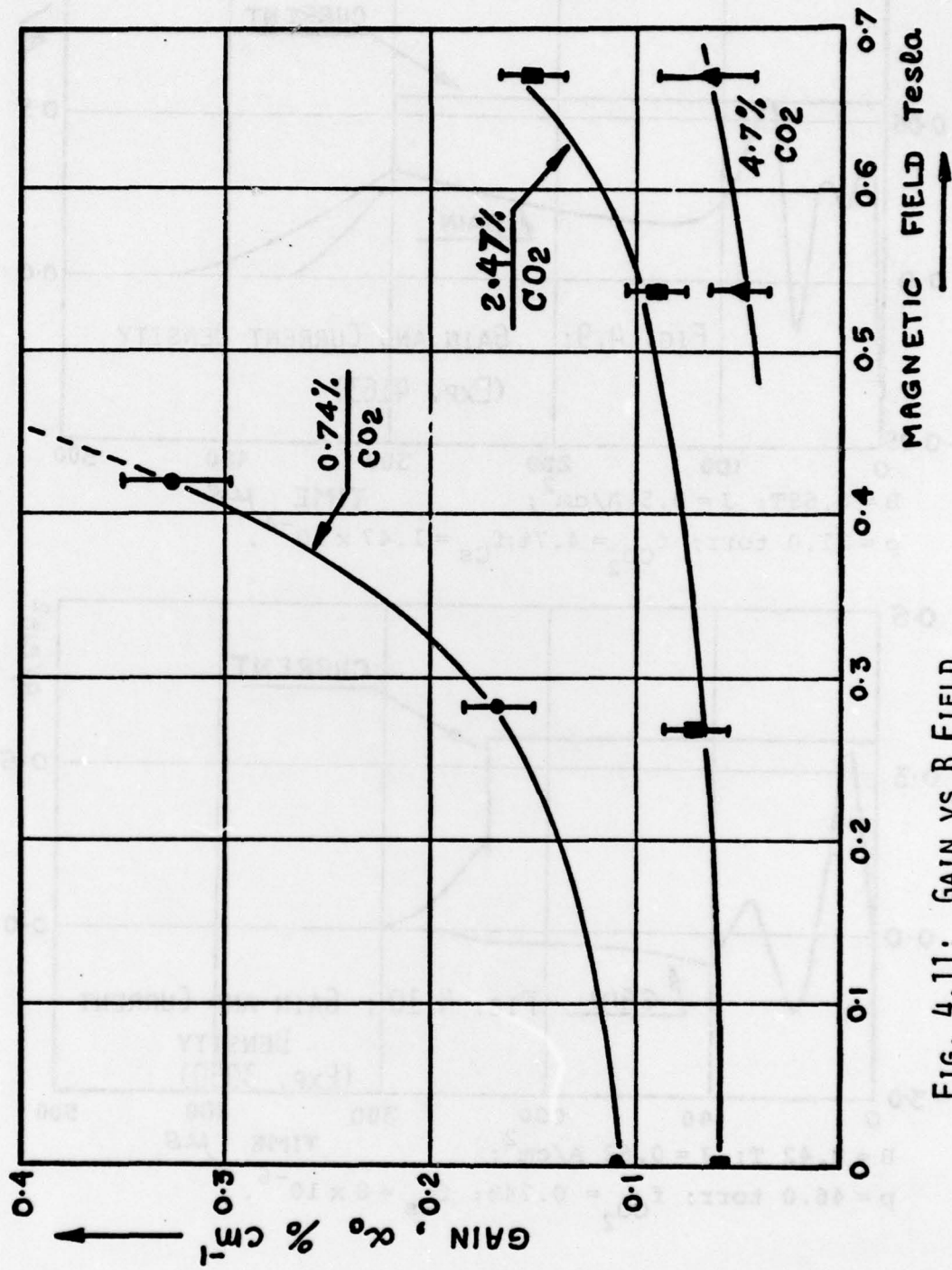


FIG. 4.11: GAIN vs B FIELD

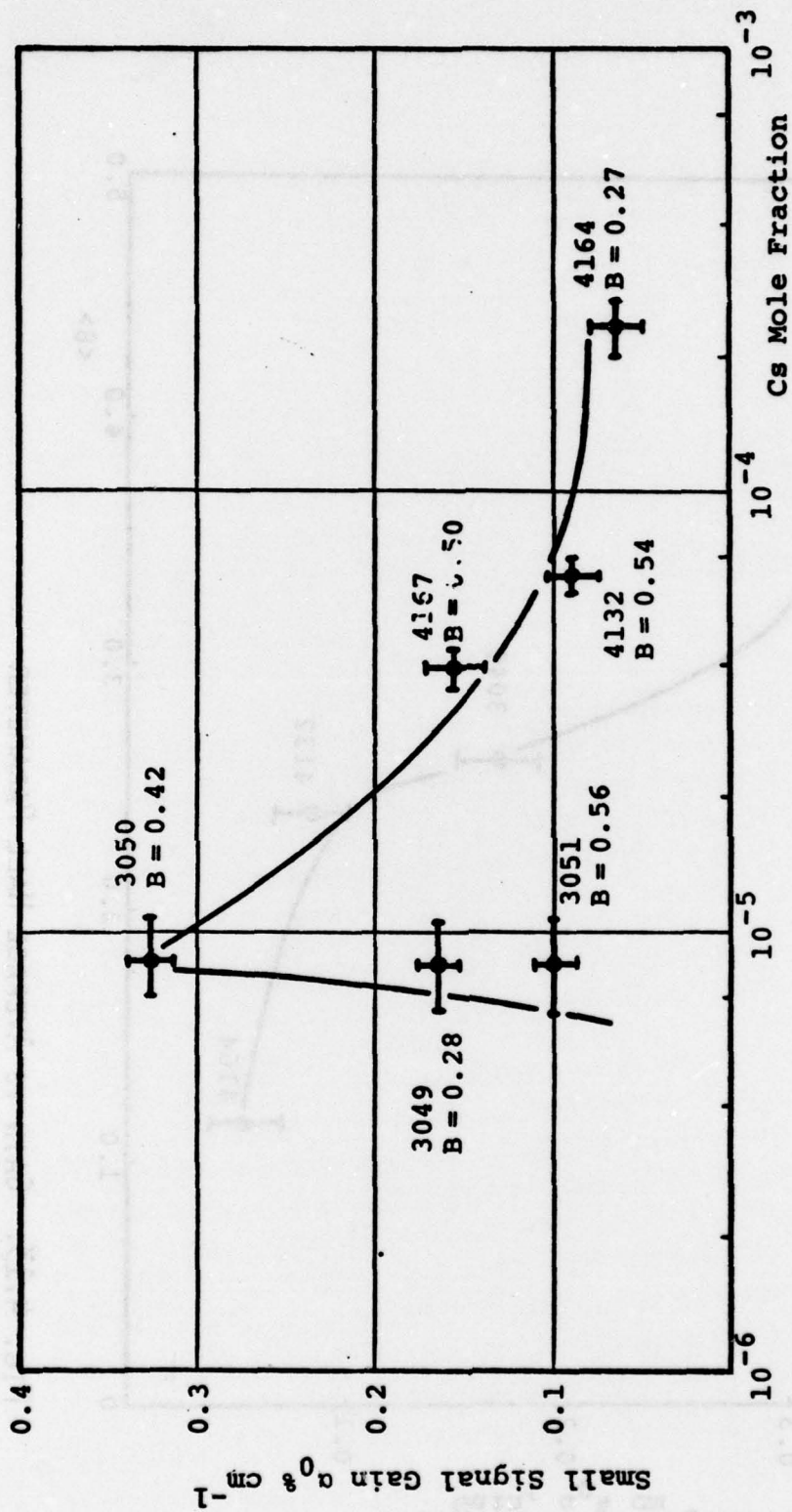


FIG. 4.12: LASER GAIN VS CS MOLE FRACTION $B \neq 0$

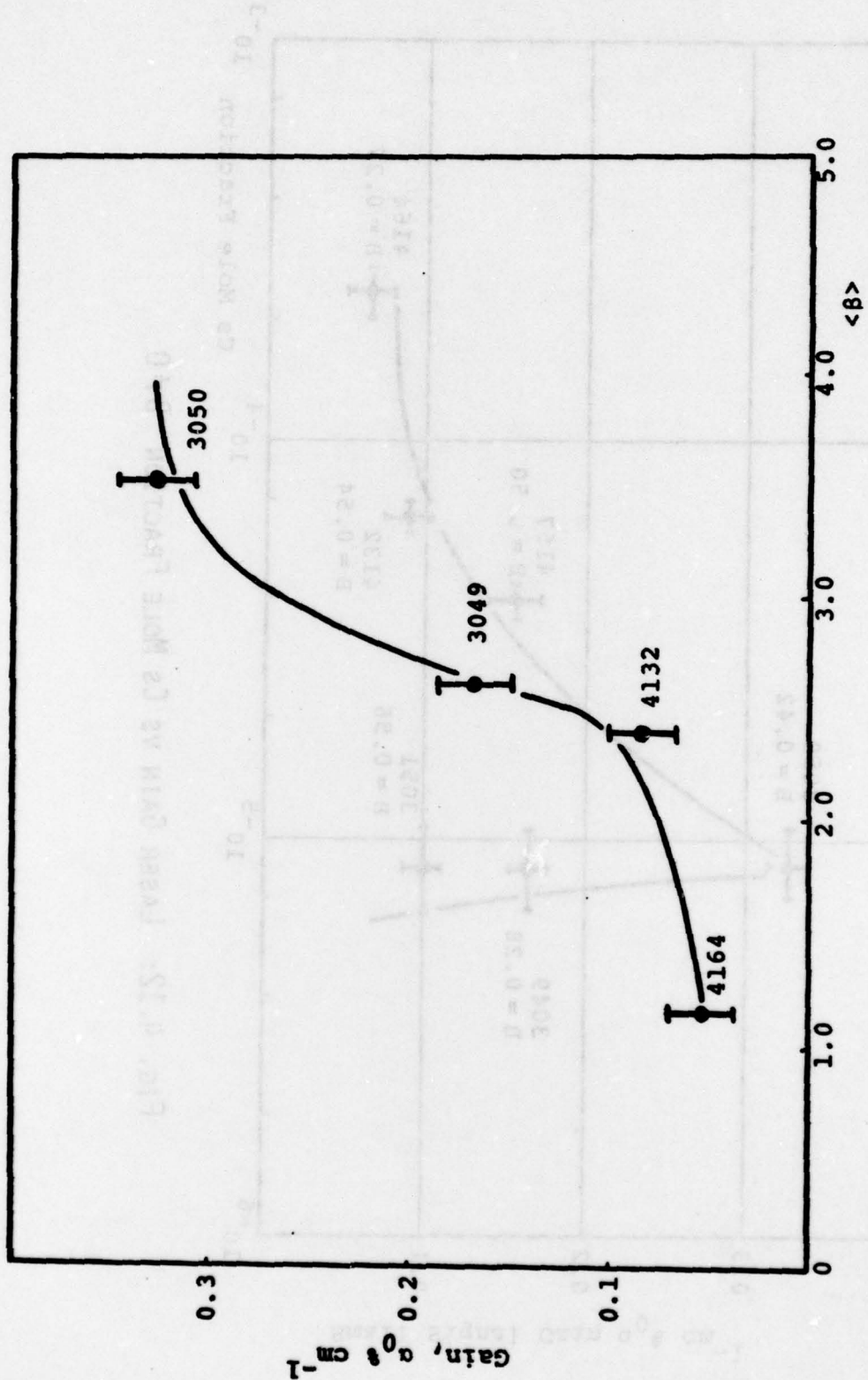


Fig. 4.13: GAIN vs AVERAGE HALL PARAMETER

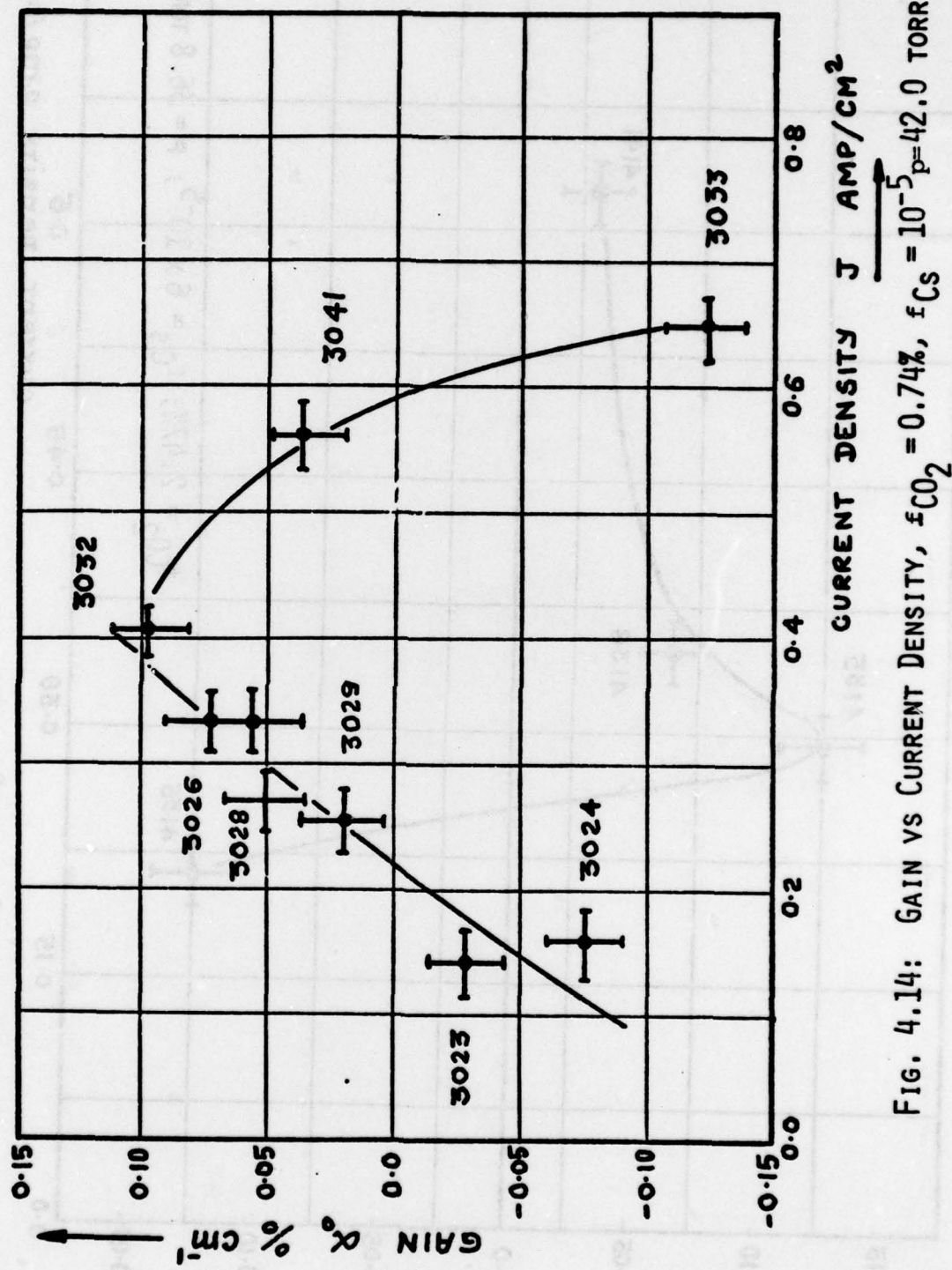


FIG. 4.14: GAIN vs CURRENT DENSITY, $\xi_{\text{CO}_2} = 0.74\%$, $f_{\text{CS}} = 10^{-5}$, $p = 42.0$ TORR

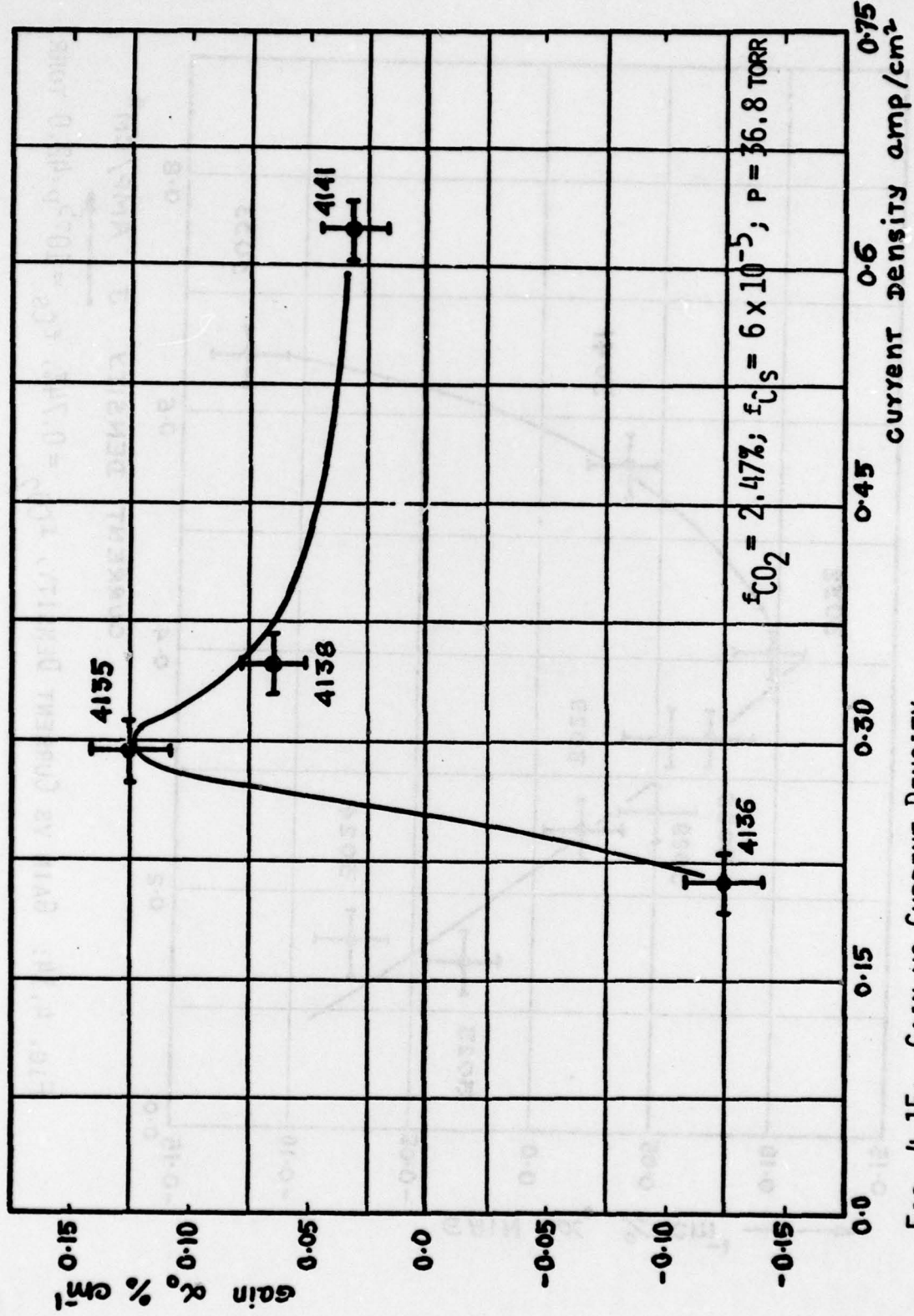


FIG. 4.15: GAIN VS CURRENT DENSITY

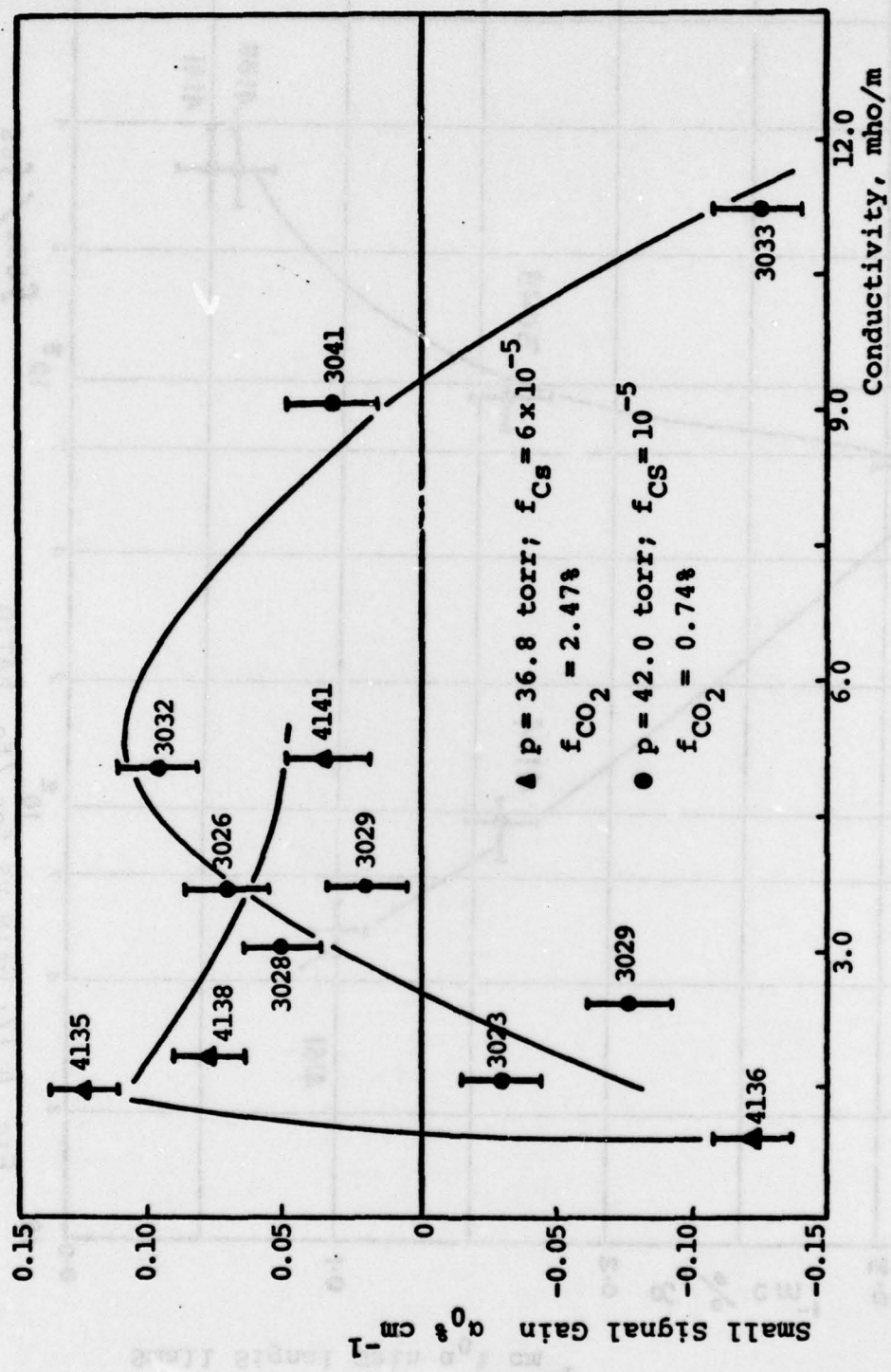


FIG. 4.16: DEPENDENCE OF GAIN ON ELECTRICAL CONDUCTIVITY

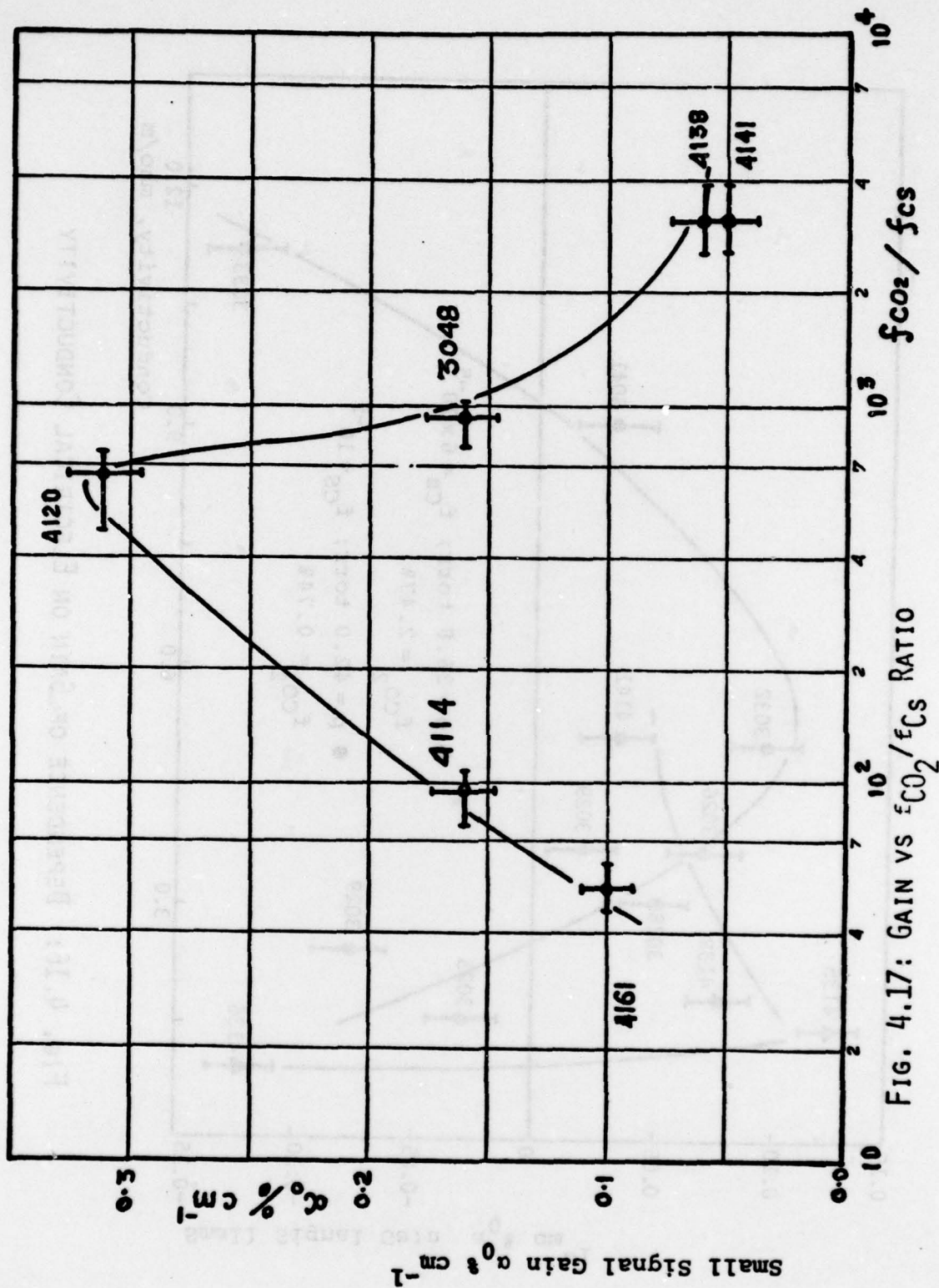


FIG. 4.17: GAIN VS $\epsilon_{\text{CO}_2} / \epsilon_{\text{CS}}$ RATIO

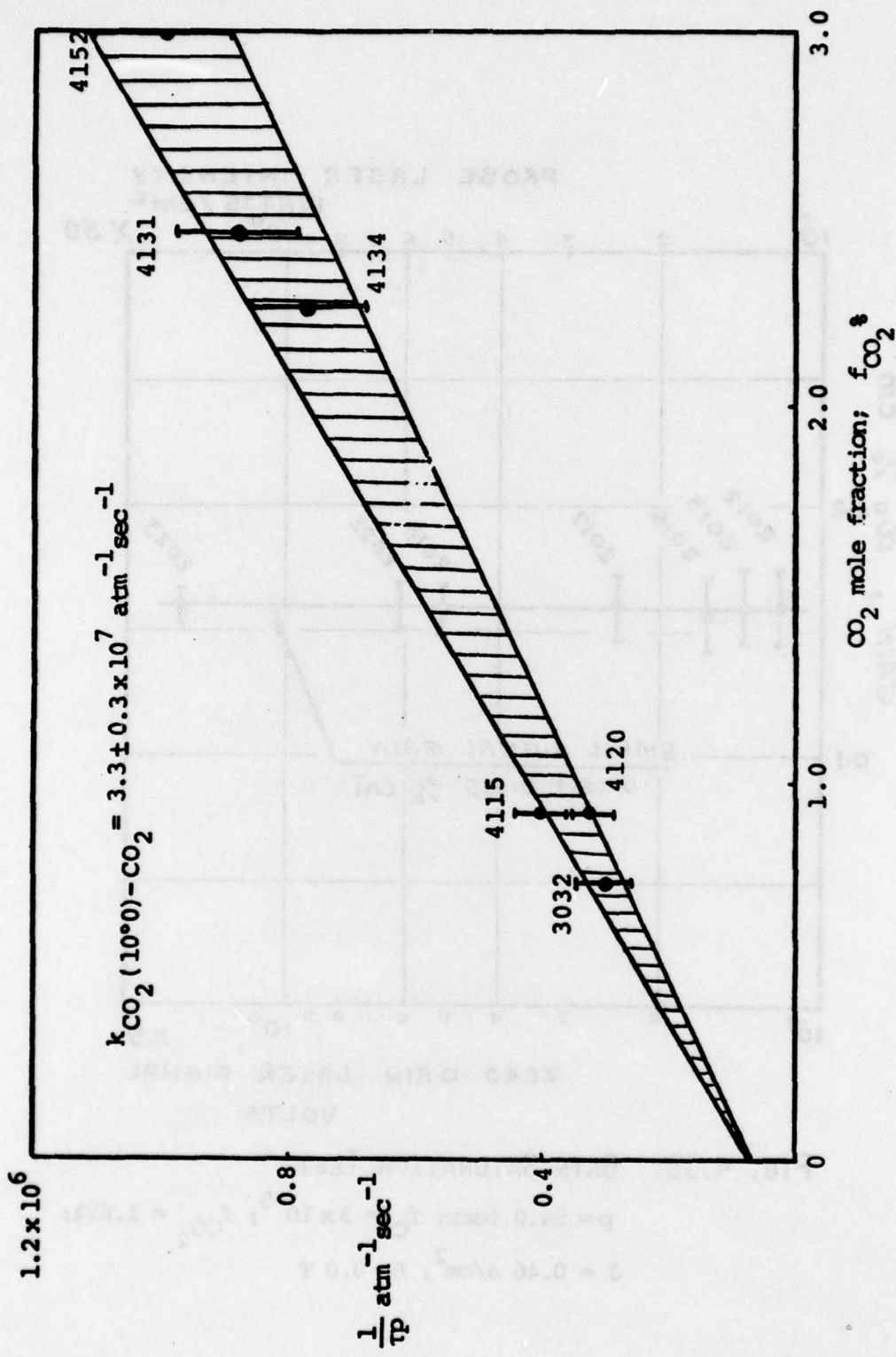


FIG. 4.18: LOWER LASER LEVEL DEACTIVATION

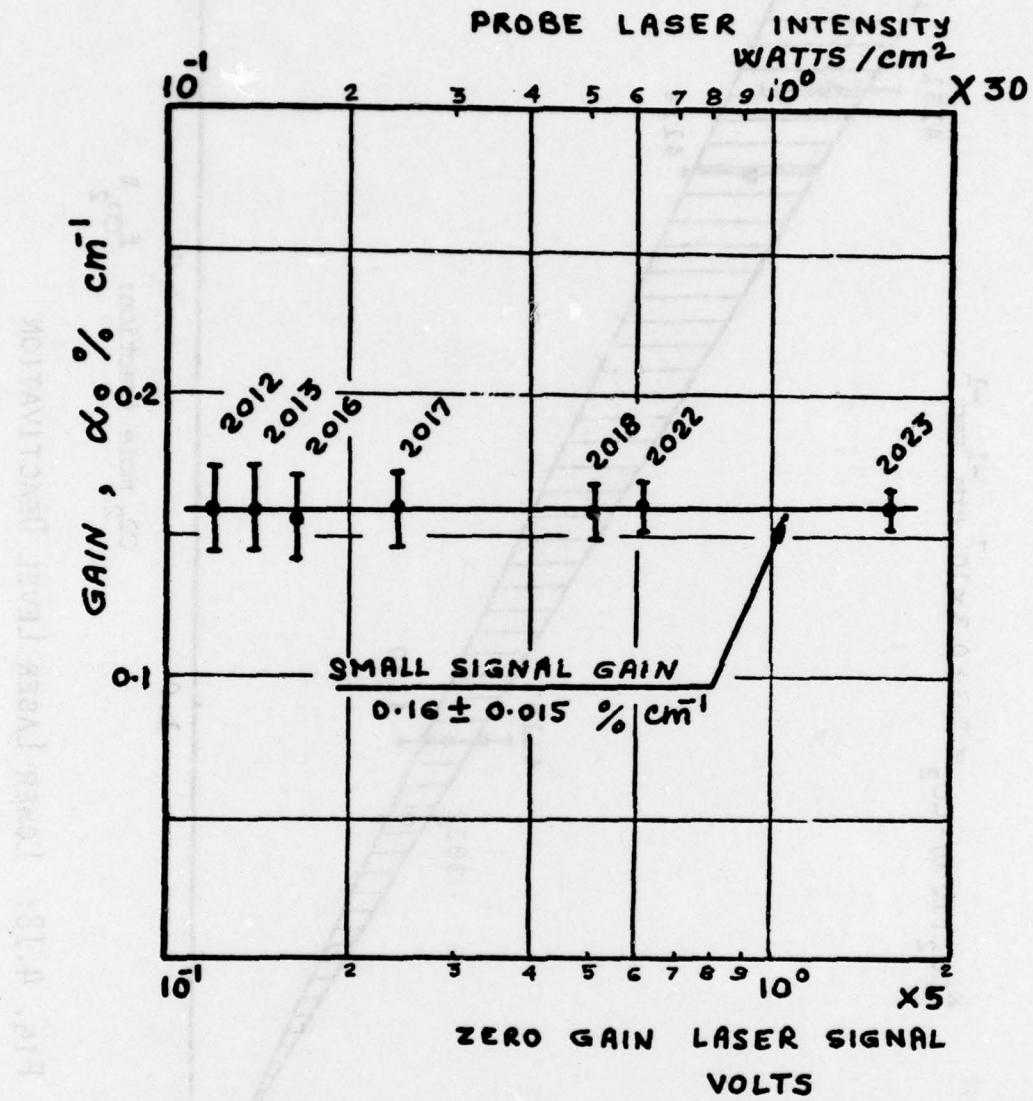


FIG. 4.19: GAIN SATURATION TEST

$$p = 54.0 \text{ torr}; f_{\text{Cs}} = 3 \times 10^{-5}; f_{\text{CO}_2} = 1.67\%;$$

$$J = 0.46 \text{ a/cm}^2; B = 0.0 \text{ T}$$

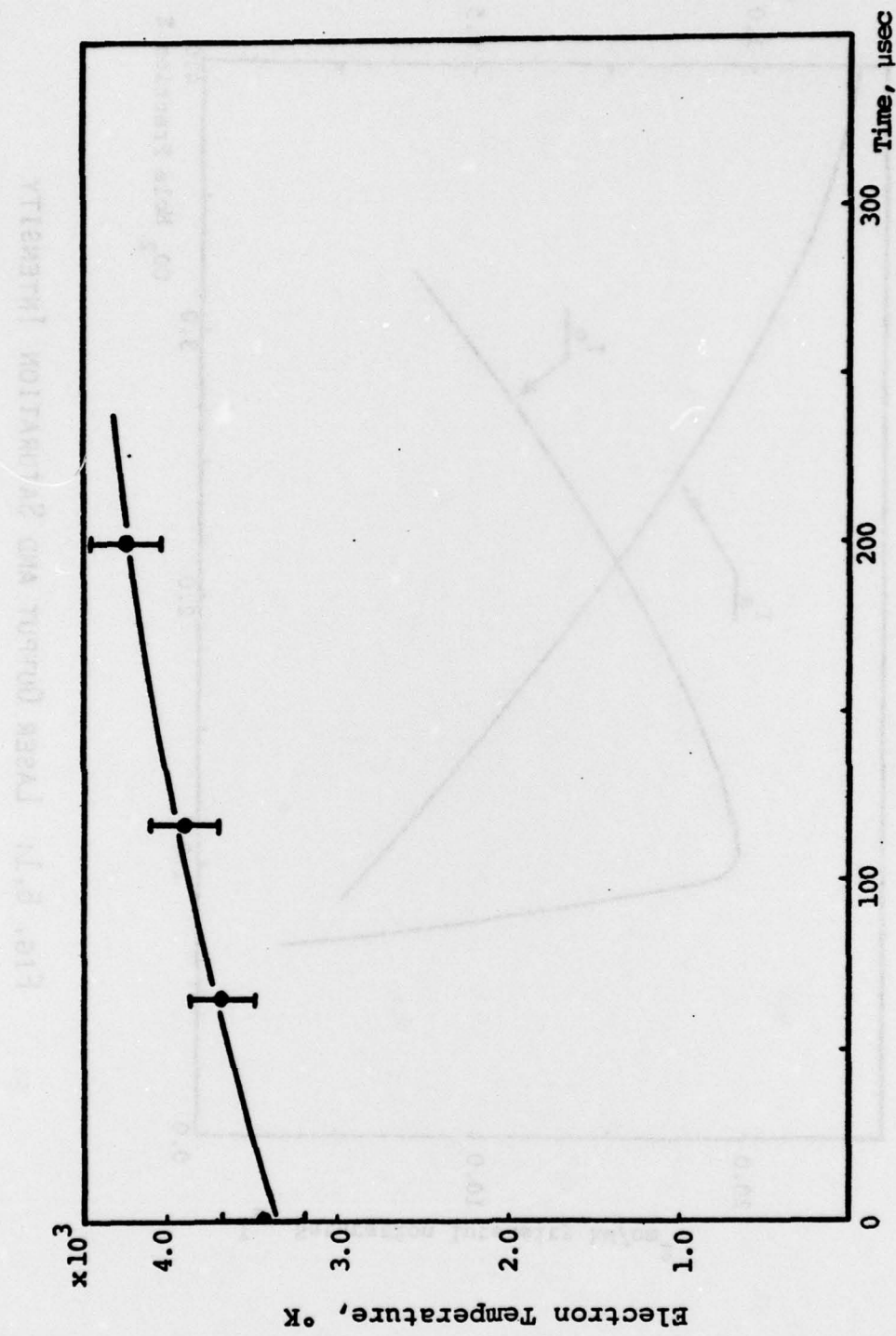


FIG. 6.1: LASER OUTPUT AND SATURATION INTENSITY

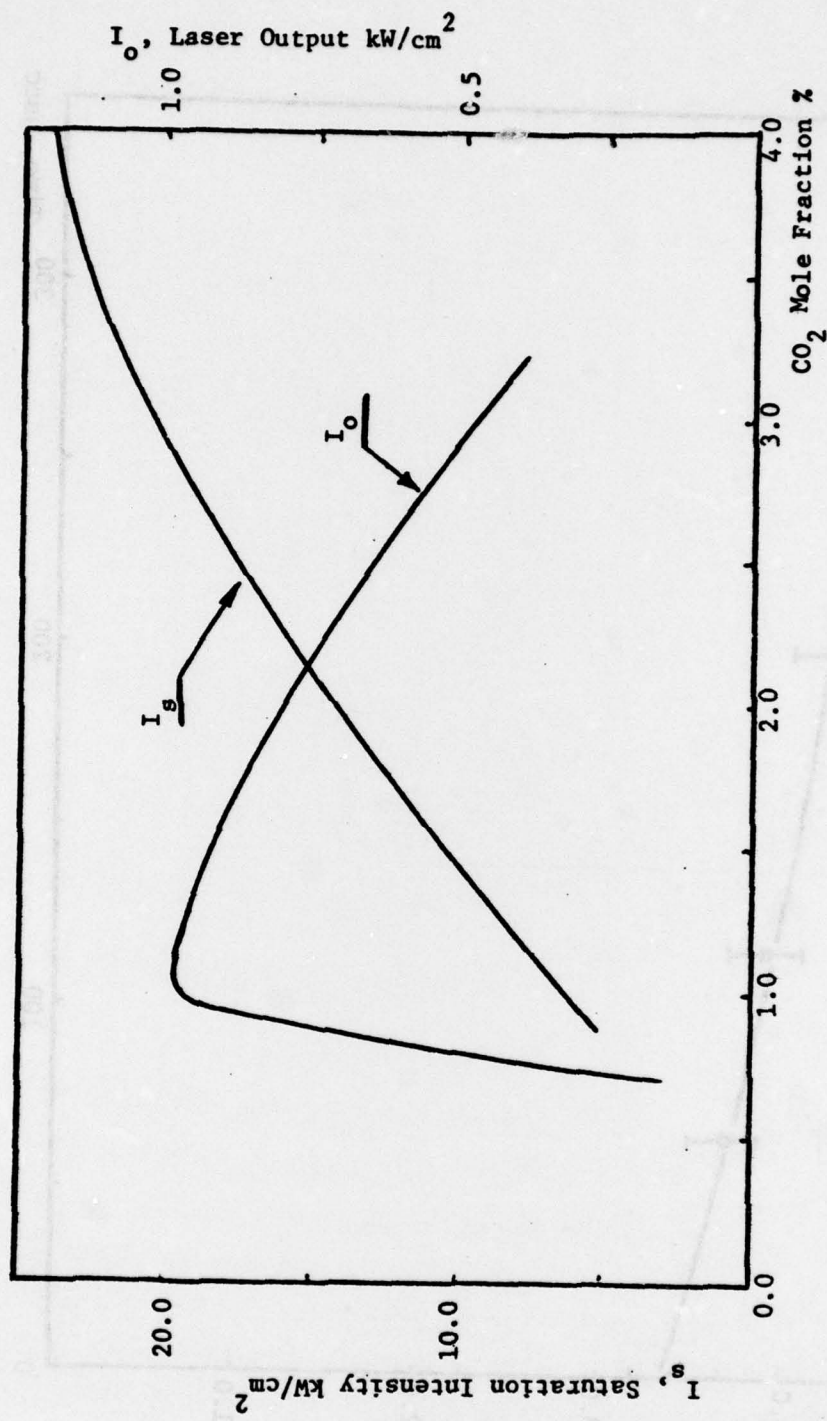


FIG. 6.1: LASER OUTPUT AND SATURATION INTENSITY

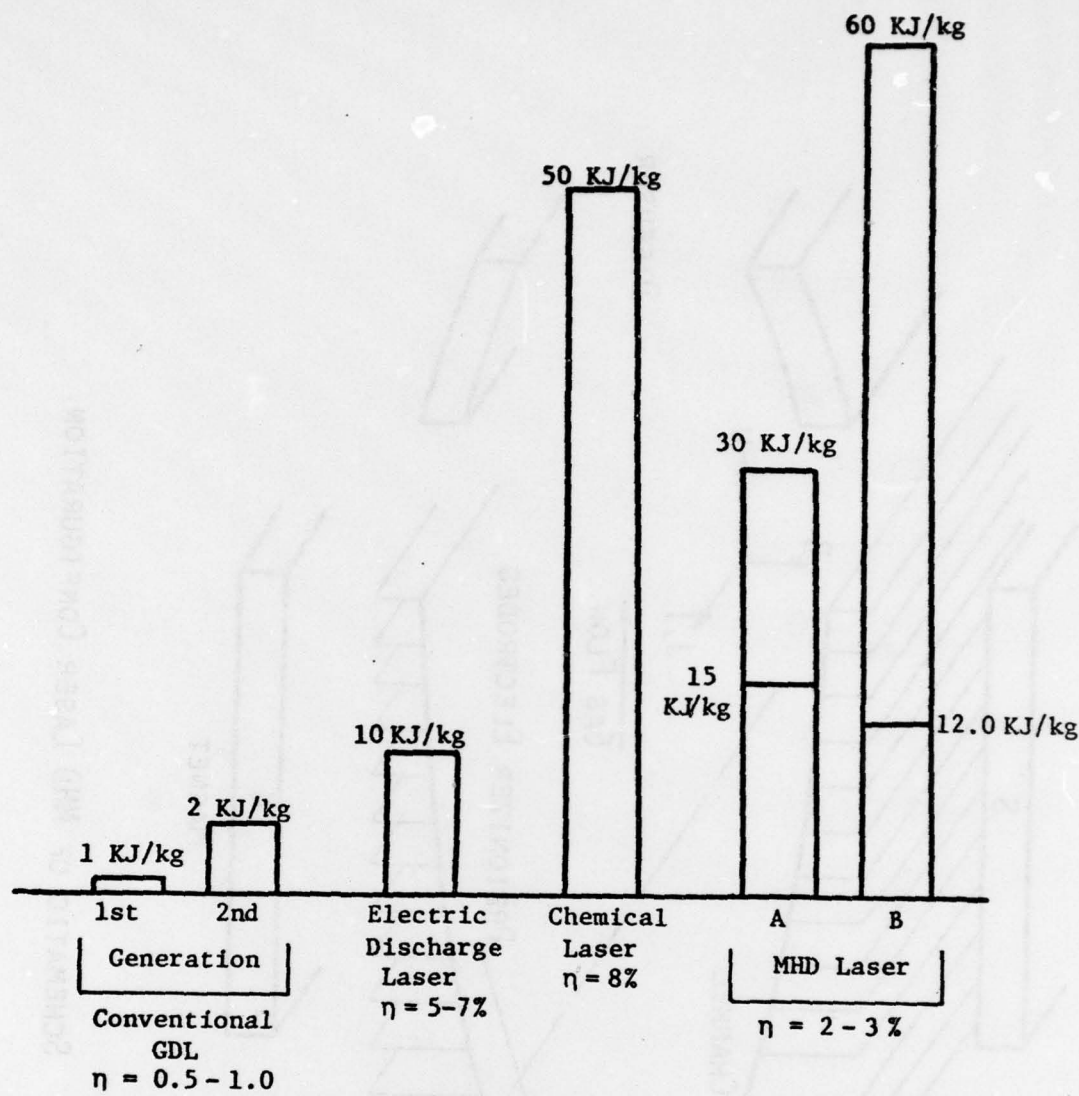


FIG. 6.2: SPECIFIC POWER OF VARIOUS LASER SYSTEMS
AFTER REF. 23

A - THIS WORK

B - WALTER'S¹² ANALYSIS

η - THERMAL TO OPTICAL ENERGY CONVERSION
EFFICIENCY

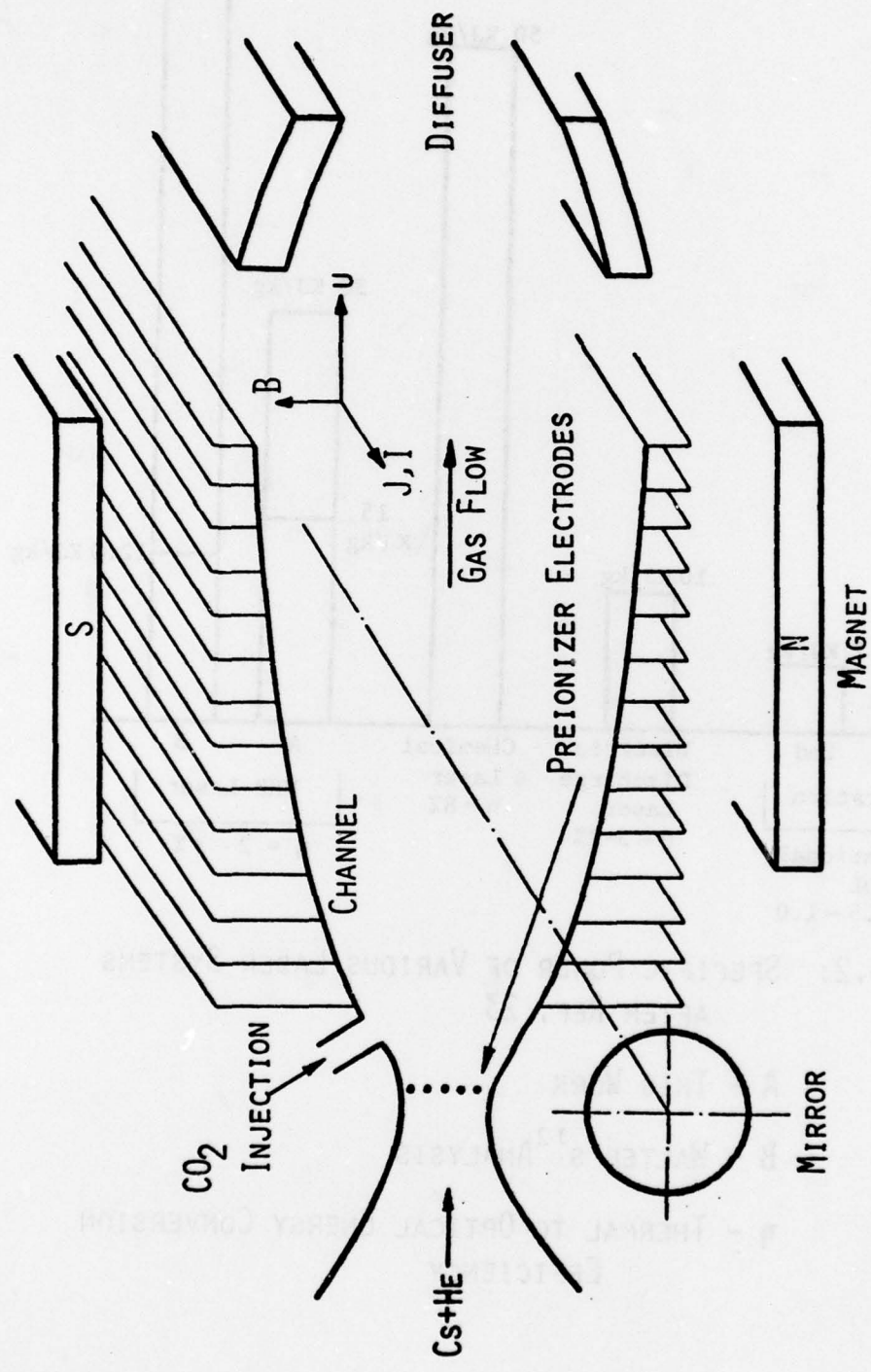


FIG. 6.3: SCHEMATIC OF MHD LASER CONFIGURATION.